

2013

Surface Modifications in Adhesion and Wetting

Jonathan E. Longley
Lehigh University

Follow this and additional works at: <http://preserve.lehigh.edu/etd>



Part of the [Chemical Engineering Commons](#)

Recommended Citation

Longley, Jonathan E., "Surface Modifications in Adhesion and Wetting" (2013). *Theses and Dissertations*. Paper 1546.

This Dissertation is brought to you for free and open access by Lehigh Preserve. It has been accepted for inclusion in Theses and Dissertations by an authorized administrator of Lehigh Preserve. For more information, please contact preserve@lehigh.edu.

Surface Modifications in Adhesion and Wetting

By

Jonathan Longley

A Dissertation

Presented to the Graduate and Research Committee

of Lehigh University

in Candidacy for the Degree of

Doctor of Philosophy

in

Chemical Engineering

Lehigh University

May 2013

Copyright

Longley, Jon

All Rights Reserved

Certificate of Approval

Approved and recommended for acceptance as a dissertation in partial fulfillment of the requirements for the degree of Doctor of Philosophy.

Date

Professor Manoj K. Chaudhury
Dissertation Advisor/Committee Chair

Accepted Date

Other Committee Members:

Anand Jagota
Professor of Chemical Engineering

Andrew Klein
Professor of Chemical Engineering

Raymond A. Pearson
Professor of Materials Science and Engineering

Mark A. Snyder
Professor of Chemical Engineering

Acknowledgements

I would like to express my sincere gratitude to my advisor, Professor Manoj K. Chaudhury, for all the guidance and support throughout the course of my PhD. I am extremely grateful to have worked with such a great scientist and look forward to applying the skills I have learned from him in my future career. In addition to discussing scientific problems, I also enjoyed our discussions on philosophy and the scientific methods of research. I appreciate the flexibility he provided, so that I was able to study a wide variety of projects, which opened my eyes to the vast array of fascinating and interesting aspects of surface science.

I would like to thank my committee members, Prof. Anand Jagota, Prof. Raymond A. Pearson, Prof. Andrew Klein and Prof. Mark A. Snyder, for all their suggestions and critical reviews of the work. I am very grateful to Prof. Anand Jagota and Prof. Raymond A. Pearson for some extremely useful discussions on fracture mechanics and epoxy formulations. I would like to express my gratitude for the opportunity to collaborate with Prof. Susan Daniel and Prof. L. Mahadevan for the work on droplet motion and blister healing. In addition, I would like to thank the team at Boeing, Dr. Douglas Berry, Dr. Jill E. Seeberg, Dr. Kay Y. Blohowiak and Dr. Joseph H. Osborne, with whom I had many discussions during our teleconferences. In particular I would like to thank Dr. Douglas Berry for his continued interest in this work and for all the help and support he provided.

The staff in the chemical engineering department has provided invaluable assistance throughout the course of my studies and so I would like to acknowledge, John Caffrey, Paul Bader, Tracy Lopez and Barbara Kessler. During my studies I designed many

experiments that required custom parts, and I thank John Caffrey for all his assistance in helping me design and make the necessary components. I would like to thank the current and previous members of Prof. Chaudhury's group for their friendship and support, Chih-Hsiu Lin, Aditi Chakrabarti, Partho Goohpattader and Srinivas Mettu. Through my lab members, I was able to learn about their interesting areas of research, which enriched my experience. During my stay at Lehigh I have been fortunate to make many great friends, Chip Roberts, Chris Keturakis, Pat Robinson, Gautam Kumar, Alex Weldon, Nichole Nadermann and Bu Xu, and I would like to thank them for all of the interesting discussions we have had about research and science. In particular, I would like to acknowledge Chip Roberts, Chris Keturakis and Gautam Kumar for all their constructive criticism of my work and their help with proof reading the dissertation. I would also like to thank my friends and family for their unwavering support throughout the course of my PhD.

The financial support provided by The Boeing Company and the Chemical engineering department is gratefully acknowledged. I appreciate the opportunity to have worked as a teaching assistant for Prof. Manoj K. Chaudhury and Prof. Kamil Klier. I thoroughly enjoyed the opportunity to teach and hope that I may come back to it one day.

Finally, I thank my wonderful wife, Gillian. She has been a source of unfaltering support throughout my studies and I am deeply indebted for her love, patience and understanding.

Table of Contents

Abstract.....	1
CHAPTER 1 Introduction and Background.....	4
1.1 Research Overview	4
1.2 Thermodynamic stability of an epoxy/aluminum joint.....	6
1.3 Silane coupling agents and sol-gel technology	7
1.4 Method of buckling instability to estimate the elastic modulus of thin films.....	13
1.5 Mechanisms of adhesion in epoxy/sol-gel/aluminum adhesive joints.....	18
1.6 Characterization of surface Roughness and the fractal dimension	21
1.7 Methods of adhesive testing and mode mixity	24
1.8 Surface energy gradients and drop motion	27
1.9 The Blister test	28
1.10 References	30
CHAPTER 2 Determination of the Modulus of Thin Sol-Gel films using Buckling Instability.....	35
Abstract	35
2.1 Introduction.....	36
2.2 Experimental Section	41
2.2.1 Preparation of Sol-Gel Solution	41
2.2.2 Surface Preparation and Modification of PDMS elastomeric substrates	41
2.2.3 Coating of sol-gel film on PDMS substrates, testing procedure and the determination of film thickness	42

2.3 Results and Discussion	44
2.3.1 Estimation of the Properties of the Silica type layer.....	44
2.3.2 Estimation of the Elastic Modulus of the sol-gel films.....	46
2.3.3 The effect of the curing temperature on the modulus of the sol-gel films....	51
2.3.4 An empirical correlation between modulus of the sol-gel coating and its adhesive performance	54
2.3.5 Duration of cure at room temperature and the modulus of the sol-gel films	56
2.3.6 Effect of Humidity on a post cured sol-gel thin film	58
2.4. Conclusion	70
2.5 References.....	72

CHAPTER 3 Investigation of Different Additives to Improve the Durability and Barrier Properties of Sol-Gel Reinforced Epoxy/Aluminum Joints in Humid Environments75

Abstract	75
3.1 Introduction.....	75
3.2 Experimental	79
3.2.1 Materials.....	79
3.2.2 Surface Pretreatment	80
3.2.3 Application of sol-gel films to aluminum surfaces	81
3.2.4 Measurement of sol-gel film thickness	81
3.2.5 Coating of sol-gel films on PDMS and the testing procedure for buckling instability	82

3.2.6 Preparation of asymmetric double cantilever beam samples for fracture testing	82
3.2.7 Subcritical crack growth kinetics and measurement of the critical and threshold fracture energies	83
3.3 Results and Discussion	88
3.3.1 Stability of Hydrophobic additives in water/ethanol solutions	88
3.3.3 Uniformity of sol-gel films spin cast from water/ethanol solutions	91
3.3.4 Plain strain modulus of sol-gel coatings modified with different concentrations of MTEOS.....	94
3.3.5 An empirical correlation between modulus of the sol-gel coating and its adhesive performance as a function of the sol-gel coating composition.....	100
3.3.6 Effect of humidity on the buckling morphology of MTEOS:GTMS sol-gel films.....	104
3.4 Summary and Conclusion	111
3.8 References.....	111
CHAPTER 4 Strength of a Sol-Gel Reinforced Joint as a Function of Sol-Gel Curing Temperature, Film Thickness and Aluminum Surface Morphology	117
Abstract	117
4.1 Introduction.....	118
4.2. Experimental.....	123
4.2.1 Surface Pretreatment.....	124
4.2.2 Characterization of surface roughness	125

4.2.3 Estimation of the Hurst exponent and fractal dimension for surface profiles	126
4.2.3.1 Structure Function	128
4.2.3.2 Standard Deviation	129
4.2.3.3 Z_{\max}	129
4.2.3.4 Power Spectrum	130
4.2.4 Evaluation of the effectiveness of the different methods used to estimate the Hurst exponent	131
4.2.5 The Lacunarity and Topothesy	137
4.3. Results and Discussion	139
4.3.1 Effect of sol-gel cure temperature and film thickness on the strength of Epoxy/sol-gel/Aluminum joints	139
4.3.1.1 Grit-blasted Substrates	139
4.3.1.2 FPL etched Substrates	141
4.3.1.3 Polished Substrates	142
4.3.1.4 120 grit sanded Substrates	145
4.3.3 Summary of fracture results	149
4.3.4 Evaluation of the Hurst Exponent on Grit-blasted and Sanded surfaces	150
4.3.4.1 Evaluation of different measurement techniques to determine the Hurst Exponent	151
4.3.4.2 The Hurst Exponent for grit-blasted and sanded surfaces	154

4.3.4.3 An anomalous diffusion coefficient (D) to characterize the Lacunarity of a simulated surface profile and a qualitative relationship between D and the expected fracture toughness of a joint	158
4.3.4.4 Estimation of the anomalous diffusion coefficient of grit-blasted and sanded surfaces	162
4.3.5 Plastic zone size fluctuation as evidence for non-uniform crack growth in grit-blasted samples	167
4.4 Summary and Conclusion	168
4.5 References	170
CHAPTER 5 Drop Motion Induced by Repeated Stretching and Relaxation on a Gradient Surface with Hysteresis.....	174
Abstract	174
5.1 Introduction.....	175
5.2 Experimental	176
5.2.1 Preparation and characterization of surface energy gradients.....	176
5.2.2 Droplet ratcheting motion on a linear gradient surface.....	177
5.3 Results and Discussion	179
5.3.1 Characterization of linear surface energy gradients.....	179
5.3.2 Characterization of radial surface energy gradients.....	181
5.3.3 The mechanism of droplet motion on linear gradients.....	182
5.3.4 Motion of drops on radial gradients	190
5.4 Summary and Conclusions	191
5.5 References	192

CHAPTER 6 How a Blister Heals	195
Abstract	195
6.1 Introduction.....	195
6.2 Experimental	197
6.2.1 Materials.....	197
6.2.2 Preparation of thin PDMS films.....	197
6.2.3 Formation of a Blister	198
6.2.4 Determination of Blister Profile.....	199
6.3 Results and Discussion	200
6.3.1 Analysis of fingering wavelength at blister edge and blister final life analysis	200
6.3.2 Analysis of blister profile and estimation of the internal pressure of the blister	203
6.3.3 The energy release rate of a blister healing on a PDMS substrate.....	205
6.3.4 Modeling the escape of air from inside the blister to the surroundings	206
6.3.5 Evidence of Channel formation	209
6.4 Summary and Conclusions	211
6.5. References.....	212
CHAPTER 7 Summary and Future Work.....	214
7.1 Summary	214
7.2 Future Work.....	219
7.2.1 Elastic modulus of ultra thin sol-gel films	219

7.2.2 Systematic study on the role of micro/nano scale roughness and surface porosity on the fracture strength of an epoxy/aluminum joint	220
7.2.3 Measurement of the diffusion of water in a thin sol-gel film	222
7.2.4 Effect of metal alkoxides as additives in the sol-gel formulation.	224
7.2.5 The use of amine functionalized silanes to form hybrid organic-inorganic sol-gel films for adhesion promotion	226
7.2.6 The effect of nanoscale surface roughness on contact angle hysteresis.....	228
7.2.7 A simple experiment to determine the solubility coefficient of a gas in a thin polymer film	229
7.2.8 Electroless deposition of copper through a hydrogel.....	231
7.7 References	239
Appendix A Preparation of Sol-Gel Solution	243
Appendix B Standard Salt Spray Tests on MTEOS Modified Sol-Gel films	245
Appendix C Analysis of the Induction Time and the Effect of Hysteresis on the Drop Step Size	248

List of Tables

Table 3.1: Stability of sols prepared by replacing GTMS with various additives. The GTMS in the standard sol-gel solution is replaced by the same number of moles of additive (Appendix A). The sols tested consist of a range of Ethanol to water ratios which make up the bulk of the sol. Suitable solution combinations are highlighted in green..... 90

Table 4.1: Thickness of sol-gel films on aluminum, and on aluminum and epoxy fracture surface of x1, x3 and x7 sol-gel reinforced epoxy/sol-gel/aluminum joints. Measurements are conducted in the subcritical crack growth regions close to the crack tip. 148

Table 4.2: Value of the Hurst exponent evaluated for a grit-blasted surface using the SF, Z_{\max} and Power spectrum methods. The adjusted Hurst exponents are calculated using the linear fit parameters given in Figure 4.5. The coefficients of proportionality are also reported. 156

Table 4.3: Value of the Hurst exponent evaluated for a sanded surface using the SF, Z_{\max} and Power spectrum methods. The adjusted Hurst exponents are calculated using the linear fit parameters given in Figure 4.5. The coefficients of proportionality are also reported. 156

Table 4.4: PDF fit results for a grit-blasted surface. The peak and tail regions of the data presented in Figure 4.19 are fit using an equation of the form $P = P_0 \exp x - \mu \sigma m$ 164

Table 4.5: PDF fit results for a sanded surface. The peak and tail regions of the data presented in Figure 4.19 are fit using an equation of the form $P = P_0 \exp x - \mu \sigma m$ 164

Table A1: Composition of standard sol-gel solutions. All values are per 100 ml de-ionized water. m and n represent the volumes used in the Boegel EPII formulation. The values for m and n are reported elsewhere^{1,2}. 244

Table A2: Composition of MTEOS modified sol-gel solutions. The volumes of TPOZ, GAA and Antarox remain the same as given in Table A2 for the standard x1 formulation. 244

List of Figures

- Figure 1.1:** Glycidoxypropyltrimethoxysilane (GTMS). One of the most widely used adhesion promoters to adhere epoxies to metallic surfaces. 9
- Figure 1.2:** Acid catalyzed hydrolysis of a silicon alkoxide. R is typically a methyl or ethyl group. R' can be chosen from a vast selection of function groups. Figure adapted from Ref 18. 10
- Figure 1.3:** Acid catalyzed condensation between two hydrolyzed silicon alkoxides. R' can be chosen from a vast selection of function groups. Figure adapted from Ref 18. 11
- Figure 1.4:** Zirconium-n-propoxide dimer stabilized with acetic acid bridges. R=C₃H₇. 12
- Figure 1.5:** Flow diagram for the formation and application of a sol-gel based adhesive primer onto a metal substrate. The Coating is generated from an aqueous sol of Glycidoxypropyltrimethoxysilane (GTMS) and Zirconium tetrapropoxide (TPOZ). XPS studies²⁸ show the sol-gel/metal interface to be rich in zirconium and the sol-gel/organic resin interface to be silane rich. 13
- Figure 1.6:** Schematic of the buckling of a thin film on a soft compliant substrate. 14
- Figure 1.7:** Interdiffusion of an adhesive into a sol-gel film leading to the formation of an interpenetrating network. Figure adapted from Ref[36]. 19
- Figure 1.8:** Topleft: Schematic of the surface morphology produced on aluminum via phosphoric acid anodizing. TopRight: A TEM image showing the penetration of PS into a porous PAA etched oxide layer on aluminum⁴⁹. Bottom: SEM images of grit-blasted and sanded surfaces²⁷. 21
- Figure 1.9:** Height profiles with different fractal dimensions. Profiles are generated in Matlab using the midpoint technique, see Chapter 4 for a more detailed description. All profiles are normalized and then shifted on the y axis for clarity. 23
- Figure 1.10:** Schematic of the three deformation modes at the crack tip, opening mode (mode I), in-plane shear (mode II), and out of plane shear (mode III). 24

Figure 1.11: Schematic of the ADCB sample. E_1 , E_2 , h_1 , h_2 , a and Δ correspond to the aluminum elastic modulus, epoxy elastic modulus, aluminum thickness, epoxy thickness, crack length and wedge height..... 26

Figure 2.1: Schematic of sol-gel coating for adhesion promotion adapted from reference 13. Coating is generated from an aqueous sol of Glycidoxypropyltrimethoxysilane (GTMS) and Zirconium tetrapropoxide (TPOZ). XPS studies¹⁴ show the sol-gel/metal interface to be rich in zirconium and the sol-gel/organic resin interface to be silane rich. 38

Figure 2.2: Schematic of the buckling of a thin sol-gel layer on a soft compliant PDMS substrate. When a compressive stress σ is applied to PDMS, buckles appear perpendicular to this force. The buckling wavelength λ is a function of the plane strain moduli of the two materials and the thickness of the sol-gel layer..... 39

Figure 2.3: Illustration of sample mount, strain micrometer and spin-coating mount. Mounting brackets (1) are used to firmly secure the PDMS sheet (25x75x2 mm) (2) to the sample mount (3). The sample mount is then loaded onto the locking pins of the micrometer (4). The distance between the fastening blocks on the sample mount can be easily adjusted to ensure that sufficient pre-strain is applied to the PDMS sheet. Locking nuts on the fastening blocks allow this strain to be locked in place. After removing the PDMS loaded sample mount from the micrometer, it was fastened to the spin coating mount (5). After the sol-gel film was spin coated on PDMS, the sample mount was removed from the spin coating mount and placed in the required curing environment. After the required cure had taken place the sample mount was then reattached to the micrometer where the strain was applied and recorded..... 43

Figure 2.4: AFM scan of a PDMS surface treated with a corona discharge buckling under an applied strain. PDMS surfaces are exposed to a corona discharge for 1 min under ambient conditions, 23 °C and 47% RH, subjected to a strain of ~8%. 46

Figure 2.5: SEM micrographs showing the thickness of the sol-gel film on PDMS films for 5 different sol-gel concentrations. Concentrations are displayed in the upper right corner of each image. Samples were cut with a scalpel and mounted on a SEM stub such that the PDMS/sol-gel interface was at 90 ° to the electron gun. Note the change of scale on the images. 47

Figure 2.6: Comparison of Film thickness (h_{SG}) vs. sol-gel concentration measured via two different techniques. Black diamonds correspond to SEM measurements for the sol-gel films cured at 120 °C on a PDMS support and the red squares correspond to the ellipsometry measurements for films cured under identical conditions on silicon wafer. Insert: Ellipsometry results for the thickness of films cured under ambient conditions (23

°C and 47% RH) for 24 hrs as a function of sol-gel concentration. On average, the oven cured films show an ~8 % decrease in thickness compared to the room temperature cured. Error bars are hidden in the marker size. 48

Figure 2.7: The effect of sol concentration ((Zr+Si) vol%) on film thickness (h_{SG}) and buckling wavelength (λ). Black diamonds represent the buckling wavelength vs. sol-gel concentration whereas the red squares represent sol-gel film thickness (as measured by SEM) vs. sol-gel concentration. A linear relationship is observed in the buckling wavelength vs. sol-gel concentration. Here, the buckling wavelength was measured using optical microscopy for films cast from sol-gel concentrations equal to and above 9 vol%. AFM was used for measuring the wavelength of films formed from sol-gel concentrations below 9 vol%. Error bars represent one standard deviation of the data. Sol-gel films were cured at 120 °C. Insert - Optical microscopy image of buckling on a film cast from a sol-gel concentration of 21 (Si+Zr) vol%. Scale bar represents 50 μ m. 49

Figure 2.8: Relation of buckling wavelength (λ) and plane-strain modulus (\bar{E}_{SG}) to sol-gel film thickness (h_{SG}). Film thickness is measured via SEM. Wavelength data displayed in Figure 3 is re-plotted against film thickness. Using the data in Figure 2.3 it is shown here that the plane-strain modulus is independent of film thickness. Black diamonds represent buckling wavelength vs. sol-gel film thickness, whereas the red squares represent the modulus of the sol-gel thin film. The black line represents a line of best fit on the Buckle wavelength vs. Film thickness data which passes through the origin. The blue dashed lines represent 95% confidence intervals on the Buckle wavelength vs. Film thickness results..... 50

Figure 2.9: Buckling wavelength (λ) and plane-strain modulus (\bar{E}_{SG}) as a function of curing temperature. Plane-strain modulus is calculated from the displayed wavelength. Cure time was 30 minutes at approximately ~47% RH. Black diamonds represent the buckling wavelength vs. sol-gel film curing temperature, whereas the red squares represent sol-gel thin film modulus vs. sol-gel film thickness. 53

Figure 2.10: AFM images of the effect of post curing a film after it is aged under ambient conditions for 2 days. The left image shows the buckling wavelength of the film after aging it under ambient conditions (23 °C, 47% RH) for 2 days. The right image shows the effect of post curing this sample at 120 °C for 30 minutes. The wavelength changes from ~1.1 μ m to ~2 μ m. This causes a change in plane strain modulus from 0.2 ± 0.03 GPa to 1 ± 0.3 GPa. If the sol-gel film (65 nm thick) is cured directly at 120 °C for 30 minutes the estimated plane strain modulus is 1.3 ± 0.4 GPa. Buckles for oven cured films are orientated perpendicular to those at room temperature as the buckling is caused by the thermal stress. Thermal stress generates one dimensional buckling due to the geometric confinement of the clamp, this effect is described in detail in the text..... 54

Figure 2.11: Fracture strength (G) of an Aluminium/sol-gel/Epoxy joint under wet and dry conditions versus the curing temperature of the sol-gel primer. The plane-strain modulus (\bar{E}_{SG}) dependence on the curing temperature is replotted from Figure 2.9 on the right axis. Black diamonds and blue triangles represent dry and wet fracture strengths respectively versus sol-gel curing temperature. Red squares represent the plane-strain modulus versus the curing temperature. Details of the wet vs. dry fracture experiments are outlined in the text. The Aluminium (2024-T3) substrates are etched in a Forest Products Laboratory solution prior to sol-gel application²⁹ 56

Figure 2.12: The effect of curing time, under ambient conditions (23 °C, 47% RH), on sol-gel film plane-strain modulus (\bar{E}_{SG}). A strain of ~3% was applied to induce buckling. The black diamonds represent the buckling wavelength vs. curing time, whereas the red squares represent sol-gel thin film modulus vs. curing time. 58

Figure 2.13: AFM scans showing the effect of humidity on oven cured sol-gel films (65 nm). The curing temperatures are as shown in the figure. The left column shows the buckling morphology observed after the oven cure for 85 °C - 150 °C cured films exposed to ambient humidity (~47% RH). The right column shows the subsequent change in the surface morphology after being exposed to a high humidity (~98% RH) environment for 15 hrs. Note the change of scale between images..... 60

Figure 2.14: Ratio of the buckling wavelength and ratio of the sol-gel flexural rigidity before exposure to high humidity (RH~98%, for 15 hrs) to that measured after exposure as a function of curing temperature. Black diamonds represent the ratio of the buckling wavelength. Red squares represent the ratio of the sol-gel film flexural rigidity. A ratio greater than 1 indicates a decrease in wavelength and flexural rigidity due to high humidity exposure. Films cured under ambient conditions (23 °C and RH~47%) were cured for 24 hrs. All other temperature cure times were 30 minutes..... 61

Figure 2.15: Ratio of the buckling amplitude before exposure to high humidity (RH~98%) for 15hrs to that measured after exposure as a function of curing temperature. A ratio greater than 1 indicates a decrease in amplitude due to high humidity exposure. Films cured under ambient conditions (23 °C and RH~47%) were cured for 24 hrs. All other temperature cure times were 30 minutes. 62

Figure 2.16: AFM scans show the morphological evolution of storing an unbuckled 65 nm thick sol-gel film on PDMS at ~98% RH. These films were cured at 55 °C for 30 minutes under ambient humidity (~47% RH) before exposure to ~98% RH. No blisters develop before T=10 min..... 65

Figure 2.17: AFM (left) and SEM (right) images show the effect of storing a 300 nm thick sol-gel films coated on PDMS at ~98% RH for 15 hrs The films were cured at 55 °C for 30 minutes at ambient humidity (47%) before exposing to the ~98% RH

atmosphere. The humidity causes the surface to buckle and blisters to form. The blisters preferentially lie in the valleys of the buckles. 66

Figure 2.18: The effect of pre-strain on the change in buckling morphology due to the storage of buckled sol-gel films in humid environments (~98% RH, for 15 hrs). Pre-strains are shown at the top of the Figure. Films buckled at $\epsilon \sim 1.5\%$ display circular blisters on exposure to high humidity. Films buckled at $\epsilon \sim 4\%$ show a decrease in buckle wavelength. Inset: Line profiles of the films after humid exposure which were initially buckled under $\epsilon \sim 4\%$ 69

Figure 2.19: Schematic of secondary buckle evolution in sol-gel films cured at low temperature $< 55\text{ }^\circ\text{C}$ as a result of humid exposure. Case one is where the film remains adhered to the PDMS substrate. Case two is where the sol-gel film delaminates from the PDMS to form straight sided blisters..... 70

Figure 3.1: Top, schematic of the ADCB sample. E1, E2, h1, h2, a and Δ correspond to the aluminum elastic modulus, epoxy elastic modulus, aluminum thickness, epoxy thickness, crack length and wedge height, respectively. Bottom, micrograph of a view through the epoxy of the ADCB sample; the crack front is clearly visualized..... 84

Figure 3.2: Schematic of the environmental chamber used to conduct the ADCB experiments¹². 86

Figure 3.3: A schematic representation of a typical stress corrosion cracking process. The three crack growth regions are identified along with the critical and threshold fracture energies. Figure is adapted from Krausz et al⁴⁰ 88

Figure 3.4: Hydrophobic additives identified as potential sol-gel modifiers. 89

Figure 3.5: AFM images of sol-gel films made with 4 different additives. In each mixture the GTMS component of the standard sol-gel solution is replaced by same number of moles of the appropriate additive (Appendix A). The MTEOS solution is water based while the BTSE, TESP, PhTEOS coatings were prepared in a 90:10 ethanol/water solution. All films cured at $120\text{ }^\circ\text{C}$. The morphology on silicon wafers is shown in the left column and the morphology on PDMS is shown on the right. 92

Figure 3.6: The effect of changing the GTMS mole fraction (relative to MTEOS) on the thickness of the sol-gel film. As the level of GTMS in the film is decreases the thickness also decreases. Blue triangles, black diamonds and red circles represent the thickness of sol-gel films cured at 45, 55 and $120\text{ }^\circ\text{C}$ for 30 minutes, respectively. 95

Figure 3.7: The effect of changing the GTMS mole fraction (relative to MTEOS) on the plain strain modulus (\bar{E}_{SG}) of the sol-gel film. Blue triangles, black diamonds and red circles represent the plain strain modulus of sol-gel films cured at 45, 55 and 120°C for 30 minutes respectively..... 98

Figure 3.8: Crack velocity vs. energy release rate for epoxy/sol-gel/grit-blasted Al joints for different sol-gel film compositions. The sol-gel composition is altered by varying the molar ratio of MTEOS:GTMS in the coating as described in the text. Open circles correspond to coating prepared with the MTEOS:GTMS ratio of 100:0. Open triangles correspond to coating prepared with the MTEOS:GTMS ratio of 75:25. Open squares correspond to coating prepared with the MTEOS:GTMS ratio of 50:50. Closed circles correspond to coating prepared with the MTEOS:GTMS ratio of 25:75. Closed triangles correspond to coating prepared with the MTEOS:GTMS ratio of 0:100. Details of the formulations are provided in Appendix A. All coatings are cured at 45°C for 30 minutes. All experiments are carried out in an environmental chamber (Figure 3.2) at 26°C and 98%RH. Three regions of subcritical crack growth are identified. 103

Figure 3.9: The effect of changing the GTMS mole fraction (relative to MTEOS) on the critical and threshold fracture energy of an Epoxy/sol-gel/Aluminum adhesive joint. The plain-strain modulus (\bar{E}_{SG}) dependence on the GTMS mole fraction is re-plotted from Figure 3.8 on the right axis. The aluminum surface pretreatment is a standard grit-blast and the sol-gel cure temperature is 45 °C for 30 minutes. The black and red lines represent the critical fracture and threshold fractures energies for an uncoated Epoxy/Aluminum joint. Non-evident error bars are contained within the marker size. 104

Figure 3.10: AFM scans showing the effect of humidity on sol-gel films cured at 120 °C for different ratios of MTEOS to GTMS. The ratio of MTEOS:GTMS is shown on the left. The left column shows the buckling morphology observed after the 120 °C oven cure for films at ambient humidity (~47% RH). The right column shows the subsequent change in the surface morphology after being exposed to a high humidity (~98% RH) environment for 15 hrs. Note the change of scale between images..... 107

Figure 3.11: Ratio of the buckling wavelength before exposure to high humidity (RH~98%, for 15 hrs) to that measured after exposure as a function of MTEOS mole fraction. A ratio greater than 1 indicates a decrease in wavelength due to high humidity exposure. Blue triangles, black diamonds and red circles represent the wavelength ratio of sol-gel films cured at 45, 55 and 120°C for 30 minutes respectively..... 108

Figure 3.12: Ratio of the buckling amplitude before exposure to high humidity (RH~98%) for 15hrs to that measured after exposure as a function GTMS mole fraction. A ratio greater than 1 indicates a decrease in amplitude due to high humidity exposure. Blue triangles, black diamonds and red circles represent the amplitude ratio of sol-gel films cured at 45, 55 and 120°C for 30 minutes respectively..... 108

Figure 3.13: AFM scans showing the effect of humidity on sol-gel films cured at 55 °C for different ratios of MTEOS to GTMS. The ratio of MTEOS:GTMS is shown on the left. The left column shows the buckling morphology observed after the 55 °C oven cure for films at ambient humidity (~47% RH). The right column shows the subsequent change in the surface morphology after being exposed to a high humidity (~98% RH) environment for 15 hrs. In order to form the buckles the samples were exposed to a strain of $\epsilon \sim 4\%$. Note the change of scale between images. 109

Figure 3.14: AFM scans showing the effect of humidity on sol-gel films cured at 45 °C for different ratios of MTEOS to GTMS. The ratio of MTEOS:GTMS is shown on the left. The left column shows the buckling morphology observed after the 45 °C oven cure for films at ambient humidity (~47% RH). The right column shows the subsequent change in the surface morphology after being exposed to a high humidity (~98% RH) environment for 15 hrs. In order to form the buckles the samples were exposed to a strain of $\epsilon \sim 4$. Note the change of scale between images. 110

Figure 4.1: Flow diagram representing the processing parameters involved in preparing an adhesive bond with a sol-gel based surface pretreatment. The diagram also shows the relationship of the elastic modulus to the processing parameters as outlined in Chapters 2 & 3. 119

Figure 4.2: Height profiles generated using the midpoint technique with different values of the Hurst exponent. 134

Figure 4.3: Illustration of the midpoint displacement technique used to generate a fractal surface. Keeping the corner points fixed the points are randomly displaced in the z direction (orthogonal to the plane of the page) according to the method outlined in the text. The numbers represent the order of the displacements. Figure adapted from Ref .11 134

Figure 4.4: Fractal surfaces generated using the midpoint technique with different values of the Hurst exponent. 135

Figure 4.5: Comparison of the output Hurst exponent obtained from the self affine analysis and the input Hurst exponent used to simulate the surfaces shown in Figure 4.4. Three different analysis procedures were investigated, structure function (blue circles), Z_{max} (red squares) and the power spectrum (green triangles). The details of these procedures are outlined in the text. The dependence of the output exponent on the input can be approximated with a linear fit using a least squares regression. The SF yields the following dependence $H_{Out}^{SF} = 0.8H_{In} + 0.08$. The Z_{max} analysis gives $H_{Out}^{Z_{max}} = 0.5H_{In} + 0.4$. Finally the power spectrum results can be approximated by $H_{Out}^{PS} = 0.7H_{In} + 0.02$ 136

Figure 4.6: Three fractal profiles generated with a Hurst exponent of 0.8 and three different values of α . The lacunarity of the profiles is changed by using a different value of α in equation 4.18 used to generate the profiles. The values of alpha used are displayed next to the corresponding profile. Each profile is generated with a different realization of random numbers. In the interest of clarity the profiles are displaced by an arbitrary shift in the direction of the y co-ordinate. 139

Figure 4.7: a. Crack velocity vs. energy release rate (G) for epoxy/sol-gel/grit-blasted-aluminum joints prepared with different sol-gel formulations and cure temperatures. Open circles and open triangles represent films cast from a x1 formulation cured at room temperature (RT, 75 mins) and 120 °C (OV, 30 mins) respectively. Filled circles and filled triangles represent films cast from a x7 formulation cured at room temperature (RT, 75 mins) and 120 °C (OV, 30 mins) respectively. See section 4.2 in the text for a detailed description of the x1 and x7 formulations. Three regions of subcritical crack growth are identified. The red lines represent a least-squares regression fit of equation 3.2 to the data. b. Critical energy release rates (G_c) for epoxy/sol-gel/grit-blasted-aluminum joints prepared with different sol-gel formulations and cure temperatures. c. Threshold energy release rates (G_{th}) for epoxy/sol-gel/grit-blasted-aluminum joints prepared with different sol-gel formulations and cure temperatures. 141

Figure 4.8: a. Crack velocity vs. energy release rate (G) for epoxy/sol-gel/FPLetched-aluminum joints prepared with different sol-gel formulations and cure temperatures. Open circles and open triangles represent films cast from a x1 formulation cured at room temperature (RT, 75 mins) and 120 °C (OV, 30 mins) respectively. Filled circles and filled triangles represent films cast from a x7 formulation cured at room temperature (RT, 75 mins) and 120 °C (OV, 30 mins) respectively. See section 4.2 in the text for a detailed description of the x1 and x7 formulations. Three regions of subcritical crack growth are identified. The red lines represent a least-squares regression fit of equation 3.2 to the data. b. Critical energy release rates (G_c) for epoxy/sol-gel/ FPLetched-aluminum joints prepared with different sol-gel formulations and cure temperatures. c. Threshold energy release rates (G_{th}) for epoxy/sol-gel/ FPLetched-aluminum joints prepared with different sol-gel formulations and cure temperatures. 143

Figure 4.9: a. Crack velocity vs. energy release rate (G) for epoxy/sol-gel/polished-aluminum joints prepared with different sol-gel formulations and cure temperatures. Open circles and open triangles represent films cast from a x1 formulation cured at room temperature (RT, 75 mins) and 120 °C (OV, 30 mins) respectively. Filled circles and filled triangles represent films cast from a x7 formulation cured at room temperature (RT, 75 mins) and 120 °C (OV, 30 mins) respectively. See section 4.2 in the text for a detailed description of the x1 and x7 formulations. Three regions of subcritical crack growth are identified. The red lines represent a least-squares regression fit of equation 3.2 to the data. b. Critical energy release rates (G_c) for epoxy/sol-gel/polished-aluminum joints prepared with different sol-gel formulations and cure temperatures. c. Threshold energy

release rates (G_{th}) for epoxy/sol-gel/polished-aluminum joints prepared with different sol-gel formulations and cure temperatures. 144

Figure 4.10: a. Crack velocity vs. energy release rate (G) for epoxy/sol-gel/120grit-sanded-aluminum joints prepared with different sol-gel formulations and cure temperatures. Open circles and open triangles represent films cast from a x1 formulation cured at room temperature (RT, 75 mins) and 120 °C (OV, 30 mins) respectively. Filled circles and filled triangles represent films cast from a x7 formulation cured at room temperature (RT, 75 mins) and 120 °C (OV, 30 mins) respectively. See section 4.2 in the text for a detailed description of the x1 and x7 formulations. Three regions of subcritical crack growth are identified. The red lines represent a least-squares regression fit of equation 3.2 to the data. b. Critical energy release rates (G_c) for epoxy/sol-gel/120grit-sanded-aluminum joints prepared with different sol-gel formulations and cure temperatures. c. Threshold energy release rates (G_{th}) for epoxy/sol-gel/120grit-sanded-aluminum joints prepared with different sol-gel formulations and cure temperatures... 148

Figure 4.11: AFM of uncoated polished aluminum (top left), polished aluminum coated with x7 sol-gel solution (top right), Aluminum fracture side of a x7 oven cured reinforced joint, (bottom left), Epoxy fracture side of a x7 oven cured reinforced joint, (bottom right). Oven cured refers to a cure cycle of 120 °C for 30 minutes. 148

Figure 4.12: Structure Function vs. window size (Δx) for a grit-blasted (a.) and sanded (b.) surfaces. Three different surface profiling step sizes were used. The blue circles, red circles and black circles correspond to step sizes of 0.16, 0.8 and 2.5 μm respectively. As the step size is increased the scan size is also increased from 170 μm , 840 μm and 5 mm. The wavy regions towards the end of each profile are an artifact generated by insufficient statistics in these regions. 153

Figure 4.13: Z_{max} vs. window size (Δx) for a grit-blasted (a.) and sanded (b.) surfaces. Three different surface profiling step sizes were used. The blue circles, red circles and black circles correspond to step sizes of 0.16, 0.8 and 2.5 μm respectively. As the step size is increased the scan size is also increased from 170 μm , 840 μm and 5 mm. 153

Figure 4.14: Normalized Structure Function vs. window size Δx for 35 different scan areas on grit-blasted and sanded surfaces. The profiling step size is 0.16 μm . The red line represents a least squares regression used to determine the Hurst exponent. 154

Figure 4.15: Normalized Z_{max} vs. window size Δx for 35 different scan areas on grit-blasted and sanded surfaces. The profiling step size is 0.16 μm . The red line represents a least squares regression used to determine the Hurst exponent. 155

Figure 4.16: Normalized Power Spectrum vs. window size Δx for 35 different scan areas on grit-blasted and sanded surfaces. The profiling step size is $0.16 \mu\text{m}$. The red line represents a least squares regression over all the data. 155

Figure 4.17: a. Three fractal profiles generated with the same Hurst exponent of 0.8 profiles re-plotted from Figure 4.6. Each profile is generated with a different realization of random numbers. The profiles are vertically displaced for clarity. The simulations are run with a step size of one so the units are arbitrary. b. The value of D is calculated from plotting the variance of the step heights against the window size Δx and using equation 4.23 to fit the data. The variance is calculated from 1024 independently generated profiles each with 1024 steps. The red, green and blue circles correspond to diffusion coefficients of 375, 150 and 25 respectively. 159

Figure 4.18: PDFs of the height differences for three different profile simulations. The profiles are generated using a Hurst exponent of 0.8 and 3 different values of α (2,4 and 8) as shown in Figures 4.6 and 4.17. For each simulation the PDF is generated from 1025 independent profiles. Each profile contains 1024 steps. The window size (Δx) used to generate the PDFs is 50 steps. The red, green and blue circles correspond to diffusion coefficients of 375, 150 and 25 respectively. The simulations are run with a step size of one so the units are arbitrary 160

Figure 4.19: Normalized PDFs of grit-blasted and sanded surfaces, different marker colors and shapes shown in the legend represent the different window sizes used to calculate the distributions. 162

Figure 4. 20: PFDs for grit-blasted and sanded surfaces re-plotted according to equation 4.25. Open circles, open triangles, open squares and open inverted triangles represent the PDFs calculated at window sizes (Δx) of 0.16, 0.64, 2.5 and $10 \mu\text{m}$ respectively. The red lines represent the linear least square fit for the peak region of the distribution. The green lines represent the linear least square fit for the tail region of the distribution..... 163

Figure 4.21: The variance of the step heights against the window size Δx for grit-blasted and sanded surfaces. Open blue circles and open squares represent grit-blasted and sanded surfaces. Each point represents the average taken from 35 independent scans. 166

Figure 4.22: Brightfield and cross polarized micrographs for a fractured epoxy/x1 120°C cured sol-gel/grit-blasted aluminum joint. The plastic zones in the epoxy can be clearly visualized in the brightfield and polarized micrographs as the light and dark regions at the fracture surface of the epoxy. 168

Figure 5.1: **a.** Schematic of the setup used to produce linear surface energy gradients. A filter paper soaked with dodecyltrichlorosilane is the source of silane. This source is placed at an angle above a plasma oxidized glass slide for 5 minutes. The surface energy gradient is formed on the surface through diffusion controlled silanization. The angle of inclination, θ , can be easily controlled to alter the length of the gradient. The source size is 3 times the width of the glass slide that reduces any lateral variation of the chemical gradient. **b.** Schematic drawing of the setup used to produce radial surface energy gradients. A cone shaped filter paper saturated with dodecyltrichlorosilane acts as the source. The plasma oxidized glass slide is placed above the cone for 5 minutes. A radial surface energy gradient is formed on the slide. 177

Figure 5.2: Schematic drawing of the setup used to induce shape fluctuation in a droplet. A signal generator is used to pass a sinusoidal output to the mechanical oscillator. The extended (solid lines) and compressed (dashed gray lines) forms of the droplet are shown. 178

Figure 5.3: Advancing and receding contact angles on gradient surfaces prepared using the setup shown in Figure 5.1. The data shown is for surfaces prepared at two different angles of inclination: 22° and 40° . Advancing and receding angles for the 22° samples are represented by the open blue circles and closed blue circles respectively. Advancing and receding angles for the 40° samples are represented by the open red circles and closed red circles respectively. Solid lines represent an empirical fit of a hyperbolic tangent function to the contact angle data. The values of $d\cos\theta/dx$ on the linear portions of the gradients are estimated to be 0.065 mm^{-1} and 0.10 mm^{-1} for the gradients prepared at 22° and 40° inclinations, respectively. 180

Figure 5.4: Tapping mode AFM images and the analysis of roughness performed along the center line of a gradient prepared at 22° . The AFM scan areas are $2 \mu\text{m}$ squares; the black scale bars represent 500 nm. The position along the gradient is noted in the upper left of each image. The nanoscale arithmetic (R_a , black circles) and RMS (R_{RMS} , open circles) roughness values of the gradient are calculated as a function of position along the gradient. The starting point of the gradient is at a position of 20 mm on the surface. Hyperbolic tan functions (solid black lines) are plotted through the roughness data in order to guide the eye. 181

Figure 5.5: The profile of the contact angle on a radial gradient surface. The open and closed circles represent the quasi-static advancing and receding angles respectively. The gradient was prepared using a cone shaped filter paper with an apex angle of $\sim 80^\circ$ 182

Figure 5.6: Ratcheting motion of $10 \mu\text{l}$ and $20 \mu\text{l}$ droplets sandwiched between two gradient surfaces. The upper surface is oscillated at a frequency of 1 Hz. The gradient of wettability here is a continuous decrease in hydrophobicity from the left side of the image to the right side. The snapshots show one complete oscillation of the bottom plate.

The droplets go through extension-compression-extension cycle. The black lines show that during compression, the left side of the droplet is pinned while during extension the right side of the droplet is pinned. The schematic on the left of the figure highlights the change in plate spacing throughout the motion. All micrographs are taken at the same magnification. 183

Figure 5.7: Velocity of droplets sandwiched between 2 gradients as a function of the frequency of vibration and the volume of the droplet. The velocities of the 10 μl and 20 μl droplets are represented by the triangles and circles respectively. The black lines are the results of a least squares regression of the data. The slopes of the lines are 1.5 and 2.5 mm/s for the 10 μl and 20 μl drops. For the velocities measured at low frequencies the error bars are less than the size of the marker..... 185

Figure 5.8: Schematic drawing of a drop sandwiched between two surfaces. The symbols are defined within the text..... 186

Figure 5.9: Dynamic advancing and receding contact angles for 10 μl and 20 μl droplets moving between two gradients prepared at an angle of inclination of 22° . The vibration frequency is 1 Hz. The open and the closed circles represent the dynamic advancing and receding angles respectively. Solid lines represent an empirical fit of a 3rd order polynomial function to the contact angle data, these functions are then used in the model as described in the text. The position zero on the x-axis is approximately the onset of the gradient. 188

Figure 5.10: Motion of the advancing and receding contact lines of a 10 μl and a 20 μl drop vibrated at 1 Hz (red squares). The black lines correspond to the fits generated from the model described in the text. The black rectangle in the 10 μl plot represents one cycle of drop compression and extension..... 189

Figure 5.11: Several 20 μl water drops sandwiched between a radial gradient and uniform hydrophobic surface. As the droplets are squeezed and compressed they move outward, toward the hydrophilic part of the gradient. The scale bar represents 5 mm. All images are of the drops in the compressed state. 191

Figure 6.1: Schematic of experimental set up used to monitor the disappearance of a blister. R is the blister radius, P_{int} the internal pressure of the blister and ζ the height of the blister. The deflection of the glass plate is greatly exaggerated in the schematic. .. 199

Figure 6.2: Blister healing on a 50 μm thick film of PDMS. The height profile of the blister can be calculated from the interference patterns. Fingering instabilities are observed around the periphery of the blister..... 200

Figure 6.3: Wavelength of the fingering instability as a function of PDMS film thickness. The length used to calculate the finger wavelength is measured along the ends of the fingers. Red circles represent the finger wavelengths calculated for the blister experiments. For the thicknesses measured below 100 μm error bars are less than the size of the marker. Black squares represent the finger wavelength data collected by Ghatak *et al.*⁹ for two different geometries. Insert: Fingering wavelength as a function of blister radius for PDMS films of thicknesses 75 μm (red circles) and 50 μm (black squares). Fingering wavelength remains constant as the blister shrinks..... 202

Figure 6.4: Optical profilometry scan of the fingering instability formed around the periphery of a blister formed on a 50 μm thick PDMS film. The scan size is 830x830 μm 202

Figure 6.5: **a.** Final branched network of fingers/channels formed just prior to blister disappearance on a 50 μm thick PDMS film. **b.** No. fingers counted at different measurement radius R. The linear relationship between No. fingers and R proves that the wavelength is independent of measurement radius. The wavelength can then be found from the equation, $No. Fingers = 2\pi\lambda R$. The gradient calculated from the linear least squares regression fit is 37 mm^{-1} which corresponds to a fingering wavelength of $\sim 170 \mu\text{m}$ 203

Figure 6.6: Height profiles of a blister on a 50 μm thick PDMS film plotted at different instances in time. The height profile, red crosses, is determined from the interference fringes observed when viewing the blister under monochromatic light ($\lambda=516 \text{ nm}$). A simple model (blue lines) which only considers the deformation of the glass cover slide is used to fit the data (equation 6.2)..... 205

Figure 6.7: **a.** Plot of $f(R)/f(R_0)$ vs. time for a blister healing on PDMS films of different thickness. The function $f_1(R)$ is defined as the left hand side of equation 6.5. $f(R_0)$ is the value of the function at $t=0$. The blue circles, red diamonds, black triangles, green squares and magenta inverted triangles represent 15, 30, 40, 140, 240 μm thick PDMS films. The gradient of each least square fit is equal to the permeability coefficient, k_D , for that particular thickness (Equation 6.5). **b.** Permeability coefficient, k_D , as a function of film thickness. The permeability coefficient increases with the film thickness obeying a power law trend of the form $k_D = A(h_{\text{PDMS}})^B$, where $A = 1.3 \times 10^{-7} \text{ (pmol m}^2/(\text{N.S}))(\mu\text{m})^{-B}$ and $B = 1.5$ 208

Figure 6.8: Outer radius of the blister (blue circles, measured at the ends of the fingers) and inner radius (red squares, measured at the base of the fingers) as a function of time for the healing of a blister on a 50 μm thick PDMS film. In the final stages of blister life the outer radius remains constant while the inner radius rapidly decreases. This final stage is characterized by a critical outer radius R_{Outer}^* , inner radius R_{Inner}^* and time (t^*)..... 209

Figure 6.9: Micrograph snapshots taken just before blister disappearance for experiments on 50, and 240 μm thick films. White scale bars represent 0.5 mm. The corresponding finger width as a function of measurement radius is shown beneath each micrograph. For 50 and 100 μm thick PDMS films the finger width decreases as we move away from the blister center..... 210

Figure 7.1: Elastic modulus and the effect of humidity on a thin (~ 10 nm) thick zirconia films prepared via the sol-gel process. The zirconia film was cured at 120°C for 30 minutes. E , λ , A and D represent the elastic modulus, buckling wavelength, buckle amplitude and flexural rigidity of the film. The elastic modulus of the film after humid exposure is not reported as the change in film thickness due to swelling is not known. 220

Figure 7.2: Schematic of buckling patterns induced by the swelling of a metal capped sol-gel film in a humid environment..... 223

Figure 7.3: Buckling patterns formed by exposing a 400 nm thick sol-gel film capped with a 10 nm thick AuPd layer to $\sim 98\%$ RH for 15 hrs. a. Buckling Pattern formed around a natural defect in the AuPd coating. b. Buckling pattern formed around a scratch in the film..... 223

Figure 7.4: Crack velocity vs. energy release rate for epoxy/sol-gel/grit-blasted Al joints for TPOT modified sol-gel coatings. The filled circles and triangles represent the results for the TPOT modified coating cured at room temperature (50% RH, 75 mins) and 120°C (30 mins) respectively. The open circles and triangles represent the results for the standard sol-gel coating cured at room temperature (75 mins) and 120°C (30 mins) respectively. 225

Figure 7.5: Crack velocity vs. energy release rate for epoxy/sol-gel/grit-blasted Al joints for AEAPTMS modified sol-gel coatings. The filled circles and triangles represent the results for the prehydrolyzed AEAPTMS modified coating cured at room temperature (50% RH, 75 mins) and 120°C (30 mins) respectively. The open circles and triangles represent the results for the standard sol-gel coating cured at room temperature (75 mins) and 120°C (30 mins) respectively..... 227

Figure 7.6: Schematic of the experimental setup for electroless deposition of copper. The typical height of the swollen hydrogel cylinder is ~ 4.5 mm. The hydrogel cylinder is compressed to a height of 3 mm for the deposition experiment. The average height of the swollen hydrogel lens is ~ 12 mm. The lenses are compressed by 1-2 mm when they are clamped to the aluminum surface. 233

Figure 7.7: a. Electroless deposition of copper from a hydrogel clamped to a grit-blasted aluminum surface. The deposition time was 20 hours and the experiment was conducted in a humid environment at ~98%RH. b. Electroless deposition of copper from a hydrogel clamped to a grit-blasted aluminum surface. The deposition time was 20 hours and the experiment was conducted in an oil environment to prevent shrinkage of the gel. 234

Figure 7.8: Stress distribution formed at the interface when a hydrogel is brought into contact with a rigid surface. 235

Figure 7.9: a. Electroless deposition of copper from a hydrogel lens clamped to a grit-blasted aluminum surface. The image was taken at deposition time of 20 hours for direct comparison with the results shown in Figure 7.7. The experiment was conducted in an oil environment. The regions labeled 1-5 are explained in the text. b. Image taken after the gel lens was removed from the aluminum after a deposition experiment lasting 140 hours. The regions labeled 1-5 are explained in the text. 237

Figure 7.10: Increase in the contact radius of a gel clamped to a grit-blasted aluminum surface. The inserts of the deposition experiment correspond to the initial and final points on the curve. Black scale bars represent 5 mm 237

Figure B1: Salt spray test results as a function of the molar ratio of MTEOS to GTMS in the sol-gel film. All films were cured at 25°C for 30 minutes..... 246

Figure B2: Salt spray test results as a function of the molar ratio of MTEOS to GTMS in the sol-gel film. All films were cured at 120°C for 30 minutes..... 246

Figure C1: Magnified region of Figure 5.10 in the text. This region shows one complete cycle of oscillation of a 10 µl drop vibrated at 1 Hz. The motion of the center of mass of the drop is represented by the blue line. The fits of the simple model are shown as solid black lines. The regions labeled as A, B and C correspond to the points when the drop is stationary. t_A , t_B and t_C are the induction times in the regions A, B and C, respectively. The left and the right sides of the plot are the compression and stretching stages respectively. The schematic on the right illustrates idealized drop behavior in regions A and B, which are used for the calculation described in the text..... 249

Figure C2: Left: The base diameters of a 10 µl drop in the fully stretched and fully compressed states as a function of the equilibrium contact angle. The red and blue lines represent the base diameter of the droplet in the fully compressed and fully stretched states, respectively. The markers A, B, C and D are used to highlight the effect of

hysteresis on the drop step size, as explained in the text. Right: Droplet foot prints for 10 μl and 20 μl droplets moving along gradients prepared at 22° . The dashed circles are drawn around the peripheries of the drops in order to guide the eye. During the compression stage, the 20 μl drop footprint becomes elliptical whereas the 10 μl drop footprint is somewhat circular in comparison. During the extension cycles, the footprints of both the drops become circular..... 251

Abstract

Advances in surface modification are changing the world. Changing surface properties of bulk materials with nanometer scale coatings enables inventions ranging from the familiar non-stick frying pan to advanced composite aircraft. Nanometer or monolayer coatings used to modify a surface affect the macro-scale properties of a system; for example, composite adhesive joints between the fuselage and internal frame of Boeing's 787 Dreamliner play a vital role in the structural stability of the aircraft. This dissertation focuses on a collection of surface modification techniques that are used in the areas of adhesion and wetting.

Adhesive joints are rapidly replacing the familiar bolt and rivet assemblies used by the aerospace and automotive industries. This transition is fueled by the incorporation of composite materials into aircraft and high performance road vehicles. Adhesive joints have several advantages over the traditional rivet, including, significant weight reduction and efficient stress transfer between bonded materials. As fuel costs continue to rise, the weight reduction is accelerating this transition. Traditional surface pretreatments designed to improve the adhesion of polymeric materials to metallic surfaces are extremely toxic. Replacement adhesive technologies must be compatible with the environment without sacrificing adhesive performance.

Silane-coupling agents have emerged as ideal surface modifications for improving composite joint strength. As these coatings are generally applied as very thin layers (<50 nm), it is challenging to characterize their material properties for correlation to adhesive performance. We circumvent this problem by estimating the elastic modulus of the

silane-based coatings using the buckling instability formed between two materials of a large elastic mismatch. The elastic modulus is found to effectively predict the joint strength of an epoxy/aluminum joint that has been reinforced with silane coupling agents. This buckling technique is extended to investigate the effects of chemical composition on the elastic modulus. Finally, the effect of macro-scale roughness on silane-reinforced joints is investigated within the framework of the unresolved problem of how to best characterize rough surfaces. Initially, the fractal dimension is used to characterize grit-blasted and sanded surfaces. It is found that, contrary to what has been suggested in the literature, the fractal dimension is independent of the roughening mechanism. Instead, the use of an anomalous diffusion coefficient is proposed as a more effective way to characterize a rough surface.

Surface modification by preparation of surface energy gradients is then investigated. Materials with gradients in surface energy are useful in the areas of microfluidics, heat transfer and protein adsorption, to name a few. Gradients are prepared by vapor deposition of a reactive silane from a filter paper source. The technique gives control over the size and shape of the gradient. This surface modification is then used to induce droplet motion through repeated stretching and compression of a water drop between two gradient surfaces. This inchworm type motion is studied in detail and offers an alternative method to surface vibration for moving drops in microfluidic devices.

The final surface modification considered is the application of a thin layer of rubber to a rigid surface. While this technique has many practical uses, such as easy release coatings in marine environments, it is applied herein to enable spontaneous healing between a rubber surface and a glass cover slip. Study of the diffusion controlled healing

of a blister can be made by trapping an air filled blister between a glass cover slip and a rubber film. Through this study we find evidence for an interfacial diffusion process. This mechanism of diffusion is likely to be important in many biological systems.

CHAPTER 1

Introduction and Background

1.1 Research Overview

For centuries, nuts, bolts, and rivets have been the dominant method for joining metallic materials. This cumbersome technique has no parallel in nature; simply put nature does not use nuts, bolts and rivets. Nature prefers to use adhesives and clever material design to join dissimilar materials such as tendons to bone¹ and the beaks of squid to soft muscle². As our understanding of adhesion and adhesives has developed, we have followed in nature's footsteps replacing the traditional rivet approach with adhesives in the aerospace and automotive industries³. Implementation of adhesives in these industries initially involved toxic pretreatments, which, due to increasing environmental concerns, need to be phased out⁴. This investigation will focus on surface modification techniques which are environmentally permissible and can be used to bond adhesives to metals without sacrificing bonded joint strength.

The use of surface modification to alter the adhesive or wetting properties of a bulk material is the general theme of this dissertation. Within this general theme, one focus will be on the development and characterization of an environmentally benign technique for promoting adhesion between epoxy and metallic surfaces. Another area of focus will examine the effect of surface modification in the areas of wetting and crack healing. While they may seem unrelated, adhesion and wetting often go hand-in-hand. For example, most structural adhesives are applied in a liquid state, therefore, the physics of

wetting becomes very important³. Similarly, the adhesion or wetting of a liquid to a surface controls many natural and industrial processes⁵. The contents of each chapter will now be outlined in detail.

Chapters 2-4 focus on the enhancement of adhesion between aluminum and an epoxy adhesive. This area of research is motivated by increasing demands in the aerospace industry to develop an environmentally benign surface pretreatment for aluminum^{4,6}. Silane coupling agents are a strong candidate, but predicting the adhesive performance can be difficult due to the large number of processing parameters involved^{7,8}. To promote the progression of this technology, we develop methods that allow rapid characterization of thin film properties as a function of various chemical and processing parameters⁹. Another challenge with using silane-coupling agents is that they underperform in high humidity environments relative to the toxic alternatives^{8,10}. We aim to improve the durability of these non-toxic coatings through the addition of hydrophobic additives. We then seek to understand the significantly stronger adhesive bonds produced by grit-blasted surfaces than sanded surfaces. This work is motivated by the result that a grit-blasted surface treated with a silane-coupling agent can approach the dry joint strength of the current industrial standard, PAA^{8,10}. However, the mechanisms through which a macro-rough surface increases the joint strength and the method to best characterize the roughness are still under debate. These issues are addressed through a detailed study of the surface fractal dimension and the introduction of an anomalous diffusion coefficient to characterize a rough surface.

Chapter 5 begins with the development of a new technique to produce surface energy gradients. The locomotion of a droplet between these gradients is systematically studied

to show potential applications in the area microfluidics and to highlight the fundamental principle that hysteresis is required for any rectification of droplet motion¹¹.

Finally, Chapter 6 will return to a common adhesive problem; the formation of a blister between two surfaces joined by a soft elastomeric adhesive¹². While the formation of this type of blister is widely studied, this final chapter will focus on the healing of the blister controlled by a diffusive process. By analyzing the process from this viewpoint, it is possible to gain insight into biological processes which are controlled by hydrodynamic and diffusive mechanisms.

This introductory chapter will provide a fundamental and theoretical basis for understanding the subsequent chapters. The topics covered include the following areas: Thermodynamic stability of an epoxy/aluminum adhesive joint, silane coupling agents and sol-gel technology, the method of buckling instability to determine the elastic modulus of thin sol-gel films, mechanisms of adhesion promotion, methods of adhesive testing, analysis of surface roughness, motion of droplets on gradient surfaces and the blister test.

1.2 Thermodynamic stability of an epoxy/aluminum joint

One of the challenges in the adhesion of epoxy to aluminum is the formation of a durable interface which is stable in a humid environment³. When an epoxy/aluminum joint is stressed in an inert environment the secondary forces acting across the interface form a stable joint, but when exposed to water the joint becomes unstable and debonds spontaneously. This effect can be understood by considering the thermodynamic stability of the epoxy/aluminum interface. The thermodynamic work of adhesion (W_A) of an

epoxy/aluminum interface in an inert environment is related to the surface and interfacial free energies by the Dupré equation,

$$W_a = \gamma_E + \gamma_{Al} - \gamma_{E/Al} \quad (1.1)$$

where γ_E , γ_{Al} and $\gamma_{E/Al}$ represent the surface free energy per unit area of the epoxy, aluminum and the epoxy/aluminum interface. The Dupré equation generally applies to a liquid/solid interface, to apply it to an adhesive/solid interface we assume that the surface free energy of the adhesive does not change significantly upon cure and that the residual stresses can be ignored. Kinloch et al. estimated the thermodynamic work of adhesion for an epoxy/aluminum oxide interface to be $W_A=232 \text{ mJ/m}^2$ in an inert medium¹³. In the presence of water equation 1.1 must be modified to give,

$$W_a = \gamma_{E/l} + \gamma_{Al/l} - \gamma_{E/Al} \quad (1.2)$$

where $\gamma_{E/l}$, $\gamma_{Al/l}$ and $\gamma_{E/Al}$ represent the surface free energy per unit area of the epoxy/water, aluminum/water and epoxy/aluminum interfaces, respectively. Under these new conditions, the work of adhesion becomes¹³ $W_A=-137 \text{ mJ/m}^2$. The sign change indicates that the interface is unstable and separation will occur spontaneously. One way to combat this issue is to form primary bonds between the epoxy and the aluminum oxide surfaces. This can be achieved through the use of silane coupling agents⁷ and will be the subject of the next section.

1.3 Silane coupling agents and sol-gel technology

Silane coupling agents were first introduced in the fiber-glass industry to solve the low moisture resistance of glass-resin composites⁷. This issue is common in many systems involving the bonding of an organic resin to a high energy inorganic surface. Silane

coupling agents, which form primary bonds between the glass and resin, were widely adopted to solve the problem. The metal/polymer adhesion industry initially took a different approach. Aggressive chemical etches were introduced which form a complex architecture of pores on the metallic surface. Examples of these etching procedures are the Forest Products Lab etch and phosphoric acid anodizing¹⁴. The adhesive then wets into the pores and, upon curing, a mechanically interlocked interface results. Over the last 10 years increasing environmental regulations have made these types of etching treatments impractical and to solve the problem the metal/polymer industry has followed in the footsteps of the fiber-glass industry and adopted silane coupling agents^{8,15,16}.

A silane coupling agent typically contains two or more functional groups. At least one of these groups is designed to react with the adherend and another to react with the adhesive. The most widely used coupling agent for bonding epoxy to metallic surfaces is the silicon alkoxide glycidoxypropyltrimethoxysilane (GTMS), figure 1.1. The epoxide tail bonds with the curing agent in the epoxy and the silane head forms Si-O-M bonds with a metallic surface¹⁷. To apply GTMS to a metallic surface, the methoxy-alkoxide groups must first be hydrolyzed to form silanol groups; this is performed via the sol-gel technique.

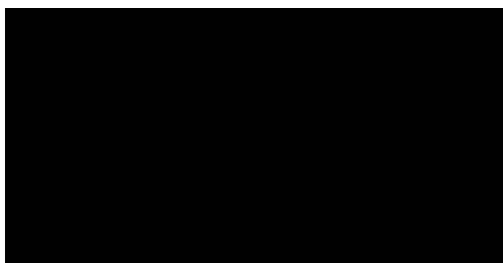


Figure 1.1: Glycidoxypropyltrimethoxysilane (GTMS). One of the most widely used adhesion promoters to adhere epoxies to metallic surfaces.

Sol-gel is a contraction of the term solution-gelation. In order to generate a GTMS film on a metallic surface the GTMS is first combined with water and in some cases a co-solvent. The hydrolysis of a silicon alkoxide such as GTMS can be catalyzed in either acidic or basic environments. Acidic catalysis results in the formation of linear chains, while basic catalysis forms branched networks which can act as seeds for particle growth^{18,19}. The adhesion promoting characteristics of a sol-gel film are optimum when the hydrolysis is performed under weakly acidic conditions (pH~5)⁸. Therefore, only the hydrolysis mechanisms when using an acidic catalyst will be described in detail.

The most generally accepted mechanism for acid catalyzed hydrolysis of a silicon alkoxide is bimolecular nucleophilic substitution (S_N2)¹⁹. In the first step, the alkoxide group is rapidly protonated, which withdraws electron density from the silicon making it more susceptible to nucleophilic attack. A water molecule then attacks the silicon and acquires a partial positive charge, forming a pentacoordinate transition state, reducing the charge on the protonated alkoxide group, thus making the alcohol a better leaving group. The transition state decays through the inversion of the silicon tetrahedron and the displacement of the alcohol group. A general schematic of this reaction is shown in Figure 1.2.

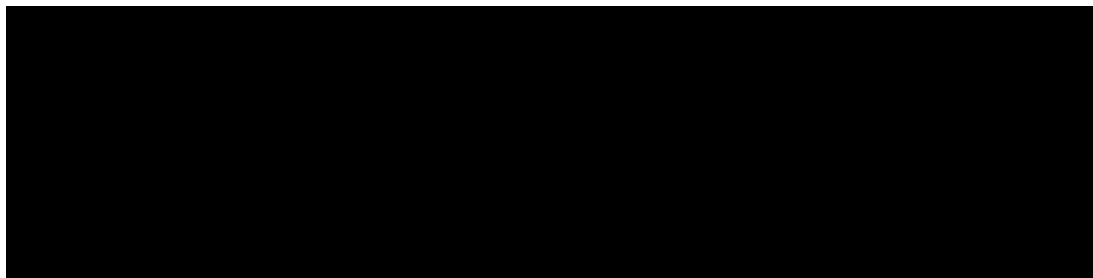


Figure 1.2: Acid catalyzed hydrolysis of a silicon alkoxide. R is typically a methyl or ethyl group. R' can be chosen from a vast selection of function groups. Figure adapted from Ref 18.

The rate of this reaction is a function of the steric effects from the size of alkoxide and alkyl groups. Increasing the size of these groups slows the rate of reaction by hindering the inversion of the transition state and sterically shielding the silicon from nucleophilic attack¹⁹. The kinetics of the hydrolysis reaction are also controlled by the pH, the ratio of silane to water in the sol and the presence of a co-solvent^{18,19}. After a certain degree of hydrolysis has taken place, the silanol groups will start to condense to form oligomers in solution. The reactions can be either water or alcohol condensation. A schematic of the water condensation reaction is shown in Figure 1.3. The reaction is initiated via the fast protonation of a silanol group, and is followed by a slow attack of a second neutral silicon species^{18,19}. As with the hydrolysis reaction the kinetics of condensation are a function of the pH, size of alkoxy and alkyl groups, silane/water ratio and a co-solvent. To maximize the performance of a GTMS adhesion promoter the degree of condensation in the solution should be minimized²⁰.

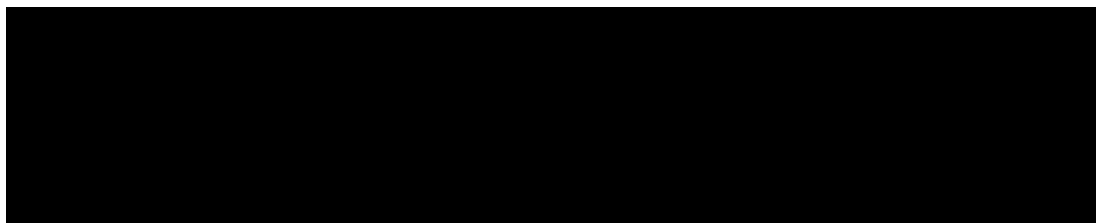


Figure 1.3: Acid catalyzed condensation between two hydrolyzed silicon alkoxides. R' can be chosen from a vast selection of function groups. Figure adapted from Ref 18.

Once the GTMS has been hydrolyzed the sol can be spray, dip or spin coated onto a clean metal surface^{21,22}. As the remaining solvent evaporates during the coating process the film will condense and the condensation reactions will continue until a crosslinked coating is formed¹⁹. This process is referred to as the gelation stage. The basic sol-gel formulation used throughout this study is a mixture of GTMS and zirconium-n-propoxide (TPOZ). TPOZ is a metal alkoxide that can be added to a silane based system to alter the final form of the sol-gel film and act as a catalyst for room temperature cure. Hoebell and co-workers have studied the effect of several metal alkoxides on the kinetics of hydrolysis, condensation and the opening of the epoxide group²³⁻²⁵. TPOZ is highly reactive with water due to the large partial charge on the Zr atom and its ability to expand its coordination state. Therefore, in order to use TPOZ in an aqueous solution it must be sterically stabilized with chelating ligands^{19,26}. In our study, we use glacial acetic acid, which stabilizes the TPOZ through the formation of a TPOZ-GAA complex, Figure 1.4. Each zirconium atom in the complex is coordinated with 6 oxygens instead of 4 making the zirconium more stable to nucleophilic attack.

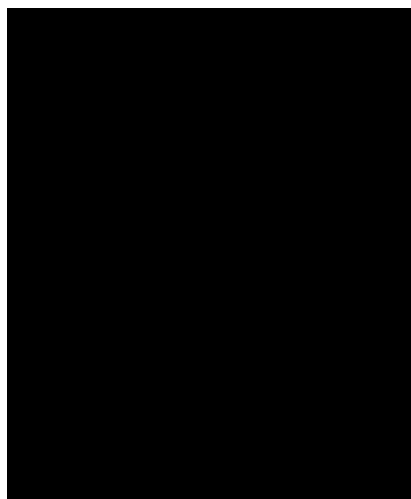


Figure 1.4: Zirconium-n-propoxide dimer stabilized with acetic acid bridges. R=C₃H₇.

The overall procedure for applying the GTMS and TPOZ formulation to improve the adhesion between aluminum and epoxy is shown in Figure 1.5. The final material properties of the sol-gel film are a strong function of the processing parameters such as pH, hydrolysis time and cure temperature. Each of these parameters can affect the final adhesion promoting performance of the sol-gel film^{8,27}. The objective of chapters 2 and 3 is to identify a bulk material property that is a function of all the processing steps and can be related to the final adhesive performance. The material property that is used is the elastic modulus of the sol-gel film. The thickness of an adhesion promoting sol-gel film is typically on the order of nanometers; therefore, typical procedures such as nanoindentation cannot be used. In order to tackle this problem the method of buckling instability is used to estimate the elastic modulus of the thin sol-gel films⁹. The next section will introduce this technique and the basics of the theory.

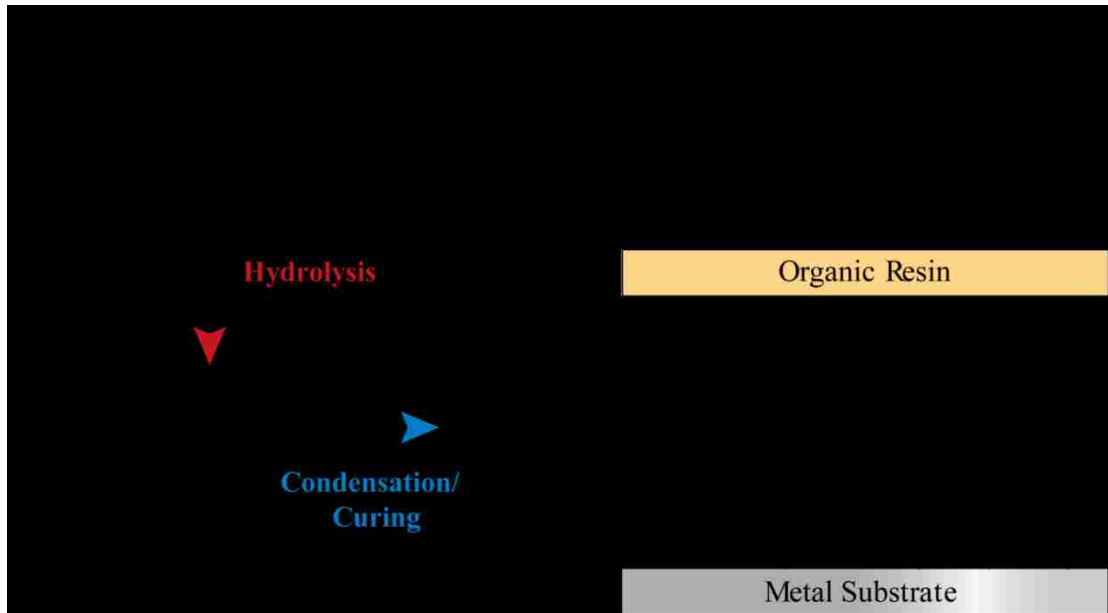


Figure 1.5: Flow diagram for the formation and application of a sol-gel based adhesive primer onto a metal substrate. The Coating is generated from an aqueous sol of Glycidoxypropyltrimethoxysilane (GTMS) and Zirconium tetrapropoxide (TPOZ). XPS studies²⁸ show the sol-gel/metal interface to be rich in zirconium and the sol-gel/organic resin interface to be silane rich.

1.4 Method of buckling instability to estimate the elastic modulus of thin films

When a system consisting of a thin hard film resting on a soft elastic substrate is compressed the surface buckles to minimize the total energy of the system, Figure 1.6. The wavelength of this instability is determined by the tradeoff between the bending energy in the thin film and the stretching energy in the substrate²⁹. Using this technique, the elastic modulus of the thin film may be estimated through the measurement of the buckling wavelength. The first systematic study on this buckling phenomenon as a metrology technique was performed by Stafford et al³⁰. Since then, buckling instability has been used to investigate the elastic modulus of numerous polymer films³¹⁻³⁵. The classical approach to solve this problem is based on a force³⁶ or energy balancing method²⁹. Before showing this result, a simple scaling argument will be used to predict

the buckling wavelength. Assuming the soft substrate can be modeled as an elastic half space, from Figure 1.6 we see that the independent parameters for the system are the modulus of the substrate (E_s), the film modulus (E_f), film thickness (h_f) and buckling wavelength (λ). At equilibrium the bending energy of the film must be proportional to $\sim E_f h_f^3$, which is the well known form of the bending rigidity of a beam. To maintain the law of symmetry, the following relationship can then be written, $E_s \lambda^3 \sim E_f h_f^3$. Rearranging this equation gives,

$$E_f \sim E_s \left(\frac{\lambda}{h_f} \right)^3 \quad (1.3)$$

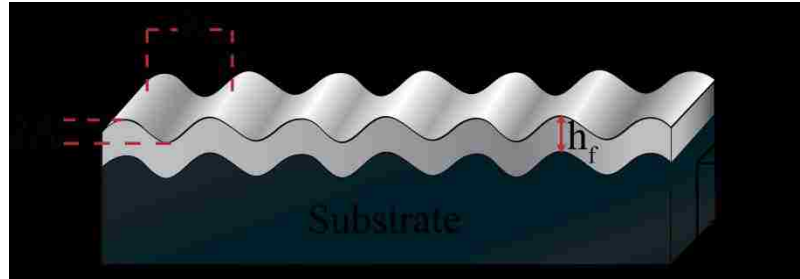


Figure 1.6: Schematic of the buckling of a thin film on a soft compliant substrate.

The full solution of the problem will now be given by minimizing the total energy of a buckled system. This analysis is adopted from the method presented by Groenewold²⁹ and assumes the condition of plane strain. First, the separate energy contributions of the film and the substrate will be calculated. We assume that the deflection of the surface occurs only in the z direction, is independent of the y coordinate and can be described by a cosine function of the form,

$$\zeta(x) = A \cos \left(\frac{2\pi}{\lambda} x \right) \quad (1.4)$$

where ζ is the deflection in the z direction, A the amplitude and λ the buckling wavelength. The energy to bend a film where the deflection is only a function of x is given by³⁷,

$$F_{Bending} = \frac{E_f h^3}{24(1 - \nu_f^2)} \iint \left(\frac{d^2 \zeta}{dx^2} \right)^2 dx dy \quad (1.5)$$

Where ν is the Poisson's ratio. This equation assumes that either the displacement of the film is small compared to the thickness of the film or that the deformation is such that no stretching is required. Substituting equation 1.4 into equation 1.5 and solving gives the bending energy for the film,

$$\bar{F}_{Bending} = \frac{\pi^4 A^2 E_f h^3}{3\lambda^4 (1 - \nu^2)} \quad (1.6)$$

where $\bar{F}_{Bending}$ is the energy per unit area.

Next we compute the energy of the substrate. The substrate used in all the buckling experiments in this dissertation is polydimethylsiloxane (PDMS). We assume the PDMS to be incompressible i.e. a Poisson ratio of $\nu=0.5$. For this condition, the deformation tensor describing the substrate must satisfy the incompressibility condition,

$$\nabla \cdot \mathbf{u} = 0 \quad (1.7)$$

where \mathbf{u} is the deformation tensor. Equation 1.7 is solved subject to the following boundary conditions,

$$\mathbf{u}(x, z = 0) = \begin{pmatrix} 0 \\ 0 \\ A \cos\left(\frac{2\pi}{\lambda} x\right) \end{pmatrix} \quad \text{and} \quad \mathbf{u}(x, z \rightarrow \infty) = \mathbf{0} \quad (1.8)$$

As the material is incompressible, the problem becomes analogous to a creeping flow problem in fluid mechanics. (The Navier-Cauchy equations for an incompressible

material have the same form as the simplified steady state Navier-Stokes equations for creeping flow). Therefore, it can be readily solved by using a stream function (ψ) that satisfies the equation $\nabla^4\psi = 0$ and the boundary conditions listed in equation 1.8. A stream function of the form $\psi = -\frac{\lambda+2\pi z}{2\pi} A e^{-\frac{2\pi}{\lambda}z} \text{Sin}\left(\frac{2\pi}{\lambda}x\right)$ satisfies these requirements.

The deformations can then be readily calculated from $u_x = \frac{\partial\psi}{\partial z}$ and $u_z = -\frac{\partial\psi}{\partial x}$ to give,

$$\mathbf{u}(x, z) = \begin{pmatrix} \frac{2\pi}{\lambda} z \text{sin}\left(\frac{2\pi}{\lambda}x\right) \\ 0 \\ \left(1 + \frac{2\pi}{\lambda}z\right) \text{cos}\left(\frac{2\pi}{\lambda}x\right) \end{pmatrix} A e^{-\frac{2\pi}{\lambda}z} \quad (1.9)$$

For the case when $\nu \neq 0.5$ the Airy stress function must be used in conjunction with the general stress strain relations. The strain energy for an incompressible homogeneous material is given by³⁸

$$F_s = \iiint \frac{E_s}{3} (\varepsilon_{xx}^2 + \varepsilon_{yy}^2 + \varepsilon_{zz}^2 + 2(\gamma_{xz}^2 + \gamma_{xy}^2 + \gamma_{yz}^2)) dx dy dz \quad (1.10)$$

where ε_{ii} and γ_{ij} represent the normal and shear strains respectively. From the definition of the strain tensor, $\varepsilon_{ij} = \frac{1}{2} \left(\frac{\partial u_i}{\partial x_j} + \frac{\partial u_j}{\partial x_i} \right)$, the values of ε_{ii} and γ_{ij} can be calculated using equation 1.9. The energy in the substrate is then,

$$\bar{F}_s = \frac{\pi E_s A^2}{3\lambda} \quad (1.11)$$

Where $\bar{F}_{Substrate}$ is the energy per unit area. A compressive strain is required to form the buckles on the surface. Assuming that $\lambda \gg A$ and that the compression of the film can be neglected, the strain (ε) can be related to the wavelength and amplitude of the buckles,

$$\varepsilon \cong \frac{\pi^2 A^2}{\lambda^2} \quad (1.12)$$

Substituting equation 1.12 into equations 1.6 and 1.11 the total energy of the system per unit area is,

$$\bar{F}_{Total} = \frac{\varepsilon}{3} \left(\frac{\lambda E_s}{\pi} + \frac{\pi^2 E_f h^3}{\lambda^2 (1 - \nu_f^2)} \right) \quad (1.13)$$

Equation 1.13 is minimized with respect to lambda to arrive at the final result,

$$\frac{E_f}{1 - \nu_f^2} = 4E_s \left(\frac{\lambda}{2\pi h} \right)^3 \quad (1.14)$$

Equation 1.14 is the classic result used in the literature to estimate the elastic modulus of thin polymer films on incompressible substrates³⁰. The total energy of the system in the buckled state is then,

$$\bar{F}_{Total} = \varepsilon h E_s \left(\frac{E_f}{4E_s (1 - \nu_f^2)} \right)^{1/3} \quad (1.15)$$

The critical compressive stress at which buckling occurs can be derived by first considering the energy per unit area in the compressed film just prior to buckling,

$$\bar{F}_{Comp} = \frac{E_f h}{2(1 - \nu_f^2)} \varepsilon^2 \quad (1.16)$$

Equating equations 1.15 and 1.16 the critical strain for the onset of buckling is,

$$\varepsilon_{crit} = \frac{1}{2} \left(\frac{4E_s (1 - \nu_f^2)}{E_f} \right)^{2/3} \quad (1.17)$$

By substituting equation 1.14 and 1.17 into equation 1.12 and defining the pre-strain as $\varepsilon_{pre} = \varepsilon + \varepsilon_{crit}$, the amplitude of the buckles can be found from,

$$A = h \sqrt{\frac{\varepsilon_{pre}}{\varepsilon_{crit}} - 1} \quad (1.18)$$

Equations 1.14, 1.17 and 1.18 will be used throughout Chapters 2 and 3 to estimate the modulus of thin sol-gel films on PSMS substrates.

1.5 Mechanisms of adhesion in epoxy/sol-gel/aluminum adhesive joints

The 3 most important parameters to consider when designing an epoxy/sol-gel/aluminum joint are,

1. Chemical crosslinking between the epoxy and aluminum
2. Interpenetration of the epoxy into the sol-gel layer
3. Surface morphology of the adherend.

In section 1.2 and 1.3, the importance of parameter 1 was outlined in detail as it follows logically from the description of silane coupling agents. We will now focus on points 2 and 3.

Silane coupling agents can improve adhesion between polymer and metallic surfaces when no obvious chemical compatibility exists between the coupling agent and the polymer. An example of this is the use of amine functionalized silanes to improve adhesion to polyolefins⁷. In this case, the enhancement of adhesion comes from the formation of an inter-penetrating network (IPN) between the coupling agent and the adhesive, Figure 1.7. Detailed studies using XPS and secondary neutral mass spectroscopy have proved the existence of this network^{39,40}. To form an IPN, it is necessary that the adhesive can diffuse into the silane layer. If the silane layer is too highly crosslinked the adhesive will not be able to diffuse into the matrix, leading to the formation of a sharp, weak polymer/silane interface. Therefore, the curing conditions of the silane film become critical when the formation of an IPN is the sole adhesion

promoting mechanism. When the silane is functionalized such that primary chemical bonds can form between it and the adhesive, the formation of an IPN is still beneficial. The IPN provides additional strength to the interface through a mechanism akin to mechanical interlocking and the diffusion of the adhesive into the network increases the number of potential bonding sites.

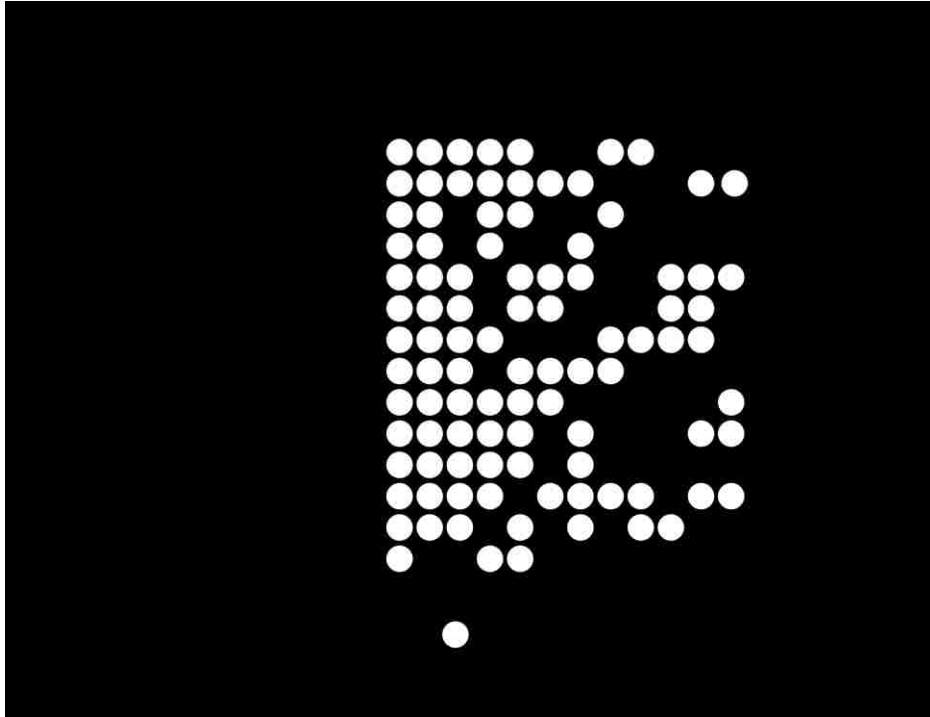


Figure 1.7: Interdiffusion of an adhesive into a sol-gel film leading to the formation of an interpenetrating network. Figure adapted from Ref[36].

The surface morphology of metal adherends can be broken up into two distinct groups, micro and macro rough surfaces, Figure 1.8. Micro-rough surfaces generally consist of porous morphologies generated through chemical etches. Macro-rough surfaces are generated via mechanic abrasion processes such as grit-blasting and sanding. When an adhesive wets a porous surface it flows into the pores to a depth dictated by the equilibration between the back pressure of trapped air in the pore and the capillary

driving pressure⁶. For complex pore morphologies with a high level of interconnectivity, when the adhesive cures within the pores it will form a strong mechanically interlocked interface¹⁴. To fracture an interface that is mechanically interlocked, cohesive failure must occur in the adhesive; this results in a very strong bond⁴¹. These complex pore architectures can be formed on aluminum by phosphoric acid anodizing¹⁴. Other chemical etches, such as the FPL etch, produce shallow, ~ 40 nm pores on the surface¹⁴. For this type of morphology, it is likely that the increase in adhesive strength is due to the additional energy required to pull the adhesive from the pores or due to the discontinuities caused by the metal fibrils formed during the pretreatment⁴². The effect has been demonstrated with a model rubber/aluminum system⁴¹. Mechanisms of adhesion promotion due to a macro-rough surface are more complex and still the subject of debate⁶.

The simplest theory of adhesion promotion due to macro-roughening is the increase in the surface area available for bonding, provided that the adhesive can completely wet the surface in the liquid state before cure⁴³. However, the increase in the surface area cannot always account for the increase in adhesion. The roughness of a biomaterial interface will change the direction of the propagation of an interfacial crack. This change in direction will alter the stress concentration at the crack tip and the mode mixity⁴⁴. The enhancement of adhesion due to this effect has been studied by several researchers in model systems where the increase in the adhesive energy could not be explained by an increase in the surface area⁴⁵⁻⁴⁷. Finally, pinning of the crack front due to regions of high fracture toughness can increase the strength of the interface⁴⁸. To qualitatively predict the degree of adhesion promotion due to macro-roughening, a reliable method to

characterize the surface must first be developed. This is not a trivial issue and will be discussed next.

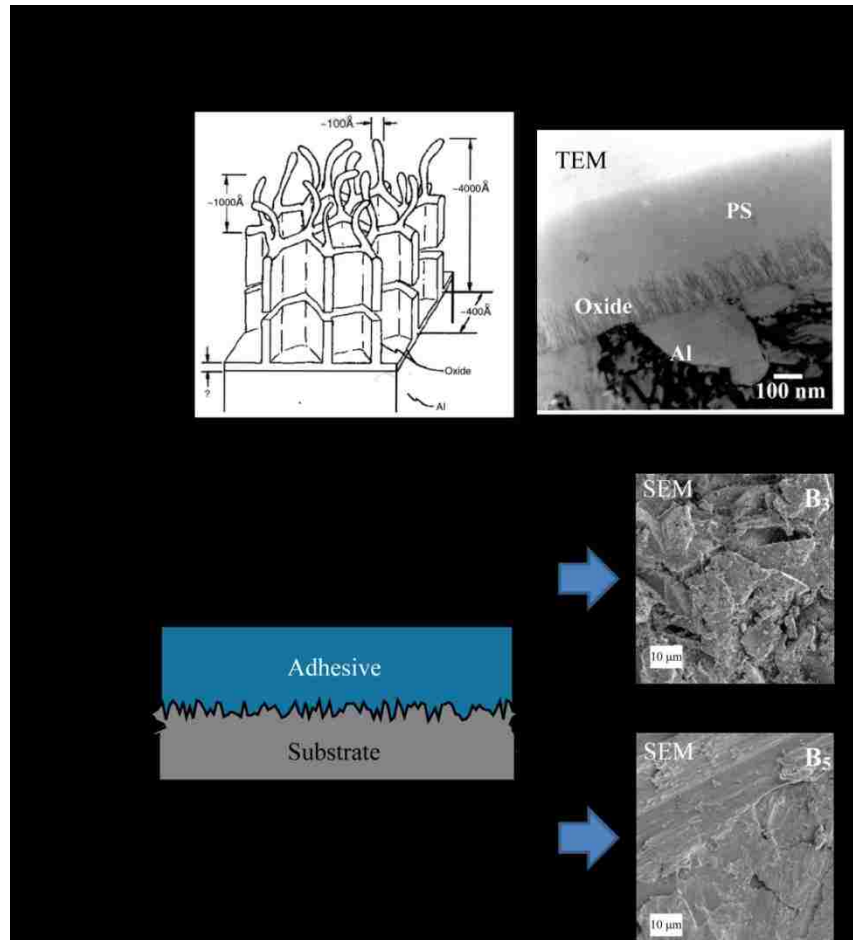


Figure 1.8: Topleft: Schematic of the surface morphology produced on aluminum via phosphoric acid anodizing. TopRight: A TEM image showing the penetration of PS into a porous PAA etched oxide layer on aluminum⁴⁹. Bottom: SEM images of grit-blasted and sanded surfaces²⁷.

1.6 Characterization of surface Roughness and the fractal dimension

Many parameters have been suggested to characterize machined surfaces, such as the center line average (CLA), root mean squared (RMS), peak-to-valley and the fractal dimension⁵⁰. The problem with most of these parameters is that they are sensitive to

sample size and the equipment used to characterize the surface. An example of a widely used technique that suffers from these problems is the root mean squared roughness (RMS). The RMS is the standard deviation of the height profile of a surface. The advantage of RMS is that it provides a characteristic length scale for the surface roughness (unlike the fractal dimension). However, the major disadvantage of the RMS technique is that it is strongly dependant on the sample size⁵¹. The result of the dependence is an inability to provide a true characterization⁵¹ of the surface unless more statistics are known, i.e. it provides no information of how the roughness of a surface evolves with different length scales. The fractal dimension emerged as a technique to study the roughness of a surface to avoid the issue of sample size⁵². The fractal dimension provides a measure of the self affinity of a surface. A self affine profile is one that remains invariant under the following transformations in height (h) and position (x).

$$x \rightarrow \lambda x \quad (1.19)$$

$$h \rightarrow \lambda^H h \quad (1.20)$$

where H is the roughness or Hurst exponent. The fractal dimension (F_D) is related to H through the following equation^{51,53}

$$F_D = 2 - H \quad (1.21)$$

If a profile can be represented by these relations over a series of length scales then we may say that the surface is statistically self affine. If a surface can be describes by the transformations shown in equation 1.19 and 1.20 then it is possible to extract a value of the fractal dimension of the surface. The fractal dimension can be calculated using several techniques but extreme care must be taken on the technique chosen as the value of F_D and the available statistics will strongly affect the reliability of different methods⁵⁴.

An example of the effect of fractal dimension on a roughness profile is given in Figure 1.9.

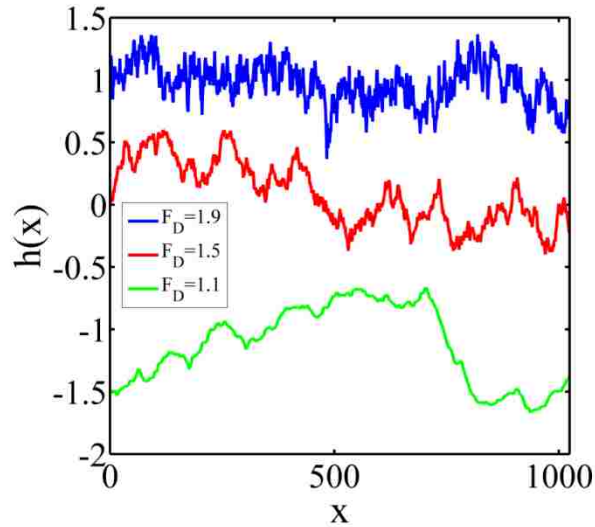


Figure 1.9: Height profiles with different fractal dimensions. Profiles are generated in Matlab using the midpoint technique, see Chapter 4 for a more detailed description. All profiles are normalized and then shifted on the y axis for clarity.

Previous studies relating surface roughness to the fracture energy of an adhesive joint have found the fractal dimension to be a more reliable means to predict the joint strength than RMS⁵⁵⁻⁶⁰. However, no theory was put forward to explain this trend. Recent work on bulk materials has suggested that the fractal dimension of a fracture surface is a universal value, independent of the material and the fracture process^{61,62}. If this is true, then any surface created through abrasive techniques (multiple fracture events) should exhibit the same fractal dimension, making the fractal dimension an inappropriate method with which to characterize surface roughness. This issue will be addressed in detail in Chapter 4 where the effect of surface roughness on the strength of an epoxy/sol-gel/aluminum joint is investigated.

1.7 Methods of adhesive testing and mode mixity

The energy required to fracture an adhesive joint can vary considerably depending on the geometry, material properties and loading configuration. The change in the mode of deformation at the crack tip is responsible for this variation. In general, there are three possible modes of deformation at the crack tip (Figure 1.10): an opening mode (mode I), an in-plane shear mode (mode II) and an out-of-plane shear mode (mode III). The term mode mixity is given to processes where two or more deformation modes act simultaneously on the crack. A joint loaded in a mode II configuration will require a higher energy input to fracture than if the joint was loaded in a mode I configuration⁶³. Therefore, when performing an adhesive test, controlling and reporting the mode mixity at the crack tip is very important.

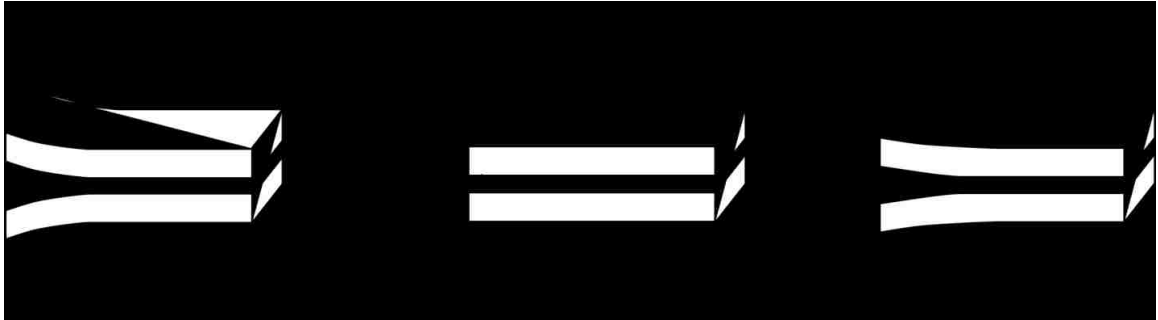


Figure 1.10: Schematic of the three deformation modes at the crack tip, opening mode (mode I), in-plane shear (mode II), and out of plane shear (mode III).

The fracture of materials is typically characterized by either the stress intensity factor (K) or the energy release rate (G). For an isotropic, homogeneous elastic material the total energy release rate can be written as⁶³,

$$G = G_I + G_{II} = \frac{K^2}{E} = \frac{K_I^2}{E} + \frac{K_{II}^2}{E} \quad (1.22)$$

where G is the energy release rate and K is the stress intensity factors. Subscripts I and II represent the mode I and II components of G and K , respectively. The parameter \bar{E} is either the elastic or plain strain modulus depending on the conditions at the crack tip. For fracture in a homogeneous material, the crack will follow a path that maximizes G_I and minimizes G_{II} , because the critical strain energy release rate is generally lower in mode I. Much like electricity the crack will follow the path of least resistance. Therefore, for the fracture of homogenous materials one need only consider G_I . At a biomaterial interface, a crack is not free to propagate in any direction to minimize G_{II} and so the deformation at the crack front will be controlled by a mixture of modes I and II. When the difference in the mechanical properties between the materials forming the interface is small, the mode mixity can be expressed as a phase angle⁴⁴,

$$\psi = \tan^{-1} \left(\frac{K_{II}}{K_I} \right) \quad (1.23)$$

When $\psi=0$, we have pure mode I loading, and at $\psi=90^\circ$, pure mode II. For the fracture of an epoxy/aluminum interface where the difference in the mechanical properties is large, the problem must be approached by introducing a complex stress intensity factor and a corresponding relationship for phase angle⁴⁴.

$$K = K_1 + iK_2 \quad \& \quad \psi = \tan^{-1} \left(\frac{K_2}{K_1} \right) \quad (1.24)$$

where K_1 and K_2 play similar roles as the conventional mode I and mode II stress intensity factors given in equation 1.23. This definition is required to take into account the oscillatory stress field near the crack tip singularity⁴⁴. The phase angle defined in equation 1.24 is for the idealized case when the Dundurs parameter β is equal 0, for a detailed treatment of the problem the reader is referred to reference 44. To test a

biomaterial interface with a large modulus mismatch, the geometry and loading of the system must be controlled to minimize the phase angle at the crack tip. Doing so will ensure a conservative value of the fracture energy is obtained and the crack will remain at the interface and not kink into the softer material to a significant degree.

The asymmetric double cantilever beam technique (ADCB) has been found to be an effective method to study the fracture toughness of the interface between a soft polymer and rigid substrate⁶⁴. By controlling the ratio of the thicknesses of the substrate and polymer the phase angle can be controlled^{65,66}. Figure 1.11 is an illustration of the ADCB set up used in this thesis. The fracture energy can then be found from Kanninens⁶⁷ model for a beam on an elastic foundation. Several numerical (finite element) studies have found this model to be accurate over the sample dimensions used throughout this dissertation^{65,66}. The energy release rate is given by,

$$G = \frac{3\Delta^2 E_1 h_1^3 E_2 h_2^3}{8a^4} \left[\frac{E_1 h_1^3 C_2^2 + E_2 h_2^3 C_1^2}{(E_1 h_1^3 C_2^3 + E_2 h_2^3 C_1^3)^2} \right] \quad (1.25)$$

where $C_1 = 1 + 0.64 \frac{h_1}{a}$, $C_2 = 1 + 0.64 \frac{h_2}{a}$, Δ is the wedge thickness, E is the elastic modulus, h is the beam thickness and a is the crack length. Subscripts 1 and 2 refer to epoxy and aluminum respectively.



Figure 1.11: Schematic of the ADCB sample. E_1 , E_2 , h_1 , h_2 , a and Δ correspond to the aluminum elastic modulus, epoxy elastic modulus, aluminum thickness, epoxy thickness, crack length and wedge height.

1.8 Surface energy gradients and drop motion

Gradients in surface energy have multiple practical uses ranging from drop microfluidics⁶⁸ and heat transfer⁶⁹ to the adsorption of proteins^{70,71}. To design a gradient for a given process it is important to have control over the length and shape of the gradient. A common technique to create a gradient is the vapor deposition of an alkyltrichlorosilane onto a reactive surface. The vapor of the alkyltrichlorosilane is allowed to diffuse in such a way that a gradient in concentration is set up across the surface. The gradient is imprinted through the reaction of the silane with the surface. The gradient of surface energy is then controlled by the density of surface coverage of the silane. The shape and size of the gradient depends on the deposition time and the position of the silane source. Due to the large number of uses for gradient surfaces, simple manufacturing techniques which offer control over the length and size of the gradient are in high demand. In Chapter 6 we will present a new method where by the shape and size of a gradient can be easily controlled through the vapor deposition of an alkyltrichlorosilane from a filter paper source¹¹.

The motion of a droplet on a gradient in surface energy was first demonstrated by Chaudhury and Whitesides⁷². In their experiment a gradient in surface energy was used to propel a droplet uphill. For a droplet to move, the driving force due to the gradient must be larger than the opposing hysteresis force⁷³,

$$\pi R^2 \gamma \frac{d\cos\theta_d}{dx} > 2\gamma R(\cos\theta_{r0} - \cos\theta_{a0}) \quad (1.26)$$

where, R is the drop radius, γ the liquid surface tension, θ_{r0} the receding contact angle, θ_{a0} the advancing contact angle, $\frac{d\cos\theta_d}{dx}$ the gradient of the wettability and θ_d the dynamic

contact angle. Hysteresis is defined as the difference between the advancing and receding contact angles of a drop. Using equation 1.26, the critical radius required for drop motion can be found. Once the hysteresis force is overcome the droplet then moves at a velocity dictated by the viscous dissipation occurring at the contact line. If the hysteresis is high, as can be the case with gradients, then the critical radius required for drop motion maybe unrealistic leading to a pinning of the drop. This problem is significant and can prevent the implementation of energy gradients in fluidic devices. A solution is to apply a vibration to the surface, which not only rectifies the drop motion but permits the control of the drop velocity through the frequency of vibration^{68,73,74}. An alternate method to induce the drop motion is to routinely squeeze and stretch the drop between two gradients surfaces^{11,74}. This method causes the drop to move along the surface with an inch worm type motion. Chapter 6 focuses on a systematic study of this type of motion to describe the velocity of the drop as a function of the drop volume and driving frequency.

1.9 The Blister test

The blister test is a widely used method to determine the strength of adhesion of thin films to their substrates. Thin films have wide commercial applications, ranging from micro-electronics to structural adhesive primers in the aerospace industry. The origin of the blister test is widely attributed to Dannenberg⁷⁵, the method later being refined by Williams^{76,77}. Numerous different models have been developed to cope with systems in which the film behaves like a plate, a membrane or somewhere between the two extremes. These different methods are reviewed in a recent paper by Briscoe and

Panesar¹². Like most fracture tests, the blister test is conducted by applying an external pressure or force to the system. The uniqueness of the work presented in Chapter 6 is derived from the fact that no external force is applied to the system and the crack healing is controlled solely by a diffusive process.

Our system consists of a blister formed between a glass cover slip and a thin elastomeric layer supported on a rigid substrate. We calculate the energy release rate of the system using a Griffith energy balance approach and assuming the layer of elastomer is so thin as to be neglected in the analysis. The energy of a plate undergoing a small bending deformation (vertical deformation \ll plate thickness) is given by^{37,78},

$$D\nabla^4\zeta = P \quad (1.27)$$

where D , ζ , P are the plate flexural rigidity, plate displacement and pressure applied to the plate respectively. Equation 1.27 is solved in cylindrical coordinates with the following clamped boundary conditions, $\zeta = 0$ at $r=R$ and $\frac{d\zeta}{dr} = 0$ at $r=R$.

$$\zeta = \frac{P}{64D}(R^2 - r^2)^2 \quad (1.28)$$

where R is the blister radius. The bending energy of a circular plate that is clamped at the edges is given by⁷⁸,

$$F_{Bending} = \iint \left\{ \frac{D}{2} \left(\frac{d^2\zeta}{dr^2} + \frac{1}{r} \frac{d\zeta}{dr} \right) - \zeta P \right\} r dr d\theta \quad (1.29)$$

The total energy in the system is then written as,

$$F_{Total} = -\frac{\pi P^2 R^6}{384D} + W_a \pi R^2 \quad (1.30)$$

where W_a is the work of adhesion. Minimizing this energy with respect to the crack length a , we arrive at the classical result of Williams⁷⁶,

$$W_a = \frac{P^2 R^4}{128D} \quad (1.31)$$

Equations 1.28 and 1.31 will be used throughout Chapter 6 as we study the healing of the blister.

1.10 References

- (1) Benjamin, M.; Evans, E. J.; Copp, L. *Journal of anatomy* **1986**, *149*, 89–100.
- (2) Miserez, A.; Schneberk, T.; Sun, C.; Zok, F. W.; Waite, J. H. *Science* **2008**, *319*, 1816–9.
- (3) Kinloch, A. J. *Adhesion and Adhesives: Science and Technology*; 1st ed.; Chapman and Hall: London and New York, 1987.
- (4) Joshua Du, Y.; Damron, M.; Tang, G.; Zheng, H.; Chu, C.-J.; Osborne, J. H. *Progress in Organic Coatings* **2001**, *41*, 226–232.
- (5) de Gennes, P. G.; Brochard-Wyart, F.; Quere, D. *Capillarity and Wetting Phenomena, Drops, Bubbles, Pearls, Waves*; Springer: New York, 2004.
- (6) Chaudhury, M. K.; Pocius, A. V. *Surfaces, Chemistry and Applications*; 1 st.; Elsevier: Amsterdam, 2002.
- (7) Plueddeman, E. P. *Silane Coupling Agents*; 1982.
- (8) Abel, M.-L.; Allington, R. D.; Digby, R. P.; Porritt, N.; Shaw, S. J.; Watts, J. F. *International Journal of Adhesion and Adhesives* **2006**, *26*, 2–15.
- (9) Longley, J. E.; Chaudhury, M. K. *Macromolecules* **2010**, *43*, 6800–6810.
- (10) Rider, A. N. *International Journal of Adhesion and Adhesives* **2006**, *26*, 67–78.
- (11) Longley, J. E.; Dooley, E.; Givler, D. M.; Napier, W. J.; Chaudhury, M. K.; Daniel, S. *Langmuir* **2012**, *28*, 13912–8.
- (12) Briscoe, B.; Panesar, S. *Proceedings of the Royal Society A* **1991**, *433*, 23–43.
- (13) Kinloch, A. J.; Dukes, W. A.; Gledhill, R. A. *Adhesion Science and Technology 9B*; Lee, L. H., Ed.; Plenum Press: New York, 1975; p.597.

- (14) Venables, J. D. *Journal of Materials Science* **1984**, *19*, 2431–2453.
- (15) Kinloch, a. J.; Korenberg, C. F.; Tan, K. T.; Watts, J. F. *Journal of Materials Science* **2007**, *42*, 6353–6370.
- (16) Digby, R. P.; Shaw, S. J. *International Journal of Adhesion and Adhesives* **1998**, *18*, 261–264.
- (17) Abel, M.; Digby, R. P.; Fletcher, I. W.; Watts, J. F. **2000**, *125*, 115–125.
- (18) Wright, J. D.; Sommerdijk, N. A. J. M. *Sol-Gel Materials, Chemistry and Applications*; 1st ed.; CRC Press: London and New York, 2001.
- (19) Brinker, C. J.; Scherer, G. W. *Sol-Gel Science: The Physics and Chemistry of Sol-Gel Processing*; 1 st.; Academic Press: San Diego, CA, 1990.
- (20) Bertelsen, C. M.; Boerio, F. J. *Progress in Organic Coatings* **2001**, *41*, 239–246.
- (21) Brinker, C.; Frye, G.; Hurd, A.; Ashley, C. *Thin Solid Films* **1991**, *201*, 97–108.
- (22) Mackenzie, J.; Bescher, E. *Journal of sol-gel science and technology* **2003**, 7–14.
- (23) Hoebbel, D.; Nacken, M.; Schmidt, H. *Journal of Sol-Gel Science and Technology* **1998**, *12*, 169–179.
- (24) Hoebbel, D.; Nacken, M.; Schmidt, H. *Journal of Sol-Gel Science and Technology* **2001**, *21*, 177–187.
- (25) Hoebbel, D.; Nacken, M.; Schmidt, H. *Journal of Sol-Gel Science and Technology* **2000**, *19*, 305–309.
- (26) Sanchez, C.; Livage, J.; Henry, M.; Babonneau, F. *Journal of Non-Crystalline ...* **1988**, *100*, 65–76.
- (27) Liu, J. Ph.D. Thesis, Lehigh University, 2006.
- (28) Greegor, R. B.; Blohowiak, K. Y.; Osborne, J. H.; Krienke, K. A.; Cherian, J. T.; Lytle, F. W. **2001**, *20*, 35–50.
- (29) Groenewold, J. *Physica A: Statistical Mechanics and its Applications* **2001**, *298*, 32–45.
- (30) Stafford, C. M.; Harrison, C.; Beers, K. L.; Karim, A.; Amis, E. J.; VanLandingham, M. R.; Kim, H.-C.; Volksen, W.; Miller, R. D.; Simonyi, E. E. *Nature materials* **2004**, *3*, 545–50.

- (31) Nolte, A.; Rubner, M.; Cohen, R. *Macromolecules* **2005**, 38, 5367–5370.
- (32) Stafford, C. M.; Vogt, B. D.; Harrison, C.; Julthongpiput, D.; Huang, R. *Macromolecules* **2006**, 39, 5095–5099.
- (33) Huang, H.; Chung, J. Y.; Nolte, A. J.; Stafford, C. M. *Chemistry of Materials* **2007**, 19, 6555–6560.
- (34) Tahk, D.; Lee, H. H.; Khang, D. **2009**.
- (35) Chan, E. P.; Page, K. a.; Im, S. H.; Patton, D. L.; Huang, R.; Stafford, C. M. *Soft Matter* **2009**, 5, 4638.
- (36) Allen, H. G. *Analysis and Design of Structural Sandwich Panels*; Pergamon: New York, 1969.
- (37) Landau, L. D.; Lifshitz, E. M. *Theory of Elasticity*; 3rd ed.; Elsevier, 1986; pp. 38–42.
- (38) Timoshenko, S.; Goodier, J. N. *Theory of Elasticity*; 1st ed.; McGraw-Hill Book Company, Inc.: New York and London, 1951.
- (39) Chaudhury, M. K.; Gentle, T. M.; Plueddemann, E. P. *Journal of adhesion science and technology* **1987**, 1, 29–38.
- (40) Gellman, A.; Naasz, B. M.; Schmidt, R. G.; Chaudhury, M. K.; Gentle, T. M. *Journal of adhesion science and technology* **1990**, 4, 597–601.
- (41) Gent, A.; Lin, C. *The Journal of Adhesion* **1990**, 32, 113–125.
- (42) Packham, D. *The Journal of Adhesion* **2010**, 86, 1231–1243.
- (43) Gent, A.; Lai, S. *Rubber Chemistry and Technology* **1995**, 68, 13–25.
- (44) Hutchinson, J. W.; Suo, Z. *Advances in Applied Mechanics* **1992**, 29, 63–191.
- (45) Singh, A. K.; Bai, Y.; Nadermann, N.; Jagota, A.; Hui, C.-Y. *Langmuir* **2012**, 28, 4213–22.
- (46) Vajpayee, S.; Khare, K.; Yang, S.; Hui, C.-Y.; Jagota, A. *Advanced Functional Materials* **2011**, 21, 547–555.
- (47) Rider, A. N.; Arnott, D. R. **1999**, 1063, 1055–1063.

- (48) Patinet, S.; Alzate, L.; Barthel, E.; Dalmas, D.; Vandembroucq, D.; Lazarus, V. *Journal of the Mechanics and Physics of Solids* **2013**, *61*, 311–324.
- (49) Namkanisorn, A.; Ghatak, A.; Chaudhury, M. K.; Berry, D. H. *Journal of Adhesion Science and Technology* **2001**, *15*, 1725–1745.
- (50) Whitehouse, D. *Wear* **1982**, *83*, 75–78.
- (51) Russ, J. C. *Fractal Surfaces*; 1st ed.; Plenum Press: New York and London, 1994.
- (52) Whitehouse, D. J. *Handbook of Surface Metrology*; 1st ed.; London and Philadelphia, 1994.
- (53) Feder, J. *Fractals*; New York, 1988.
- (54) Schmittbuhl, J.; Vilotte, J.; Roux, S. *Physical Review E* **1995**, *51*, 131–147.
- (55) Liu, J.; Chaudhury, M. K.; Berry, D. H.; Seebergh, J. E.; Osborne, J. H.; Blohowiak, K. Y. *The Journal of Adhesion* **2006**, *82*, 487–516.
- (56) Amada, S.; Hirose, T. *Surface and Coatings Technology* **1998**, *102*, 132–137.
- (57) Amada, S.; Satoh, A. *Journal of Adhesion Science and Technology* **2000**, *14*, 27–41.
- (58) Amada, S.; Yamada, H. *Surface and Coatings Technology* **1996**, *78*, 50–55.
- (59) Bahbou, M. F.; Nylén, P.; Wigren, J. *Journal of Thermal Spray Technology* **2004**, *13*, 508–514.
- (60) Harris, A. F.; Beevers, A. *Adhesion and Adhesives* **1999**, *19*, 445–452.
- (61) Bouchaud, E.; Lapasset, G.; Planes, J. *EPL* **1990**, *13*, 73–79.
- (62) Bonamy, D.; Bouchaud, E. *Physics Reports* **2011**, *498*, 1–44.
- (63) Papini, M.; Spelt, J. K. *The Mechanics of Adhesion*; Dillard, D. A.; Pocius, A. V., Eds.; 1st ed.; New York and London, 2002; pp. 303–350.
- (64) Brown, H. *Journal of Materials Science* **1990**, *25*, 2791–2794.
- (65) Xiao, F.; Hui, C.-Y.; Washiyama, J.; Kramer, E. J. *Macromolecules* **1994**, *27*, 4382–4390.

- (66) Xiao, F.; Hui, C.-Y; Kramer, E.J *Journal of materials science* **1993**, 28, 5620-5629.
- (67) Kanninen, M. *International Journal of Fracture* **1973**, 9, 83–92.
- (68) Daniel, S.; Chaudhury, M. K.; de Gennes, P.-G. *Langmuir* **2005**, 21, 4240–8.
- (69) Daniel, S.; Chaudhury, M. K.; Chen, J. C. *Science* **2001**, 291, 633–6.
- (70) Genzer, J.; Bhat, R. *Langmuir* **2008**, 2294–2317.
- (71) Morgenthaler, S.; Zink, C.; Spencer, N. D. *Soft Matter* **2008**, 4, 419.
- (72) Chaudhury, M.; Whitesides, G. *Science* **1992**, 256, 1539–1541.
- (73) Daniel, S.; Chaudhury, M. K. *Langmuir* **2002**, 3404–3407.
- (74) Daniel, S.; Sircar, S.; Gliem, J.; Chaudhury, M. K. *Langmuir* **2004**, 20, 4085–92.
- (75) Dannenberg, H. *Journal of Applied Polymer Science* **1961**, 5, 125–134.
- (76) Williams, M. L. *Journal of Applied Polymer Science* **1969**, 13, 29–40.
- (77) Williams, M. L. *Journal of Applied Polymer Science* **1970**, 14, 1121–1126.
- (78) Timoshenko, S. *The theory of Plates and Shells*; McGraw-Hill Book Company, Inc.: New York and London.

CHAPTER 2

Determination of the Modulus of Thin Sol-Gel films Using Buckling Instability¹

Abstract

Buckling instabilities have been used to estimate the elastic modulus of thin sol-gel films. The sol-gel films (65-400 nm) were coated on elastomeric supports, which were then subjected to a compressive strain imposed directly or as a result of thermal stresses generated during the curing cycle. Atomic force and optical microscopies were used to characterize the buckling wavelength, and electron microscopy was used to estimate the thickness of the films. Elastic modulus was calculated using the classical buckling theory. This procedure, which was demonstrated previously by others starting with the systematic studies of Stafford et al (Nature Materials, 2004, 3, 545-550), proves to be an effective way of determining the elastic modulus of thin films. The technique is used to study the effects of the concentration of the chemical precursors, curing temperature, the duration of cure and humidity on the moduli of sol-gel films, which provide valuable information about its performance when used as an adhesion promoter.

¹This work has been published as: Jonathan E. Longley and Manoj K. Chaudhury, "Determination of the Modulus of Thin Sol-Gel films Using Buckling Instability", *Macromolecules*, **2010**, 43, 6800-6810

2.1 Introduction

Hybrid organic-inorganic thin films prepared using sol-gel processing are useful in such areas as adhesion promotion^{1,2}, responsive coatings³ and corrosion resistance⁴ technologies. Their popularity stems from the fact that they are easily processable in terms of dip, spin or spray coatings and are curable at reasonably low temperature, i.e. below ~150 °C. These sol-gel systems generally involve the reaction between silanes and metal alkoxides. The detailed chemistry of the formation of the sol-gel coating is, however, complex depending on the relative concentrations and types of the various constituents used to prepare them^{1,3,5,6}. Predicting the effect of one of these parameters on the final film properties, such as modulus, porosity and cross-link density, is not obvious. What would be ideal for further progress of these technologies is to develop methods that would allow rapid characterization of the properties of the thin film as a function of the various chemical and processing parameters. Estimation of elastic modulus is one such property that is intrinsically linked to the cross-link density and thus the extent to which the film is cured. Determination of the modulus of a sol-gel film is typically carried out via indentation methods^{7,8}. However, a number of issues such as the effect of the support and their viscoelastic behavior cause difficulties in accurate estimation of elastic modulus of thin films^{7,9}. In some cases, these problems are somewhat circumvented by testing the bulk gel. It is, however, likely that the elastic properties of bulk gels are different from their counterparts as thin films. We report in this paper that the recently developed buckling based metrology technique¹⁰ is quite suitable for the estimation of the modulus of thin sol-gel films.

The adhesion promoting sol-gel film of interest here is the Boegel EPII formulation developed by The Boeing Company¹¹. Development of Boegel EPII was fueled by the increasing concern of the environmental effects of the traditionally used chromate conversion coatings¹², which are potentially toxic. The system is based on a dilute aqueous solution of zirconium and epoxy functionalized silicon alkoxides, details of which are described in references 11 and 13. The alkoxides are first hydrolyzed in solution so that they react with the hydroxyl groups on the metal surface through condensation reactions. The organic functional groups are chosen such that they are compatible with the adhesive. The glycidoxy functional group is ideally suited to react with the amine functionalized crosslinker used in epoxy systems. In between the metal and organic resin the Boegel film forms a hybrid organic-inorganic coating through crosslinking condensation reactions (Figure 2.1).

Throughout the rest of this Chapter we will refer to Boegel EPII simply as sol-gel. The major advantage of the sol-gel formulation is its ability to cure at room temperature, which allows its easy processing on tempered aluminium parts used in airplane manufacturing. At this low temperature cure, however, it is likely that the sol-gel film is not fully cross-linked; residual hydroxyl groups may remain. Previous studies in our lab using a model epoxy adhesive elucidated that the fracture energies of the sol-gel reinforced joints are strong functions of the curing history^{13,15} in both dry and wet and environments. This suggests that the performance of the sol-gel is a function of the degree of cross-linking within the film. It is expected that a fully cured sol-gel film should impart higher adhesion strength and hydrolytic stability compared to an incompletely cross-linked film provided that the excessive curing of a sol-gel film does

not degrade the chemical functional groups. This issue can become quite complex, as a number of system parameters may play their roles in a conflicting manner. Our main objective in the current study is to characterize the modulus of the sol-gel film as a function of different curing parameters in order to gain some understanding of the mechanical properties of these films.

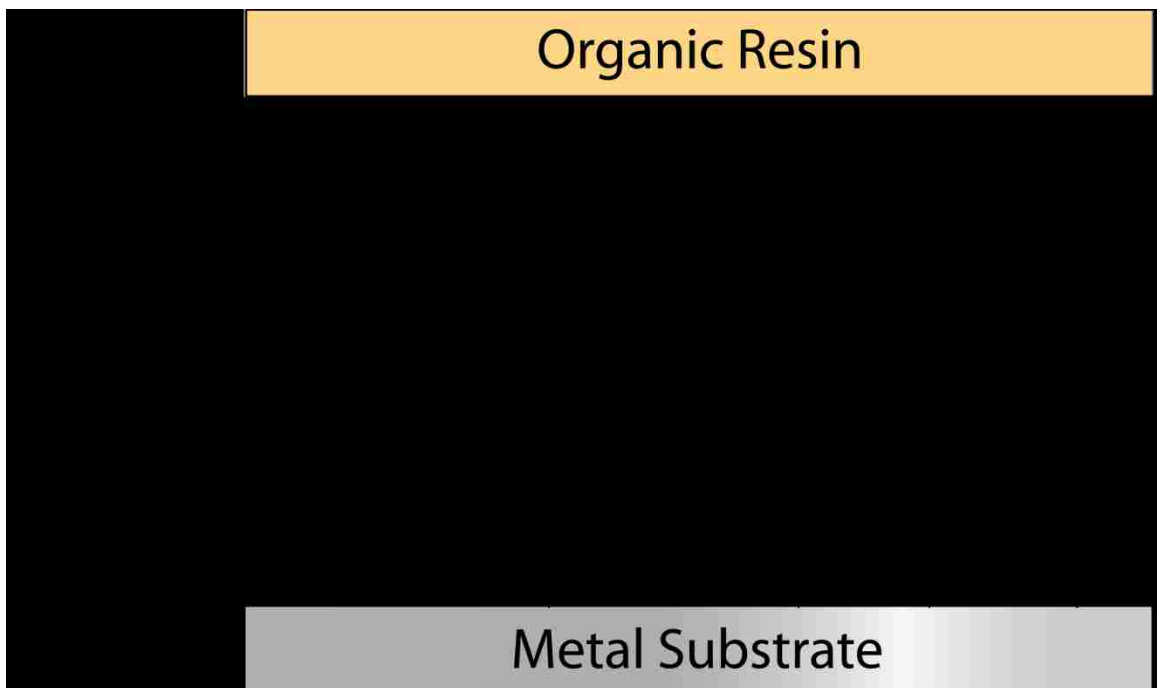


Figure 2.1: Schematic of sol-gel coating for adhesion promotion adapted from reference 13. Coating is generated from an aqueous sol of Glycidoxypropyltrimethoxysilane (GTMS) and Zirconium tetrapropoxide (TPOZ). XPS studies¹⁴ show the sol-gel/metal interface to be rich in zirconium and the sol-gel/organic resin interface to be silane rich.

When a thin rigid film adhered to a softer elastic substrate is exposed to an external stress, the surface can buckle due to the mismatch of strain in the adjacent layers. As each layer tries to obtain a minimum energy state due to compression and bending, the surface buckles to minimize the overall energy of the system (Figure 2.2).

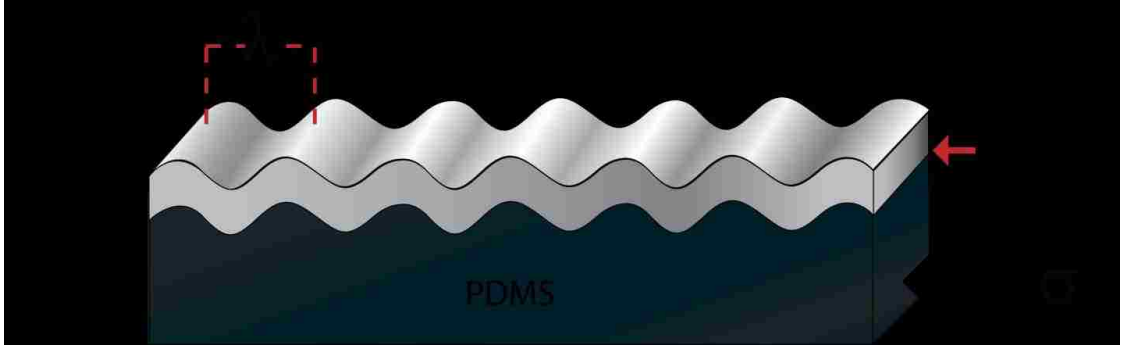


Figure 2.2: Schematic of the buckling of a thin sol-gel layer on a soft compliant PDMS substrate. When a compressive stress σ is applied to PDMS, buckles appear perpendicular to this force. The buckling wavelength λ is a function of the plane strain moduli of the two materials and the thickness of the sol-gel layer.

The classical approach to solving this problem of relating the buckling wavelength to the material parameters is based on a force¹⁶ or an energy¹⁷⁻¹⁹ balancing method. For a semi-infinite substrate, i.e. when its thickness is much larger than the thin coating, the wavelength of the buckling instability can be given by equation 2.1:

$$\lambda = 2\pi h_{SG} \left[\frac{(1 - \nu_{PDMS}^2) E_{SG}}{3(1 - \nu_{SG}^2) E_{PDMS}} \right]^{1/3} \quad (2.1)$$

where E_{SG} , E_{PDMS} , ν_{SG} , ν_{PDMS} , h_{SG} , λ are the elastic modulus of the sol-gel layer, elastic modulus of the PDMS, the Poisson ratio of the sol-gel, the Poisson ratio of the PDMS, the thickness of the sol-gel film and the buckling wavelength respectively. In this work we are primarily interested in the relative change of the modulus of the sol-gel film as a function of different curing parameters. Given this interest and that the Poisson's ratio of the sol-gel film is an uncertain parameter, we will present the data in terms of the plain strain modulus, which is defined as $\bar{E}_{SG} = \frac{E_{SG}}{(1 - \nu_{SG}^2)}$. Equation (2.1) can then be rearranged

to solve for the plain strain modulus of the sol-gel film. Where elastic modulus is

required, for comparison to the literature, we have estimated the value assuming a range of suitable Poisson ratios.

This buckling instability has been studied in detail for a wide variety of systems such as thin metallic films and silica type layers on PDMS²⁰⁻²². The general method used to achieve the above goal^{10,22} is now commonly referred to as the strain induced elastic buckling instability for mechanical measurement (SIEBIMM). In this regard the most studied system is the buckling of polystyrene films on PDMS substrates, although the modulus of several other polymers, polyelectrolytes and dielectric films have also been determined using this method^{10,23,24}. In this Chapter we apply the buckling instability technique to determine the elastic modulus of a sol-gel film under various conditions.

A roadmap of this Chapter is as follows. After the description of the experimental section, we present data showing that the wavelength of the buckling instability of the sol-gel film varies linearly with its thickness in its fully cured state. This initial part of the study demonstrates that the relationship between the wavelength and the thickness of the sol-gel film is quite robust, this allows us to estimate the modulus of the film either from the gradient of their linear correlation or from a single measurement of wavelength for a given film thickness. The former method can be used when the property of the film does not change as a function of thickness. However, we are bound here to make measurements from a single set of data in many cases, where the properties of the incompletely cross-linked films are likely to depend on its thickness. Using the measurements of the latter kind, we present data showing how the modulus of the sol-gel film depends on the curing temperature. These data allow a correlation to be made between the modulus and the adhesive performance of the film when it is used as a thin

film adhesion promoter for the adhesion of epoxy to aluminum. Being encouraged by these findings, we extend the scope of this study to incorporate the dependence of other variables, such as the duration of cure of the sol-gel films and the effect of humidity on its properties. The paper then ends with a discussion on the relevance of these studies and a conclusion.

2.2 Experimental Section

2.2.1 Preparation of Sol-Gel Solution

Details on the formulation of the sol-gel solution can be found in the literature ^{11,13}. Here, we present only a brief summary. The sol-gel films are formed from a dilute aqueous solution of Glycidoxypropyltrimethoxysilane (GTMS) (97% Gelest), Zirconium tetrapropoxide (TPOZ) (70% w/w in n-propanol, Alfa Aesar), glacial acetic acid (Sigma-Aldrich) and Antarox BL-240 (Rhodia Inc). The thickness of the film was controlled by changing the concentration of the GTMS and TPOZ in the sol. Immediately before applying the sol-gel coating to PDMS, it was passed through a 2 μm qualitative filter paper (Whatman). PDMS substrates were coated within 2 hr of the preparation of the sol.

2.2.2 Surface Preparation and Modification of PDMS elastomeric substrates

Sylgard 184 (Dow Corning) was used as the elastomeric support. Curing agent was mixed thoroughly with the base in the ratio of 1:10. After degassing the mixture for 12 hours, the mixture was cured at 65 °C for 4 hours in a convection oven (Tenny Jr, Thermal Product Solutions), in the form of thin (2 mm) sheets. These sheets are cut into coupons measuring 25 mm x 75 mm. After loading them to a sample holder, as described

in the next section, they were washed with DI water and blown dry with nitrogen. The sample mount is then placed on a conductive surface and exposed to the corona generated from a Tesla coil for 1 min. This treatment produces a thin silica like layer, which is wettable by water (contact angle of $<5^\circ$). These surfaces do reconstruct slowly; hence they have been used within 3 minutes after coronal treatment. Bowden et al²⁵ have studied the effect with PDMS exposed to oxygen plasma, and conjectured that increasing the exposure time to plasma increases the silica layer thickness. In the present study, the low energy corona discharge is used for a short duration in order to oxidize the surface that minimizes the formation of a thin silica-like layer. The difference of the elastic modulus between this thin silica type layer and the bulk PDMS itself causes surface buckling upon application of a compressive stress. The silica type layer, created from the corona treatment, and its effect on the measured sol-gel buckling wavelength is addressed in the start of the results and discussion section.

2.2.3 Coating of sol-gel film on PDMS substrates, testing procedure and the determination of film thickness

A customized apparatus (Figure 2.3) was designed for surface modification, spin coating and application of controlled strains to the PDMS samples. This design avoids the need to remove the PDMS from the sample holder, which eliminates un-wanted stress causing film delamination. The PDMS was securely fastened to the sample mount and then pre-stressed to minimize any sagging of the film during the spin coating process (Figure 2.3a). The amount of strain in the sample was recorded from the micrometer reading. After securing the sample mount in this position and removing it from the

micrometer, the surface of PDMS was exposed to corona discharge as described above. Next it was mounted onto the spin coater (Headway Instruments) after attaching it to a spin coating plate (Figure 2.3b). Sol-gel solution was applied to the PDMS with a pipette and allowed to thoroughly wet it for 2 minutes. Samples were spun at 1200 rpm for 50 seconds, then cured either at the ambient condition or inside a convection oven.

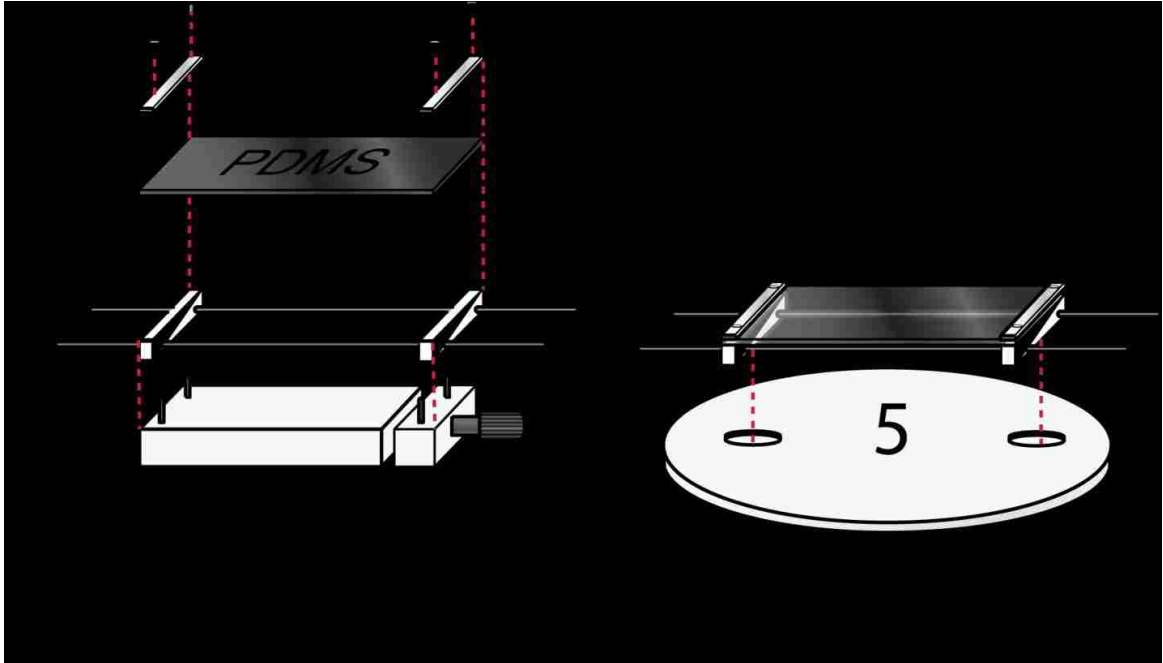


Figure 2.3: Illustration of sample mount, strain micrometer and spin-coating mount. Mounting brackets (1) are used to firmly secure the PDMS sheet (25x75x2 mm) (2) to the sample mount (3). The sample mount is then loaded onto the locking pins of the micrometer (4). The distance between the fastening blocks on the sample mount can be easily adjusted to ensure that sufficient pre-strain is applied to the PDMS sheet. Locking nuts on the fastening blocks allow this strain to be locked in place. After removing the PDMS loaded sample mount from the micrometer, it was fastened to the spin coating mount (5). After the sol-gel film was spin coated on PDMS, the sample mount was removed from the spin coating mount and placed in the required curing environment. After the required cure had taken place the sample mount was then reattached to the micrometer where the strain was applied and recorded.

For the samples cured at temperatures above 75 °C, the thermal expansion provides a level of strain that is sufficient to cause buckling in the film. The wavelength of the

buckling is independent of the applied strain provided that it is low enough i.e. < 10%. For other samples, strains of ~1.5-4% were applied to the system by relaxing the pre-stressed PDMS. Buckling wavelength was estimated by imaging three areas on the substrates selected at random. Images were taken using either an optical microscope in a reflectance mode (Nikon) or with an atomic force microscope (Nano-dimension V) when the buckling wavelength is below ~ 2 μm .

The thickness of the sol-gel films on PDMS was determined with a scanning electron-microscope (Hitachi 4300). Typically, the thicknesses of the thin films on PDMS are analyzed^{23,24} using variable angle spectroscopic ellipsometry (VASE). While the throughput rate with the SEM analysis is not as high as the VASE, it has the advantage that the film thickness can be clearly visualized on the substrate and that the measurements can be made in absolute scale. Samples were cut with a scalpel and mounted in such a way that the film thickness is perpendicular to the field of view. Samples were then sputtered with Iridium for 10 seconds (Electron Microscopy Sciences EMS 575x). The thickness of the film was determined from the SEM images using an image analysis software at a number of positions along the interface. As a separate study, the thicknesses of the sol-gel films deposited on silicon wafers were determined with ellipsometry (Rudolph Research AutoEL III).

2.3 Results and Discussion

2.3.1 Estimation of the Properties of the Silica type layer

Oxidation of the surface of PDMS causes the formation of a thin silica-like layer. The mismatch in elastic moduli of this film and that of the bulk PDMS causes the surface to

buckle when a compressive stress is applied. Bowden et al ²⁵ have found that the buckling wavelength increases with oxidation time, suggesting that the thickness of this stiff layer also increases. In the aforementioned work oxygen plasma is used to modify the surface of PDMS. In the present study a corona discharge was used to oxidize the surface of PDMS, as outlined in the experimental section. Although this treatment is lower in energy than oxygen plasma, it must still be assumed that a thin film is formed on the surface of PDMS. When this treated surface is strained above ~8%, small buckles can be seen on the surface (Figure 2.4). The presence of these buckles indicates that a silica type layer is formed on the surface due to the corona exposure, which could affect the measurements of the properties of the sol-gel films deposited on it. The surface bucklings on the oxidized PDMS have an amplitude and wavelength of ~2.2 nm and ~0.18 μm respectively (Figure 2.4) at ~8% strain. In order to make an estimate as to what extent the measurements could be affected, let us compare the bending rigidities of the corona generated silica layer on PDMS and that of the most weakly crosslinked sol-gel films in our studies. We can combine the standard expression for the flexural rigidity of an elastic plate with equation 2.1 as follows,

$$D_{Silica} = \frac{\bar{E}_{Silica} h_{Silica}^3}{12} = \frac{\bar{E}_{PDMS}}{4} \left(\frac{\lambda}{2\pi} \right)^3 \quad (2.2)$$

where E_{Silica} and h_{Silica} are the plane strain modulus and thickness of the silica layer respectively. Using the wavelength of the buckling of the oxidized PDMS (~0.18 μm), a value of the flexural rigidity of the silica-like layer is estimated as $D_{Silica} = 1.6 \times 10^{-17}$ Nm. By comparison, the flexural rigidity of a thin (50 nm) weakly cross-linked sol-gel film of an elastic modulus of 2 MPa and Poisson's ratio of 0.25 is $D_{solgel} = 2.2 \times 10^{-17}$

Nm. As these bending rigidities are very close to each other, we expect the silica layer to have a significant effect on the determination of the elastic property of the weakly crosslinked and very thin sol-gel film. In this work, however, the moduli of the sol-gel films for the vast majority of cases are significantly higher than 2 MPa with the corresponding flexural rigidities orders of magnitude larger than that of the corona generated thin oxide layer on PDMS.

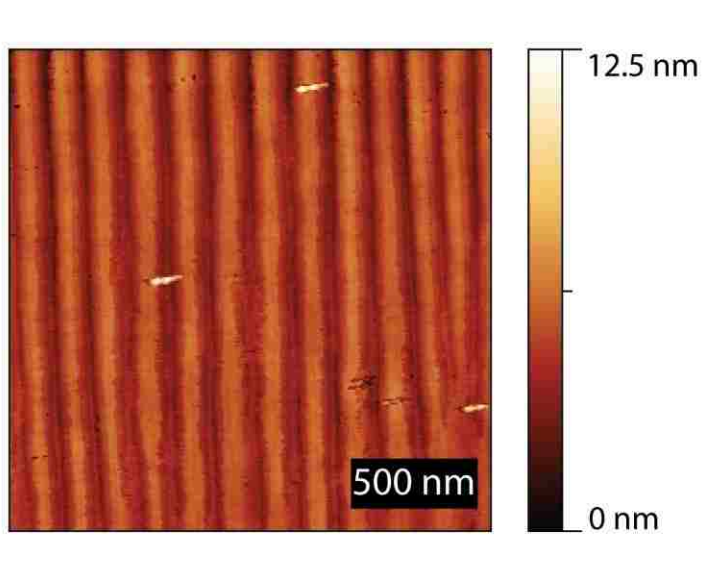


Figure 2.4: AFM scan of a PDMS surface treated with a corona discharge buckling under an applied strain. PDMS surfaces are exposed to a corona discharge for 1 min under ambient conditions, 23 °C and 47% RH, subjected to a strain of ~8%.

2.3.2 Estimation of the Elastic Modulus of the sol-gel films

In order to validate the method of buckling instability to estimate the properties of the sol-gel films, the effects of the concentration of the sol-gel precursor on the thickness and the elastic modulus of the resultant film were evaluated. A curing temperature of 120 °C was chosen in order to avoid the degradation of the GTMS component²⁶ of the sol-gel

film that could occur at a higher temperature. This is also a reasonably high temperature at which the film is cured completely. Figure 2.5 displays the SEM images of the sol-gel films from which their thicknesses were measured. Figure 2.6 compares the thicknesses of the sol-gel films measured using the above method with those of the films deposited on a silicon wafer under similar conditions using the method of ellipsometry. This comparison shows that both methods yield similar results. We use the thickness measured by SEM in these studies for the convenience of measurements done on PDMS rubber; it also provides the measurements to be done in absolute scale.

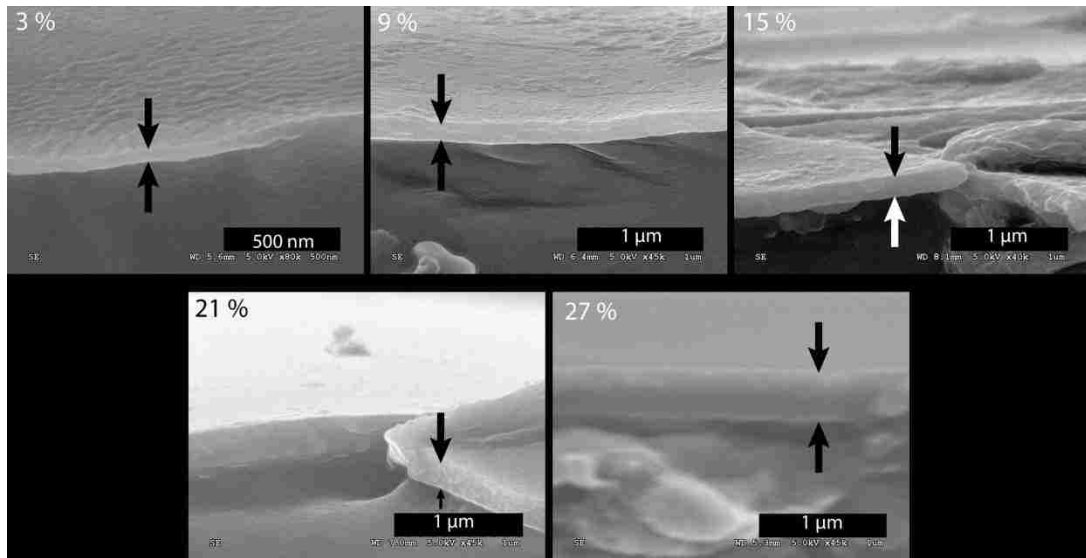


Figure 2.5: SEM micrographs showing the thickness of the sol-gel film on PDMS films for 5 different sol-gel concentrations. Concentrations are displayed in the upper right corner of each image. Samples were cut with a scalpel and mounted on a SEM stub such that the PDMS/sol-gel interface was at 90 ° to the electron gun. Note the change of scale on the images.

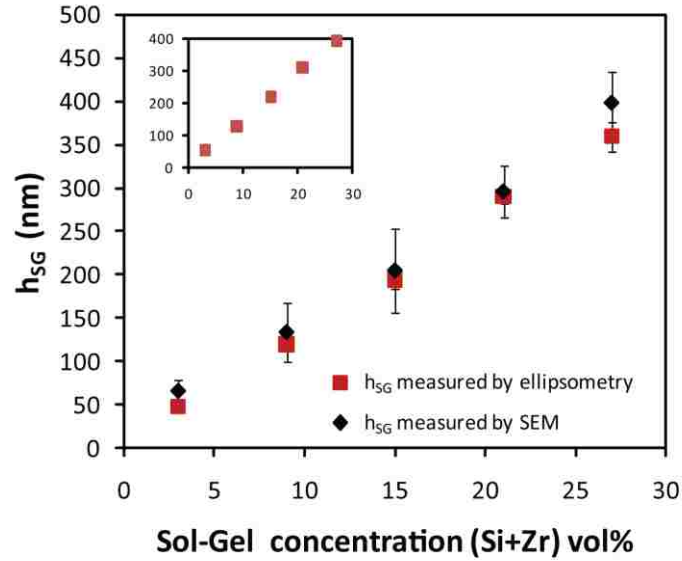


Figure 2.6: Comparison of Film thickness (h_{SG}) vs. sol-gel concentration measured via two different techniques. Black diamonds correspond to SEM measurements for the sol-gel films cured at 120 °C on a PDMS support and the red squares correspond to the ellipsometry measurements for films cured under identical conditions on silicon wafer. Insert: Ellipsometry results for the thickness of films cured under ambient conditions (23 °C and 47% RH) for 24 hrs as a function of sol-gel concentration. On average, the oven cured films show an ~8 % decrease in thickness compared to the room temperature cured. Error bars are hidden in the marker size.

Figure 2.7 shows that the thickness of the sol-gel film as well as the buckling wavelength increases linearly with the concentration of the starting sol precursor. From here onward, all the data will be presented as a function of the thickness of the sol-gel film instead of the sol concentration. Figure 2.8 summarizes the buckling wavelength vs. film thickness data for sol-gel films cured at 120 °C. From the gradient of the line passing through the experimental points, its plane strain modulus is estimated to be 1.7 ± 0.2 GPa. In the same figure, the plane strain modulus of each film as estimated using equation 2.1 is reported. As expected, these values closely cluster around their mean. Based on this obvious comparison, we conclude that either method can be used to

accurately determine the elastic modulus of the sol-gel film. It can be seen from this figure that the largest error in the data and indeed the major limit of accuracy of the technique is the measurement of the thickness of the film. The statistical error is comparable to those of other techniques such as nano-indentation and three point bending tests (for bulk gels).

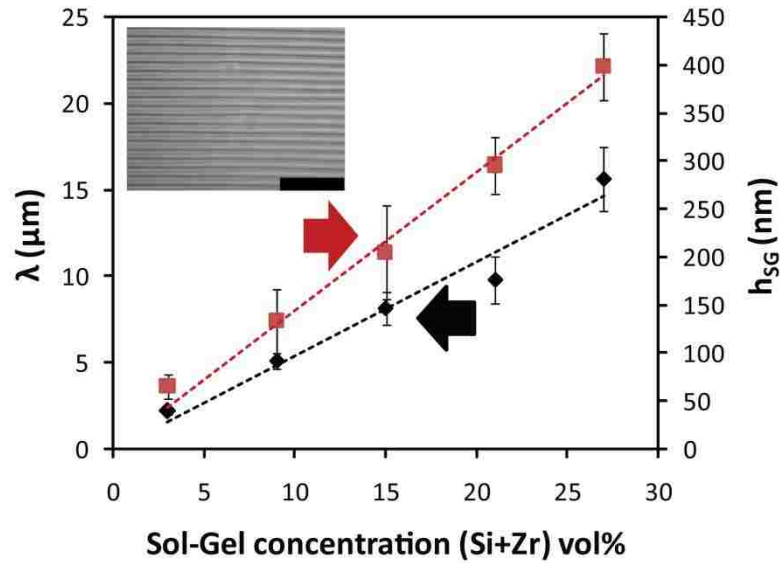


Figure 2.7: The effect of sol concentration ((Zr+Si) vol%) on film thickness (h_{SG}) and buckling wavelength (λ). Black diamonds represent the buckling wavelength vs. sol-gel concentration whereas the red squares represent sol-gel film thickness (as measured by SEM) vs. sol-gel concentration. A linear relationship is observed in the buckling wavelength vs. sol-gel concentration. Here, the buckling wavelength was measured using optical microscopy for films cast from sol-gel concentrations equal to and above 9 vol%. AFM was used for measuring the wavelength of films formed from sol-gel concentrations below 9 vol%. Error bars represent one standard deviation of the data. Sol-gel films were cured at 120 °C. Insert - Optical microscopy image of buckling on a film cast from a sol-gel concentration of 21 (Si+Zr) vol%. Scale bar represents 50 μm .

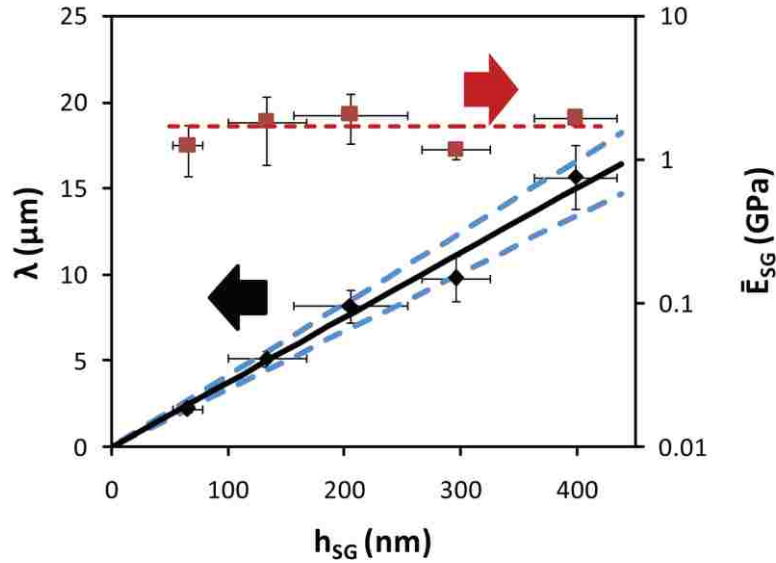


Figure 2.8: Relation of buckling wavelength (λ) and plane-strain modulus (\bar{E}_{SG}) to sol-gel film thickness (h_{SG}). Film thickness is measured via SEM. Wavelength data displayed in Figure 3 is re-plotted against film thickness. Using the data in Figure 2.3 it is shown here that the plane-strain modulus is independent of film thickness. Black diamonds represent buckling wavelength vs. sol-gel film thickness, whereas the red squares represent the modulus of the sol-gel thin film. The black line represents a line of best fit on the Buckle wavelength vs. Film thickness data which passes through the origin. The blue dashed lines represent 95% confidence intervals on the Buckle wavelength vs. Film thickness results.

As the properties of a sol-gel film strongly depend on its chemical formulation and curing history, it is difficult to compare our results to any similar results published in the literature. Nevertheless, it is instructive to look at two particular examples. However, before this comparison is made it is necessary to define a suitable Poisson's ratio for the sol-gel film in order to convert the plane-strain modulus to the elastic modulus. It is difficult to ascertain the exact value of the Poisson's ratio for this film as it contains both organic and inorganic components. Thus we used an approximate method. Poisson's ratio for mesoporous silica films²⁷ is reported to be 0.25, while that for amorphous polymeric solids²⁸ is in the range of 0.3-0.4. Given the above values of the Poisson's

ratio we used a range of 0.25-0.35 to estimate the elastic modulus of the sol-gel film. The elastic modulus of the film cured at 120 °C is then estimated to be in the range of 1.5 to 1.6 GPa. Atanacio et al⁷ reported the moduli of various organic-inorganic hybrid films based on the mixtures of TEOS (tetraethoxysilane) and alkyltriethoxysilanes of various kinds as obtained using nano-indentation. Of particular relevance here is that of the TEOS and GTMS formulation. The Young's modulus of this film was found to be around 1.68 GPa and 1.81 GPa when measured on silicon and copper substrates respectively⁷. In a separate study, bulk gels of TEOS+GTMS+TPOZ have been investigated using Knoop microindentation for which the elastic modulus was estimated to be around 0.57 GPa when the gels were cured at 125 °C for 72 hr⁸. The value of the modulus of the sol-gel films estimated by us fall in between those reported in the above two studies, although direct comparison cannot be made.

2.3.3 The effect of the curing temperature on the modulus of the sol-gel films

The curing temperature of the sol-gel based coating is an important contributor to the final strength of the adhesive joint. It is generally believed that the coating needs to be cured to a degree that does not affect the ability of primers or adhesives to wet and penetrate it to some extent so that a defect free interface can be formed. Figure 2.9 shows that the curing temperature has a pronounced effect on the modulus of the thin (65±13 nm) sol-gel films. The modulus, and thus the cross linking density, of the film sharply increases with the curing temperature until all the major cross links are formed leading to a plateau in modulus. The exact nature of these cross links is, however, unclear although silicon - oxygen - silicon, zirconium - oxygen - zirconium, zirconium - oxygen -

silicon, and silicon - oxygen - substrate or zirconium - oxygen - substrate are all possible. The epoxy ring of GTMS can also open to form a diol but it is unclear whether these functional groups are involved in any cross linking reaction. The specific cross-links aside, nearly a 17 fold rise in elastic modulus occurs when the curing temperature is increased from 45 °C to 85 °C. It is assumed that within the range of temperature used in these studies, the maximum possible degree of cross linking is achieved at the above temperature. This result coincides with the previously reported²⁶ IR spectroscopy studies with the GTMS films, which found that no significant change in the degree of condensation occurs within a curing temperature range of 93-180 °C. The previously mentioned ellipsometric studies (Figure 2.6) on film thickness show a ~8 % decrease in film thickness between room temperature cure and 120 °C cured films. This decrease is within the statistical variation in the SEM thickness measurement and as such is not directly measurable. However, it is worthwhile to note that this decrease in thickness would accentuate the trend of elastic modulus with curing temperature which we observe here.

The compressive strain required for buckling can be generated either by an externally applied force or due to the stresses developed in the film due to the mismatch of thermal expansion coefficients during a thermal curing cycle. As noted in the experimental section, sol-gel films cured below 75 °C were buckled mechanically by releasing the pre-stained PDMS substrate. Films cured above 75 °C buckled due to thermally induced stress. It is important here to consider a potential artifact in the estimation of the modulus of thin films which arises due to thermal stress. The modulus of a thin polymer brush, in which buckling was induced by thermal stress, is about four times lower than when the

buckling was induced mechanically.²³ Should a similar effect be present in our system, elastic modulus at room temperature of the thermally buckled sol-gel films would be higher than our current estimation. This would accentuate the trend that the elastic modulus increases with curing temperature.

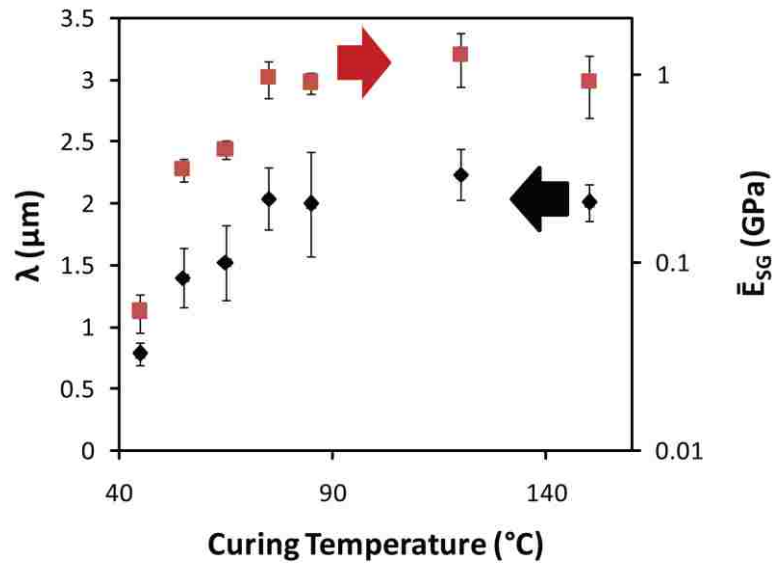


Figure 2.9: Buckling wavelength (λ) and plane-strain modulus (\bar{E}_{SG}) as a function of curing temperature. Plane-strain modulus is calculated from the displayed wavelength. Cure time was 30 minutes at approximately ~47% RH. Black diamonds represent the buckling wavelength vs. sol-gel film curing temperature, whereas the red squares represent sol-gel thin film modulus vs. sol-gel film thickness.

It is worthwhile to note that if the film is cured at 120 °C after aging it for 2 days at room temperature (23 °C) it shows the increase in the modulus (Figure 2.10) of the film that is comparable to that cured directly at 120 °C. This change of modulus suggests that the un-reacted hydroxyl groups remain within the film that are activated when exposed to higher temperature. This is important for achieving good adhesion with an epoxy or other adhesives that can be post cured on the sol-gel film at higher temperature. We bring up

this issue next as we attempt to find a relationship between the modulus of sol-gel coating and its adhesion performance with epoxy under dry and wet conditions.

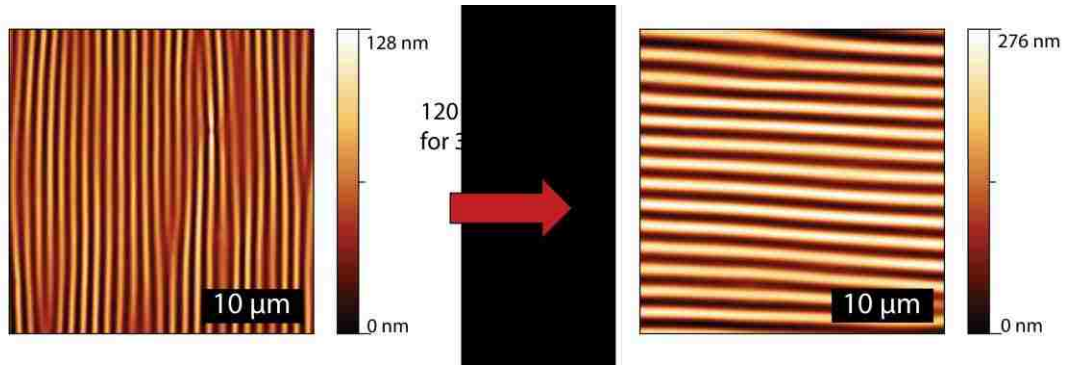


Figure 2.10: AFM images of the effect of post curing a film after it is aged under ambient conditions for 2 days. The left image shows the buckling wavelength of the film after aging it under ambient conditions (23 °C, 47% RH) for 2 days. The right image shows the effect of post curing this sample at 120 °C for 30 minutes. The wavelength changes from $\sim 1.1 \mu\text{m}$ to $\sim 2 \mu\text{m}$. This causes a change in plane strain modulus from $0.2 \pm 0.03 \text{ GPa}$ to $1 \pm 0.3 \text{ GPa}$. If the sol-gel film (65 nm thick) is cured directly at 120 °C for 30 minutes the estimated plane strain modulus is $1.3 \pm 0.4 \text{ GPa}$. Buckles for oven cured films are orientated perpendicular to those at room temperature as the buckling is caused by the thermal stress. Thermal stress generates one dimensional buckling due to the geometric confinement of the clamp, this effect is described in detail in the text.

2.3.4 An empirical correlation between modulus of the sol-gel coating and its adhesive performance

In our laboratory, Liu²⁹ studied the effect of sol-gel cure temperature on the fracture strength of the aluminium/sol-gel/epoxy joint under wet and dry conditions. The critical energy release rates of these joints were measured using the method of an asymmetric double cantilever beam. Fracture experiments under ambient conditions were carried out at 23 °C and 47% RH, whereas those under wet conditions were conducted by inserting a water droplet into the crack tip for 2 minutes before extending it with a wedge. Here, we attempt to seek if any correlation exists between the critical fracture strength of the adhesive joints and the elastic moduli of the sol-gel films as found in our experiments.

The results summarized in Figure 2.11 show that the dry joint strength of the adhesive joint decrease considerably with increasing modulus. From this comparison we surmise that increasing the cross-link density of the film, thus increasing its modulus, possibly decreases the interpenetration of the epoxy into the sol-gel layer. The correlation also suggests that this effect is predominant after a critical modulus (~50 MPa) is exceeded, above which any further increase in modulus is extremely detrimental to the joint. The wet strength results show a similar trend as well, although the effect of the modulus of the sol-gel film is less prominent here. The fact that the lower cross linked sol-gel films display superior joint strength under both dry and wet conditions suggest that the sol-gel layer is further cross linked during the cure of the epoxy adhesive which occurs at 100 °C. As previously mentioned, sol-gel films aged at a low temperature can be post cured at higher temperatures, Figure 2.10. This observation suggests the following scenario when they are used as adhesion promoters. The adhesive can diffuse into the low temperature cured sol-gel films and react with the available epoxy groups to some extent. When the adhesive is aged at a temperature of 100 °C, the crosslinking of the sol-gel films also increases, thus allowing the formation of an interpenetrating network. This post cure idea has been previously speculated in the literature and is reviewed nicely by Abel *et al.*³⁰. This is of relevance to industrial applications, where it is important to ensure that a surface remains chemically active after pretreatment, as there is often a lag time between surface treatment and adhesive joint preparation.

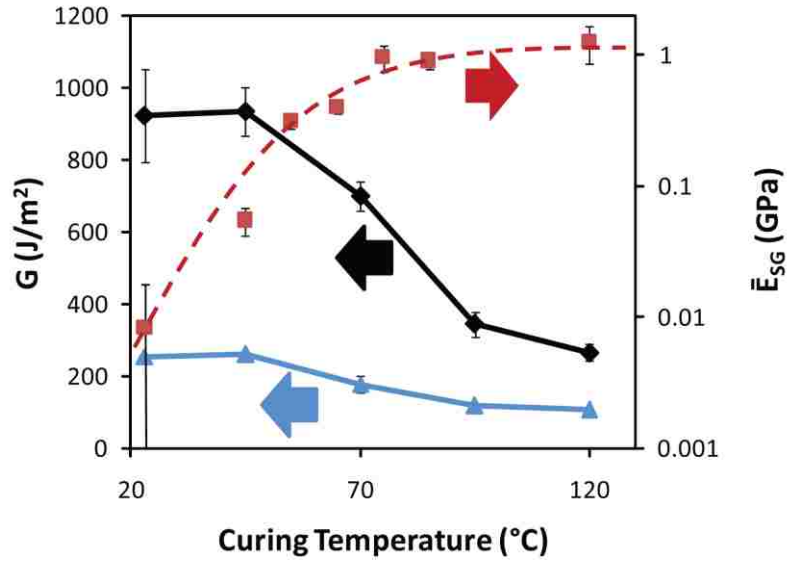


Figure 2.11: Fracture strength (G) of an Aluminium/sol-gel/Epoxy joint under wet and dry conditions versus the curing temperature of the sol-gel primer. The plane-strain modulus (\bar{E}_{SG}) dependence on the curing temperature is replotted from Figure 2.9 on the right axis. Black diamonds and blue triangles represent dry and wet fracture strengths respectively versus sol-gel curing temperature. Red squares represent the plane-strain modulus versus the curing temperature. Details of the wet vs. dry fracture experiments are outlined in the text. The Aluminium (2024-T3) substrates are etched in a Forest Products Laboratory solution prior to sol-gel application²⁹.

Having established a strong correlation between the modulus of the sol-gel films and its adhesive performance, we now present some data on how this modulus is affected by the duration of cure and humidity.

2.3.5 Duration of cure at room temperature and the modulus of the sol-gel films

The previous studies performed in our laboratory¹⁵ show that the highest increase in adhesion occurs when the gel is cured at room temperature for 75 min. In our current study, we do not observe buckling for room temperature cured films until a minimum of 3 hours is passed since the coating step. The plane strain modulus of the sol-gel film at

this cure time (3 hrs) is estimated to be ~8 MPa. The critical strain (ϵ_{crit}) for buckling to occur is given by equation 2.3.

$$\epsilon_{crit} = \frac{1}{4} \left[\frac{3\bar{E}_{PDMS}}{\bar{E}_{SG}} \right]^{2/3} \quad (2.3)$$

For a sol-gel film of modulus ~8 MPa, equation 2.3 predicts that the critical strain needs to be about ~24% before the buckles are formed. In our experiments, we see buckles even when the sol-gel films are subjected to a strain of ~1.5-4%. The single film buckling equation does not describe the formation of the buckles for such films, although the prediction (3% strain) is reasonably good for films aged for 9 hours or more (Figure 2.12). The origin of the above discrepancy is not clear. We surmise that the elastic modulus of the sol-gel film is very low at cure times of < 3 hrs under ambient conditions (23 °C, 47% RH), which is not measurable by this technique. Films cured for 24 hrs under 20% RH at 23 °C gave a plane strain modulus of 200±70 MPa. Compared to the value recorded at 47% RH and 23 °C of plane strain modulus 170±30 MPa we can conclude that lowering the humidity does not have an appreciable effect on the rate of cure of the sol-gel film.

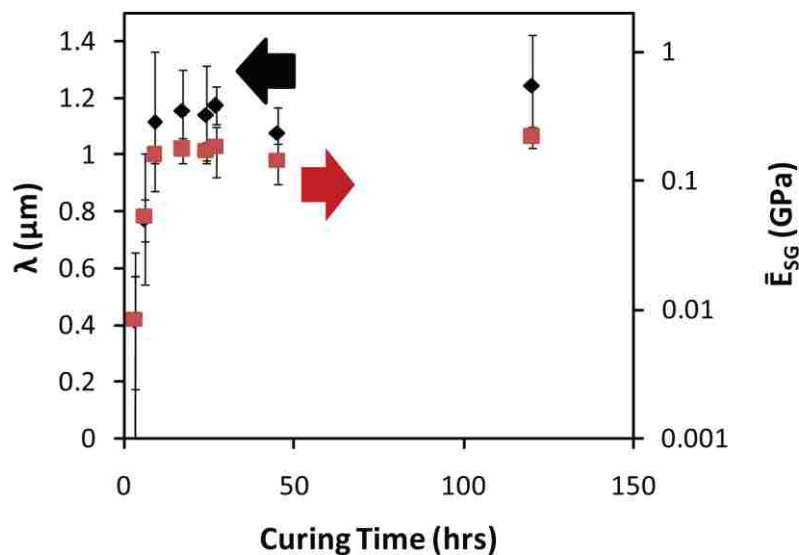


Figure 2.12: The effect of curing time, under ambient conditions (23 °C, 47% RH), on sol-gel film plane-strain modulus (\bar{E}_{SG}). A strain of ~3% was applied to induce buckling. The black diamonds represent the buckling wavelength vs. curing time, whereas the red squares represent sol-gel thin film modulus vs. curing time.

2.3.6 Effect of Humidity on a post cured sol-gel thin film

We now describe the final segment of our study, where we report the effect of humidity on the properties of the sol-gel film. It is well-known that the strength of any adhesive promoted by a sol-gel coating in an humid environment is of paramount importance to various industrial applications. As mentioned above, Liu et al^{13,15} investigated the adhesive performance of epoxy/Boegel EPII/aluminium joints under wet conditions. The overall conclusion of these studies is that water decreases the durability of the joint, thus decreasing its threshold fracture energy. Other studies³¹⁻³³ show as well that water is capable of penetrating into the adhesive joints and damaging the integrity of the sol-gel film over time by hydrolyzing the interface. Polymer films are also known to swell in the presence of many solvents, which induce instabilities within the film or the relaxation of

residual stresses^{17,23}. With these facts in mind, we investigate the effects of humidity on the behavior of buckled sol-gel films.

Figure 2.13 depicts the effect of humidity on the morphology of the buckled sol-gel coatings when they are stored under ~98% RH (relative humidity) for 15 hours. A number of intriguing pattern formations are evident. The change in the buckling pattern when the films are cured at low temperatures (45-65 °C) and then exposed to high humidity is different from those cured at higher temperatures (85-150 °C) and stored under similar conditions. It is important here to clarify a point made briefly in the experimental section. When cured at temperatures below 75 °C, the films do not buckle upon removal from the oven. Buckling is induced by releasing the pre-strain in the PDMS, therefore the compressive strain is applied in the x direction (see Figure 2.2). This results in the formation of buckles parallel to the y coordinate. For samples cured at temperatures above 75 °C, we observe buckling upon cooling due to the mismatch in the thermal expansion coefficients of the sol-gel coating and PDMS. The buckling however is oriented parallel to the x coordinate. This 90 degree rotation in the buckling pattern can be explained by considering the way in which the PDMS expands in the metal clamp. As Figure 2.3 shows, the PDMS is securely clamped at both ends. During the heating process, the film is free to expand in the y direction anywhere other than near the clamps where it is constrained. The pre-strain in the x direction is chosen to ensure that the thermal expansion does not cause sagging of the PDMS. Were it not for this confined geometry, buckles in the herringbone or labyrinth conformation should occur as a result of thermal stress²⁰. Upon cooling the PDMS, contractions in the y direction generate a

compressive force within the cured sol-gel layer. This results in the formation of buckles orientated perpendicular to this force.

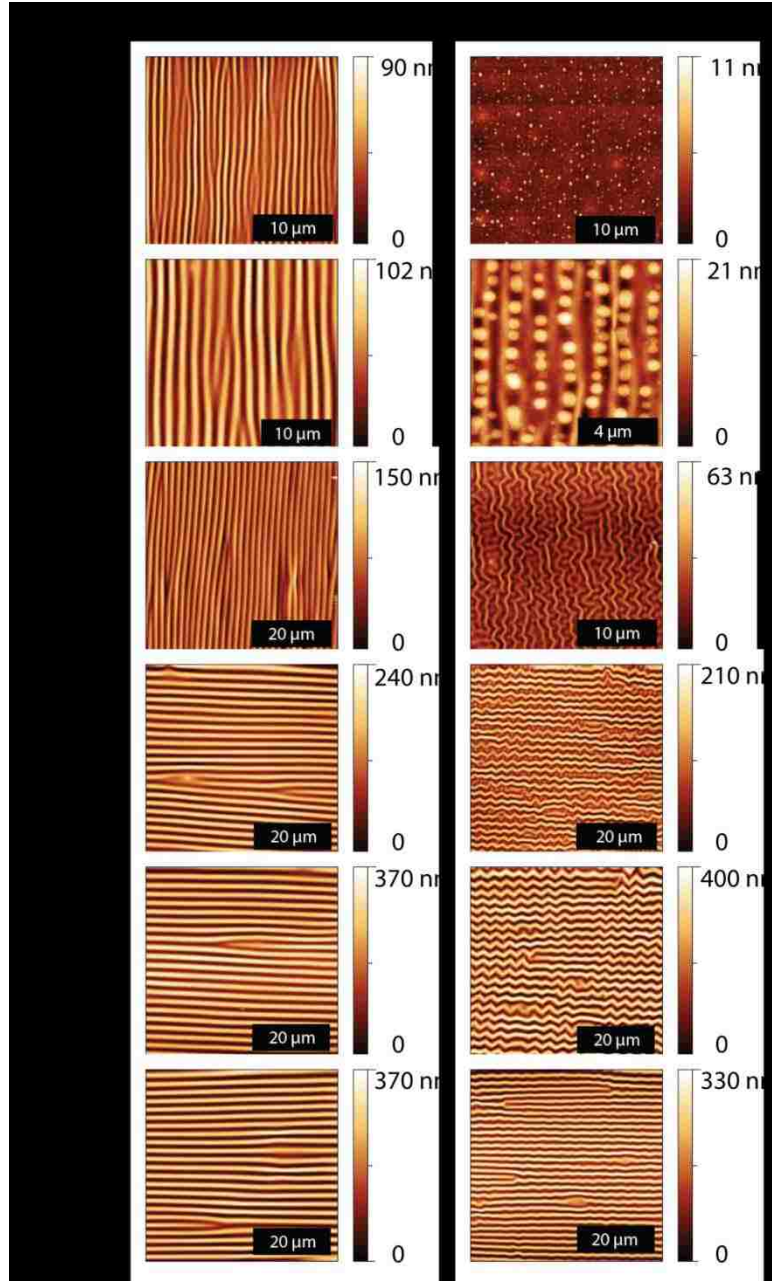


Figure 2.13: AFM scans showing the effect of humidity on oven cured sol-gel films (65 nm). The curing temperatures are as shown in the figure. The left column shows the buckling morphology observed after the oven cure for 85 °C - 150 °C cured films exposed to ambient humidity (~47% RH). The right column shows the subsequent change in the surface morphology after being exposed to a high humidity (~98% RH) environment for 15 hrs. Note the change of scale between images.

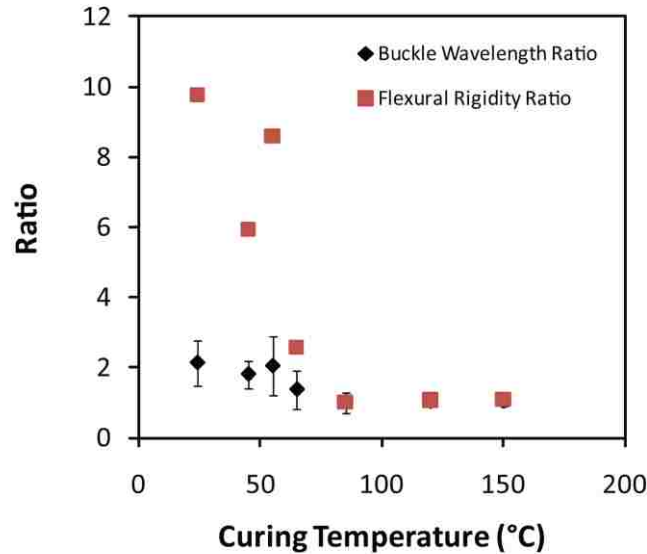


Figure 2.14: Ratio of the buckling wavelength and ratio of the sol-gel flexural rigidity before exposure to high humidity (RH~98%, for 15 hrs) to that measured after exposure as a function of curing temperature. Black diamonds represent the ratio of the buckling wavelength. Red squares represent the ratio of the sol-gel film flexural rigidity. A ratio greater than 1 indicates a decrease in wavelength and flexural rigidity due to high humidity exposure. Films cured under ambient conditions (23 °C and RH~47%) were cured for 24 hrs. All other temperature cure times were 30 minutes.

Films cured at 85 °C to 150 °C show neither any significant change in the buckling wavelength in the x direction (Figures 2.13 & 2.14) nor in their amplitude (Figures 2.13 & 2.15) when they are placed in the humid environment. Were the elastic modulus or film thickness to change as a result of exposure to high moisture, the ratio of the buckling wavelength at high humidity to that of ambient should also change. One would also expect a decrease in the buckling amplitude. Figures 2.14 and 2.15 however show that these ratios are constant, indicating that films cured above 85 °C undergo a minimal level of swelling in humid environment. Nevertheless, a definite change in the buckling morphology occurs in humid atmosphere, indicating that water is able to penetrate into

the film and thus modify its stress state. The 1 D buckling pattern evolves to a classical herringbone buckling pattern.

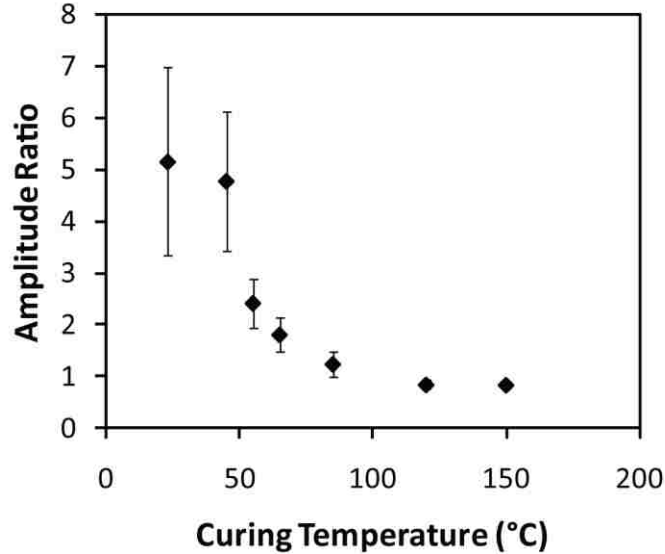


Figure 2.15: Ratio of the buckling amplitude before exposure to high humidity (RH~98%) for 15hrs to that measured after exposure as a function of curing temperature. A ratio greater than 1 indicates a decrease in amplitude due to high humidity exposure. Films cured under ambient conditions (23 °C and RH~47%) were cured for 24 hrs. All other temperature cure times were 30 minutes.

The herringbone morphology is characterized by the development of kinks on the original buckles. The formation of this herringbone pattern implies that the compressive stress in the x direction increases above the critical stress for surface instability. Recent simulations by Huang et al³⁴ suggest that similar patterns can be formed on membranes subject to a mismatch of stress. These simulations further show that as the anisotropy of the stress state is increased, the buckling morphology goes through 3 major transitions: labyrinth to herringbone to the one dimensional mode. We observe a similar trend in the change in humidity driven buckling between films cured at 65 °C and above. Films cured at 65 °C appear to display a hybrid labyrinth-herringbone conformation upon

exposure to humidity whereas films cured above 85 °C display herringbone buckles. Our results also coincide with the experimental data presented recently by Lin and Yang³⁵, who studied the formation of herringbone and labyrinth morphologies on surface oxidized PDMS. These experiments investigated the effect of a bi-axial stress condition, either sequentially or simultaneously, on the buckling morphology. Herringbone patterns are formed by sequentially applying the bi-axial stresses. Labyrinth patterns are formed with the simultaneous application of bi-axial stress. In our studies, the kinks do not appear uniformly throughout the film cured at 150 °C, whereas for films cured at 65 °C and 85 °C the kinks are uniform across the sample area. Comparison of our results with the simulation³⁴ and experimental results³⁵, implies that an increase in the compressive stress generated through a resistance to swelling could be responsible for these buckling transitions. Films cured at higher temperatures are subject to a higher stress upon cooling. Therefore the transition in the buckling states with increase in temperature could be due to a higher initial 1D buckling stress with higher cure temperature or an increase in the swelling stress from increased moisture penetration.

The effect of moisture on the lower temperature (23 °C, 45 °C and 55 °C) cured films is more complex. For these temperature cures, the amplitude of the buckles decreases significantly upon exposure to high humidity (Figure 2.15) and in some cases it becomes difficult to observe them on the surface. Films cured at 45 °C and room temperature show a small decrease in amplitude when stored under ambient conditions, ~10-20%, however this is small compared to the decrease observed in the humid environment (a ~5 fold decrease). This decrease under ambient conditions suggests that the sol-gel film is able to creep to relax the stress. Creep in low temperature cured GTMS based sol-gel

films has also been observed by Atanacio et al⁷. Equation 2.4 relates the amplitude of the buckles to the system parameters.

$$A = h \sqrt{\frac{\varepsilon_{Pre}}{\varepsilon_{Crit}} - 1} \quad (2.4)$$

where ε_{Pre} is the pre-strain and ε_{Crit} is defined in equation 2.3. Assuming that the thickness increases due to swelling and the pre-strain remains more or less constant (interfacial slip is minimized) then the decrease in amplitude must occur due to the increase of the critical strain. In order for critical strain to increase, the elastic modulus of the sol-gel must decrease. Therefore, it is likely that the penetration of water in to the sol-gel layer reduces the elastic modulus. It appears that the humid environment is capable of swelling the film and thus relaxing the stress. Water vapor appears to have the opposite effect on the films cured at higher temperatures owing to their higher cross linking density compared to those cured at lower temperatures.

The relaxation of the amplitude of the buckled sol-gel films cured at low temperature is one of two types of morphological changes that occur upon exposure to a high humidity environment. The second morphological change is dictated by the level of strain applied to the sample to induce buckling prior to humid exposure. We will first deal with the effect of storing films buckled initially under 1.5% strain. For films cured at 23 °C, 45 °C and 55 °C and buckled under 1.5% strain, droplets are formed on the surface after storage in a humid environment. This effect is also observed occasionally on the films cured at 65 °C. In order to better understand the origin of these surface features, the growth kinetics of the droplets were studied in the un-buckled state on PDMS substrates (Figure 2.16). Dewetting of the sol-gel layer as a cause of these features was ruled out as

no definitive long range order of the droplets was found via Fourier image analysis. Furthermore, the rate of increase of the size of the droplets (Figure 2.16) is much too high for it to be attributed to the subsequent Ostwald ripening of the dewetted droplets. The height (~5 nm) of the droplets is an order of magnitude smaller than the film thickness. The effect of storing sol-gel coated glass substrates, cured at 55 °C and at a high humidity (~98%) was also studied. No droplets are observed on these surfaces after 15 hrs. This suggests that the droplets are not a low molecular weight polymer which diffuses to the surface upon humid exposure. It is possible that these droplets are blisters caused by the delamination of the sol-gel film from the PDMS surface.

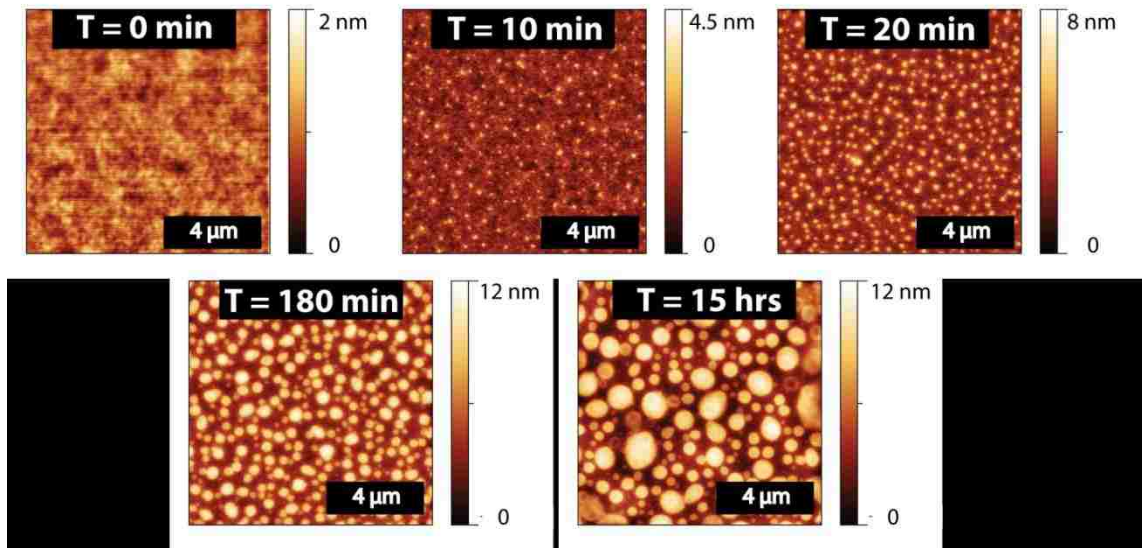


Figure 2.16: AFM scans show the morphological evolution of storing an unbuckled 65 nm thick sol-gel film on PDMS at ~98% RH. These films were cured at 55 °C for 30 minutes under ambient humidity (~47% RH) before exposure to ~98% RH. No blisters develop before T=10 min.

Films as thin as 300 nm were also studied in order to discern the effect of film thickness on droplet formation. These films coated on PDMS were stored under ~98% humidity for 15 hrs in the unbuckled state. While the droplets on the 65 nm thick film could not be observed due to their small vertical height (~5nm), they were readily visible in the SEM (Figure 2.17) on the 300 nm thick films. This 300 nm thick film also exhibits buckling after exposure to ~98% RH humidity, the pattern of which corresponds to an isotropic stress state.

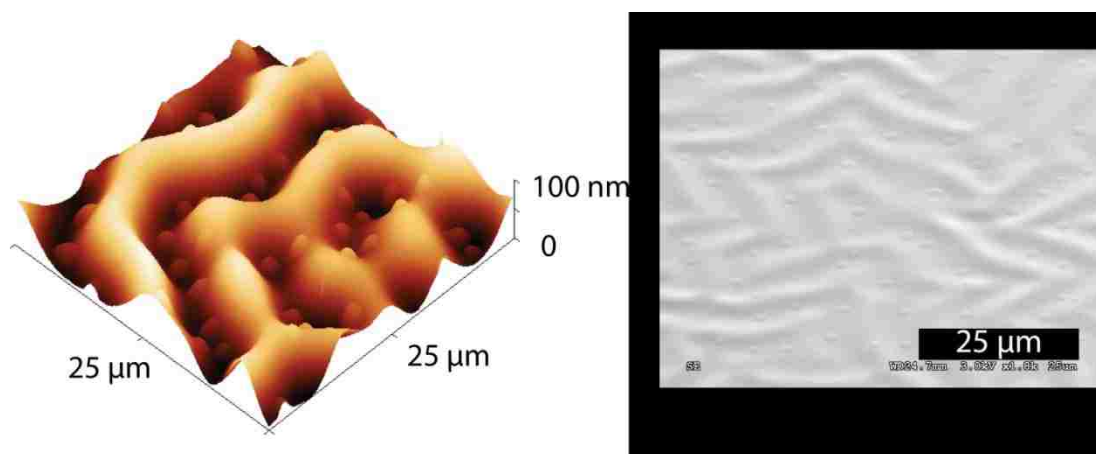


Figure 2.17: AFM (left) and SEM (right) images show the effect of storing a 300 nm thick sol-gel films coated on PDMS at ~98% RH for 15 hrs. The films were cured at 55 °C for 30 minutes at ambient humidity (47%) before exposing to the ~98% RH atmosphere. The humidity causes the surface to buckle and blisters to form. The blisters preferentially lie in the valleys of the buckles.

Numerous blistering patterns, from circular to telephone cord ³⁶, have been widely reported in the literature and are comprehensively reviewed by Hutchinson and Suo³⁷. The blisters observed in our experiments lie preferentially in the valleys of the buckles with an orientation parallel to the direction of the buckles. Figure 2.16 shows that the blister size increases with storage time, which is consistent with solvent induced

blistering phenomena in thin films³⁸. Interestingly these droplets differ in one significant way to the blisters in the previously mentioned work³⁸, in that the vast majority of the blisters in our case do not collapse upon removal from the solvent environment. The blisters also remain in the sample after it has been stored in a vacuum for 48 hrs. The presence of these blisters in the SEM image shown in Figure 2.17 also illustrates their stability under vacuum. This is counter to the typical blisters, which collapse after the external stress is released.

Mei et al³⁹ investigated the effect of simultaneous surface buckling and blister formation in thin film systems. Both phenomena have a characteristic critical stress below which they do not occur. They found that whether or not a film buckles or blisters depends on the ratio of the substrate to the film elastic moduli and the ratio of the width of delamination to the film thickness. For a fixed size of the debonded region, a low ratio of elastic moduli ($E_{\text{substrate}}/E_{\text{film}}$) favours surface buckling, whereas a high ratio favors the formation of blisters. As previously mentioned, the change in buckle amplitude for films cured at and below 65 °C due to exposure to high humidity (98% RH) suggests a decrease in the elastic modulus (Figure 2.15). This raises the value of the substrate to film elastic modulus ratio and thus it is possible that the critical stress for blister formation is surpassed. It is also possible that the influx of water into the film could increase the size of the debonded region by attacking the chemical bonds at the surface. The increase in the size of the debonded region would also lower the critical stress required for blister formation.

At higher strain levels, ~4%, a different change in surface morphology is observed. Figure 2.14 shows approximately an 8 fold change in the flexural rigidity for films cured

at 23 °C, 45 °C, and 55 °C upon exposure to high humidity. This corresponds to a 2 fold decrease in the wavelength due to the humid exposure. Closer inspection of these buckles in certain regions reveals some interesting profiles as shown in Figure 2.18. It is observed from these profiles that the amplitude of the buckles increases and decreases in a regular pattern across the profile for the room cured and 45 °C cured samples. This effect of alternating amplitude is uniform over the 45 °C cured samples whereas for room cured and 55 °C cured samples, some variation exists. The reason for this variation is not clear. Two possibilities exist for these secondary buckles, i.e. either the sol-gel film is delaminated from the surface forming a straight sided blister or remains adhered to the PDMS substrate (Figure 2.19).

It is not possible to state which is the actual case at this time. However, we conjecture that these secondary buckles are blisters formed by the delamination of the sol-gel from the substrate due to the influx of water. The multiple blisters observed for films stored at a lower strain strengthen this argument as it is well documented that straight sided blisters can become unstable and break up into small circular blisters⁴⁰. This helps to explain the ordering of the blisters along the buckle directions on the surface. It is possible that some interesting surface patterning techniques could be developed using this methodology.

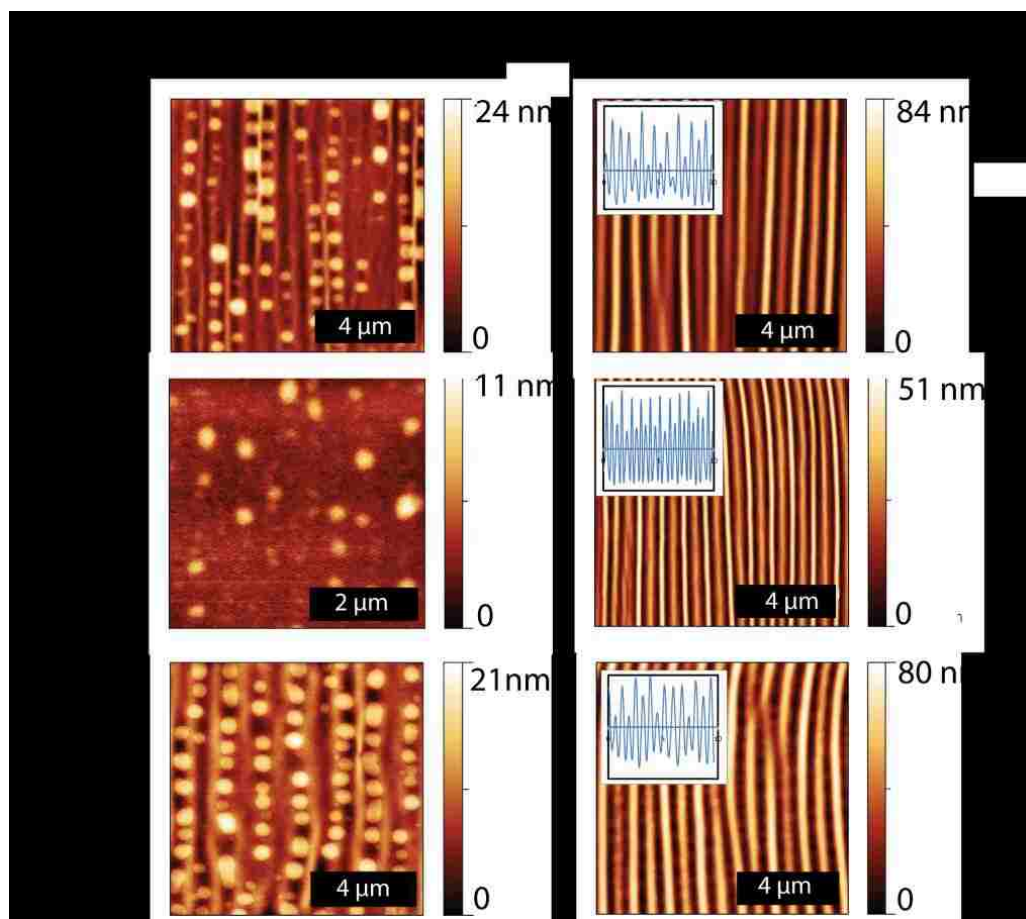


Figure 2.18: The effect of pre-strain on the change in buckling morphology due to the storage of buckled sol-gel films in humid environments ($\sim 98\%$ RH, for 15 hrs). Pre-strains are shown at the top of the Figure. Films buckled at $\epsilon \sim 1.5\%$ display circular blisters on exposure to high humidity. Films buckled at $\epsilon \sim 4\%$ show a decrease in buckle wavelength. Inset: Line profiles of the films after humid exposure which were initially buckled under $\epsilon \sim 4\%$.

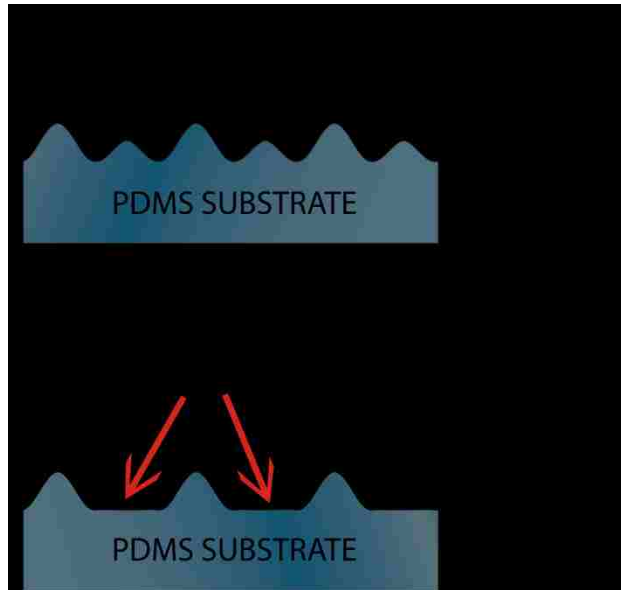


Figure 2.19: Schematic of secondary buckle evolution in sol-gel films cured at low temperature $< 55\text{ }^{\circ}\text{C}$ as a result of humid exposure. Case one is where the film remains adhered to the PDMS substrate. Case two is where the sol-gel film delaminates from the PDMS to form straight sided blisters.

From the above discussion it is clear that the simultaneous buckling and delamination of the sol-gel films under humid atmosphere is a complex situation. Irrespective of the exact nature and formation of the blisters on the sol-gel surface, it can be reasoned that exposure to a humid environment has a greater effect on films cured at and below $65\text{ }^{\circ}\text{C}$ than those cured above it.

2.4. Conclusion

The elastic modulus of a sol-gel based adhesion promoting film has been estimated using the method of buckling instability. For a sol-gel curing temperature of $120\text{ }^{\circ}\text{C}$, the plane strain modulus of the film is independent of the film thickness and estimated to be $1.7\pm 0.2\text{ GPa}$. From this result and accounting for the uncertainty in the Poisson's ratio

we estimate the elastic modulus to be in the range of 1.5-1.6 GPa. This value is consistent with literature values for similar sol-gel based films. The technique was used to characterize the modulus as a function of sol-gel curing history and also to qualitatively describe the effect of moisture on the film. Elastic modulus was found to be a strong function of curing temperature up to curing temperatures of 85 °C. Increasing the cure temperature above this value does not yield any substantial change in elastic modulus. Room temperature cured films displayed no buckling at cure times below 3 hours. A plateau in modulus was reached at cure times above 9 hrs. Change in the buckling morphology due to exposure to high humidity suggests that the lower the film cure temperature the more susceptible it is to moisture penetration and swelling. The presence of the hydroxyl groups in the imperfectly crosslinked film appear to facilitate the influx of water. The higher the water concentration the greater the expected driving force for the cleavage of cross-links via hydrolysis⁴¹ ; so the films cured at lower temperatures are more susceptible to hydrolytic attack than their high temperature cure counterparts. Thus, the low temperature films should perform poorly in wet adhesion experiments. As this is not the observed trend (Figure 2.11), it provides further weight to the argument that the sol-gel film undergoes further crosslinking during the epoxy cure cycle. These results call for a study to be conducted using a room temperature cure epoxy to determine the importance of the adhesive cure step. The buckling technique presented here would be of great use in such a study as the temperature effect on film cross-linking can be studied in detail alongside a qualitative assessment of the film moisture resistance.

2.5 References

- (1) Plueddemann, E. P. *Silane Coupling Agents*; 1982.
- (2) Brinker, C. J.; Scherer, G. W. *Sol-Gel Science: The Physics and Chemistry of Sol-Gel Processing*; Elsevier Science (USA), 1989.
- (3) Chaudhury, M. K.; Pocius, A. V. *Surfaces, Chemistry and Applications*; 1 st.; Elsevier: Amsterdam, 2002.
- (4) Zheludkevich, M. L.; Salvado, I. M.; Ferreira, M. G. S. *Journal of Materials Chemistry* **2005**, *15*, 5099–5111.
- (5) Hoebbel, D.; Nacken, M.; Schmidt, H. *Journal of Sol-Gel Science and Technology* **2000**, *19*, 305–309.
- (6) Hoebbel, D.; Nacken, M.; Schmidt, H. *Journal of Sol-Gel Science and Technology* **2001**, *21*, 177–187.
- (7) Atanacio, A. J.; Latella, B. A.; Barbé, C. J.; Swain, M. V. *Surface and Coatings Technology* **2005**, *192*, 354–364.
- (8) Innocenzi, P.; Esposito, M.; Maddalena, A. *Journal of Sol-Gel Science and Technology* **2001**, *20*, 293–301.
- (9) VanLandingham, M. R.; Villarrubia, J. S.; Guthrie, W. F.; Meyers, G. F. *Macromol. Symp.* **2001**, *167*, 15–43.
- (10) Stafford, C. M.; Harrison, C.; Beers, K. L.; Karim, A.; Amis, E. J.; VanLandingham, M. R.; Kim, H.-C.; Volksen, W.; Miller, R. D.; Simonyi, E. E. *Nature materials* **2004**, *3*, 545–50.
- (11) Blohowiak, K. Y.; Osborne, J. H.; Krienke, K. A. US Patent 5814137 **1998**.
- (12) Joshua Du, Y.; Damron, M.; Tang, G.; Zheng, H.; Chu, C.-J.; Osborne, J. H. *Progress in Organic Coatings* **2001**, *41*, 226–232.
- (13) Liu, J.; Chaudhury, M. K.; Berry, D. H.; Seebergh, J. E.; Osborne, J. H.; Blohowiak, K. Y. *Journal of Adhesion Science and Technology* **2006**, *20*, 277–305.
- (14) Greegor, R. B.; Blohowiak, K. Y.; Osborne, J. H.; Krienke, K. A.; Cherian, J. T.; Lytle, F. W. **2001**, *20*, 35–50.

- (15) Liu, J.; Chaudhury, M. K.; Berry, D. H.; Seebergh, J. E.; Osborne, J. H.; Blohowiak, K. Y. *Journal of Adhesion Science and Technology* **2008**, *22*, 1159–1180.
- (16) Allen, H. G. *Analysis and Design of Structural Sandwich Panels*; Pergamon: New York, 1969.
- (17) Genzer, J.; Groenewold, J. *Soft Matter* **2006**, *2*, 310.
- (18) Groenewold, J. *Physica A: Statistical Mechanics and its Applications* **2001**, *298*, 32–45.
- (19) Cerda, E.; Mahadevan, L. *Physical Review Letters* **2003**, *90*, 074302.
- (20) Bowden, N.; Brittain, S.; Evans, A. G.; Hutchinson, J. W.; Whitesides, G. M. **1998**, *393*, 146–149.
- (21) Chan, E. P.; Crosby, A. J. *Soft Matter* **2006**, *2*, 324.
- (22) Volynskii, A. L.; Bazhenov, S.; Lebedeva, O. V.; Bakeev, N. F. **2000**, *5*, 547–554.
- (23) Huang, H.; Chung, J. Y.; Nolte, A. J.; Stafford, C. M. *Chemistry of Materials* **2007**, *19*, 6555–6560.
- (24) Nolte, A.; Rubner, M.; Cohen, R. *Macromolecules* **2005**, *38*, 5367–5370.
- (25) Bowden, N.; Huck, W. T. S.; Paul, K. E.; Whitesides, G. M. *Applied Physics Letters* **1999**, *75*, 2557.
- (26) Bertelsen, C. M.; Boerio, F. J. *Progress in Organic Coatings* **2001**, *41*, 239–246.
- (27) Tsai, C.-T.; Lu, H.-Y.; Ting, C.-Y.; Wu, W.-F.; Wan, B.-Z. *Thin Solid Films* **2009**, *517*, 2039–2043.
- (28) Brown, D.; Clarke, J. H. R. *Macromolecules* **1991**, *24*, 2075–2082.
- (29) Liu, J. Ph.D. Thesis, Lehigh University, 2006.
- (30) Abel, M.-L.; Allington, R. D.; Digby, R. P.; Porritt, N.; Shaw, S. J.; Watts, J. F. *International Journal of Adhesion and Adhesives* **2006**, *26*, 2–15.
- (31) Abel, M.-L.; Adams, a. N. N.; Kinloch, a. J.; Shaw, S. J.; Watts, J. F. *International Journal of Adhesion and Adhesives* **2006**, *26*, 50–61.

- (32) Kinloch, a. J.; Korenberg, C. F.; Tan, K. T.; Watts, J. F. *Journal of Materials Science* **2007**, *42*, 6353–6370.
- (33) Chaudhury, M. K.; Gentle, T. M.; Plueddemann, E. P. *Journal of adhesion science and technology* **1987**, *1*, 29–38.
- (34) Huang, Z. Y.; Hong, W.; Suo, Z. *Journal of the Mechanics and Physics of Solids* **2005**, *53*, 2101–2118.
- (35) Lin, P.-C.; Yang, S. *Applied Physics Letters* **2007**, *90*, 241903.
- (36) Thouless, M. D. *J. Am. Ceram. Soc.* **1993**, *76*, 2936–2938.
- (37) Hutchinson, J. W.; Suo, Z. *Advances in Applied Mechanics* **1992**, *29*, 63–191.
- (38) Sharp, J.; Jones, R. *Physical Review E* **2002**, *66*, 011801.
- (39) Mei, H.; Huang, R.; Chung, J. Y.; Stafford, C. M.; Yu, H.-H. *Applied Physics Letters* **2007**, *90*, 151902.
- (40) Parry, G.; Coupeau, C.; Colin, J.; Cimetière, A; Grilhé, J. *Acta Materialia* **2004**, *52*, 3959–3966.
- (41) Benkoski, J. J.; Kramer, E. J.; Yim, H.; Kent, M. S.; Hall, J. *Langmuir* **2004**, *20*, 3246–58.

CHAPTER 3

Investigation of different additives to improve the durability and barrier properties of sol-gel reinforced epoxy/aluminum joints in humid environments

Abstract

The effect of hydrophobic additives on the material properties and adhesion performance of a sol-gel film has been investigated. The method of buckling instability has been used to estimate the elastic modulus of the sol-gel films as a function of chemical composition and curing temperature. The performance of the sol-gel to promote adhesion between epoxy and aluminum was characterized for different chemical compositions using an asymmetric double cantilever beam technique. The elastic modulus of the sol-gel film is inversely correlated with the fracture toughness of the joint. The modulus of the sol-gel film proved to be an effective metric with which to estimate the adhesive performance of a joint. Increasing the level of hydrophobic additive in the sol-film adversely affected the adhesive performance.

3.1 Introduction

Over the last 10 years sol-gel films have emerged as effective adhesion promoters between metal and polymeric surfaces^{1,2}. Although sol-gel films have long been used as surface pretreatments in the fiber-glass industry,¹ metal surfaces are typically treated with

aggressive chemical etches such as Forest Product Laboratories (FPL) and Phosphoric Acid Anodizing (PAA)³. The growing environmental concern with FPL and PAA etches coupled with the growing need for in-field repair has motivated the use of sol-gel based adhesion promoters. Despite this rapid growth, sol-gel reinforced interfaces still suffer from hydrolytic degradation in aggressive environments^{1,4}. Another family of related sol-gel films with growing applications are designed expressly to resist these aggressive environments and act as barrier coatings for metallic and polymeric surfaces^{5,6}. Numerous sol-gel coatings can be found in the literature which significantly improve the corrosion resistance of metals such as steel and aluminum⁷⁻¹⁰. Is it possible then, to combine the adhesion promoting characteristics and the barrier properties of these two families of emerging sol-gels to produce a more durable adhesive joint? This is the question which will be the subject of the current Chapter. Additionally, a second question will also be considered, can the buckling methodology developed in Chapter 2 be used to correlate the adhesive performance of a chemically modified sol-gel film to its elastic modulus

Several important differences are evident between sol-gel films used for adhesion promotion and those used for corrosion protection. Silane based adhesion promoters are typically cast from dilute solutions^{1,11-13}, leading to the formation of thin films with thicknesses in the 10-200 nm range. The sol-gel films are typically glass-like and brittle. Fracture may occur cohesively in the sol-gel layer if the interpenetration of the adhesive within the film is minimal and the layer is too thick. This mode of failure will bypass the energy dissipation mechanisms in the adhesive and lead to a weak joint. It is also preferable that an adhesion promoter has chemical functionalities which can react with

the adhesive and the metal substrate^{1,14}. In order to achieve the maximum level of adhesion the sol-gel layer must also have some degree of permeability to the adhesive^{1,15,16}. If the sol-gel is sufficiently permeable to the adhesive, causing interpenetration, it need not contain functional groups to react with the adhesive¹. Yet, the sol-gel must have a higher surface energy than the adhesive, low cross link density or coated when it is partially cured in order for interpenetration to occur.

Sol-gel based barrier coatings are generally thicker than their adhesion promoting counter parts, having thicknesses on the order of microns⁶. They are generally fully cured using heat cycles and are engineered to have chemically inert surfaces. To improve the resistance of the coating to penetration of water, thus increasing corrosion resistance, hydrophobic silanes are typically used as additives⁶. A typical coating formulation consists of an inorganic network former (tetraethoxysilane (TEOS), or zirconium-n-propoxide (TPOZ)) with a hydrophobic silane. Silanes capable of forming organic and inorganic networks, such as glycidoxypropyltrimethoxysilane (GTMS), may also be used⁶. Here we define a hydrophobic silane as containing at least one low energy functional group that will remain stable during the hydrolysis and condensation reactions. Hydrophobic silanes have also been used as additives in adhesion promoters to improve the durability in aggressive humid environments⁴.

When combined with a grit-blasted aluminum surface, the standard GTMS based silane pretreatment yields critical fracture energies comparable to phosphoric acid anodizing (PPA)¹⁷. However, the silane pretreatment falls short relative to PAA regarding the resultant threshold fracture energy as measured in humid or wet environments. In this case, water is able to penetrate the sol-gel film and damage either the aluminum-oxygen-

silane interfacial bonds or the aluminum oxide directly causing failure^{17,18}. In addition, water is able to hydrolyze the siloxane bonds in the sol-gel film, which are unable to reform due to the high stresses at the crack tip¹⁹. Independent of the exact mechanism increasing the barrier properties of the sol-gel film would be expected to solve both issues. Reducing the flux of water through the film limits the rate of corrosion of the native oxide and increases the stability of the silane layer to hydrolytic cleavage. To increase the barrier properties of our sol-gel films, hydrophobic silanes will be added; their effect on sol stability, film uniformity, adhesive performance and barrier properties will be investigated.

A roadmap of the Chapter is as follows:

1. Five promising candidates are identified from the large number of hydrophobic silanes available in the literature
2. The aqueous stability of modified sols is then studied to address the strong environmental and industrial driving forces for water based sol-gels²⁰.
3. A study on the uniformity of the sol-gel coatings follows as uniformity is essential to the production of an effective barrier coating, and to the utilization of the buckling technique developed in Chapter 2.
4. Steps 2 and 3 reveal methyltriethoxysilane (MTEOS) as the most promising hydrophobic additive. The elastic modulus and fracture behavior of MTEOS modified sol-gel coatings is subsequently investigated as a function of the ratio of MTEOS to GTMS in the coating

5. Finally, the barrier properties of the coating are then qualitatively assessed using the method developed at the end of Chapter 2. This method tracks the change in the buckling morphology of the sol-gel films after exposure to 98% RH for 15 hours.

3.2 Experimental

3.2.1 Materials

The standard aluminum alloy used in the aerospace industry, Bare Al -2024-T3 (supplied by The Boeing Company), is used in this study. The elastic modulus of Al-2024-T3 is reported to be 72.4 GPa²¹. The base epoxy resin is a diglycidyl ether of bisphenol-A (DGEBA) with an epoxide equivalent weight of ~187.5 g/eq (Dow, DER331). The curing agent used is aminoethylpiperazine (AEP, EPICURE 3200, Hexicon Chemicals). Core-shell rubber (Kane Ace® MX120, Kaneka) is used as the epoxy toughening agent. The advantage of the MX120 over more traditional tougheners such a carboxyl terminated butadiene acrylonitrile (CTBN) is that the final epoxy is clear to slightly cloudy. This property facilitates clear visualization of the crack front during fracture experiments. To produce an adduct, 5 parts of MX120 per 100 parts epoxy resin were mixed together under vacuum for 4 hrs at 80 °C. Curing of the epoxy was achieved by thorough mixing of the adduct and curing agent in the stoichiometric ratio for 5 minutes, followed by centrifugal degassing at 8000 rpm for an additional 5 minutes. Mixing and degassing steps are limited to 5 minutes as the workable pot life for this AEP cured epoxy is ~20 minutes. Once the epoxy is applied to the sol-gel treated aluminum it is cured using the following procedure; ramp from 25°C to 100°C over a period of 4 hrs, hold at 100°C for 2 hours and cool down to 25°C over 6 hours. Using a temperature

controlled oven (Tenny Jr. oven with Whatman controller) this process was automated. This cure cycle was chosen as it has previously been shown to minimize the thermal stress in the final sample²². The fracture toughness of the MX120 toughened DGEBA was measured according to the procedure outlined in the ASTM standard D5045 and found to be $2.02 \pm 0.06 \text{ MPa}\cdot\text{m}^{1/2}$. This toughness is comparable to that reported for a CTBN toughened system, $1.95 \text{ MPa}\cdot\text{m}^{1/2}$,^{23,24}. The elastic modulus of the MX120 toughened epoxy was measured to be 2.45 GPa using a 3 point bending test and is within the typical range for a rubber toughened epoxy prepared with DER331 and AEP²⁵.

Standard sol-gel films were made using the documented procedure for Boegel EPII²⁶⁻³². This procedure is outlined in Appendix A. The sol-gel components, glycidoxypropyltrimethoxysilane (GTMS, Gelest), Zirconium-n-Propoxide (TPOZ, 70% w/w in propanol, Alfa Aesar), glacial acetic acid (GAA, Sigma Aldrich) and Antarox BL-240 (Rhodia Inc.) were used as-received. Ethanol (200 Proof, Decon Labs Inc) was used as a co-solvent when required. The additives used in this study are Methyltriethoxysilane (MTEOS), Bis(Triethoxysilyl)ethane (BTSE), Phenyltriethoxysilane (PhTEOS), Bis[3(Triethoxysilyl)propyl]tetrasulfide (TESP); all supplied by Gelest and used as-received. The exact procedure for addition of the additives into the base sol-gel solution is explained in the relevant section of the results and discussion. All sol-gel applications are completed within 2 hours of mixing.

3.2.2 Surface Pretreatment

Grit-blasting is used as the standard surface pretreatment throughout this study. Before grit-blasting it is necessary to remove any organic contamination from the metal so that it

does not become embedded in the surface. First, the coupons are wiped with methylethylketone (MEK, ACS grade, EMD) and acetone (HPLC/ACS grade, Pharmco-AAPER) until no organic residue can be seen on the wipe. Next the coupons are submerged in a degreasing solution of Isoprep 44 (supplied by Boeing) at 60°C for 10 mins. Coupons are then thoroughly rinsed with deionized water. The final surfaces should be water break free. Grit-blasting is conducted in a chamber using 220 grit alumina. The grit is fluidized in pressurized air at a discharge pressure of 4.1 Bar. Grit-blasting is conducted for a total time of 45s to ensure a uniform reproducible surface. To remove any residual grit and organic contamination the samples are blown with compressed air and cleaned in an Ultra Violet Ozone cleaner for 10 minutes. This procedure results in a surface with a water contact angle of $<5^\circ$ i.e. the water drop spontaneously wets the surface.

3.2.3 Application of sol-gel films to aluminum surfaces

Grit-blasted samples are treated with sol-gel solution within 1 hour of the pretreatment. Samples are wet with the sol-gel solution for 2 minutes and then spun at 1200 rpm for 50s using a Headway Research spin coater. This spin coating method yields a uniform film of reproducible thickness. For elevated temperature cures the coatings are held at 45, 55 or 120°C for 30 mins.

3.2.4 Measurement of sol-gel film thickness

In Chapter 2, the thickness of the sol-gel films was measured using two techniques. The first involved coating silicon wafers with sol-gel film and using ellipsometry to

measure the film thickness. In the second method the sol-gel film is coated on a soft rubber which is then sectioned and viewed end on in a scanning electron microscope (SEM). These two methods were shown to yield equivalent results³³. For the sol-gel solutions containing MTEOS, ellipsometry was used to provide the film thickness as it is not possible to accurately resolve film thicknesses <50 nm using the above method in the SEM. As noted above, since both methods were proven to yield similar results, we can be confident in using ellipsometry for the thinner coatings.

3.2.5 Coating of sol-gel films on PDMS and the testing procedure for buckling instability

The coating of PDMS films and buckling procedure is described in detail in Chapter 2 section 2.2.3. The identical procedure is used here. For films cured at 45°C and 55°C, a strain of $\epsilon \sim 4\%$ was used to initiate buckling on the samples. All buckle wavelengths and amplitudes are determined using atomic force microscopy (AFM).

3.2.6 Preparation of asymmetric double cantilever beam samples for fracture testing

The asymmetric double cantilever beam (ADCB) samples were made by casting the rubber toughened epoxy onto a sol-gel treated aluminum coupon, Figure 3.1. Aluminum coupons of dimensions 1.6 x 10 x 63.5mm (height x width x length) are used. First, the ends of the sol-gel treated coupons are treated with a film of PTFE to act as a pre-crack. Next, the coupon is placed in a silicon mold of dimensions 8 x 10 x 63.5mm and epoxy is poured into the mold. The excess epoxy is squeezed out using a monolayer treated glass

slide. (The monolayer was formed by exposing a plasma cleaned glass slide to a filter paper soaked in dodecyltrichlorosilane.) The height of the epoxy beam is controlled by the depth of the mold. The ratio of the aluminum thickness to epoxy thickness (h_{Al}/h_{epoxy}) is maintained constant at 0.25. This ratio has been found to decrease the level of mode mixity of the system and keep the crack travelling along the Al/Epoxy interface^{22,34}. From numerical studies reported in the literature, this system geometry gives rise to a phase angle of $\psi \sim 4^\circ$ ^{35,36}.

3.2.7 Subcritical crack growth kinetics and measurement of the critical and threshold fracture energies

The fracture energy of the ADCB joint is found by evaluating the strain energy release rate (G). To evaluate this property we use the model proposed by Kanninen³⁷ for a beam on an elastic foundation. Several numerical (finite element) studies have found this model to be accurate over our sample dimensions^{35,36}. The energy release rate is found to be,

$$G = \frac{3\Delta^2 E_1 h_1^3 E_2 h_2^3}{8a^4} \left[\frac{E_1 h_1^3 C_2^2 + E_2 h_2^3 C_1^2}{(E_1 h_1^3 C_2^3 + E_2 h_2^3 C_1^3)^2} \right] \quad (3.1)$$

where $C_1 = 1 + 0.64 \frac{h_1}{a}$, $C_2 = 1 + 0.64 \frac{h_2}{a}$, Δ is the wedge thickness, E is the elastic modulus, h is the beam thickness and a is the crack length. Subscripts 1 and 2 refer to epoxy and aluminum respectively. From Figure 3.1 we observe that the crack length is not constant across the width of the sample. The curvature is thought to be due to anticlastic bending of the epoxy beam^{38,39}. Complex numerical calculations are required to account for the effect of anticlastic bending on the energy release rate. For our system,

numerical calculations reveal that neglecting the crack front curvature will result in a ~10% under estimation³⁹ of the energy release rate when using equation 3.1. As this estimate is conservative, we use equation 3.1 with the average crack length calculated across the curved front.

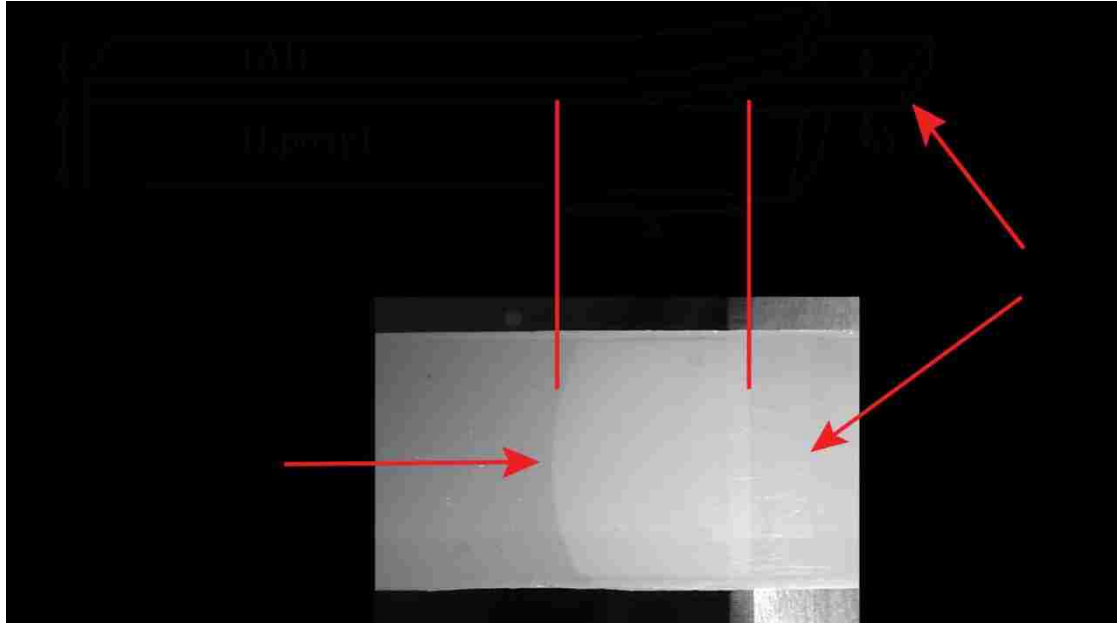


Figure 3.1: Top, schematic of the ADCB sample. E_1 , E_2 , h_1 , h_2 , a and Δ correspond to the aluminum elastic modulus, epoxy elastic modulus, aluminum thickness, epoxy thickness, crack length and wedge height, respectively. Bottom, micrograph of a view through the epoxy of the ADCB sample; the crack front is clearly visualized.

The difference in the thermal expansion coefficients of the epoxy and aluminum causes the ADCB sample to become slightly curved upon cooling from the curing temperature to room temperature. Equation 3.1 assumes that the sample is initially in a stress-free state and, therefore, the effect on the energy release rate due to the thermal loading (G_T) needs to be taken into account. A study was conducted by Liu *et al.*¹² and G_T was found to be around $\sim 26 \text{ J/m}^2$. While this value is insignificant for the stronger joints, it could

represent up to 20% of the fracture energy for the weak joints. However, as G_T is independent of crack length the trends and conclusions drawn from the fracture analysis remain valid.

As highlighted in the introduction, one of the major shortcomings of sol-gel based adhesion promoters is their lack of stability in aggressive hydrolytic environment. Therefore, it is imperative that both the critical fracture energy (G_c) and the threshold fracture energy (G_{th}) are evaluated. To extract both G_c and G_{th} from a single experiment, fracture experiments are conducted in an environmental chamber at 98% RH and $26\pm 1^\circ\text{C}$, Figure 3.2. First, a razor blade 0.3 mm thick is inserted into the pre-crack region of the ADCB sample. Next, the sample is placed into the environmental chamber and sealed inside with a glass cover and parafilm. The humidity inside the chamber is controlled by partially filling it with DI water. A temperature controller maintains the temperature at $26\pm 1^\circ\text{C}$. Before running the experiment, the sample is allowed to equilibrate in the environment for one hour. Previous studies have shown that increasing the equilibration time above one hour has no effect on the measured fracture energy³⁴.

After the equilibration time the razor blade is advanced into the sample at a speed of 70 $\mu\text{m/s}$ until the crack grows at a steady rate for $\sim 2\text{-}3$ mm. The motor is then stopped and the crack growth is monitored over 24-48 hours. The experiment is stopped when no further crack growth is observed. This entire procedure is recorded using a microscope (InfiniVar) connected to a CCD camera (MTI CCD72). The critical fracture energy (G_c) is calculated using equation 3.1 and the measured crack length at the time just before the motor is switched off. The threshold fracture energy (G_{th}) is evaluated using the final

crack length. An advantage of using a constant displacement system is that the crack growth is stable.

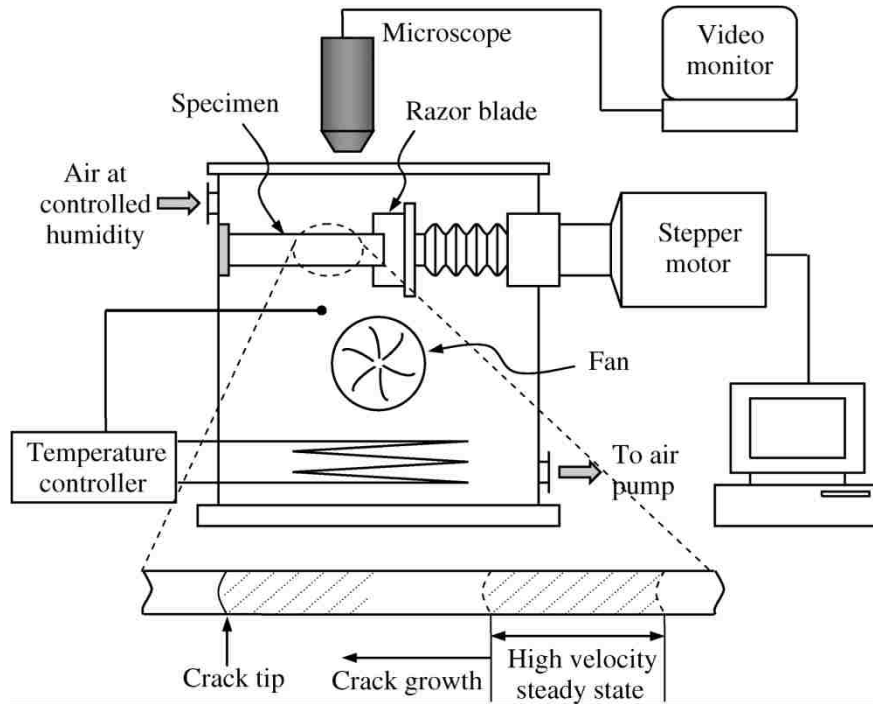


Figure 3.2: Schematic of the environmental chamber used to conduct the ADCB experiments¹².

To ensure we are measuring the true threshold fracture energy, it is necessary to consider the crack growth kinetics. Our experiment is a typical example of Environmentally Assisted cracking (EAC) or stress corrosion cracking, this subject was reviewed by Krausz et al⁴⁰. The kinetics of crack growth due to environmental degradation can be broken down into three main regions, Figure 3.3. These regions may be generalized as follows: in region I the kinetics of crack growth are controlled by the reaction rate of chemical bond breaking and reforming at the crack tip. In region II the

rate limiting step associated is the transport of reactive species to the crack tip. In region III crack growth was originally considered to be independent of the environment, however, in some cases the environment may influence this subcritical growth⁴¹. It must be noted though that these are generalizations as EAC is an extremely complicated process. Figure 3.3 also indentifies the two extrema of the system, the critical fracture energy and the threshold fracture energy. By plotting the experimental data in the same form as Figure 3.3 we can determine if we are measuring the true values of G_c and G_{th}

To aid the identification of the three main EAC regions, the following empirical equation is used to fit the data,

$$\frac{da}{dt} = CG^n \left(\frac{1 - \left(\frac{G_{th}}{G}\right)^{n1}}{1 - \left(\frac{G}{G_c}\right)^{n2}} \right) \quad (3.2)$$

where G_{th} and G_c are the threshold and critical fracture energies respectively. The fit parameters are C , n , $n1$, $n2$. It is very important to note that equation 3.2 is strictly empirical and was formulated to describe corrosion fatigue experiments⁴². As corrosion fatigue exhibits three well defined regions it is perhaps not surprising that this equation fits data from EAC³⁴. However, corrosion fatigue is a different process and the empirical nature of the equation makes it is difficult to draw any meaningful results from the value of the parameters. Therefore, it will be used here solely to provide a frame of reference. The interested reader is referred to recent work that has attempted to model regions I and II using standard rate theory concepts^{41,43-45}.

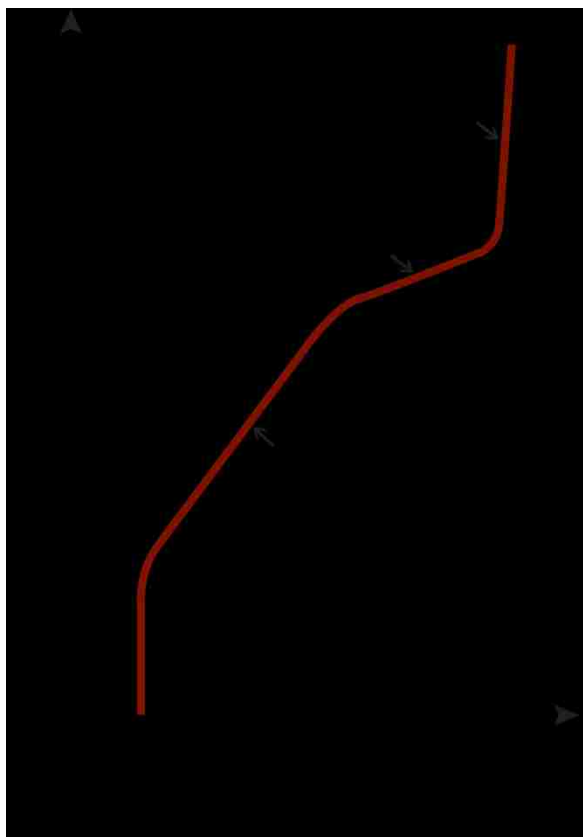


Figure 3.3: A schematic representation of a typical stress corrosion cracking process. The three crack growth regions are identified along with the critical and threshold fracture energies. Figure is adapted from Krausz et al⁴⁰.

3.3 Results and Discussion

3.3.1 Stability of Hydrophobic additives in water/ethanol solutions

The following hydrophobic additives were identified as potential modifiers to the sol-gel solution, MTEOS, BTSE, TESP and PhTEOS, Figure 3.4. MTEOS has been used in numerous barrier coatings and adhesion promoters to improve the durability^{4,46-50}. BTSE is an effective crosslinking silane which has been found to increase the density of the silane network and thus increase the barrier properties^{4,51-53}. TESP and PhTEOS have both been used as additives in barrier coatings with high levels of success^{4,46,47,54-57,58}. The above silanes were used to replace GTMS on a molar basis in the standard sol-gel

formulation (Appendix A). With the end goal of testing a range of Additive/GTMS ratios in mind, stability tests were conducted at the molar ratio of 1:0 (i.e. with no GTMS initially present in the solution) to identify which additives will be unstable in an aqueous solution. The sol-gel formation follows the same procedure as outlined in Appendix A with the exception that the GTMS is replaced by a molar equivalent of the additive to be tested. This procedure presents a truly difficult challenge, to create a film with hydrophobic components from an aqueous solution. For certain additives it was not possible to obtain a stable solution in water so different mixtures of ethanol and water were investigated.

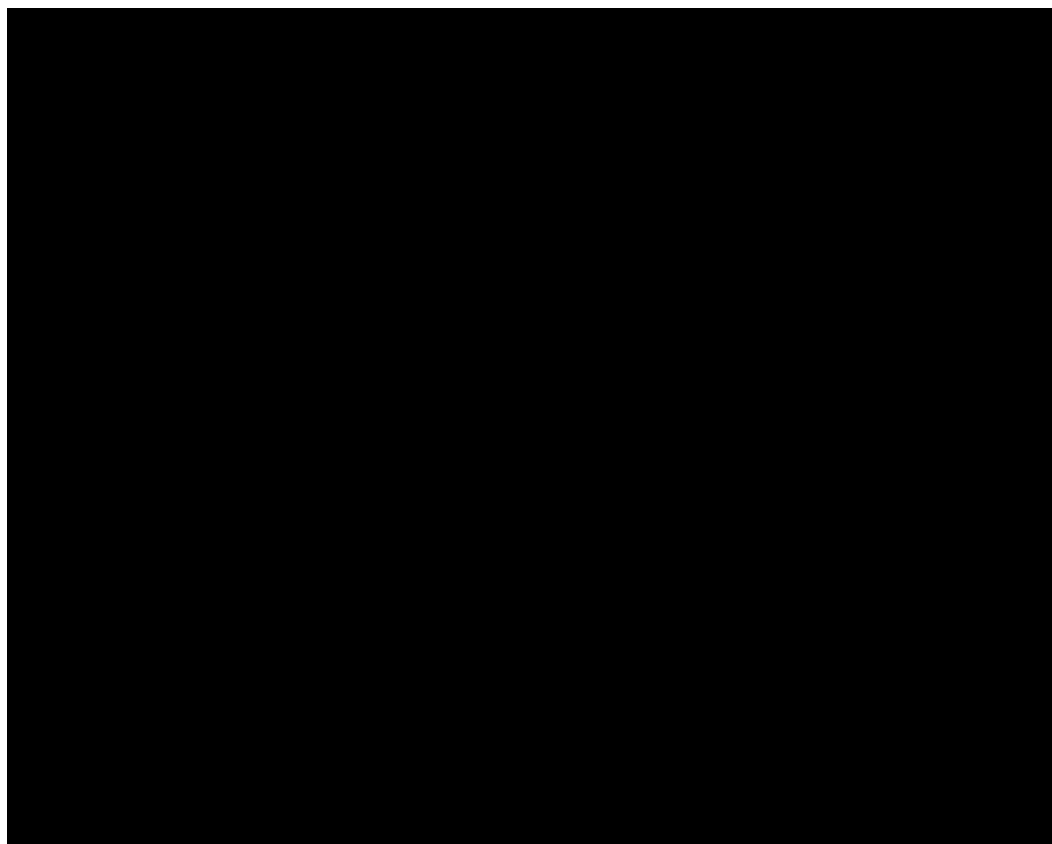


Figure 3.4: Hydrophobic additives identified as potential sol-gel modifiers.

	Ratio of Ethanol to Water in the Sol (V/V)				
Additive	0:100	30:70	50:50	70:30	90:10
MTEOS	Stable	Stable	Stable	Stable	Stable
BTSE	Unstable with precipitate	Unstable with precipitate	Forms an emulsion after stirring for 1 hr	Stable	Stable
TESP	Unstable with precipitate	Unstable with precipitate	Unstable with precipitate	Cloudy solution	Stable
PhTEOS	Unstable with precipitate	Unstable with precipitate	Unstable with precipitate	Cloudy solution	Stable

Table 3.1: Stability of sols prepared by replacing GTMS with various additives. The GTMS in the standard sol-gel solution is replaced by the same number of moles of additive (Appendix A). The sols tested consist of a range of Ethanol to water ratios which make up the bulk of the sol. Suitable solution combinations are highlighted in green.

The stability of these sols in water and various water alcohol mixtures is shown in table 3.1. The only additive stable in an aqueous solution is MTEOS. All other additives require ethanol to form clear sols.

Stability here is defined as ensuring the sol is clear to slightly cloudy after mixing for 1 hour. The situation inside the sols is very complex, involving an interplay of hydrolysis and condensation reactions and the growth of linear chains, cyclics and nanoparticles⁵⁹. However, at this point it is easy to assess by eye if the sol has formed either two distinct phases or consists of large aggregates (>1 μ m, causing significant scattering of light) which will invariably lead to a non-uniform coating. From table 3.1, it is evident that

MTEOS is the only additive which can produce a stable sol in a pure water system. All other additives require either a 70:30 or 90:10 ethanol water mix to form stable solutions.

3.3.3 Uniformity of sol-gel films spin cast from water/ethanol solutions

The ability to produce stable solutions in ethanol/water mixtures enables the subsequent assessment of the uniformity of the resultant sol-gel coatings. In order to produce an effective barrier coating, a uniform coating must be produced on the surface. To study uniformity, the modified sol-gel solutions identified in section 3.3.1 are spin coated onto silicon wafers and silicon rubber (PDMS), cured at 120°C for 30 minutes, and then investigated with AFM. In addition, application of the buckling technique developed in Chapter 2 necessitates that the films be uniform on PDMS substrates. All films tested contain no GTMS in the system, i.e. they have a additive to GTMS molar ratio of 1:0. The MTEOS additive solution was made in DI water and the BTSE, PhTEOS and TESP solutions were made in a 90:10 (V/V) ethanol water mix.

MTEOS films produce uniform films when cast from aqueous-based sols on both silicon wafers and PDMS, Figure 3.5. The remaining additives produced much more complex film morphologies. Locally, BTSE modified films formed uniform coatings on silicon wafers. On PDMS the BTSE films did not form a uniform thickness which can be inferred from the buckling pattern shown in Figure 3.5. It is not evident from the AFM of the BTSE modified films, however, is that large scale striations form in the film, which are easily observed by eye.

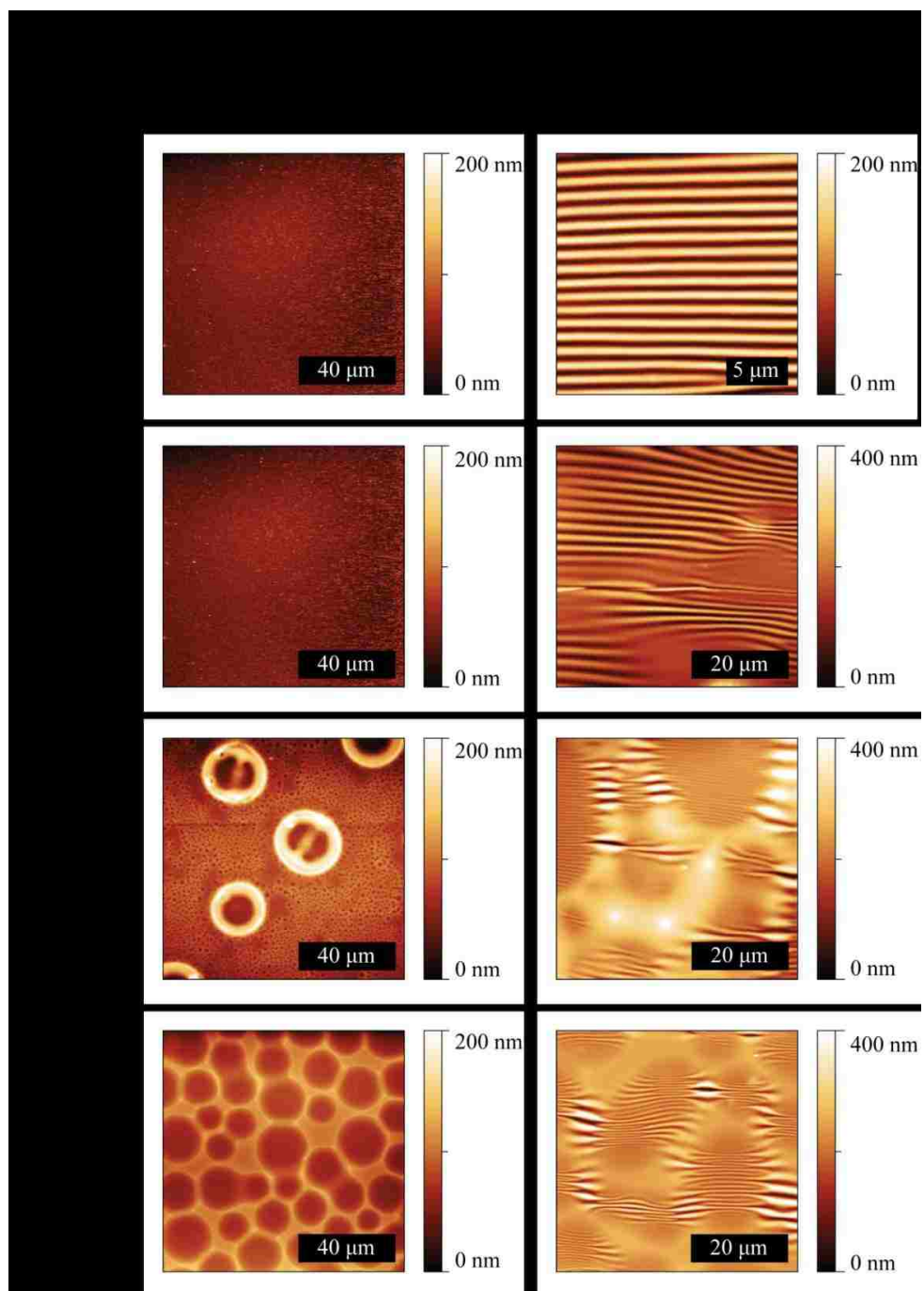


Figure 3.5: AFM images of sol-gel films made with 4 different additives. In each mixture the GTMS component of the standard sol-gel solution is replaced by same number of moles of the appropriate additive (Appendix A). The MTEOS solution is water based while the BTSE, TESP, PhTEOS coatings were prepared in a 90:10 ethanol/water solution. All films cured at 120 °C. The morphology on silicon wafers is shown in the left column and the morphology on PDMS is shown on the right.

These striations are magnified when coating on PDMS. Whether this is due to the soft coating surface or the change in air flow patterns of the spin coating (affecting the rate of evaporation) is not clear. One possible cause of these striations is the difference in the evaporation rates of the ethanol water system. As the ethanol at the surface of the film evaporates the water concentration in this region increases causing an increase in surface tension. The formation of a surface tension gradient induces instability and leads to the formation of striations⁶⁰⁻⁶². If we use an alcohol/water mixture above its azeotrope, the effect can be eliminated. Investigation of this effect, surface instability in a rapidly thinning film, is reserved for future work.

The TESP, PhTEOS modified coatings produce porous films on silicon, Figure 3.5. The pores/defects observed on the PhTEOS films appear uniform in nature while the ones on the TESP film have a unique morphology. A similar morphology appears when the films are coated on PDMS surfaces. The presence of buckling instability across the film shows that the pores do not travel through the entire film. While these defects are not suitable for barrier coatings it is worthwhile noting that this method can produce semi-porous coating. Any defect in a barrier coating is clearly a weak point as the water may reach the metallic surface and cause corrosion.

The only additive to pass both the aqueous stability test (section 3.3.2) and the uniform coating requirement (section 3.3.3) is MTEOS. Therefore, we shall now turn our attention to investigating this additive exclusively.

3.3.4 Plain strain modulus of sol-gel coatings modified with different concentrations of MTEOS

The buckling technique developed in Chapter 2 will be applied to the films containing the MTEOS additive to investigate the elastic modulus as a function of curing temperature and chemical composition. Three curing temperatures 45, 55 and 120 °C were investigated to enable direct comparison with the previous data collected for the unmodified sol-gel. Investigation of the concentration of MTEOS in the standard sol-gel formulation utilized the following approach. The total number of moles of the silane is kept constant in the solution. The standard solution contains 0.01 moles of GTMS; a solution prepared in the molar ratio of 50:50 MTEOS:GTMS will then contain 0.005 moles of MTEOS and 0.005 moles of GTMS. Coatings prepared with the MTEOS:GTMS molar ratios of 0:100, 25:75, 50:50, 75:25 were investigated. When referring to these coatings the mole fraction of GTMS to MTEOS will be used, i.e. 0.25 mole fraction of GTMS represents the MTEOS:GTMS ratio of 75:25 (Appendix A). All other components of the sol-gel, the TPOZ, GAA and Antarox remain the same.

The thickness of the sol-gel films as a function of the GTMS mole fraction was evaluated by spin casting the thin films on silicon wafers and using single wavelength ellipsometry to measure the thickness. As mentioned in section 3.2.4 this method is an effective means for estimating the thickness on PDMS. The thickness of the films is reduced by decreasing the mole fraction of GMTS in the coating, Figure 3.6. This result is expected; as the methyl group on MTEOS is a shorter alkyl chain than the glycidoxy group on GTMS it is likely that the sol-gel film can pack more densely, thus decreasing

thickness. This effect of reducing the length of the alkyl-chain on film thickness has been reported in the literature for similar systems^{63,64}.

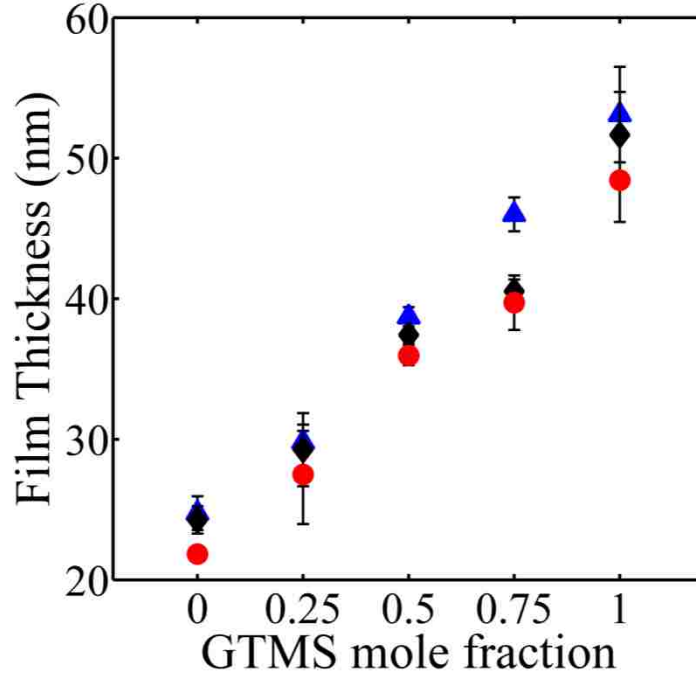


Figure 3.6: The effect of changing the GTMS mole fraction (relative to MTEOS) on the thickness of the sol-gel film. As the level of GTMS in the film is decreases the thickness also decreases. Blue triangles, black diamonds and red circles represent the thickness of sol-gel films cured at 45, 55 and 120°C for 30 minutes, respectively.

Now that the thickness of the film is known as a function of the GTMS mole fraction the plain strain modulus (\bar{E}_{SG}) can be calculated by measuring the buckling wavelengths of the sol-gel films using the method developed in Chapter 2. From equation 3.3 the plain strain modulus of the coating is evaluated, Figure 3.7,

$$\bar{E}_{SG} = 3\bar{E}_{PDMS} \left(\frac{\lambda}{2\pi h} \right)^3 \quad (3.3)$$

where \bar{E}_{SG} , \bar{E}_{PDMS} , λ and h are the sol-gel plain strain modulus, the PDMS plain strain modulus, buckling wavelength and sol-gel film thickness, respectively. The plain strain

modulus is defined as $\frac{E}{(1-\nu^2)}$, where E and ν are the elastic modulus and Poisson's ratio. As we increase the molar ratio of GTMS to MTEOS the elastic modulus of the film decreases, Figure 3.7. The decrease in elastic modulus is accompanied by an increase in the film thickness. Both of these effects can be explained by the decrease in the length of the hydrocarbon chain associated with the MTEOS and GTMS. The glycidoxypropyl chain on the GTMS is much larger than the methyl group on MTEOS; effecting how tightly the network can pack, thus increasing the thickness and decreasing the crosslink density in the vicinity of the glycidoxypropyl group. This decrease in cross link density leads to a decrease in the elastic modulus. A reduction in the elastic modulus as a result of increasing the size of the alkyl group has been found for MTMS:TEOS, VTMS:TEOS and GTMS:TEOS films where the elastic modulus was evaluated using nanoindentation^{63,64}. Where VTMS is an abbreviation for vinyltrimethoxysilane and MTMS is methyltrimethoxysilane. This result further verifies the ability of the buckling instability method to estimate the modulus of thin sol-gel films. Figure 3.7 also shows that, in all but one case, as we increase the curing temperature we increase the elastic modulus of the film. This result agrees with the trend observed in section 2.3.3 for GTMS:TPOZ films and is the expected result, as an increase in cure temperature will result in an increase in the cross link density of the film. However, for films made with a MTEOS:GTMS molar ratio of 100:0 (i.e. a GTMS mole fraction of 0) the coating cured at 45°C exhibits a higher modulus than coatings cured at 55°C and 120°C. The large error associated with this value (Figure 3.7) makes it unlikely to be a real effect. This error for the films prepared from a MTEOS:GTMS ratio of 100:0 likely arises due to the coating thickness. As the coating thickness decreases, the error inherent in the

measurement process will become more significant. Given that the elastic modulus is proportional to h^{-3} , any error in the measurement of h will be multiplied by a factor of 3 in the elastic modulus value, leading to a larger observed error. Another important consideration is the mode in which the buckling is induced in the system. For films cured at 120 °C the buckling arises due to thermal stress generated upon cooling the sample. Films cured at 45 °C and 55 °C are buckled mechanically. The modulus of a thin polymer brush, in which buckling was induced by thermal stress, is about four times lower than when the buckling was induced mechanically.⁶⁵ Should a similar effect be present here, the elastic modulus at room temperature of the thermally buckled sol-gel films would be higher than the value reported in Figure 3.7. The result would be an accentuation of the trend shown in Figure 3.7 that the elastic modulus increases with curing temperature.

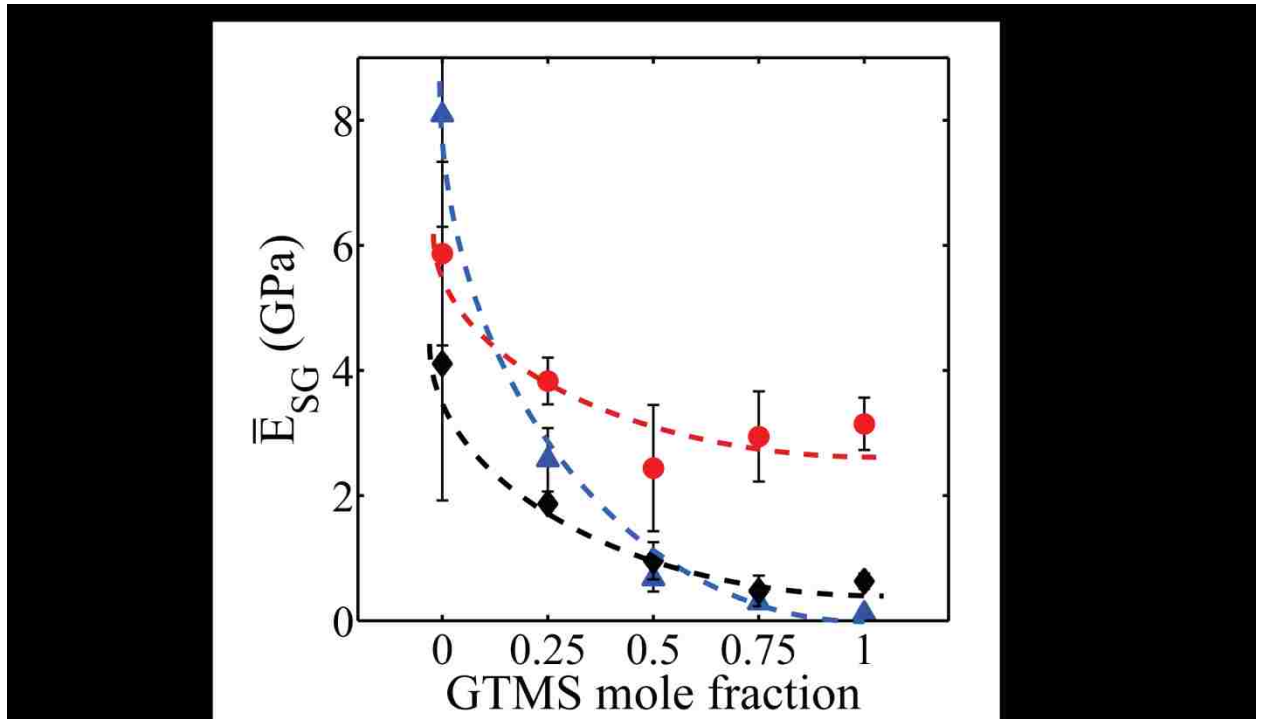


Figure 3.7: The effect of changing the GTMS mole fraction (relative to MTEOS) on the plain strain modulus (\bar{E}_{SG}) of the sol-gel film. Blue triangles, black diamonds and red circles represent the plain strain modulus of sol-gel films cured at 45, 55 and 120°C for 30 minutes respectively.

As noted in Chapter 2, the properties of a sol-gel film strongly depend on its chemical formulation and curing history. Therefore, it is difficult to compare our results to any similar results published in the literature. Nevertheless, it is instructive to look at an example available in the literature for sol-gel films prepared from TEOS and MTMS⁶⁴. In order to make this comparison we will again assume the Poisson's ratio of the sol-gel film to vary between 0.25-0.35^{66,67} (For a detailed explanation of this assumption please refer to section 2.3.2). The elastic modulus of a film prepared from TPOZ and MTEOS (GTMS mole fraction of 0) cured at 120 °C is then estimated to be in the range of 5.2-5.5 GPa. Atanacio *et al.*⁶⁴ reported the moduli of various organic-inorganic hybrid films based on the mixtures of TEOS and alkyltriethoxysilanes of various kinds as obtained

using nano-indentation. Of particular relevance here is the modulus of the TEOS and MTMS formulation. The elastic modulus of this film was found to be 12.4 GPa and 15.6 GPa when measured on silicon and copper substrates, respectively⁶⁴. Thus, our elastic modulus is roughly half that reported for a similar coating. It is possible that this discrepancy is due to the differences in the chemical composition, the thickness and/or buckling mechanisms. These different causes will now be examined in turn.

As reported in Chapter 2, the TPOZ+GTMS sol-gel film gave an elastic modulus of 1.5-1.6 GPa, which is close to the value reported for a TEOS+GTMS coating 1.68-1.8⁶⁴. From this result it appears that the use of TEOS vs. TPOZ does not change the modulus of the film significantly. Therefore, the modulus discrepancy noted above for the TPOZ+MTEOS vs. TEOS+MTMS films is unlikely to be due to the use of TPOZ instead of TEOS. Due to the increase in the length of the alkoxide chains, MTEOS is more resistant to hydrolysis than MTMS⁵⁹. Incomplete hydrolysis will reduce the number of hydroxyl groups in the coating, which will decrease the crosslink density of the film. The decrease in crosslink density will reduce the elastic modulus. It is, therefore, possible that the use of MTEOS vs. MTMS can decrease the elastic modulus. As discussed in Chapter 2, inducing the buckles through thermal stress may also lead to a low estimation for the elastic modulus⁶⁵. Finally it has been shown experimentally and theoretically that as the thickness of a polymer film is reduced below ~40 nm, the apparent elastic modulus (measured using buckling instability) also decreases⁶⁸⁻⁷⁰. The thickness of the TPOZ + MTEOS coating is ~ 25 nm; below the critical value of 40 nm, making it possible that this effect is also present in our system.

3.3.5 An empirical correlation between modulus of the sol-gel coating and its adhesive performance as a function of the sol-gel coating composition

The fracture strength of MTEOS modified sol-gel coatings were evaluated using ADCB technique, Figures 3.1-3.3. The fracture results for coatings made from a range of MTEOS:GTMS ratios are presented in Figures 3.8 and 3.9. A curing temperature of 45°C was chosen for this study to maximize the potential for the epoxy to interpenetrate into the sol-gel film to form a strong interlocking layer. Figure 3.8 illustrates the subcritical crack growth for all the coating formulations. Three crack growth regions can be clearly observed for all the sol-gel films tested.

It should be noted that, while three subcritical growth regions are present, it is difficult to relate them to the idealized regions identified in the schematic shown in Figure 3.3. In the idealized case of subcritical crack growth, region II corresponds to a diffusion limited process. A one dimensional moving boundary diffusion model⁷¹, predicts the crack velocity in this region to be independent of the energy release rate. Other models, which take into account Knudsen diffusion close to the crack tip, report a linear dependence of the crack velocity on the energy release rate⁷². From Figure 3.8, we observe that region II is actually characterized by an exponential dependence of the velocity on the energy release rate. Such dependence is indicative of a reaction limited regime. Therefore, in the present case it may not be possible to separate the reactive and diffusion limited regimes. To resolve this issue experiments should be performed at different temperatures and humidity's following the method reported by Kook and Dauskardt⁴⁴. This study will not be performed here as we are primarily concerned with the critical and threshold energy release rates.

From Figure 3.8, the critical and threshold energies are extracted and plotted vs. the sol-gel composition in Figure 3.9. Films containing no GTMS act like a release coating, having a lower critical (G_c) and threshold (G_{th}) fracture energies than untreated aluminum samples, Figure 3.9. This is due to the lack of any compatible chemical functionality with the epoxy and the formation of a highly cross-linked film with an elastic modulus around three times higher than the epoxy, as shown in Figure 3.7. At this high level of cross-linking it is unlikely that interpenetration of the epoxy into the sol-gel film can occur; implying that only relatively weak secondary forces exist between the epoxy and the MTEOS film. As the ratio of GTMS to MTEOS in the film increased, both G_c and G_{th} steadily increase, Figure 3.9. For this aluminum surface pretreatment (grit-blast) and sol-gel curing temperature (45 °C for 30 minutes), the addition of MTEOS to the sol-gel formulation has a detrimental effect on the joint performance from the viewpoint of both the critical and threshold fracture energies.

We now attempt to seek a correlation between the elastic modulus and adhesive performance when the formulation of the sol-gel coating is changed. Figure 3.9 shows that both the threshold and critical fracture energies decrease significantly with increasing modulus. This result leads us to form the same conclusions as in Chapter 2 for the dependence on curing temperature; the level of interpenetration of the epoxy into the sol-gel layer remains an important mechanism in predicting the adhesive strength. The strong correlation between elastic modulus and adhesive performance for coatings of different chemical composition broadens the scope of this methodology used to predict adhesive performance from a sol-gel film material property. It is also possible that the

addition of MTEOS to the coating decreases the number of GTMS groups on the surface available to bond to the epoxy. From Langmuir's principle of independent surface action we predict that the low energy functional groups on MTEOS will tend to organize at the interface. However due to the entropic effects the epoxide groups will still be present on the surface in some degree. It is not clear what critical concentration of epoxide groups is required on the surface to ensure optimal bonding. Ramrus *et al.*⁷³ have investigated the effect of micropatterning a surface with GTMS and octadecyltrichlorosilane (ODTS). In this study, reducing the surface coverage of GTMS to 75% had no effect on the strength of the joint. Surface coverages of less than 75% were not studied and so the critical surface coverage of GTMS remains an open question. Now that the effect of adding MTEOS to the sol-gel film on the adhesive performance has been investigated, we turn our attention to the characterization of the barrier properties of the modified sol-gel coating.

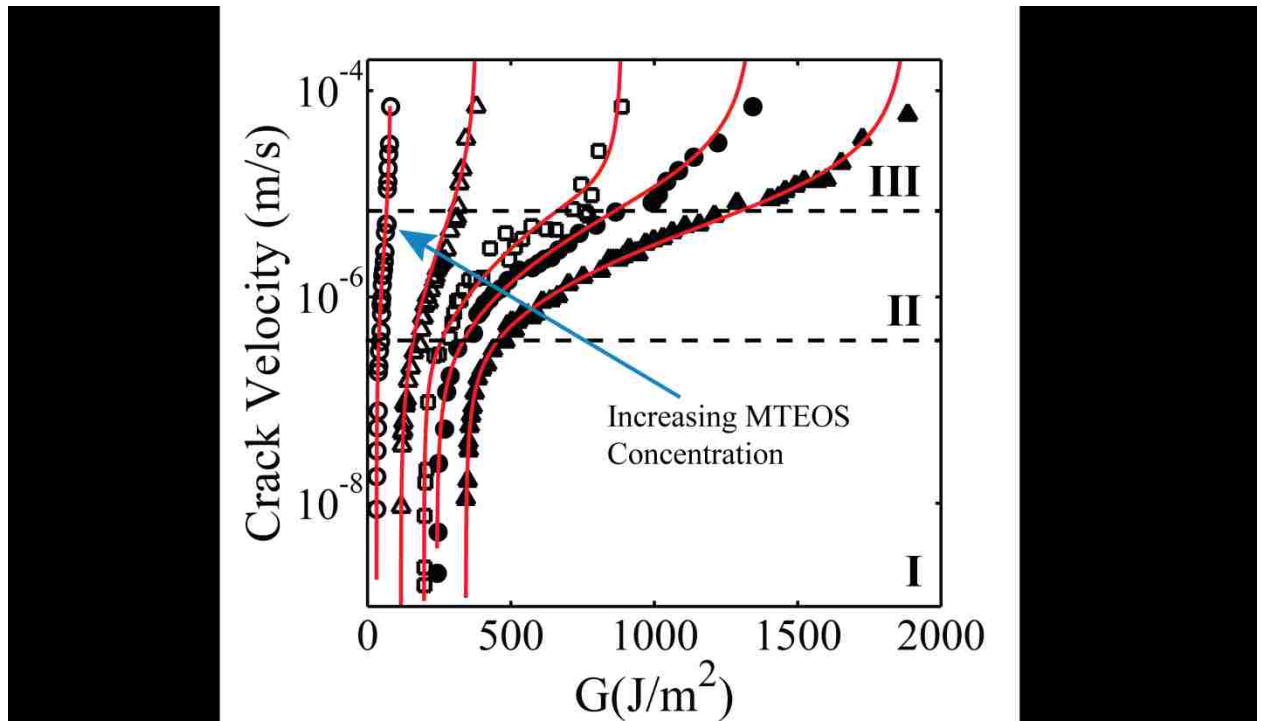


Figure 3.8: Crack velocity vs. energy release rate for epoxy/sol-gel/grit-blasted Al joints for different sol-gel film compositions. The sol-gel composition is altered by varying the molar ratio of MTEOS:GTMS in the coating as described in the text. Open circles correspond to coating prepared with the MTEOS:GTMS ratio of 100:0. Open triangles correspond to coating prepared with the MTEOS:GTMS ratio of 75:25. Open squares correspond to coating prepared with the MTEOS:GTMS ratio of 50:50. Closed circles correspond to coating prepared with the MTEOS:GTMS ratio of 25:75. Closed triangles correspond to coating prepared with the MTEOS:GTMS ratio of 0:100. Details of the formulations are provided in Appendix A. All coatings are cured at 45°C for 30 minutes. All experiments are carried out in an environmental chamber (Figure 3.2) at 26°C and 98%RH. Three regions of subcritical crack growth are identified.

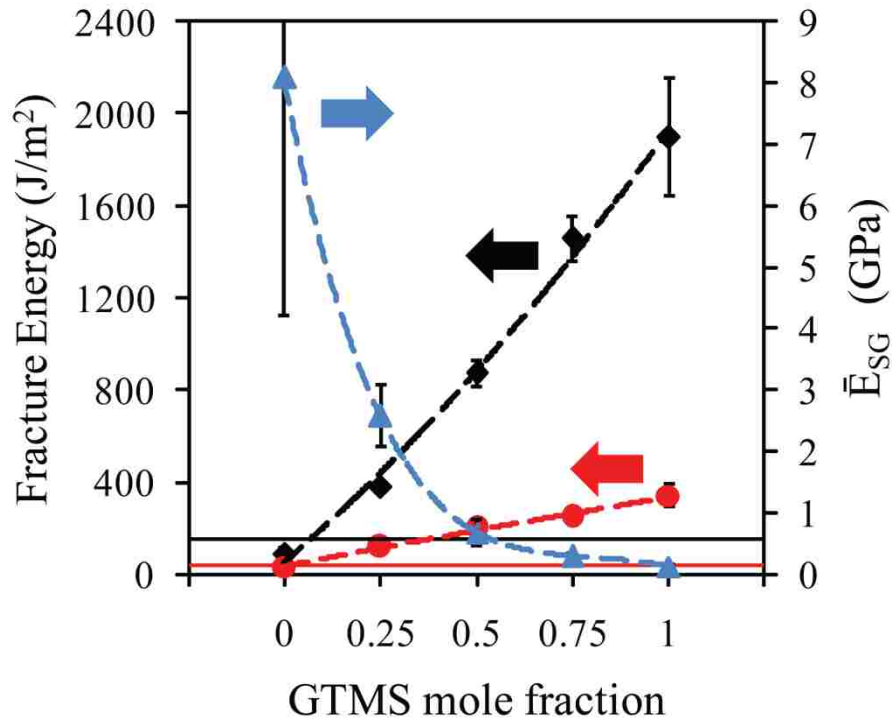


Figure 3.9: The effect of changing the GTMS mole fraction (relative to MTEOS) on the critical and threshold fracture energy of an Epoxy/sol-gel/Aluminum adhesive joint. The plain-strain modulus (\bar{E}_{SG}) dependence on the GTMS mole fraction is re-plotted from Figure 3.8 on the right axis. The aluminum surface pretreatment is a standard grit-blast and the sol-gel cure temperature is 45 °C for 30 minutes. The black and red lines represent the critical fracture and threshold fractures energies for an uncoated Epoxy/Aluminum joint. Non-evident error bars are contained within the marker size

3.3.6 Effect of humidity on the buckling morphology of MTEOS:GTMS sol-gel films

In Chapter 2 we saw how exposing the buckled sol-gel films to a humid environment lead to various changes in the buckling morphology. From these changes it was possible to qualitatively assess the barrier properties of the sol-gel film as a function of curing temperature. The same analysis is applied here to determine the effect of moisture on sol-gel films as a function of chemical composition and curing temperature. Figure 3.10 shows the effect of exposing sol-gel films, prepared from various ratios of

MTEOS:GTMS and cured at 120 °C for 30 minutes, to 98% RH for 15 hrs. The kinks in the buckling morphology which form in the films of MTEOS:GTMS ratios 25:75 and 0:100 are known as herringbone buckles and are indicative of a biaxial stress state^{74,75}. This stress state arises due to the swelling of the coating with water. Unfortunately, it is not possible to precisely quantify the change in the stress state as the overall energy in the system is relatively insensitive to the wavelength and amplitude of these secondary buckles⁷⁴. For films prepared from MTEOS:GTMS ratios of 100:0 and 75:25, exposure to humidity has little effect on the buckling morphology, only slightly disturbing the buckles in some places. This observation strongly suggests that the films with a higher content of MTEOS resist the penetration of water more effectively and agrees with the salt spray data collected at Boeing (Appendix B). To summarize these salt spray results, the addition of MTEOS to the sol-gel formulation was found to improve the barrier properties of the coating. The enhancement became more significant as the cure temperature of the sol-gel film was increased. Analysis of the ratio of the buckling wavelength before and after humid exposure shows that for all films cured at 120°C no change in wavelength was observed, Figure 3.11. The same result is observed from studying the change in amplitude before and after humid exposure, Figure 3.12. Therefore, the elastic moduli of the coatings cured at 120°C are not changed through exposure to high humidity and the degree of swelling is low.

For coatings cured at 45°C and 55°C the wavelength and amplitude of the coatings are significantly reduced upon exposure to 98% RH, Figures 3.11-3.14. This effect is more pronounced for the coating cured at 45°C suggesting that the coating cured at 55°C exhibits a higher level of moisture resistance. Despite the increase in the MTEOS

content of the film the ratio of the buckling wavelength before and after humid exposure remains constant (around ~2) for the film cured at 55°C, Figure 3.11. The amplitude ratio also remains independent of the MTEOS content, Figure 3.12, suggesting that the addition of MTEOS does not provide any additional barrier properties to the coating when cured at 55°C. This result is unexpected given the results for the 120 °C cured films revealed that increasing the MTEOS content increases the barrier properties of the film. In addition, the salt spray data indicated an improvement in the barrier properties of room cured sol-gel film with the addition of MTEOS (Appendix B). As the modulus of the film increases with increasing MTEOS content, we expect the higher cross link density to provide increased coating stability in a humid environment. For the films cured at 45°C the wavelength and amplitude ratios actually increase with increasing MTEOS content, Figures 3.11 and 3.12. In order to reduce both the wavelength and the amplitude of the coating the elastic modulus of the coating must decrease, equation 3.1. A possible explanation can be found by considering the stress state within the coating in conjunction with the hydrolysis of the crosslinks. For all cases the strain applied to induce buckling is kept constant at $\epsilon \sim 4\%$. Thus, as the modulus of the film increases, the stress in the film will also increase. As the compressive stress is only applied in one direction, a tensile stress will develop in the film perpendicular to the compressive direction due to the Poisson ratios of the coating and substrate. The stretching of the –Si-O-Si- bond (one of the major crosslinks in the coating) decreases the Gibbs free energy change of hydrolysis⁷⁶. This decrease will promote bond degradation and, due to the tensile nature of the coating, the bonds will not be able to heal, i.e. the process is irreversible. The scission of these bonds will reduce the elastic modulus of the coating.

This stress dependence effect is a viable source for the increase in the wavelength and amplitude ratios with MTEOS concentration for the sol-gel films cured at 45°C.

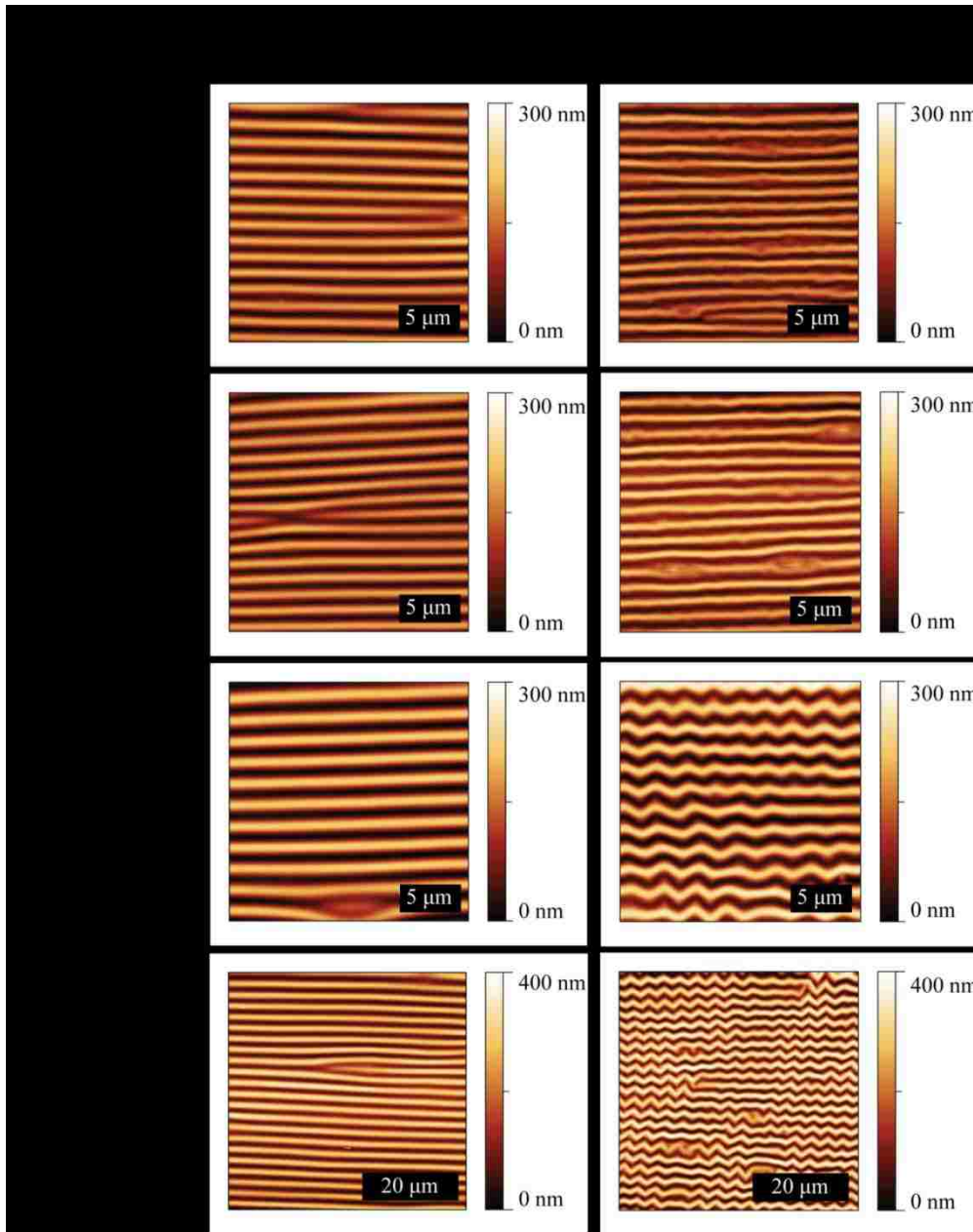


Figure 3.10: AFM scans showing the effect of humidity on sol-gel films cured at 120 °C for different ratios of MTEOS to GTMS. The ratio of MTEOS:GTMS is shown on the left. The left column shows the buckling morphology observed after the 120 °C oven cure for films at ambient humidity (~47% RH). The right column shows the subsequent change in the surface morphology after being exposed to a high humidity (~98% RH) environment for 15 hrs. Note the change of scale between images.

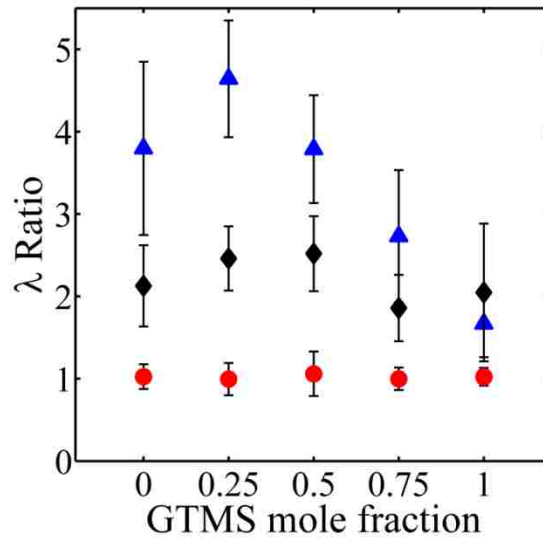


Figure 3.11: Ratio of the buckling wavelength before exposure to high humidity (RH~98%, for 15 hrs) to that measured after exposure as a function of MTEOS mole fraction. A ratio greater than 1 indicates a decrease in wavelength due to high humidity exposure. Blue triangles, black diamonds and red circles represent the wavelength ratio of sol-gel films cured at 45, 55 and 120°C for 30 minutes respectively.

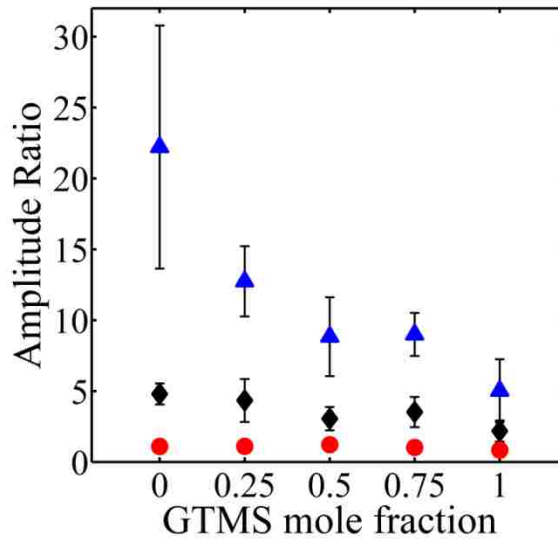


Figure 3.12: Ratio of the buckling amplitude before exposure to high humidity (RH~98%) for 15hrs to that measured after exposure as a function of GTMS mole fraction. A ratio greater than 1 indicates a decrease in amplitude due to high humidity exposure. Blue triangles, black diamonds and red circles represent the amplitude ratio of sol-gel films cured at 45, 55 and 120°C for 30 minutes respectively.

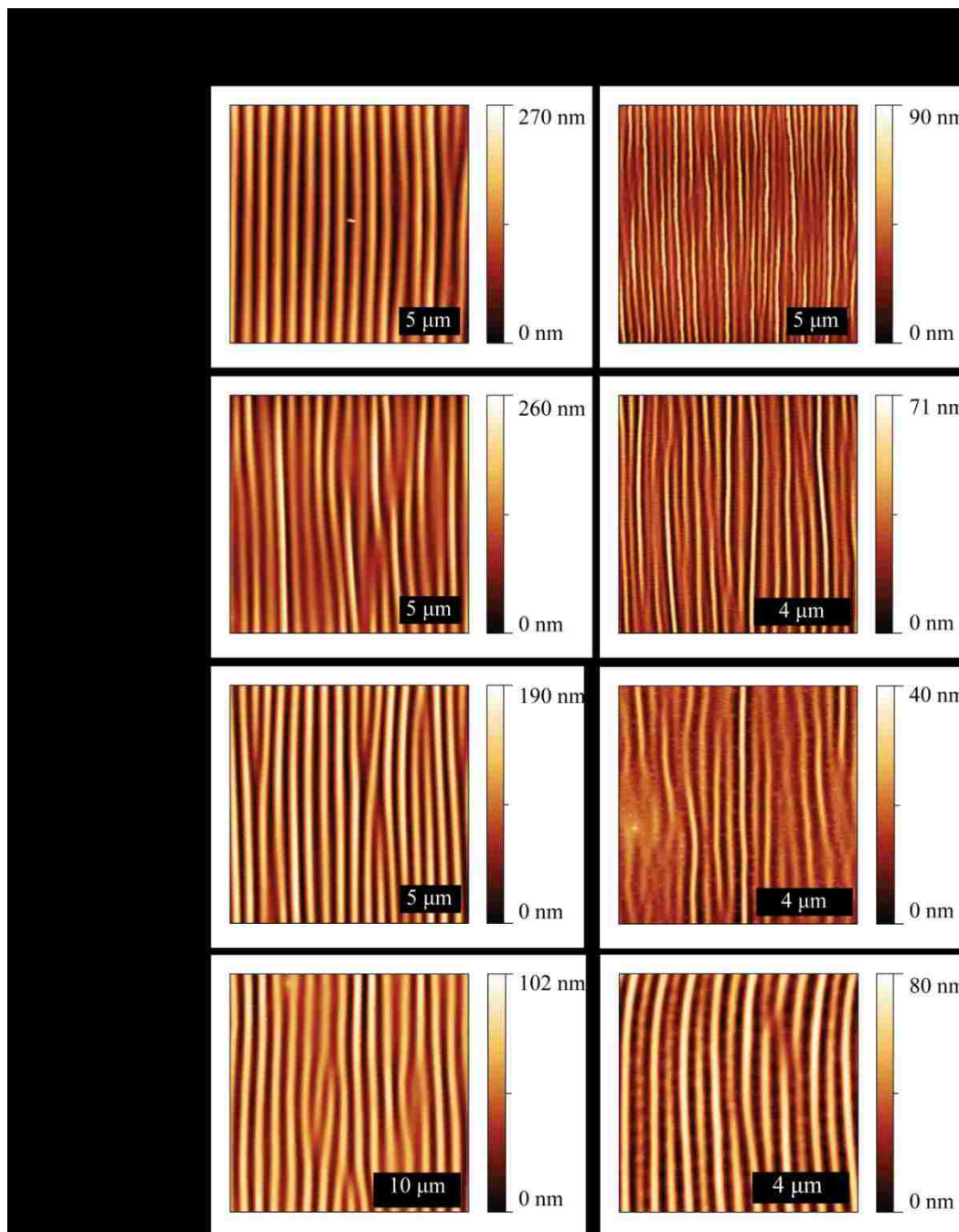


Figure 3.13: AFM scans showing the effect of humidity on sol-gel films cured at 55 °C for different ratios of MTEOS to GTMS. The ratio of MTEOS:GTMS is shown on the left. The left column shows the buckling morphology observed after the 55 °C oven cure for films at ambient humidity (~47% RH). The right column shows the subsequent change in the surface morphology after being exposed to a high humidity (~98% RH) environment for 15 hrs. In order to form the buckles the samples were exposed to a strain of $\epsilon \sim 4\%$. Note the change of scale between images.

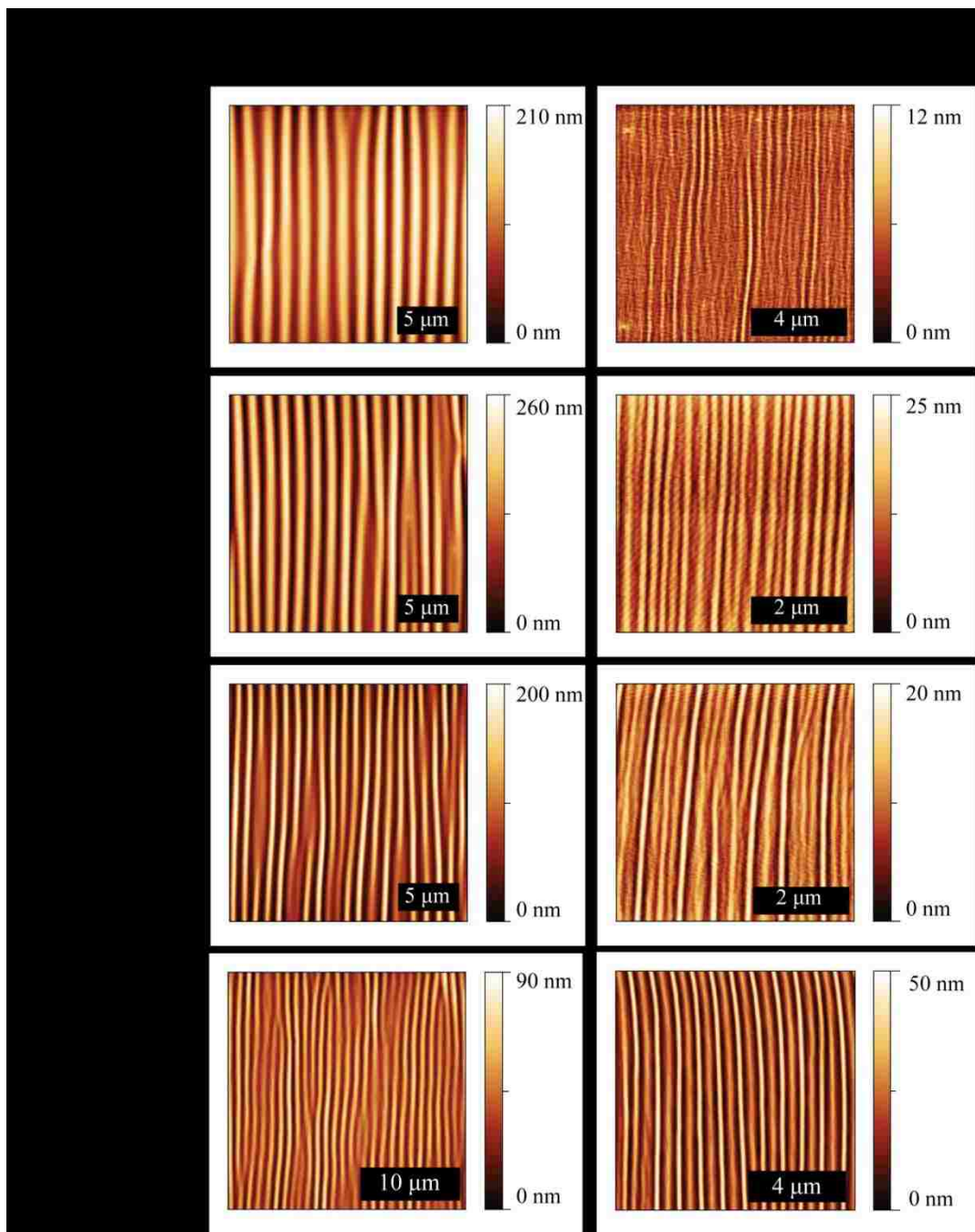


Figure 3.14: AFM scans showing the effect of humidity on sol-gel films cured at 45 °C for different ratios of MTEOS to GTMS. The ratio of MTEOS:GTMS is shown on the left. The left column shows the buckling morphology observed after the 45 °C oven cure for films at ambient humidity (~47% RH). The right column shows the subsequent change in the surface morphology after being exposed to a high humidity (~98% RH) environment for 15 hrs. In order to form the buckles the samples were exposed to a strain of $\epsilon \sim 4$. Note the change of scale between images.

3.4 Summary and Conclusion

To improve the barrier properties of the standard sol-gel formulation, various hydrophobic additives were investigated. MTEOS was the only additive found which formed a stable aqueous based solution and formed a uniform film. The buckling instability technique introduced in Chapter 2 was further extended to measure the modulus of the film as a function of MTEOS concentration, highlighting the versatility of the buckling method and paving the way for investigation of other sol-gel films. The new MTEOS formulation improved the barrier properties of the Boegel coating, as found using salt spray and buckling instability, but decreased the adhesive strength of an adhesive joint reinforced with a sol-gel film cured at 45°C. The elastic modulus of the modified sol-gel coating was found to be inversely correlated with both the critical and threshold fracture energies. This study shows that methods which increase the performance of barrier properties in sol-gel films do not necessarily translate to increased durability in their adhesion promoting counterparts. Future studies should investigate other techniques used in barrier coatings, such as the incorporation of inorganic salts, to improve the durability of joints reinforced with sol-gel coatings.

3.8 References

- (1) Plueddemann, E. P. *Silane Coupling Agents*; 1982.
- (2) Digby, R. P.; Shaw, S. J. *International Journal of Adhesion and Adhesives* **1998**, *18*, 261–264.

- (3) Davis, G. D.; Venables, J. D. *Surfaces, Chemistry and Applications*; Chaudhury, M. K.; Pocius, A. V., Eds.; Elsevier: London - New York, 2002; pp. 947–1008.
- (4) Pape, P. G.; Plueddemann, E. P. *Silanes and Other Coupling Agents*; Mittal, K. L., Ed.; VSP BV, 1992; pp. 105–116.
- (5) Sanchez, C.; Julián, B.; Belleville, P.; Popall, M. *Journal of Materials Chemistry* **2005**, *15*, 3559.
- (6) Zheludkevich, M. L.; Salvado, I. M.; Ferreira, M. G. S. *Journal of Materials Chemistry* **2005**, *15*, 5099–5111.
- (7) Cunliffe, A. V.; Evans, S.; Tod, D. A.; Torry, S. A.; Wylie, P. *International Journal of Adhesion and Adhesives* **2001**, *21*, 287–296.
- (8) Poznyak, S. K.; Zheludkevich, M. L.; Raps, D.; Gammel, F.; Yasakau, K. a.; Ferreira, M. G. S. *Progress in Organic Coatings* **2008**, *62*, 226–235.
- (9) Vreugdenhil, a. J.; Gelling, V. J.; Woods, M. E.; Schmelz, J. R.; Enderson, B. P. *Thin Solid Films* **2008**, *517*, 538–543.
- (10) Zheludkevich, M. L.; Serra, R.; Montemor, M. F.; Salvado, I. M. M.; Ferreira, M. G. S. *Surface and Coatings Technology* **2006**, *200*, 3084–3094.
- (11) Abel, M.-L.; Allington, R. D.; Digby, R. P.; Porritt, N.; Shaw, S. J.; Watts, J. F. *International Journal of Adhesion and Adhesives* **2006**, *26*, 2–15.
- (12) Liu, J. Ph.D. Thesis, Lehigh University, 2006.
- (13) Bell, J. P.; Schmidt, R. G.; Malofsky, A.; Mancini, D. *Silanes and Other Coupling Agents*; Mittal, K. L., Ed.; VSP BV, 1992; pp. 49–66.
- (14) Abel, M.; Digby, R. P.; Fletcher, I. W.; Watts, J. F. **2000**, *125*, 115–125.
- (15) Chaudhury, M. K.; Gentle, T. M.; Plueddemann, E. P. *Journal of adhesion science and technology* **1987**, *1*, 29–38.
- (16) Gellman, A. J.; Naasz, B. M.; Schmidt, R. G.; Chaudhury, M. K.; Gentle, T. M. *Journal of adhesion science and technology* **1990**, *4*, 597–601.
- (17) Rider, A. N. *International Journal of Adhesion and Adhesives* **2006**, *26*, 67–78.
- (18) Abel, M.-L.; Adams, a. N. N.; Kinloch, a. J.; Shaw, S. J.; Watts, J. F. *International Journal of Adhesion and Adhesives* **2006**, *26*, 50–61.

- (19) Benkoski, J. J.; Kramer, E. J.; Yim, H.; Kent, M. S.; Hall, J. *Langmuir : the ACS journal of surfaces and colloids* **2004**, *20*, 3246–58.
- (20) Joshua Du, Y.; Damron, M.; Tang, G.; Zheng, H.; Chu, C.-J.; Osborne, J. H. *Progress in Organic Coatings* **2001**, *41*, 226–232.
- (21) *Metals Handbook*; 10th ed.; International, ASM, 1990; p. 70.
- (22) Liu, J.; Chaudhury, M. K.; Berry, D. H.; Seebergh, J. E.; Osborne, J. H.; Blohowiak, K. Y. *Journal of Adhesion Science and Technology* **2006**, *20*, 277–305.
- (23) Bagheri, R.; Pearson, R. A. *Polymer* **1996**, *37*, 4529–4538.
- (24) Bagheri, R.; Pearson, R. A. *Polymer* **2000**, *41*, 269–276.
- (25) Bagheri, R.; Pearson, R. A. *Journal of materials science* **1996**, *31*, 3945–3954.
- (26) Blohowiak, K. Y.; Osborne, J. H.; Krienke, K. A.; Sekits, D. F. *Proc. 28th International SAMPE Symposium* **1996**, 440.
- (27) Blohowiak, K. Y.; Osborne, J. H.; Krienke, K. A. US Patent 5814137 **1998**.
- (28) Blohowiak, K. Y.; Osborne, J. H.; Krienke, K. A. US Patent US5869141 **1999**.
- (29) Blohowiak, K. Y.; Osborne, J. H.; Krienke, K. A. US Patent 5849110 **1998**.
- (30) Blohowiak, K. Y.; Osborne, J. H.; Krienke, K. A. US Patent 5939197 **1999**.
- (31) Blohowiak, K. Y.; Krienke, K. A.; Osborne, J. H.; Mazza, J. J.; Gaskin, G. B.; Arnold, J. R.; DePiero, W. S.; Brescia, J. *Proc. The Second Joint NASA/FAA/DoD Conference on Aging Aircraft* **1998**, 313.
- (32) Blohowiak, K. Y.; Cadwell-Stancin, L.; Anderson, R. A.; Mazzitelli, C. M.; Preedy, K.; Grob, J. W.; Glidden, M. *Proc. 47th International SAMPE Symposium* **2002**, 279.
- (33) Longley, J. E.; Chaudhury, M. K. *Macromolecules* **2010**, *43*, 6800–6810.
- (34) Liu, J.; Chaudhury, M. K.; Berry, D. H.; Seebergh, J. E.; Osborne, J. H.; Blohowiak, K. Y. *The Journal of Adhesion* **2006**, *82*, 487–516.
- (35) Xiao, F.; Hui, C.-Y.; Kramer, E. J. *Journal of materials science* **1993**, *28*, 560–5629.

- (36) Xiao, F.; Hui, C.-Y.; Washiyama, J.; Kramer, E. J. *Macromolecules* **1994**, *27*, 4382–4390.
- (37) Kanninen, M. *International Journal of Fracture* **1973**, *9*, 83–92.
- (38) Jumel, J.; Shanahan, M. E. R. *The Journal of Adhesion* **2008**, *84*, 788–804.
- (39) Jumel, J.; Budzik, M. K.; Shanahan, M. E. R. *Engineering Fracture Mechanics* **2011**, *78*, 3253–3269.
- (40) Kraus, A. S.; Kraus, K. *Fracture Kinetics of Crack Growth*; 1st ed.; Kluwer Academic Publishers, 1988.
- (41) Gurumurthy, C. K.; Kramer, E. J.; Hui, C.-Y. *International journal of fracture* **2001**, *109*, 1–28.
- (42) Kinloch, A. J.; Osiyemi, S. . *Journal of Adhesion* **1993**, *43*, 79–90.
- (43) Vanel, L.; Ciliberto, S.; Cortet, P.-P.; Santucci, S. *Journal of Physics D: Applied Physics* **2009**, *42*, 214007.
- (44) Kook, S.-Y.; Dauskardt, R. H. *Journal of Applied Physics* **2002**, *91*, 1293.
- (45) Ciccotti, M. *Journal of Physics D: Applied Physics* **2009**, *42*, 214006.
- (46) Dillingham, R. G.; Boerio, F. J. *Silanes and Other Coupling Agents*; Mittal, K. L., Ed.; VSP BV, 1992; pp. 493–511.
- (47) Schutt, J. B. US Patent 2001/0056141 A1 **2001**.
- (48) Subasri, R.; Jyothirmayi, A.; Reddy, D. S. *Surface and Coatings Technology* **2010**, *205*, 806–813.
- (49) Castro, Y.; Duran, A.; Damborenea, J. J.; Conde, A. *Electrochimica Acta* **2008**, *53*, 6008–6017.
- (50) Conde, A.; Duran, A.; de Damborenea, M. *Progress in Organic Coatings* **2003**, *46*, 288–296.
- (51) Song, J.; Ooij, W. V. *Journal of adhesion science and technology* **2003**, *17*, 37–41.
- (52) Susac, D.; Sun, X.; Mitchell, K. a. R. *Applied Surface Science* **2003**, *207*, 40–50.
- (53) Franquet, A.; De Laet, J.; Schram, T.; Terryn, H.; Subramanian, V.; van Ooij, W. J.; Vereecken, J. *Thin Solid Films* **2001**, *384*, 37–45.

- (54) van Ooij, W. J.; Zhu, D. *Corrosion* **2001**, *57*, 413–427.
- (55) Pan, G.; Schaefer, D. W.; van Ooij, W. J.; Kent, M. S.; Majewski, J.; Yim, H. *Thin Solid Films* **2006**, *515*, 2771–2780.
- (56) Pan, G.; Schaefer, D. W.; Ilavsky, J. *Journal of colloid and interface science* **2006**, *302*, 287–93.
- (57) Zhu, D.; van Ooij, W. J. *Electrochimica Acta* **2004**, *49*, 1113–1125.
- (58) Plueddemann, E. *Journal of adhesion science and technology* **1988**, *2*, 3–5.
- (59) Brinker, C. J.; Scherer, G. W. *Sol-Gel Science: The Physics and Chemistry of Sol-Gel Processing*; 1 st.; Academic Press: San Diego, CA, 1990.
- (60) Birnie, D. P. *Journal of Materials Research* **2001**, *16*, 1145–1154.
- (61) Birnie, D. P.; Kaz, D. M.; Taylor, D. J. *Journal of Sol-Gel Science and Technology* **2008**, *49*, 233–237.
- (62) Taylor, D. J.; Birnie, D. P. *Chemistry of Materials* **2002**, *14*, 1488–1492.
- (63) Latella, B. A.; Gan, B. K.; Barbe, C. J.; Cassidy, D. J. *Journal of Materials Research* **2008**, *23*, 2357–2365.
- (64) Atanacio, A. J.; Latella, B. A.; Barbé, C. J.; Swain, M. V. *Surface and Coatings Technology* **2005**, *192*, 354–364.
- (65) Huang, H.; Chung, J. Y.; Nolte, A. J.; Stafford, C. M. *Chemistry of Materials* **2007**, 6555–6560.
- (66) Tsai, C.-T.; Lu, H.-Y.; Ting, C.-Y.; Wu, W.-F.; Wan, B.-Z. *Thin Solid Films* **2009**, *517*, 2039–2043.
- (67) Brown, D.; Clarke, J. H. R. *Macromolecules* **1991**, *24*, 2075–2082.
- (68) Yoshimoto, K.; Jain, T. S.; Nealey, P. F.; de Pablo, J. J. *The Journal of chemical physics* **2005**, *122*, 144712.
- (69) Mansfield, K. F.; Theodorou, D. N. *Macromolecules* **1991**, *24*, 6283–6294.
- (70) Stafford, C. M.; Vogt, B. D.; Harrison, C.; Julthongpiput, D.; Huang, R. *Macromolecules* **2006**, *39*, 5095–5099.
- (71) Wiederhorn, S. M. *Journal of the American Ceramic Society* **1967**, *50*, 407.

- (72) Lawn, B. *Fracture of Brittle Solids*; 2nd ed.; Cambridge University Press: Cambridge, 1993.
- (73) Ramrus, D. A.; Berg, J. C. *Journal of Adhesion Science and Technology* **2006**, *20*, 1615–1623.
- (74) Chen, X.; Hutchinson, J. W. *Journal of Applied Mechanics* **2004**, *71*, 597.
- (75) Huang, Z. Y.; Hong, W.; Suo, Z. *Journal of the Mechanics and Physics of Solids* **2005**, *53*, 2101–2118.
- (76) Benkoski, J. J.; Kramer, E. J.; Yim, H.; Kent, M. S.; Hall, J. *Langmuir* **2004**, *20*, 3246–58.

CHAPTER 4

Strength of a sol-gel reinforced joint as a function of sol-gel curing temperature, film thickness and aluminum surface morphology

Abstract

The fracture strength of an epoxy/sol-gel/aluminum joint depends strongly on the processing parameters of the sol-gel film. Three of these parameters, the sol-gel curing temperature, concentration and aluminum surface pretreatment are studied simultaneously to determine a set of stringent operating guidelines. From this study, we find that grit-blasted surfaces significantly outperform their sanded counterparts. Quantification of surface roughness is sought for the aluminum surfaces pretreated with both macro roughening methods in an attempt to correlate surface roughness with adhesive performance. To this end, the fractal dimension of the macro-rough surfaces is rigorously evaluated and found to be independent of surface pretreatment. Differentiation between the grit-blasted and sanded surfaces is achieved through the use of an anomalous diffusion coefficient. Thus, a correlation between surface roughness and adhesive performance is proposed by examining the qualitative relationship between the diffusion coefficient and the expected fracture toughness of an epoxy/sol-gel/aluminum joint.

4.1 Introduction

Despite the large amount of research performed on sol-gel based adhesion promoters the optimum cure temperature for the sol-gel film remains under debate¹. The question remains open due, in part, to the large number of processing variables that can alter the ability of the sol-gel coating to act as an adhesion promoter: solution pH and temperature, solvent/co-solvent, chemical composition, hydrolysis time, cure temperature, surface pretreatment and the type of adhesive/adherend¹⁻⁴ (Figure 1). With such a wide range of parameters, cross comparison of results is difficult to perform between research groups. To combat this issue, Digby and Shaw⁴ headed an international research program to assess the effect of the aforementioned processing variables on the adhesive performance. This program defined a model silane system based on glycidoxypropyltrimethoxysilane (GTMS) in a water solution with an acetic acid catalyst⁴. A thorough review of the results is presented by Abel *et al.*^{1,5}. The program applied a general methodology throughout the process: each variable was optimized in turn (with respect to adhesive performance) before moving onto optimization of the next process variable. While this did generate a robust set of optimum processing parameters it neglected the interaction of the parameters with one another, i.e. the feedback loops illustrated in Figure 4.1 were largely ignored. Therefore, the generality of the results is somewhat limited. The initial focus of this Chapter is to show that a more general set of operating conditions can be defined by studying the previously ignored feedback loops. In doing so some of the discrepancies in the cure temperature results outlined by Abel *et al.*¹ can be resolved. The current study will include the feedback loops that arise from the

relationships between the cure temperature, sol-gel concentration (film-thickness) and surface pretreatment of the aluminum adherend. The different variables studied and the methodology used to choose them will now be discussed in detail.

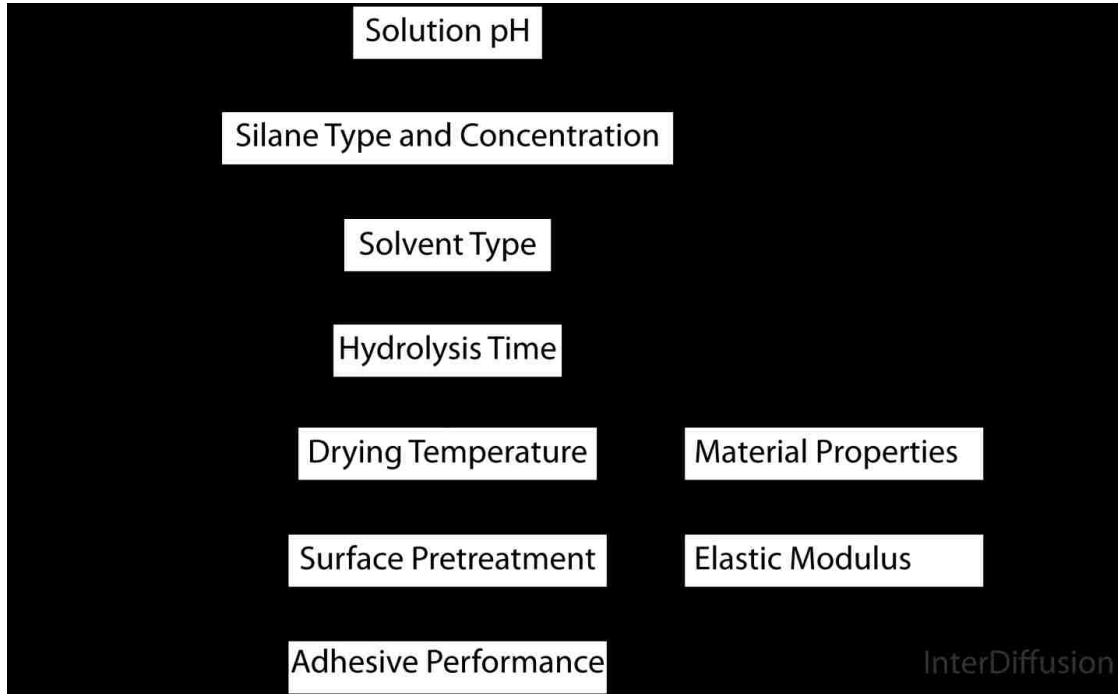


Figure 4.1: Flow diagram representing the processing parameters involved in preparing an adhesive bond with a sol-gel based surface pretreatment. The diagram also shows the relationship of the elastic modulus to the processing parameters as outlined in Chapters 2 & 3.

The most common surface pretreatments for aluminum used in the aviation industry are sanding, chemical etching and anodizing. These techniques produce very different surface morphologies on aluminum. Sanding creates macro-rough surfaces, while chemical etching and anodizing produce micro-rough porous surfaces^{6,7}. Here we define roughness according to the range specified by Venables⁶; macro roughness is defined as having characteristic bumps and jagged features on the order of $\sim 1 \mu\text{m}$ and micro-roughness as a fine structure with dimensions $< 0.1 \mu\text{m}$. In order to encompass this broad

range of roughness four different surface pretreatments were studied, polishing, FPL etching, sanding and grit-blasting. The effects of thickness and temperature were studied by examining the upper and lower limits of each parameter. For the sol-gel considered in this study these limits are 50 nm and 310 nm, with the upper limit arising due to solution stability at higher concentrations. The temperatures investigated were 24°C cure for 75 mins at 50% RH and 120°C for 30 mins. The lower limit was chosen based on the previous studies on the same system⁸. The upper limit is fixed to minimize any thermal degradation of the organic components of the film. After investigating the effect of the optimization feedback loops on adhesive performance, we turn our attention to the detailed analysis of the macro-rough surfaces and the effect of macro-roughness on the adhesive performance.

The two most common methods to mechanically roughen a surface prior to adhesive bonding are sanding and grit-blasting. While grit-blasting generally produces a stronger more durable adhesive joint, implementation is difficult in many practical applications. Sanded surfaces typically yield fracture energies 2-4 times lower than their grit-blasted counter parts yet due to the flexibility of the technique it is much more widely used in the aviation industry^{9,10}. This is somewhat of a generalization as, due to the wide range of grit sizes available in sanding and grit-blasting processes, it may be possible to have some combinations where specific sanded surfaces will outperform grit-blasted surface. The important aspect to consider in this study is that the two procedures produce very different patterns of surface roughness. For the current study on an Epoxy/Aluminum joint, the roughened surfaces obtained by both methods are characterized to seek relationship between the type of macro-roughness and fracture energy.

One of the simplest and widely used methods to characterize surface roughness is the root mean squared (RMS) technique. The RMS is the standard deviation of the height profile of a surface. The advantage of RMS is that it provides a characteristic length scale for the surface roughness (unlike the fractal dimension). However, as noted in Chapter one the major disadvantage of the RMS technique is that it is strongly dependant on the sample size¹¹. This size dependence means that it cannot provide a true characterization¹¹ of the surface unless more statistics are known, i.e. the change in RMS as a function of sample size and instrument resolution. The other prominent parameter used to characterize surfaces is the fractal dimension. Previous studies relating surface roughness to the fracture energy of an adhesive joint have found the fractal dimension to be a more reliable than RMS as a means to predict the joint strength¹²⁻¹⁷. As the fractal dimension is a measure of the scale invariance of a surface it does not provide a characteristic length scale of the system. In order to get an idea of this length scale other parameters, also obtained from fractal analysis, such as the lacunarity and topothesy must used^{11,18}. These topics will be outlined in more detail in the experimental section. The fractal dimension will be used as a starting point to characterize the roughness of surfaces prepared via grit-blasting and sanding.

In recent years, the fractal dimension has seen resurgence in its use to characterize the roughness of surfaces produced through the fracture of a bulk material¹⁹. These studies used the Hurst exponent (H) to characterize the fracture surface. The Hurst exponent is related to the fractal dimension (F_D) via the following equation, $H=2-F_D$ ²⁰. The fracture of a wide range of bulk materials, from glass to aluminum alloys, have been studied in this manner and the Hurst exponent of the fracture surface has been found to lie in the

range 0.77-0.80^{19,21-23}, prompting researchers to suggest that it is a universal factor for the fracture of any rigid material^{19,21}. The origin of this exponent remains a debated topic in the literature²⁴. Models ranging from damage coalescence processes to the movement of a crack front through randomly distributed obstacles have been proposed; these models are reviewed by Bonamy and Bouchaud¹⁹. The fracture of an epoxy/aluminum interface presents a different scenario to that of bulk fracture; the direction of the crack path is predetermined by the roughness of the aluminum substrate, providing the fracture remains interfacial. The surface roughness created by the grit-blasting or sanding of aluminum are both examples of multiple fracture processes occurring on the surface of a homogeneous material. The principle fracture mechanisms are erosion^{25,26} and scratching for grit-blasting and sanding respectively. While long scale correlations over the surface are not expected due to the multiple random fracture events, correlations are expected to exist over regions on the order of the grit size. This idea was proposed but not tested by Schmittbul *et al.*²⁷. This raises the question, is surface fracture governed by the same underlying principles as that in the bulk? To the authors' knowledge this question has not previously been considered in detail. Thus, the fractal dimensions of sanded and grit-blasted surfaces were investigated to see if the universal law predicting a Hurst exponent $\sim 0.77-0.80$ holds for surface fracture. If indeed the universal law holds, an alternative method to distinguish between the surfaces is necessary. In such a case, we introduce a new technique based on an anomalous diffusion coefficient which can differentiate the two surface pretreatments

A road map of the Chapter follows. First, the adhesive strength of sol-gel reinforced joints is tested as a function of surface roughness, cure temperature and film thickness.

From this study we find that thick, highly crosslinked films generally reduce the adhesive performance and it is shown to be directly related to the level of interpenetration of the epoxy into the sol-gel layer by conducting variable angle spectroscopic ellipsometry (VASE) on fracture surfaces. The remainder of the Chapter focuses on a detailed examination of the surface roughness generated on aluminum through grit-blasting and sanding. Finally a new technique to characterize surface roughness is proposed.

4.2. Experimental

The materials, sol-gel preparation procedures, preparation of ADCB samples and fracture testing were all the same as described in Chapter 3. The adhesive performance is again quantified by measuring the critical (G_c) and threshold (G_{th}) energy release rates. sol-gel films were dried at two temperatures, either 24°C, 50% RH for 75 minutes or 120°C for 30 minutes. These curing conditions will be represented by the abbreviations RT and OV in the text. Two different sol-gel concentrations were investigated. The first concentration refers to the standard sol-gel formulation described in detail in Appendix A. This concentration will be referred to as the x1 formulation throughout the Chapter. The second concentration contains 7 times the reactive components (GTMS+TPOZ) than in the x1 formulation and so will be designated as x7. The breakdown of components in the x7 solution is also shown in Appendix A. The x1 and x7 sol-gel formulations form films 50 and 310 nm thick on silicon wafers respectively (Chapter 2). In this study we do not refer to the coating with respect to thickness as it is not possible to measure the thickness of the sol-gel films on grit-blasted and sanded surfaces.

4.2.1 Surface Pretreatment

Four different surface pretreatments are used in this study; grit-blasting, sanding, Forest Product Laboratory etch (FPL) and polishing. Before each surface pretreatment, it is necessary to remove any organic contamination from the metal. First, the coupons are wiped with methyl ethyl ketone (MEK) and acetone until no organic residue can be seen on the wipe. Next, the coupons are submerged in a degreasing solution of Isoprep 44 at 60°C for 10 mins. Coupons are then rinsed with deionized water. The final surfaces should be water break free.

Grit-blasting is conducted in a chamber using 220 grit alumina. The grit is fluidized in pressurized air at a discharge pressure of 4.1 Bar. Grit-blasting is conducted for a total of 45s to ensure a uniform, reproducible surface. To remove any residual grit and organic contamination the samples are blown with compressed air and placed in a UV Ozone cleaner for 10 minutes.

FPL etch is conducted using the same procedure as outlined by Venables⁶. The aluminum coupons are immersed for 10 minutes in a solution of $\text{Na}_2\text{Cr}_2\text{O}_7 \cdot 2\text{H}_2\text{O}$, H_2SO_4 and H_2O in a weight ratio of 1:10:30. The solution is maintained at 68°C.

The polishing procedure uses an automatic polisher in a counter-clockwise rotation. Samples are first ground down using a 600 grit silicon carbide paper. Then the samples are polished with 6 μm , 1 μm and 1/4 μm diamond sprays to leave a mirror like surface. Between each polishing stage and after the final stage the samples are cleaned with ethanol. Prior to bonding, the samples are waved through the flame of a blow torch to remove any polishing residues¹².

Sanding is performed using a random orbital sander with 120 grit sand paper (Merit Abrasives), this type of sand paper minimizes the residue on the surface^{9,10}. The samples are sanded for a total time of 45 s. After sanding, samples are blown with compressed N₂ and placed in a UV Ozone cleaner for 10 minutes.

4.2.2 Characterization of surface roughness

Three techniques have been used to evaluate the surface roughness of the various pretreatments discussed above; atomic force microscopy (AFM, NanoDimension V), optical profilometry (Stil Micromesure), and interference optical profilometry (Zegage, Zometrics). Due to the roughness of the grit-blasted and sanded surfaces, AFM can only be used to characterize the polished surfaces. Optical profilometry has a height resolution of 10 nm, a lateral resolution of 2.5 μm and a scan length of 5 mm. Interference profilometry has a height resolution of 10 nm, and the lateral resolution and scan size are dictated by the objective used. The x10 objective has a lateral resolution of 0.8 μm and a scan size of 840 μm . The x50 objective has a lateral resolution of 0.16 μm and a scan size of 170 μm . The advantage of interference profilometry over optical profilometry is that it rapidly (2-3 minutes) generates a scan containing 1024 profiles, each profile containing 1024 points. The same size scan is not feasible on the optical profilometer. Both forms of optical profilometry ‘drop’ data when faced with a very steep surface feature. The amount of dropped data varies from scan to scan and is generally between 5-20%. These data points are filled using inbuilt software (ZMaps) which extrapolates the data from the surrounding points. It should be noted that

mechanical profilometers suffer from the same issue, but it is much harder to determine when you are visualizing the tip and not the surface.

4.2.3 Estimation of the Hurst exponent and fractal dimension for surface profiles

The Hurst exponent has recently gained favor over the more familiar fractal dimension to explain self affinity in naturally occurring systems. (H. E. Hurst developed the scaling technique, in 1965, to predict the water level in reservoirs²⁸.) Not only does the Hurst exponent provide information on the self affinity of a process it also contains information on any underlying correlation in the system. The fractal dimension can be calculated from the Hurst exponent through the simple equation²⁰

$$F_D = D - H \quad (4.1)$$

Where D , F_D and H are the number of dimensions in the system, fractal dimension and the Hurst exponent. Equation 4.1 assumes the real surface can be approximated by fractional Brownian motion (fBM)²⁰. The value of the fractal dimension or Hurst exponent for a surface can vary as a function of the method used to calculate it. For example, the value obtained using the method of box counting can vary depending on the geometry (such as aspect ratio) of the box used²⁰. Therefore, when computing the Hurst exponent, it is important to take advantage of more than one method. Four methods widely used to compute the Hurst exponent are the structure function (SF), standard deviation (SD), Z_{\max} and power spectrum (PS). The first 3 methods can be grouped under the more general heading of ‘variable bandwidth methods’. Different methods have different accuracies as a function of the actual value of H , the sample size and number of samples²⁹.

A statistically self affine profile is one that remains invariant under the following transformations in height (h) and position (x),

$$x \rightarrow \lambda x \quad (4.2)$$

$$h \rightarrow \lambda^H h \quad (4.3)$$

where H is the Hurst exponent. If a profile can be represented by these relations over a series of length scales, then we may say that the surface is statistically self affine. If a surface can be described by the transformations shown in equation 4.2 and 4.3, then it is possible to extract a value of the Hurst exponent for the surface.

The meaning of the numerical value of the Hurst exponent is more easily understood by considering the autocorrelation function. For the idealized case of fractional Brownian motion, which approximate most real situations, the autocorrelation function (normalized covariance on one data set) can be defined as²⁰,

$$C(t) = \frac{\langle [B_H(0) - B_H(-t)][B_H(t) - B_H(0)] \rangle}{\langle B_H(t)^2 \rangle} = 2^{2H-1} - 1 \quad (4.4)$$

where B_H is the displacement at time t of a Brownian particle following a trajectory governed by a given Hurst exponent H. We note here that for surface profiles the time parameter t can be replaced with a spatial coefficient x with no loss of generality of equation 4.4. For standard Brownian motion consisting of independent steps, the value of H is 0.5. Substituting this into equation 4.4 gives the expected result of $C(t)=0$ because true Brownian motion should be uncorrelated. When $H > 1/2$ we have persistence, which means an increasing trend in the past will yield an increasing trend in the future. When $H < 1/2$ we have antipersistence, which means an increasing trend in the past will give a decreasing trend in the future. Current work in bulk fracture reports a value of H for the

fracture surfaces ranging between 0.77-0.8 for the fracture surfaces¹⁹, suggesting persistence. The origin of this effect is still not fully understood. The four methods used to calculate H outlined above will now be considered individually.

4.2.3.1 Structure Function

The structure function was first defined by Sayles *et al.*³⁰ for use in evaluating the roughness of rock profiles.

$$SF(\Delta x) = \langle (h(\Delta x + x) - h(x))^2 \rangle_x \quad (4.5)$$

where Δx represents the size of the measurement window. The structure function is then related to the Hurst exponent through the following relation³¹,

$$SF \sim \Delta x^{2H} \quad (4.6)$$

Therefore, a plot of $\ln(SF)$ vs. $\ln(\Delta x)$ is expected to produce a straight line of gradient $2H$. The computational method for estimating the SF from a profile begins by placing a window of width Δx across the region $x=0$ to $x= \Delta x$. The value of $h(\Delta x+x)-h(x)$ is calculated, the window is then shifted to the next data point and the process repeated for the entirety of the profile. If only one profile is to be considered, then the mean is calculated across all windows of width Δx . After one Δx set is evaluated, the program defines the next window size and repeats for all possible window sizes. If multiple profiles are to be evaluated, the mean for a given Δx is calculated from all the SF measurements across all the profiles. It should be noted here that taking the average over multiple realizations yields a better fit and more reliable value of H by effectively reducing the noise in the sample.

4.2.3.2 Standard Deviation

The Standard Deviation method calculates the standard deviation across each window of size Δx across the profile. The standard deviation values are then averaged for each window size across the profile over all profiles. The following equation describes the standard deviation method.

$$SD(\Delta x) = \left\langle \left(\frac{\sum h(x')_{x \leq x' \leq x + \Delta x} - \bar{h}_{x \leq x' \leq x + \Delta x}}{N_{x \leq x' \leq x + \Delta x} - 1} \right)^2 \right\rangle_x \quad (4.7)$$

The SD is related to Δx in the following manner²⁹

$$SD \sim \Delta x^H \quad (4.8)$$

The SD function is evaluated over all possible window sizes and position as described for the structure function method, section 4.2.3.1. The SD method is included here for completeness, but it is not used to study the grit-blasted and sanded surfaces due to excessive computational time and a reputation to be unreliable¹¹.

4.2.3.3 Z_{\max}

The Z_{\max} method calculates the range of each window of size Δx across the profile. The Z_{\max} values are then averaged for each window size across the profile over all profiles. The following equation describes the method:

$$Z_{Max}(\Delta x) = \langle \text{Max}\{h(x')\}_{x \leq x' \leq x + \Delta x} - \text{Min}\{h(x')\}_{x \leq x' \leq x + \Delta x} \rangle_x \quad (4.9)$$

Z_{\max} is related to Δx in the following manor²⁹

$$Z_{Max} \sim \Delta x^H \quad (4.10)$$

The Z_{\max} function is evaluated over all possible window sizes and position as described for the structure function method, section 4.2.3.1.

4.2.3.4 Power Spectrum

The final important method used to estimate the Hurst exponent is the power spectrum. Because this method converts the data into the frequency space, it inherently views the results without the cumbersome sliding of an observation window across the profile. Thus, the power spectrum has the distinct advantage of greatly reduced computational times. The discrete Fourier transform (DFT) of our data set is defined as,

$$C_k = \sum_{j=0}^{N-1} x_j e^{2\pi ijk/N} \quad k = 0, \dots, N-1 \quad (4.11)$$

where N is the number of points in the set. The power spectrum is then defined from the following equations:³²

$$P(0) = P(f_0) = \frac{1}{N^2} |C_0|^2 \quad (4.12)$$

$$P(f_k) = \frac{1}{N^2} [|C_k|^2 + |C_{N-k}|^2] \quad k = 1, 2, \dots, \left(\frac{1}{N^2} - 1\right) \quad (4.13)$$

$$P(f_c) = P(f_{N/2}) = \frac{1}{N^2} |C_{N/2}|^2 \quad (4.14)$$

At this point it is important to make two points regarding the computation of the power spectrum. First, this method approximates the power spectrum as a series of ‘square’ bins, which can cause an error in the analysis as one frequency can ‘leak’ into adjacent bins, skewing the result. More advanced windowing techniques are available, however, the sample size is most likely the limiting factor in the present case not the square bin approximation. Second, most computer software packages (Matlab, Origin etc.) use the fast fourier transform (FFT) algorithm to calculate the DFT. Use of the FFT algorithm requires the size of the data to be a power of 2, therefore, unless told otherwise, most

softwares will ‘pad’ the data set with zeros to achieve the desired size. This addition to the data set must be taken into account when normalizing the data with N . The Hurst exponent can be found from the power spectrum via the following relation^{20,33},

$$P(f) \sim f^{-2H-1} \quad (4.15)$$

4.2.4 Evaluation of the effectiveness of the different methods used to estimate the Hurst exponent

The accuracy of the above methods must be considered when calculating the Hurst exponent for a given system. Schmittbuhl *et al.*²⁹ showed that different methods have different accuracies based on the value of the Hurst exponent and the size of the data set. For example, the Zmax method was found to estimate well the Hurst exponent in the range 0.6-0.8, but yielded large errors for $H < 0.4$. In the same work, it was also found that the size of the data set is very important, i.e. a large number of statistics is necessary for these methods to approximate the actual Hurst exponent²⁹. The size of the scan taken by the interference profilometer limits the available statistics. Per scan, the profilometer takes 1024 line scans, each containing 1024 points. The data sets considered by Schmittbuhl *et al.*²⁹ consisted of 100 independently generated profiles of different sizes. As the profiles obtained from the profilometer’s scan represent an area of the surface, we cannot assume that the profiles are statistically independent from one another. This issue is resolved by generating surfaces with a range of fractal dimensions and by studying the validity of the methods outlined in sections 4.2.3.2-4 on these surfaces. To this end, we simulated surfaces using values of the Hurst exponent ranging from 0.1 to 0.9. These surfaces are generated using the midpoint method¹⁸, which is a simple technique used to approximate fractional Brownian motion. We will first describe how this technique is

used to generate a profile and then extend it to a surface. To generate a profile, the midpoint method uses equation 4.16²⁹:

$$h_{\frac{i+j}{2}} = \frac{1}{2}(h_i + h_j) + |i - j|^H N(0, \sigma) \quad (4.16)$$

Where h , i , j , H and N are the height, first x coordinate, second x coordinate, Hurst exponent and a random number from a Gaussian distribution of zero mean and standard deviation σ respectively. The midpoint method displaces the midpoint between two points by taking the height average of the 2 points, as indicated by the first term of equation 4.16. The height average is then added to a random value, which has been scaled by distance between the two points and the Hurst exponent (second term of equation 4.16). This dividing process continues until the desired profile is reached. The aim of this process is to produce a profile with the following variance function,

$$\text{var}(h(x_2) - h(x_1)) = |x_2 - x_1|^{2H} \sigma^2 \quad (4.17)$$

While the midpoint method is widely used to simulate fractal profiles and to test the reliability of self affine measurements²⁹, it should be noted that it sacrifices mathematical purity for ease of implementation. Therefore, the value generated in each step are non-stationary, which can lead to profiles that are ‘unnatural’ in appearance¹⁸. Equations 4.16 and 4.17 yield the standard result for Brownian motion when $H=0.5$. Figure 4.2 shows profiles of fractional Brownian motion generated using the midpoint method in Matlab. The effect of the Hurst exponent on the profile is clearly evident, the lower the Hurst exponent the ‘rougher’ the profile appears. These profiles are generated using 1024 points to simulate the amount of data generated in a typical profilometry scan. The midpoint displacement technique can be extended to produce a surface by adopting the

square and diamond technique^{11,18}. Figure 4.3 shows the first 5 steps of this procedure. Firstly a square of dimensions 2^N-1 is chosen and the four corner values are given from a random number generator. The center point of the square is then the mean of the four corners plus a random value scaled with the width of the square and the Hurst exponent, this procedure has the same form as equation 4.16. Step 2 is the diamond step, the points in the center of the diamonds are then displaced by the mean of the four corners plus a random value scaled with the width of the edge of the diamond and the Hurst exponent. The process is then repeated until all points in the square are filled. Figure 4.3 shows the first 5 steps of this process. For points on the edge, the value is assigned by using the mean of the 3 surrounding points. Three selected surfaces that were generated using this method with differing Hurst exponents are displayed in Figure 4.4. Having established a method to generate surfaces with different Hurst exponents, the accuracy of the SF, Z_{\max} and power spectrum techniques will be assessed.

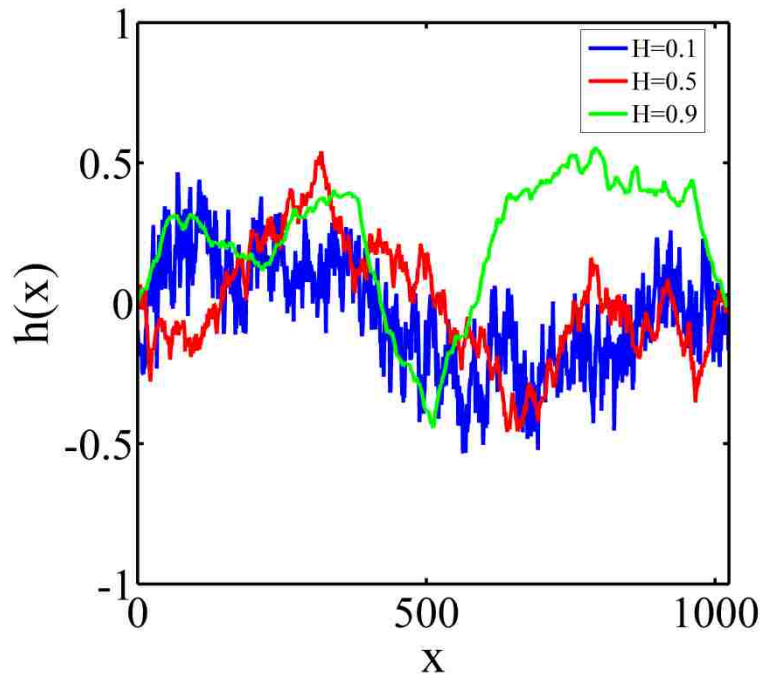


Figure 4.2: Height profiles generated using the midpoint technique with different values of the Hurst exponent.

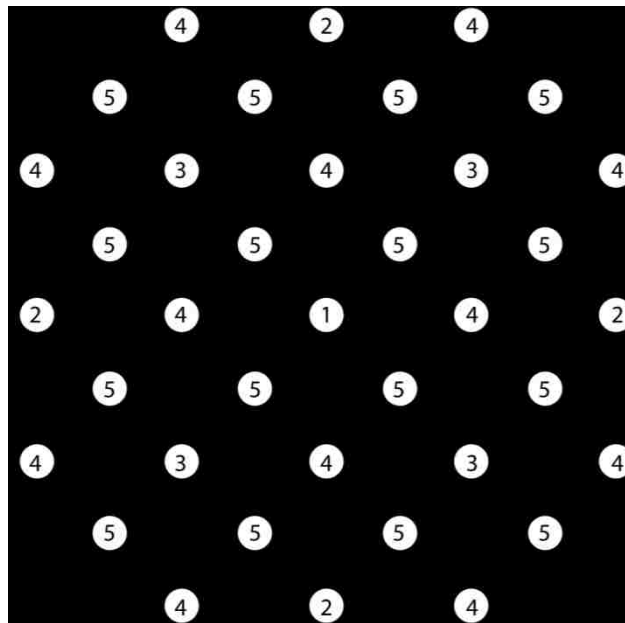


Figure 4.3: Illustration of the midpoint displacement technique used to generate a fractal surface. Keeping the corner points fixed the points are randomly displaced in the z direction (orthogonal to the plane of the page) according to the method outlined in the text. The numbers represent the order of the displacements. Figure adapted from Ref .11

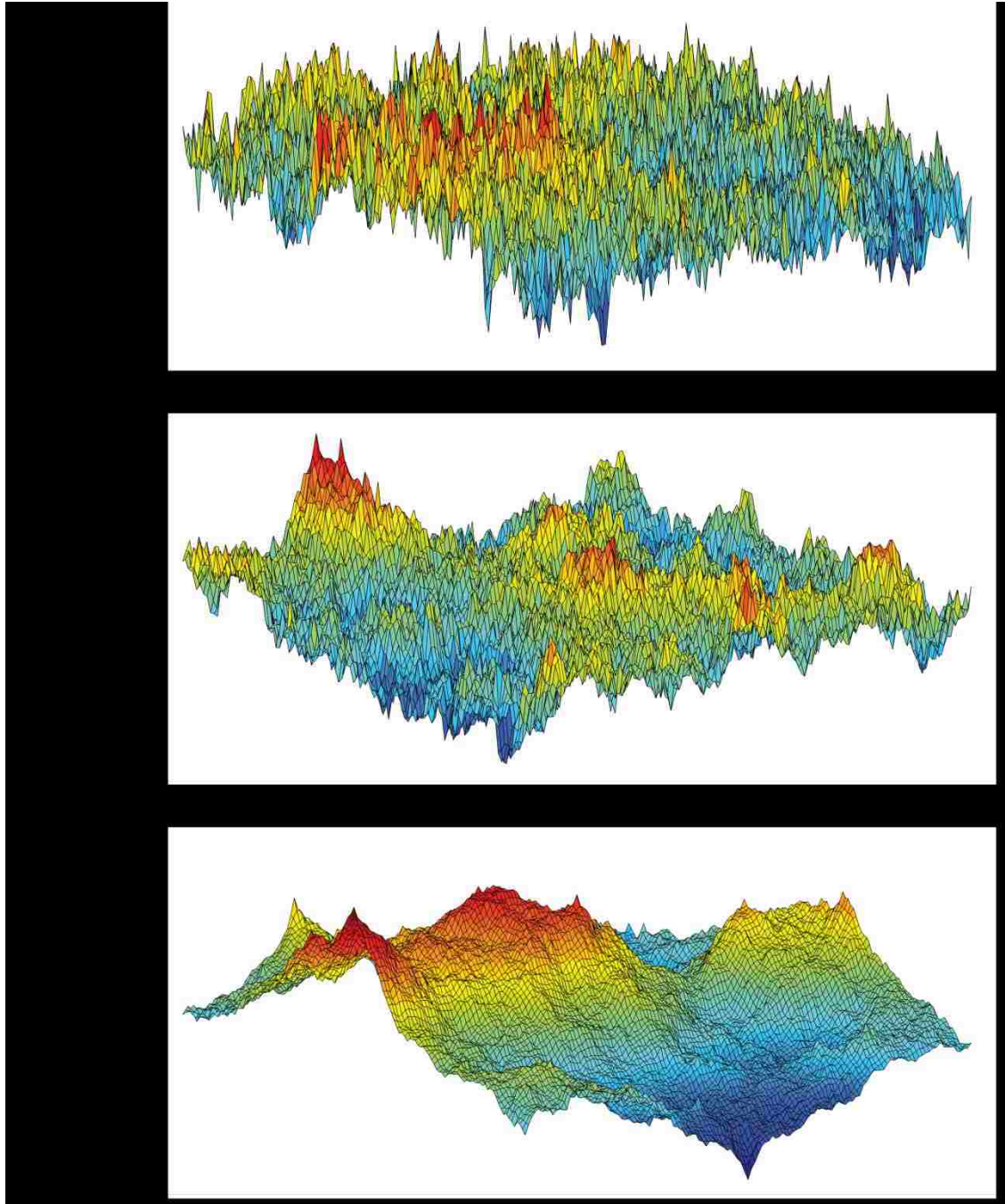


Figure 4.4: Fractal surfaces generated using the midpoint technique with different values of the Hurst exponent.

Surface profiles containing 1025 by 1025 points are generated to mimic the typical data set obtained from a scan using the interference profilometer. Profiles are generated for 9 different values of the Hurst coefficient ranging from 0.1 to 0.9. These surfaces are analyzed using the SF, Z_{\max} and PS techniques outlined in the previous sections. The Hurst exponent estimated using these techniques is then plotted vs. the Hurst exponent used to construct the surfaces, Figure 4.5.

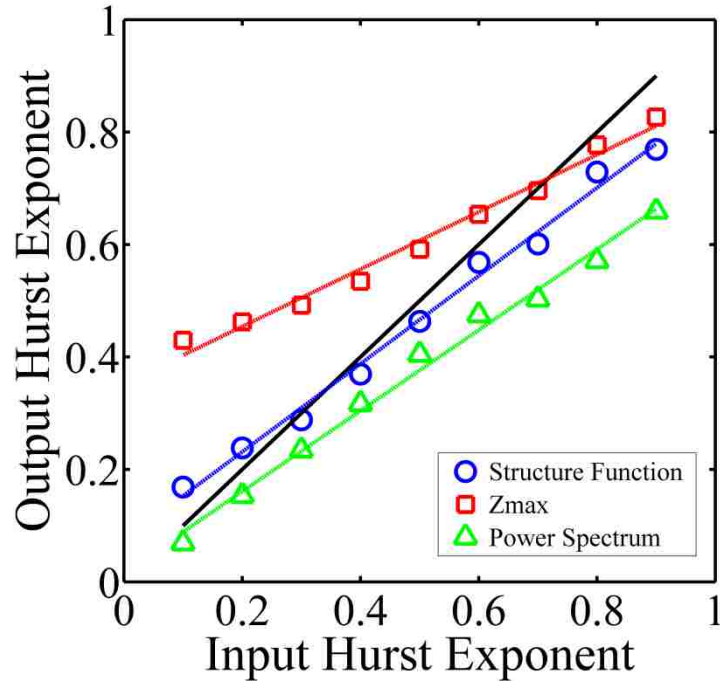


Figure 4.5: Comparison of the output Hurst exponent obtained from the self affine analysis and the input Hurst exponent used to simulate the surfaces shown in Figure 4.4. Three different analysis procedures were investigated, structure function (blue circles), Z_{\max} (red squares) and the power spectrum (green triangles). The details of these procedures are outlined in the text. The dependence of the output exponent on the input can be approximated with a linear fit using a least squares regression. The SF yields the following dependence $H_{\text{Out}}^{\text{SF}}=0.8H_{\text{In}}+0.08$. The Z_{\max} analysis gives $H_{\text{Out}}^{\text{Zmax}}=0.5H_{\text{In}}+0.4$. Finally the power spectrum results can be approximated by $H_{\text{Out}}^{\text{PS}}=0.7H_{\text{In}}+0.02$.

From Figure 4.5 we observe that the SF analysis is generally the most accurate for predicting the Hurst exponent in the region $H < 0.6$. The Z_{\max} analysis is the most accurate in the range $H > 0.6$. The power spectrum predicts a Hurst exponent that is below the actual value and error is exacerbated with increasing values of H . The general trend of these results matches the results of Schmittbuhl *et al.*²⁹. Their findings indicated the variable band width methods (SF, SD and Z_{\max}) to be mainly sensitive to the value of the Hurst exponent, while the power spectrum is more sensitive to the size of the data set²⁹. From the current simulation, we conclude that the SF and Z_{\max} methods are the most suitable for the scan sizes available from the interference profilometer. The dependence of the output Hurst exponent on the input value can be closely approximated with a linear fit, Figure 4.5.

4.2.5 The Lacunarity and Topothesy

To this point we have only considered the value of the exponent in the power law expression in equations 4.6, 4.8, 4.10 and 4.15. As will be shown in the results section, it is also important to consider the coefficient of proportionality to determine a characteristic length scale for the surface. Changes in the value of this coefficient are effected using the midpoint displacement method. To do so requires that the standard deviation of the random number added in each step be scaled to change the displacement magnitude. Adjusting equation 4.16 accordingly we get,

$$h_{\frac{i+j}{2}} = \frac{1}{2}(h_i + h_j) + \alpha|i - j|^H N(0, \sigma) \quad (4.18)$$

where α is the scaling factor. Figure 4.6 shows the effect of changing the value of alpha on 3 profiles generated with the same Hurst coefficient of 0.8. Mandelbrot³⁴ has proposed a term called the ‘Lacunarity’ to take this effect into account. However, no meaningful interpretation has been developed¹¹. Another method used to provide meaning to this value is the topothesy, Λ ³⁵ of a surface. The formal definition of the topothesy in terms of the structure function is given in equation 4.19,

$$\frac{SF(\Lambda)}{\Lambda} = \frac{\langle (h(\Lambda + x) - h(x))^2 \rangle_x}{\Lambda} = 1 \quad (4.19)$$

Inserting this definition into equation 4.6 we arrive at equation 4.20 for the structure function³⁶.

$$SF = \Lambda^{2-2H} \Delta x^{2H} \quad (4.20)$$

The topothesy is formally defined as the distance along a profile for which the expected angle between two points is one radian. For most surfaces, this distance corresponds to a length scale below the resolution of the instrument used to measure the surface. In some cases it gives a length scale smaller than the atoms which make up the material¹¹. It is difficult then to attribute a physical meaning to the topothesy. In the results section, we will introduce a new description for the Lacunarity based on an anomalous diffusion coefficient.

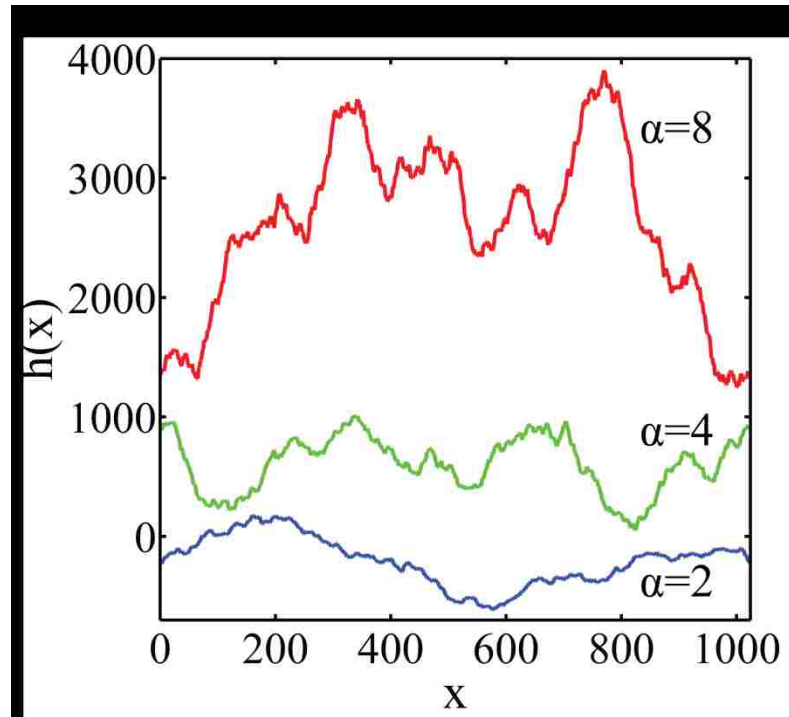


Figure 4.6: Three fractal profiles generated with a Hurst exponent of 0.8 and three different values of α . The lacunarity of the profiles is changed by using a different value of α in equation 4.18 used to generate the profiles. The values of alpha used are displayed next to the corresponding profile. Each profile is generated with a different realization of random numbers. In the interest of clarity the profiles are displaced by an arbitrary shift in the direction of the y co-ordinate.

4.3. Results and Discussion

4.3.1 Effect of sol-gel cure temperature and film thickness on the strength of Epoxy/sol-gel/Aluminum joints.

4.3.1.1 Grit-blasted Substrates

Figure 4.7 shows the effect of sol-gel cure temperature and film thickness on the critical and threshold energy release rates of an epoxy/sol-gel/grit-blasted Aluminum joint. Film thickness is altered by varying the concentration of precursors in the sol, as described in the experimental section. Two different cure conditions were investigated either 120 °C for 30 minutes or at room temperature for 75 minutes. The critical fracture

energy (G_c) of these joints is shown in Figure 4.7b. For x1 sol-gel films, the G_c increases with increased cure temperature. While for x7 sol-gel films, no statistical difference in G_c is observed with elevated cure temperature. From a design stand point, the threshold fracture energy (G_{th}) is generally of greater importance than G_c . The results for G_{th} are presented in Figure 4.7c. For both the x1 and the x7 films, G_{th} increases significantly with an increase in sol-gel cure temperature. The importance of this result is to show that for grit-blasted surfaces, increased cross link density in the sol-gel film improves resistance to hydrolytic degradation of the adhesive joint. In addition, it suggests that the sol-gel film cannot cross link fully during the elevated epoxy cure temperature. It is expected that as the cross link density of the sol-gel film is increased, the level of interpenetration into the epoxy film is decreased^{12,37}. Therefore, for this set of processing parameters we conclude that the dominant adhesion promoting mechanisms for grit-blasted surfaces are the density of epoxy functional groups on the surface of the sol-gel film and the macroscale surface roughness.

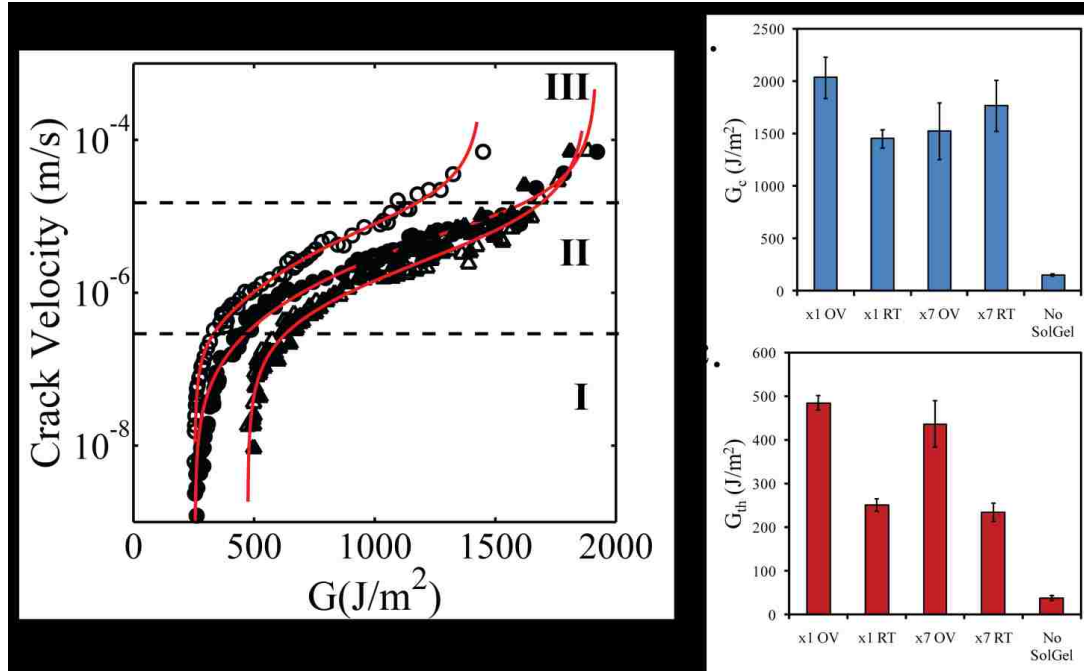


Figure 4.7: a. Crack velocity vs. energy release rate (G) for epoxy/sol-gel/grit-blasted-aluminum joints prepared with different sol-gel formulations and cure temperatures. Open circles and open triangles represent films cast from a x1 formulation cured at room temperature (RT, 75 mins) and 120 °C (OV, 30 mins) respectively. Filled circles and filled triangles represent films cast from a x7 formulation cured at room temperature (RT, 75 mins) and 120 °C (OV, 30 mins) respectively. See section 4.2 in the text for a detailed description of the x1 and x7 formulations. Three regions of subcritical crack growth are identified. The red lines represent a least-squares regression fit of equation 3.2 to the data. b. Critical energy release rates (G_c) for epoxy/sol-gel/grit-blasted-aluminum joints prepared with different sol-gel formulations and cure temperatures. c. Threshold energy release rates (G_{th}) for epoxy/sol-gel/grit-blasted-aluminum joints prepared with different sol-gel formulations and cure temperatures.

4.3.1.2 FPL etched Substrates.

Next, the effect of film thickness and cure temperature on FPL etched surfaces was investigated and the results are presented in Figure 4.8. While FPL etching is no longer widely used, it still provides an ideal model system with which to study the effects of micro surface roughness on adhesion. For x1 sol-gel films on FPL etched aluminum, the sol-gel film curing temperature only has a minor effect on G_c , as shown in Figure 4.8.

However, a significant effect is noticed for the x7 films. Both G_c and G_{th} drop significantly upon raising the sol-gel cure temperature; the opposite effect than that seen for the grit-blasted surfaces. It is likely that when curing these thicker films at 120 °C, the epoxy is no longer able to diffuse through the sol-gel film and into the micropores formed by the FPL etch, thus, reducing the adhesive strength of the joint. A high value of G_c is obtained for x7 coatings cured at room temperature, implying that the epoxy can diffuse into the coating and hence into the pores on the aluminum surface forming a strong mechanically interlocked interface.

4.3.1.3 Polished Substrates.

Figure 4.9 displays the critical and threshold fracture energies of Epoxy/sol-gel/polished-Al surfaces for different sol-gel curing temperatures and thicknesses. In contrast to the grit-blasted and FPL etched surfaces, the x1 high cure temperature (120 °C for 30 mins) films significantly reduced the critical and threshold fracture energies of the joint. Increasing the thickness of the high cure temperature films to ~120 nm (x3) and ~250 nm (x7) caused a catastrophic drop in both the critical and threshold adhesive energies. The critical fracture energy for these joints is essentially the same as a joint untreated with the sol-gel solution. Increased crosslink density of the sol-gel film causes a significant drop in the adhesion promoting characteristics for polished surfaces.

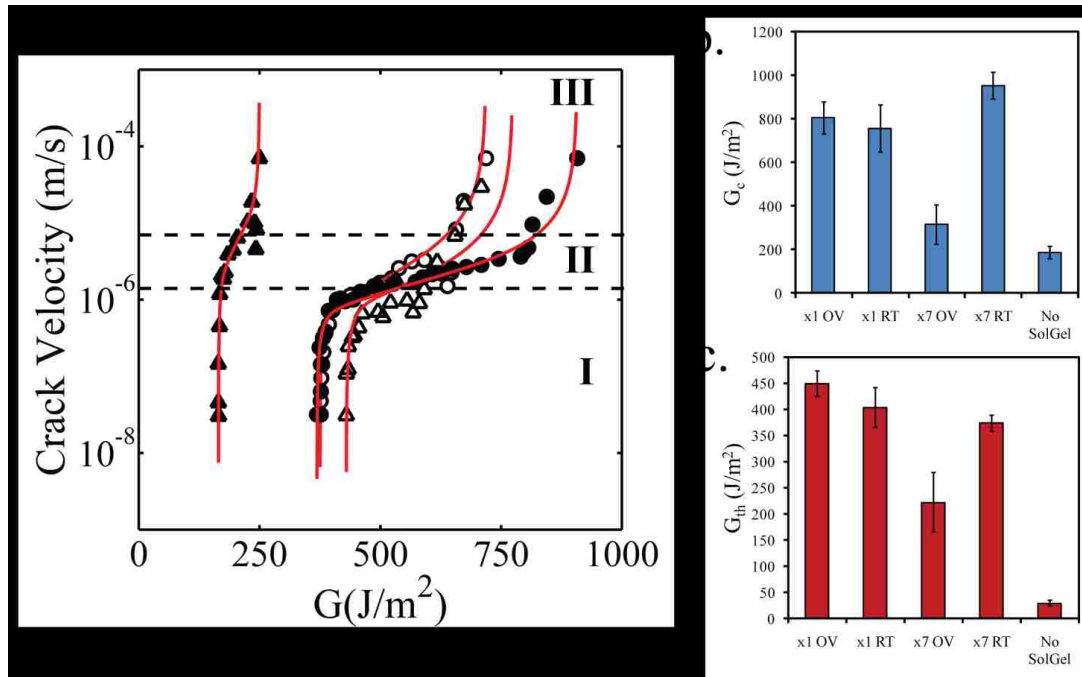


Figure 4.8: a. Crack velocity vs. energy release rate (G) for epoxy/sol-gel/FPLetched-aluminum joints prepared with different sol-gel formulations and cure temperatures. Open circles and open triangles represent films cast from a x1 formulation cured at room temperature (RT, 75 mins) and 120 °C (OV, 30 mins) respectively. Filled circles and filled triangles represent films cast from a x7 formulation cured at room temperature (RT, 75 mins) and 120 °C (OV, 30 mins) respectively. See section 4.2 in the text for a detailed description of the x1 and x7 formulations. Three regions of subcritical crack growth are identified. The red lines represent a least-squares regression fit of equation 3.2 to the data. b. Critical energy release rates (G_c) for epoxy/sol-gel/ FPLetched-aluminum joints prepared with different sol-gel formulations and cure temperatures. c. Threshold energy release rates (G_{th}) for epoxy/sol-gel/ FPLetched-aluminum joints prepared with different sol-gel formulations and cure temperatures.

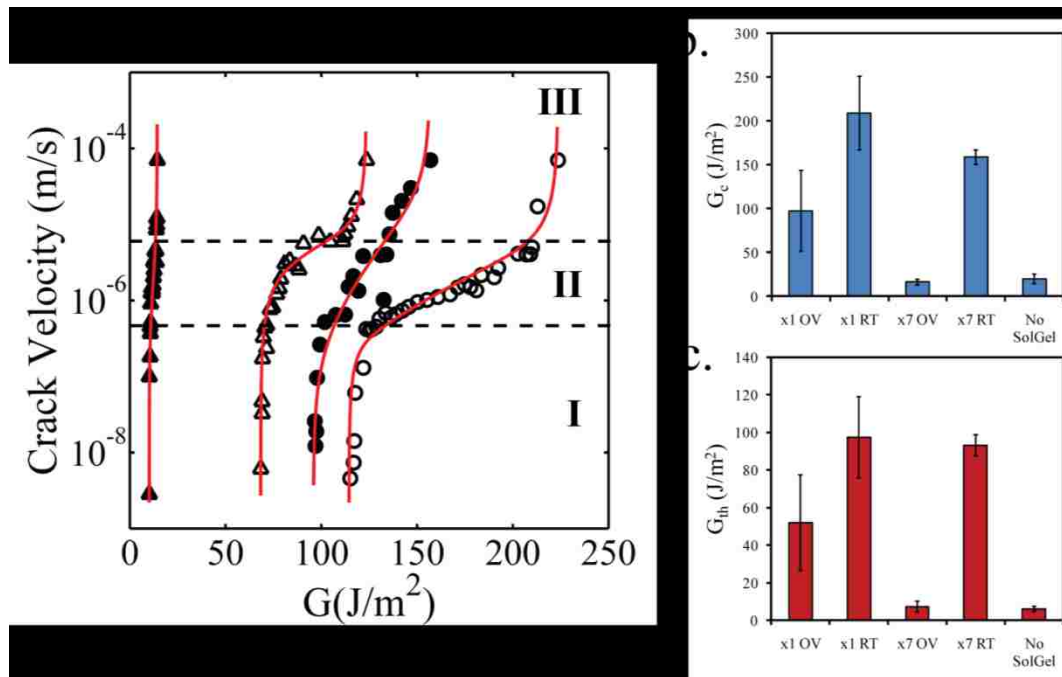


Figure 4.9: a. Crack velocity vs. energy release rate (G) for epoxy/sol-gel/polished-aluminum joints prepared with different sol-gel formulations and cure temperatures. Open circles and open triangles represent films cast from a x1 formulation cured at room temperature (RT, 75 mins) and 120 °C (OV, 30 mins) respectively. Filled circles and filled triangles represent films cast from a x7 formulation cured at room temperature (RT, 75 mins) and 120 °C (OV, 30 mins) respectively. See section 4.2 in the text for a detailed description of the x1 and x7 formulations. Three regions of subcritical crack growth are identified. The red lines represent a least-squares regression fit of equation 3.2 to the data. b. Critical energy release rates (G_c) for epoxy/sol-gel/polished-aluminum joints prepared with different sol-gel formulations and cure temperatures. c. Threshold energy release rates (G_{th}) for epoxy/sol-gel/polished-aluminum joints prepared with different sol-gel formulations and cure temperatures.

4.3.1.4 120 grit sanded Substrates.

Fracture experiments were extended to 120 grit sanded surfaces. The results are shown in Figure 4.10. As with the FPL and grit-blasted surfaces, oven curing the x1 sol-gel formulation produced joints with a higher threshold fracture energy than the equivalent room temperature cured film. This finding suggests that the highly crosslinked sol-gel layer is more stable to hydrolytic attack. Also of importance is the observation that, as opposed to the grit-blasted surface results, the fracture energy of the x7 oven cured sol-gel joint decreases dramatically. Both surfaces display a roughness on the macro-scale, so this parameter alone is not responsible for changes in the performance of the x7 oven cured sol-gel film. The x7 oven cured sol-gel film is expected to be both a good barrier coating and adhesion promoter only on grit-blasted surfaces. It is, therefore, important to understand how the fracture energy is influenced by the relationship between the different surface morphologies and the oven curing of the sol-gel film. In addition, the grit-blasted joints are considerably stronger than the sanded surfaces. These issues will be addressed in the detailed analysis of surface roughness which begins at section 4.3.4.

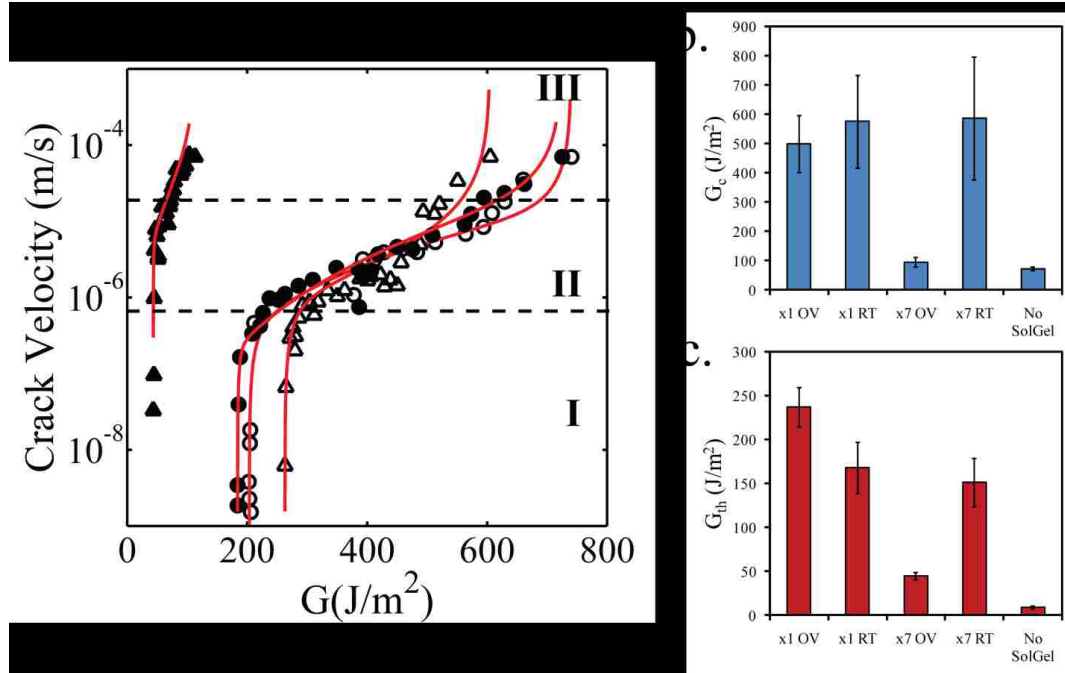


Figure 4.10: a. Crack velocity vs. energy release rate (G) for epoxy/sol-gel/120grit-sanded-aluminum joints prepared with different sol-gel formulations and cure temperatures. Open circles and open triangles represent films cast from a x1 formulation cured at room temperature (RT, 75 mins) and 120 °C (OV, 30 mins) respectively. Filled circles and filled triangles represent films cast from a x7 formulation cured at room temperature (RT, 75 mins) and 120 °C (OV, 30 mins) respectively. See section 4.2 in the text for a detailed description of the x1 and x7 formulations. Three regions of subcritical crack growth are identified. The red lines represent a least-squares regression fit of equation 3.2 to the data. b. Critical energy release rates (G_c) for epoxy/sol-gel/120grit-sanded-aluminum joints prepared with different sol-gel formulations and cure temperatures. c. Threshold energy release rates (G_{th}) for epoxy/sol-gel/120grit-sanded-aluminum joints prepared with different sol-gel formulations and cure temperatures.

4.3.2 Origin of fracture in Epoxy/Sol-gel/Polished Aluminum joints

Increasing the curing temperature for a x7 sol-gel film caused a significant decrease in the adhesive performance for polished, FPL etched and sanded surfaces (section 4.3.1). To examine this effect in more detail, we focus on samples prepared with polished aluminum, where the drop in adhesive performance is the most prominent. Variable

angle spectroscopic ellipsometry (VASE) is used to estimate the sol-gel film thickness on the epoxy and aluminum surfaces after fracture. The fracture surfaces of 3 different sol-gel film thicknesses (x1, x3, x7) and 2 curing conditions (room temperature for 75 minutes and 120°C for 30 minutes) are studied. Table 4.1 reports the thickness of the sol-gel film on the aluminum before bonding and on the aluminum and epoxy fracture surfaces. All scans are taken in the subcritical crack growth region close to the crack tip. No film is detectable on the aluminum surface after fracture for every oven cured film. Sol-gel is detected on the epoxy fracture surface and correlates closely with the sol-gel thickness on the aluminum surface prior to fracture, table 4.1. This strongly implies that the fracture is occurring very close to the Al/sol-gel interface which agrees with XPS data for similar systems⁸. AFM scans of the fracture surfaces (Figure 4.11) further support this conclusion as only the roughness left from the polishing process is observable. The strong correlation between the sol-gel thickness on the aluminum prior to bonding and the thickness on the epoxy fracture surfaces implies that the interpenetration into the epoxy is minimal for oven cured films. If the ellipsometric fit is altered to allow for an interdiffuse region, a better fit of the spectra is not achieved. Despite this low interpenetration the weak interface is still close to the Al/sol-gel interface not the sol-gel/Epoxy interface. This suggests that a low level of interpenetration and/or chemical crosslinking must occur between the sol-gel and the epoxy.

For the room cured sol-gel films either a very thin 2-3 nm thick layer of sol-gel is detected on the aluminum or epoxy surfaces or no evidence of the film is found. Therefore, the epoxy is able to penetrate deep into the sol-gel layer very close to the aluminum surface. This short ellipsometric study proves that the interpenetration of the

epoxy into the sol-gel film is significantly altered as we increase the film curing temperature. Next we will use this information along with the fracture results to summarize the results for sol-gel reinforced joints.

Sol gel Coating Concentration	Coating thickness on Al (nm) prior to bonding	Al fracture side sol-gel thickness (nm)	Epoxy Fracture side sol-gel Thickness (nm)
X1 OV	37	0	21
X3 OV	120	0	108
X7 OV	253	0	254
X1 RT	53	0	4
X3 RT	158	2	3
X7 RT	345	0	No fit, but evidence of a film present

Table 4.1: Thickness of sol-gel films on aluminum, and on aluminum and epoxy fracture surface of x1, x3 and x7 sol-gel reinforced epoxy/sol-gel/aluminum joints. Measurements are conducted in the subcritical crack growth regions close to the crack tip.

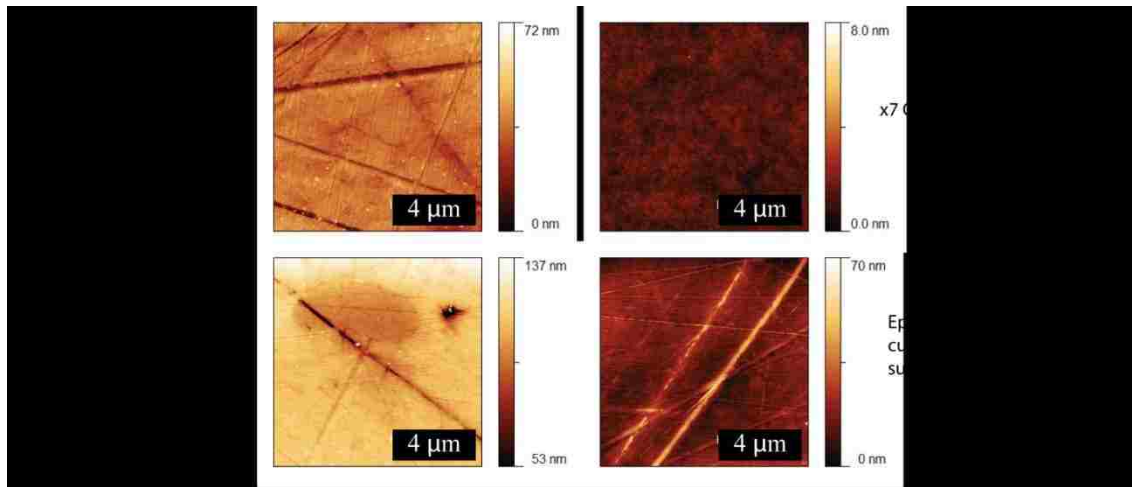


Figure 4.11: AFM of uncoated polished aluminum (top left), polished aluminum coated with x7 sol-gel solution (top right), Aluminum fracture side of a x7 oven cured reinforced joint, (bottom left), Epoxy fracture side of a x7 oven cured reinforced joint, (bottom right). Oven cured refers to a cure cycle of 120 °C for 30 minutes.

4.3.3 Summary of fracture results

The key finding in the previous section is that the fracture energy of an epoxy/sol-gel/aluminum joint depends strongly on the interplay of the surface roughness, sol-gel concentration and curing temperature. For grit-blasted surfaces increasing the cure temperature of the sol-gel film increases both the critical (G_c) and threshold (G_{th}) fracture energies of the joint, Figure 4.7. This result agrees with the optimum curing procedure for GTMS on grit-blasted surfaces reported in the literature³⁸. Increasing the sol-gel concentration causes a small drop in the joint strength. For sanded surfaces with sol-gel films cast from a x1 solution, the room cured films exhibit a higher value of G_c but a lower value of G_{th} than the oven cured films. Sanded surfaces underperform the grit-blasted surfaces by a factor of 2-4 depending on the sol-gel concentration and curing temperature. For these sanded surfaces, oven curing a sol-gel film cast from a x7 solution causes a dramatic drop in the adhesive strength of the joint, Figure 4.10. A similar effect is observed for the FPL etched and the polished surfaces. On polished surfaces, oven curing the sol-gel film at all concentrations tested lead to a reduction in the adhesive performance. This is in agreement with similar systems in the literature³⁹. Therefore, we can conclude that the optimum curing temperature for an x1 sol-gel film is 120°C on grit-blasted or porous substrates, but room temperature on polished surfaces. This effect of surface roughness on the optimal cure temperature explains some of the discrepancies noted by Abel *et al.*¹ and so the roughness should always be considered simultaneously with the curing temperature of the sol-gel film. Not only does the scale of the roughness (i.e. macro vs. micro) alter the adhesive performance, but also the type of the roughness plays a significant role. For the remainder of this Chapter, the difference

between the macro-rough surface pretreatments (grit-blasting and sanding) will be studied in detail.

4.3.4 Evaluation of the Hurst Exponent on Grit-blasted and Sanded surfaces

The fracture results presented in section 4.3.1 raise a number of important questions with regards to the optimal sol-gel film thickness as a function of curing temperature. The remainder of this Chapter shall address one of these questions; why do grit-blasted surfaces outperform sanded surfaces. Both pretreatments generate micro rough surfaces, yet sanded surfaces underperform grit-blasted ones, as shown in this work and elsewhere¹². Previous works that have attempted to relate the adhesive performance of macro rough surfaces through RMS have been unsuccessful¹²⁻¹⁵. Relating the fractal dimension of the surface to the adhesive performance has been attempted by several researchers^{12-14,40}. In some cases the fractal dimension technique is successful; the higher the fractal dimension, i.e. the more tortuous the surface, the higher the fracture toughness. This interpretation seems reasonable from a fracture mechanics view point as causing a crack to change direction alters the energy release rate⁴¹.

Fracture of bulk materials has been narrowing in on a universal Hurst Exponent constant for a range of materials. Both grit-blasting and sanding processes are examples of fracture occurring at the interface of a material. Grit-blasting can be likened to typical erosion processes and sanding to a high rate scratching process. If a universal Hurst exponent exists for the bulk then one may expect it to hold for the surface also. Through this reasoning, one would expect the fractal dimension of grit-blasted and sanded surfaces to be equal. This statement is somewhat contrary to the results reported in the literature

and this section will address this discrepancy through detailed evaluation of the surface of grit-blasted and sanded aluminum.

4.3.4.1 Evaluation of different measurement techniques to determine the Hurst Exponent

Figure 4.12 highlights the effect of measurement step size on the structure function for grit-blasted and sanded surfaces. The linear region of the structure function in Figure 4.12 represents the region where the surface can be modeled using equation 4.6. Within this region, the surface exhibits self-affine behavior. Fitting a straight line through the linear regions of Figure 4.12 the Hurst exponents for the different step sizes are found to be $H_{0.16 \mu\text{m}}=0.61$, $H_{0.8 \mu\text{m}}=0.68$ and $H_{2.5 \mu\text{m}}=0.24$ for grit-blasted surfaces and $H_{0.16 \mu\text{m}}=0.60$, $H_{0.8 \mu\text{m}}=0.67$ and $H_{2.5 \mu\text{m}}=0.33$ for sanded surfaces. For the grit-blasted surfaces, the self-affine region ends at a length scale of $\sim 10 \mu\text{m}$, independent of the technique used to measure it. The self affine region on the sanded surfaces extends to a length of $\sim 20 \mu\text{m}$, Figure 4.12b. The difference between these length scales could be due to the difference in the grit size between the sanding and grit-blasting technique. This will be elaborated on in the next section. Towards the end of the profiles shown in Figure 4.12, the SF becomes wavy; this is a sign of insufficient statistics available at large window sizes.

The same set of profilometry data was analyzed using the Z_{Max} technique, Figure 4.13. Fitting a straight line through the linear regions of Figure 4.13 the Hurst exponents for the different step sizes are found to be $H_{0.16 \mu\text{m}}=0.78$, $H_{0.8 \mu\text{m}}=0.83$ and $H_{2.5 \mu\text{m}}=0.61$ for grit-blasted surfaces and $H_{0.16 \mu\text{m}}=0.75$, $H_{0.8 \mu\text{m}}=0.77$ and $H_{2.5 \mu\text{m}}=0.57$ for sanded surfaces. Unlike the SF analysis, the Z_{max} analysis provides evidence for self affine behavior across the entire profile. This behavior can be broken up into two distinct regions represented

by the two linear regions in the Z_{\max} curves, Figure 4.13. Two regions in the Z_{\max} analysis have been previously observed for the self affine behavior of a crack travelling through a sheet of paper⁴². It was suggested that the transition is caused by a cross over between 3D fracture surfaces at small scales and two-dimension crack lines at large scales. Such a cross over is unlikely to be the case in our situation as the geometry is quite different from that of a paper sheet. The transition between the two regions occurs around $\sim 20 \mu\text{m}$ for grit-blasted surfaces and $\sim 40 \mu\text{m}$ for sanded surfaces. In our case this transition is likely evidence for multi-affine behavior.

We expect the size of the correlated regions to be on the same order as the grit size used to roughen the surface: $60 \mu\text{m}$ for grit-blasting and $110 \mu\text{m}$ for sanding. The smallest step size, $0.16 \mu\text{m}$, will produce the most accurate results for both the SF and the Z_{\max} analysis at the length scales dictated by grit size. Thus, the $0.16 \mu\text{m}$ step size will be used for all future roughness analysis.

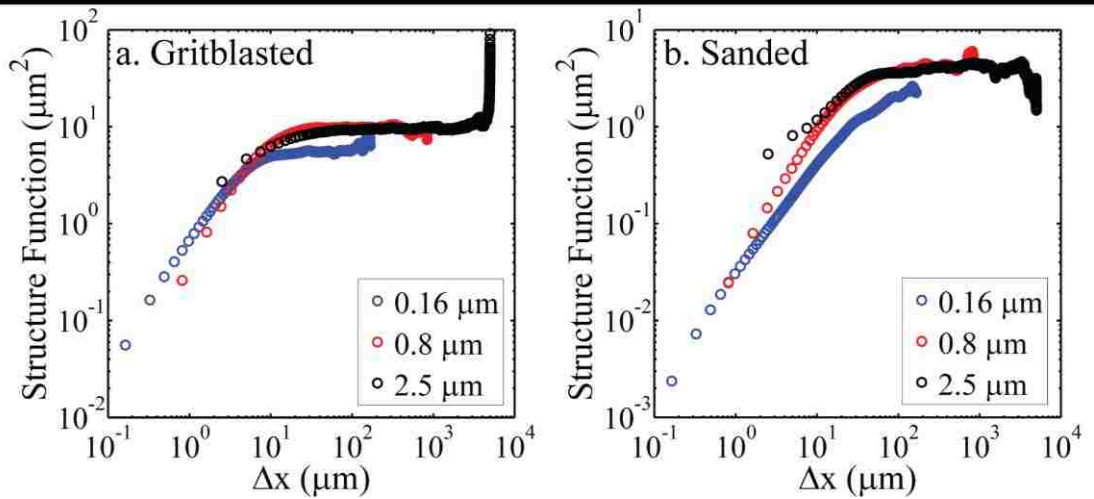


Figure 4.12: Structure Function vs. window size (Δx) for a grit-blasted (a.) and sanded (b.) surfaces. Three different surface profiling step sizes were used. The blue circles, red circles and black circles correspond to step sizes of 0.16, 0.8 and 2.5 μm respectively. As the step size is increased the scan size is also increased from 170 μm , 840 μm and 5 mm. The wavy regions towards the end of each profile are an artifact generated by insufficient statistics in these regions.

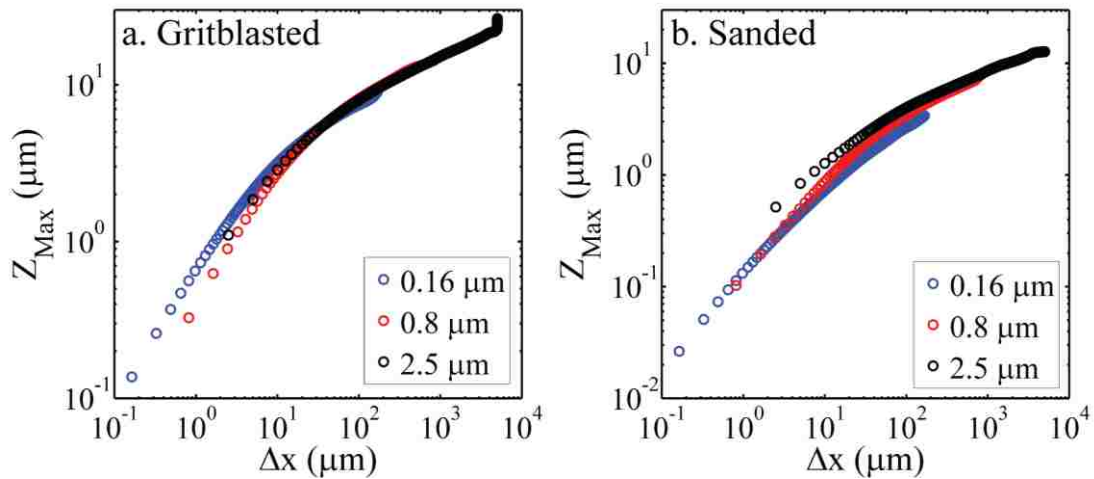


Figure 4.13: Z_{Max} vs. window size (Δx) for a grit-blasted (a.) and sanded (b.) surfaces. Three different surface profiling step sizes were used. The blue circles, red circles and black circles correspond to step sizes of 0.16, 0.8 and 2.5 μm respectively. As the step size is increased the scan size is also increased from 170 μm , 840 μm and 5 mm.

4.3.4.2 The Hurst Exponent for grit-blasted and sanded surfaces

The structure function, Z_{\max} and power spectrum methods are used to evaluate 5 different regions on 7 grit-blasted and 7 sanded surfaces, Figures 4.14, 4.15 and 4.16. The results are normalized by the initial value and collapsed onto a master curve for the evaluation of the Hurst exponent. For the SF and Z_{\max} methods, the Hurst exponent is calculated from a least squares fit over the linear region of the curves, represented by the red line in Figures 4.14 and 4.15. Choosing the optimum fit region for the power spectrum is more complex. Typically, the 10 smallest frequencies (largest wavelengths) are not considered in the fit due to poor statistics¹¹. The lower boundary of the power spectrum fit is dictated by the instrument resolution. The Z resolution of the profilometer is $0.01 \mu\text{m}$. Therefore, the smallest power that the instrument can resolve is $0.0001 \mu\text{m}^2$. Powers below this represent the contributions from wavelengths where the magnitude cannot be resolved by the instrument and so should not be included in the calculation of H.

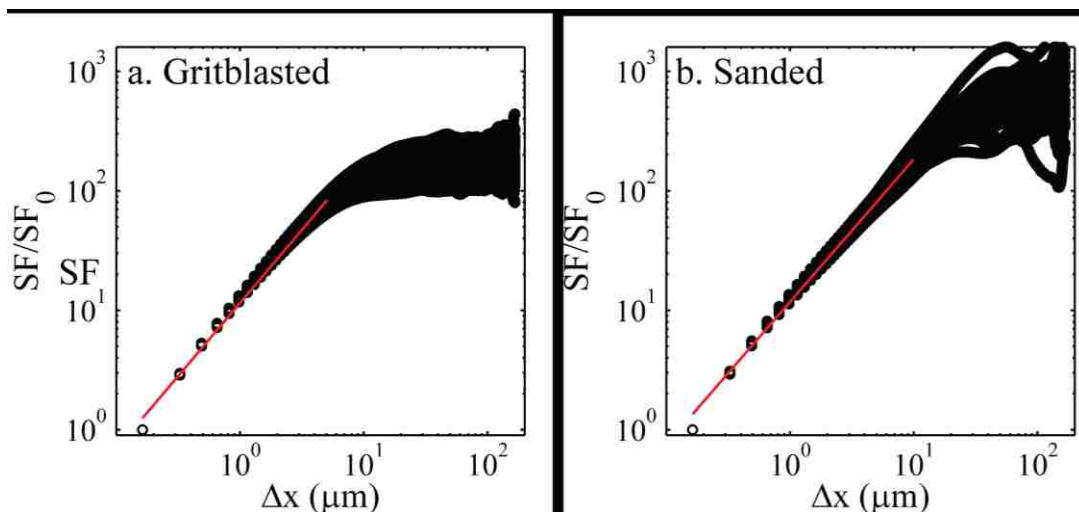


Figure 4.14: Normalized Structure Function vs. window size Δx for 35 different scan areas on grit-blasted and sanded surfaces. The profiling step size is $0.16 \mu\text{m}$. The red line represents a least squares regression used to determine the Hurst exponent.

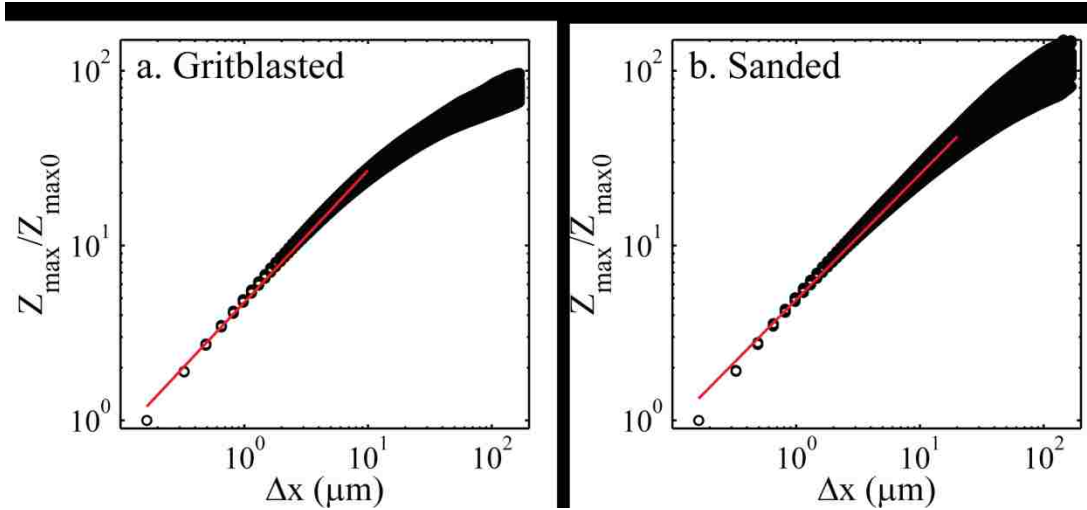


Figure 4.15: Normalized Z_{\max} vs. window size Δx for 35 different scan areas on grit-blasted and sanded surfaces. The profiling step size is $0.16 \mu\text{m}$. The red line represents a least squares regression used to determine the Hurst exponent.

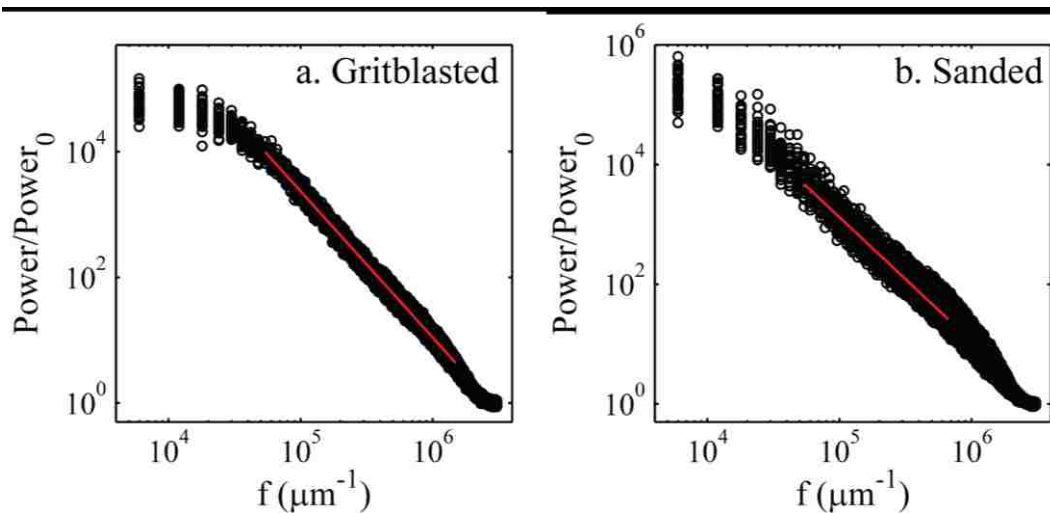


Figure 4.16: Normalized Power Spectrum vs. window size Δx for 35 different scan areas on grit-blasted and sanded surfaces. The profiling step size is $0.16 \mu\text{m}$. The red line represents a least squares regression over all the data.

The Hurst exponent is calculated from all the data presented in Figures 4.14-4.16. In addition the coefficients of proportionality of the fits are calculated. These values are reported in Table 4.2 for grit-blasted surfaces and table 4.3 for sanded surfaces. The

Hurst exponents are also adjusted according to the equations obtained in the experimental section (4.2.4) to assess the reliability of the various methods.

GRIT-BLASTED RESULTS	Hurst Exponent	Adjusted Hurst Exponent	Coefficient of proportionality
Structure Function	0.62±0.02	0.70	0.79±0.13 (μm^{2-2H})
Z_{max}	0.75±0.01	0.75	0.71±0.03 (μm^{1-H})
Power Spectrum	0.66±0.02	0.9	4.2±1.9 x 10 ¹⁰ (μm^{1-2H})

Table 4.2: Value of the Hurst exponent evaluated for a grit-blasted surface using the SF, Z_{max} and Power spectrum methods. The adjusted Hurst exponents are calculated using the linear fit parameters given in Figure 4.5. The coefficients of proportionality are also reported.

SANDED RESULTS	Hurst Exponent	Adjusted Hurst Exponent	Coefficient of proportionality
Structure Function	0.6±0.03	0.67	0.06±0.02 (μm^{2-2H})
Z_{max}	0.72±0.03	0.72	0.2±0.03 (μm^{1-H})
Power Spectrum	0.54±0.04	0.73	2.5±2.9 x 10 ¹⁰ (μm^{1-2H})

Table 4.3: Value of the Hurst exponent evaluated for a sanded surface using the SF, Z_{max} and Power spectrum methods. The adjusted Hurst exponents are calculated using the linear fit parameters given in Figure 4.5. The coefficients of proportionality are also reported.

From tables 4.2 and 4.3 we observe that, within the standard deviation, the Hurst exponent is equal for grit-blasted and sanded surfaces for the SF and Z_{max} analysis. The power spectrum yields different values for sanded and grit-blasted surfaces. The Hurst exponents can be adjusted using the relationship between the input and output Hurst exponent, see the experimental section and Figure 4.5. Using these adjustments it is possible to assess which technique is the most accurate for our particular case. The larger the difference in the estimated values of H to the adjusted values the lower the accuracy

of the method. Using the data in tables 4.2 and 4.3 it is possible to rank the methods in terms of the level of accuracy; in descending order with Z_{\max} being the most accurate, $Z_{\max} > SF > PS$. The adjusted values of Z_{\max} are identical to the estimated values, strongly suggesting this method is the most accurate to use for our system. The Hurst exponent for sanded and grit-blasted surfaces lies in the range 0.72-0.75; close to the range suggested for the universal roughness exponent 0.77-0.80¹⁹. This finding is significant in that it builds on recent work in fracture¹⁹ by showing that a universal Hurst exponent is applicable to aluminum surface fracture. Therefore, using fractal dimension is not applicable to distinguish between the fracture behavior of grit-blasted and sanded surfaces and we must search for an alternate technique.

While the fractal dimension is independent of the abrasion process, the coefficient of proportionality is ~2-4 times larger for grit-blasted surfaces vs. sanded surfaces. Therefore, we will look to this coefficient to differentiate the two surfaces. As described in the experimental section, this coefficient may be related to a parameter called the toposethy (Λ). Using the coefficients obtained from the structure function it is found that $\Lambda_{\text{Grit-blasted}} = 0.8 \mu\text{m}$ and $\Lambda_{\text{Sanded}} = 0.03 \mu\text{m}$. There is a large difference in the toposethy for the 2 surfaces. In order to understand the toposethy it is helpful to write the definition in the following form,

$$\langle (h(\Lambda + x) - h(x))^2 \rangle_x^{1/2} = \Lambda \quad (4.21)$$

Thus, the toposethy is the length at which the RMS value of height fluctuations is equal to the length over which they are observed. The toposethy parameter has been found to effectively differentiate the surface roughness of rock samples, when the fractal dimension was unable to do so³⁶. However, it is difficult to relate the toposethy to a

familiar physical meaning and so it is not clear how it would change the fracture toughness of a joint. Instead, we now view the surface from the frame work of fractional Brownian motion and calculate an anomalous diffusion coefficient in place of the topothesy.

4.3.4.3 An anomalous diffusion coefficient (D) to characterize the Lacunarity of a simulated surface profile and a qualitative relationship between D and the expected fracture toughness of a joint

Fractional Brownian motion offers a convenient way to characterize many real systems^{20,34}. A fractional Brownian process can be described with the following equation²⁰,

$$Var(h(t) - h(t_0)) = 2D\tau^{1-2H}(|t - t_0|)^{2H} \quad (4.22)$$

where Var, h, D, t, τ are the variance, vertical position, diffusion coefficient, time and step size. The step size is equivalent to the lateral resolution of the instrument used to measure the topography of the surface. The time in equation 4.22 can be replaced with a spatial coordinate with no loss of generality, equation 4.23

$$Var(h(x) - h(x_0)) = 2D\tau^{1-2H}(|x - x_0|)^{2H} \quad (4.23)$$

The replacement of time with a spatial variable changes the units of the diffusion coefficient from m²/s to m²/m. For a given window size, the diffusion coefficient provides a measure of how much area the surface has explored. Equation 4.23 is used to calculate a value of D for the computer generated profiles shown in Figure 4.6. The value of D is shown next to the re-plotted profiles in Figure 4.17.

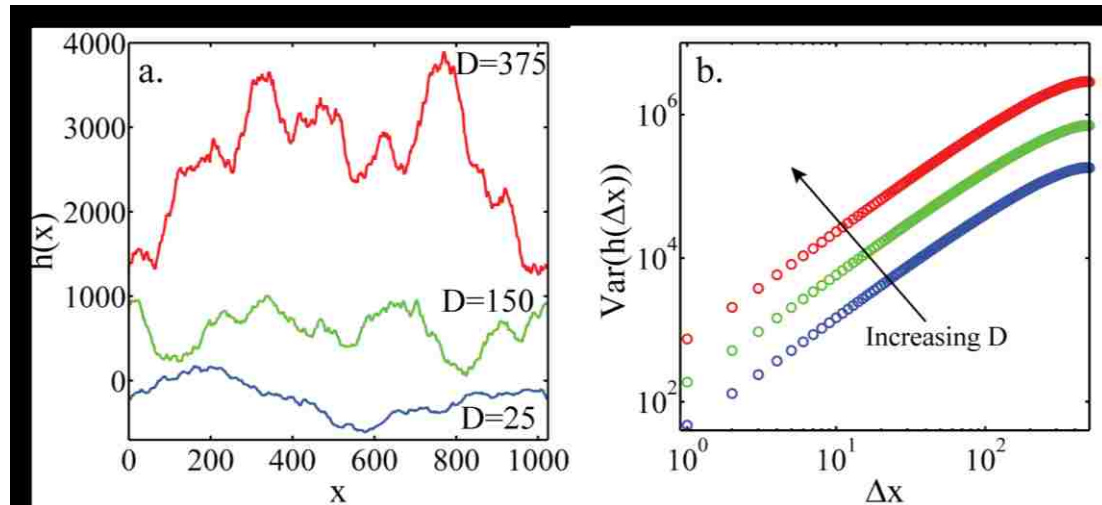


Figure 4.17: a. Three fractal profiles generated with the same Hurst exponent of 0.8 profiles re-plotted from Figure 4.6. Each profile is generated with a different realization of random numbers. The profiles are vertically displaced for clarity. The simulations are run with a step size of one so the units are arbitrary. b. The value of D is calculated from plotting the variance of the step heights against the window size Δx and using equation 4.23 to fit the data. The variance is calculated from 1024 independently generated profiles each with 1024 steps. The red, green and blue circles correspond to diffusion coefficients of 375, 150 and 25 respectively.

As D increases so does the scale of the roughness, the expected result from equation 4.23 as an increase in D will lead to an increase in the variance of the height differences. These profiles only represent one realization; therefore, to rigorously visualize the effect of D on the profile, it is necessary to plot the probability density functions for multiple realizations. Figure 4.18 shows the PDFs for the three different diffusion coefficients outlined in Figure 4.17. As expected from equation 4.23, increasing the diffusion coefficient increases the variance of the PDF, Figure 4.18. The physical interpretation of this effect is that increasing the diffusion coefficient will increase the probability of a large height fluctuation between two points on the surface. This will lead to profiles with regions of rapidly changing height and direction, Figure 4.17a. It is these regions that are of interest from a fracture mechanics viewpoint. A qualitative argument will now be

presented where we suggest that an increase in the diffusion coefficient of a surface would be expected to increase the fracture toughness of an epoxy/aluminum joint where the crack follows the contours of the aluminum surface.

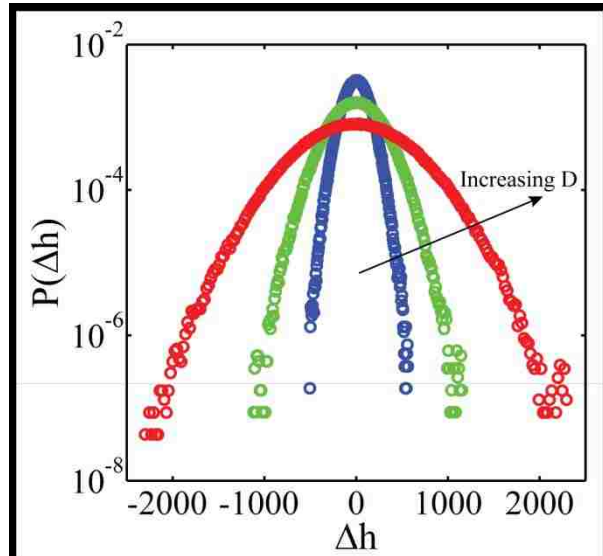


Figure 4.18: PDFs of the height differences for three different profile simulations. The profiles are generated using a Hurst exponent of 0.8 and 3 different values of α (2,4 and 8) as shown in Figures 4.6 and 4.17. For each simulation the PDF is generated from 1025 independent profiles. Each profile contains 1024 steps. The window size (Δx) used to generate the PDFs is 50 steps. The red, green and blue circles correspond to diffusion coefficients of 375, 150 and 25 respectively. The simulations are run with a step size of one so the units are arbitrary

When a crack is forced to change direction, the crack can become trapped, which will lead to an enhancement of the adhesion. Recently, a model system was developed by Vajpayee *et al.*⁴¹ to study the effect of the fracture path on the strength of a joint prepared with complementary rippled surfaces. As the crack front is deflected from the horizontal plane the enhancement of adhesion was related to the angle of deflection; the larger the angle of deflection the larger the threshold energy release rate required to separate the surfaces. The two factors which lead to this enhancement in adhesion are the change in

the mode mixity at the crack tip and the change in the stress intensity factor due to the crack deflection⁴¹. A similar enhancement of adhesion was found both experimentally^{43–45} and theoretically^{46,47} for bi-material interfaces when the adherend was patterned with groves or dots; increasing the aspect ratio of these surface features lead to an increase in adhesion.

It was shown in the previous section that an increase in the diffusion coefficient describing a surface will increase the probability that a sudden change in the height difference will occur. These sudden changes in height will lead to a large angle of deflection, causing an increase in the local fracture toughness. The ideal surfaces used by Vajpayee *et al.*⁴¹ effectively reduce the fracture to a 2D problem. For the grit-blasted and sanded surfaces considered here we must also consider the out of plane variation in roughness. Previous studies have found an enhancement in adhesion on surfaces with 3D roughness patterns such as dots, grooves and islands^{43,44,48}.

From the above argument and the profiles shown in Figure 4.17 we may consider the interface between the roughened aluminum and epoxy to consist of randomly distributed regions of variable toughness. Therefore, we expect a surface with a large diffusion coefficient is to contain a higher density of high toughness regions than a surface with a low diffusion coefficient. The problem of a crack propagating through a random field of local fracture toughnesses (K_c) was first addressed by Gao and Rice⁴⁹. This work has been extended by Roux *et al.*⁵⁰ to predict the effective toughness of a heterogeneous material. They found that as the density of high toughness regions is increased the effective toughness of the joint also increases⁵⁰. Therefore, for a system where the crack path is dictated by a predefined surface roughness we predict than an increase in the

value of D for a surface will lead to an enhancement of the joint strength. This hypothesis will be tested by calculating the diffusion coefficients of grit-blasted and sanded surfaces.

4.3.4.4 Estimation of the anomalous diffusion coefficient of grit-blasted and sanded surfaces

In Figure 4.19, the PDFs of representative grit-blasted and sanded surfaces are plotted. The PDFs are constructed for window sizes between 0.16 and 10 μm . For both the sanded and the grit-blasted surfaces, the variance of the distributions increases with increasing the size of the measurement window. Above a certain size of the measurement window, 15 μm for grit-blasted and 25 μm for sanded, the variance of the distributions remains constant, suggesting that the system is constrained in some way (addressed below).

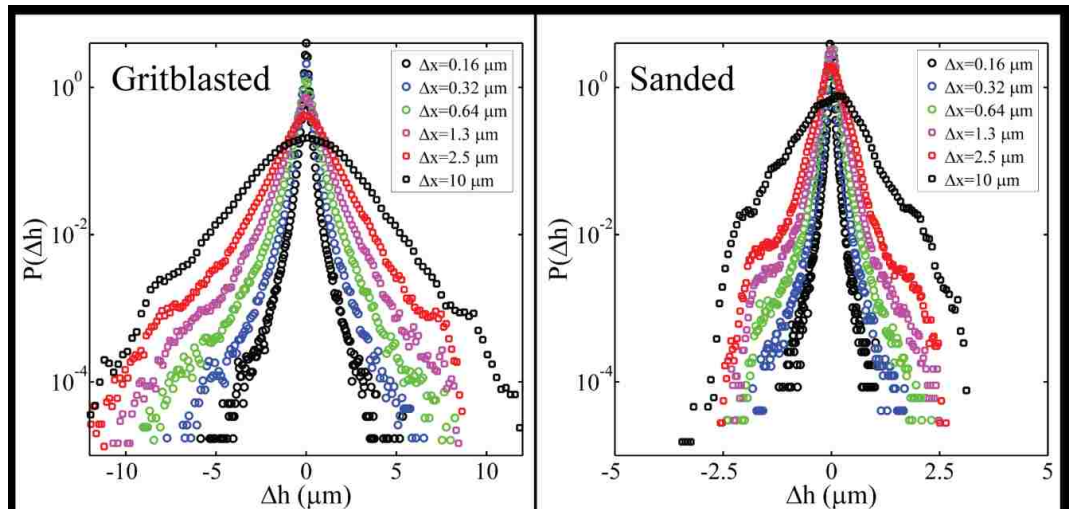


Figure 4.19: Normalized PDFs of grit-blasted and sanded surfaces, different marker colors and shapes shown in the legend represent the different widow sizes used to calculate the distributions.

The PDFs can be fit with a combination of stretched exponentials and stretched Gaussian distributions of the form,

$$P = P_0 \exp \left\{ \left[\frac{\Delta h - \mu}{\sigma} \right]^m \right\} \quad (4.24)$$

where $0 < m < 1$ represents a stretched exponential and $1 < m < 2$ a stretched Gaussian. Equation 4.24 can be rearranged to give equation 4.25 for a zero mean.

$$\ln \left(\ln \left(\frac{P}{P_0} \right) \right) = m \ln(\Delta h) - m \ln(\sigma) \quad (4.25)$$

Using equation 4.25 the PDFs shown in Figure 4.19 are replotted, Figure 4.20. The PDFs constructed from window sizes below $10 \mu\text{m}$ show two linear regions. The existence of two regions implies that the central portion of the PDF can be fit with one distribution and the tails with another. Tables 4.3 and 4.4 give the values of m and σ used to fit the data in the two regions for the grit-blasted and sanded surfaces.

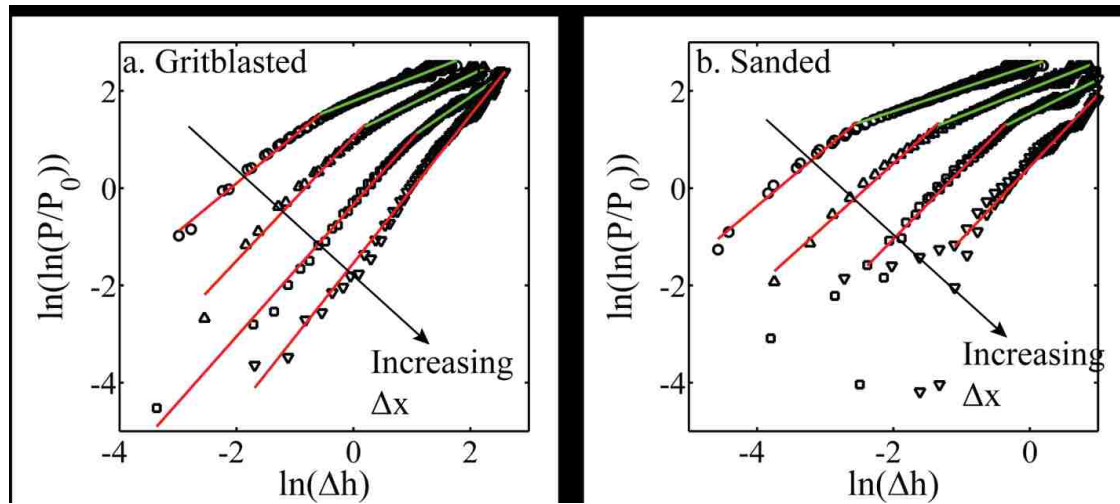


Figure 4. 20: PFDs for grit-blasted and sanded surfaces re-plotted according to equation 4.25. Open circles, open triangles, open squares and open inverted triangles represent the PDFs calculated at window sizes (Δx) of 0.16, 0.64, 2.5 and 10 μm respectively. The red lines represent the linear least square fit for the peak region of the distribution. The green lines represent the linear least square fit for the tail region of the distribution.

Grit-blasted		PDF Peak Region		PDF Tail Region	
Window Size, Δx (μm)		m	σ	m	σ
0.16		0.99	0.12	0.47	0.023
0.32		1.01	0.24	0.5	0.05
0.64		1.28	0.44	0.59	0.14
1.3		1.33	0.75	0.68	0.32
2.5		1.36	1.28	0.81	0.74
10		1.52	2.76	-	-
15		2.06	3.48	-	-
25		1.8	3.33	-	-
50		1.9	3.43	-	-

Table 4.4: PDF fit results for a grit-blasted surface. The peak and tail regions of the data presented in Figure 4.19 are fit using an equation of the form $P = P_0 \exp \left\{ \left[\frac{x-\mu}{\sigma} \right]^m \right\}$.

Sanded		PDF Peak Region		PDF Tail Region	
Window Size, Δx (μm)		m	σ	m	σ
0.16		1.18	0.03	0.47	0.005
0.32		1.29	0.05	0.51	0.01
0.64		1.27	0.09	0.56	0.03
1.3		1.39	0.16	0.64	0.06
2.5		1.43	0.28	0.7	0.11
10		1.49	0.74	-	-
15		1.75	0.98	-	-
25		2.35	1.45	-	-
50		2.37	1.81	-	-

Table 4.5: PDF fit results for a sanded surface. The peak and tail regions of the data presented in Figure 4.19 are fit using an equation of the form $P = P_0 \exp \left\{ \left[\frac{x-\mu}{\sigma} \right]^m \right\}$.

For a measurement window size $< 10 \mu\text{m}$ the PDFs of both surface treatments can be fit with a stretched Gaussian distribution in the peak region and with a stretched exponential distribution in the tail region, see tables 4.4-4.5. Thus, the tails of the distribution have a higher probability of large fluctuations than would be suggested by the peak of the distribution. Therefore, the probability of a rare event (large height fluctuation) is increased. The exponents for the grit-blasted and sanded surfaces are similar for the fits in the tail region. The standard deviation for the grit-blasted surfaces is much larger than the corresponding value for the sanded surface, meaning that not only is the probability of a large height fluctuation increased, but also its magnitude. Therefore, based on the qualitative argument put forward in section 4.3, this PDF analysis suggests that a grit-blasted surface will form a stronger joint than a sanded surface, which is in agreement with the experimental results. The value of the diffusion coefficient for the grit-blasted and sanded surfaces will now be calculated to see if the same predication can be made regarding the joint strength.

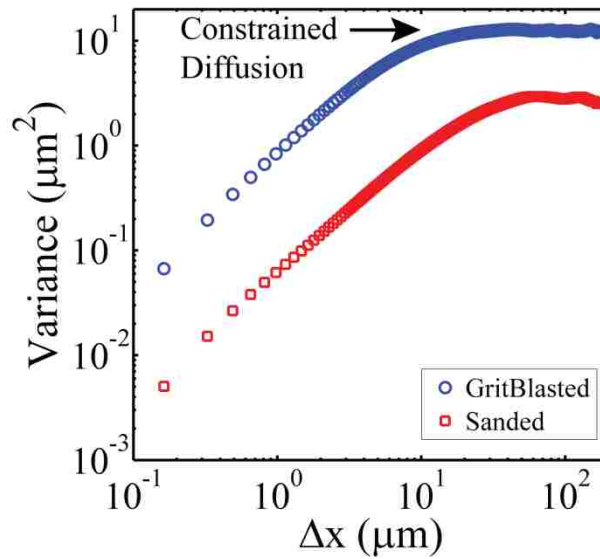


Figure 4.21: The variance of the step heights against the window size Δx for grit-blasted and sanded surfaces. Open blue circles and open squares represent grit-blasted and sanded surfaces. Each point represents the average taken from 35 independent scans.

Equation 4.23 is used to replot the surface profile data and calculate the diffusion coefficient for sanded and grit-blasted surfaces. The diffusion coefficient for the grit-blasted surface is found to be $0.23 \pm 0.04 \mu\text{m}^2/\mu\text{m}$ and for the sanded surface $0.02 \pm 0.01 \mu\text{m}^2/\mu\text{m}$. Therefore, as $G_{\text{grit}} > G_{\text{sand}}$ (see section 4.3.1) we find that the larger the diffusion coefficient of a surface the higher the joint strength. This finding agrees with the theory of toughness enhancement (developed in the previous section) due to a crack pinning at regions of high local toughness; the abrupt changes in surface height are responsible for these regions of high local toughness. It also demonstrates that it is the occurrence of rare events which truly control the process, not the high probability events close to the mean. This phenomenon is prevalent in many natural systems such as chemical reaction kinetics and sub critical crack growth⁵¹.

From Figure 4.21 we observe that the variance does not increase above a critical window size, 10 μm for grit-blasted surfaces and 25 μm for sanded surfaces. The independence of the variance on the measurement window size is a characteristic of constrained diffusion. It is possible that this is due to the confinement imposed by the mechanical abrasion techniques. Regardless of the origin of this constraint it raises the important question, what is the important length scale of surface roughness with respect to the fracture process? For example, if the size of the fracture process zone is on the order of microns then the above diffusion analysis is applicable. However, if the length scale which determines the fracture strength corresponds to the constrained diffusion region an alternative technique must be sort. In order to address this issue, model fracture experiments will be designed to investigate the effect of the scale of the roughness on the fracture energy of a joint. A detailed discussion of these experiments and suitable methods with which to pattern the metallic surface are discussed in detail in the future work section.

4.3.5 Plastic zone size fluctuation as evidence for non-uniform crack growth in grit-blasted samples

The conclusions drawn in sections 4.3.4.3 and 4.3.4.4 are based on a crack travelling through regions of varying toughness as it propagates along a surface. To obtain physical proof of this assumption, a fractured epoxy/sol-gel/grit-blasted aluminum joint was mounted in epoxy, sanded down to 150 μm thick and inspected using brightfield and cross polarized microscopy. Using this technique, the size of the plastic zone, a measure of fracture toughness, can be observed, Figure 4.22. The plastic zone size fluctuates in

size along the crack direction, lending support to the theory of a crack moving through regions of different toughness described in the previous section.

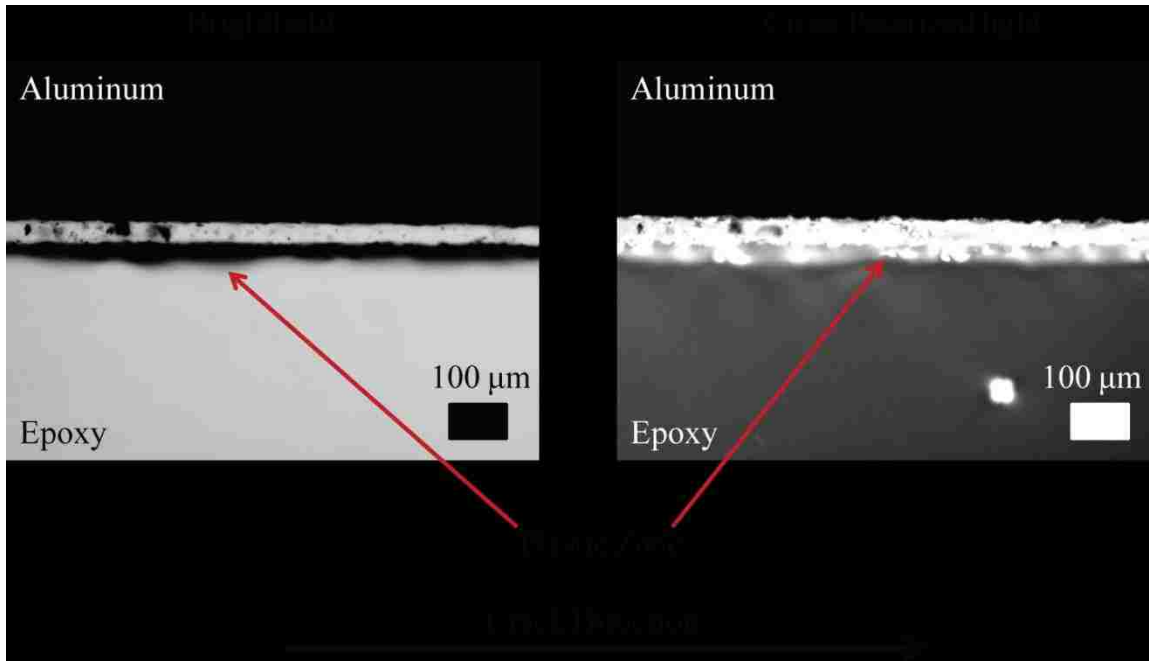


Figure 4.22: Brightfield and cross polarized micrographs for a fractured epoxy/x1 120°C cured sol-gel/grit-blasted aluminum joint. The plastic zones in the epoxy can be clearly visualized in the brightfield and polarized micrographs as the light and dark regions at the fracture surface of the epoxy.

4.4 Summary and Conclusion

This chapter has thoroughly investigated the effects of sol-gel film thickness/ sol-gel cure temperature and aluminum surface morphology on the strength of an epoxy/sol-gel/aluminum joint. This investigation has found that, depending on the surface pretreatment, increasing the thickness of the sol-gel layer above a critical value while curing at a high temperature has a detrimental effect on the strength of the joint. Polished and sanded aluminum surfaces are particularly sensitive to this effect. This thickness dependence is important as the current drive to produce a coating with both adhesion promoting and barrier properties requires an increase in the sol-gel film thickness. A

novel ellipsometric study was used to show that the fracture occurs very close to the aluminum surface for oven cured sol-gel films on polished aluminum substrates and that the interpenetration of the epoxy into sol-gel films cured at 120°C is low.

The remainder of the chapter focused on an old but significant question in industrial fracture: what is the relationship between the surface morphology of a mechanically abraded substrate and its performance in an adhesive joint? To this end a thorough study of the fractal dimension of sanded and grit-blasted surfaces was conducted. While this study was motivated from various literature sources claiming a link between fractal dimension and fracture toughness, we found the two factors to be independent of one another as the fractal dimension is shown to be independent of surface pretreatment. In addition, this independence is easily supported by current work in the area of homogeneous fracture²². Finally, we suggested using an anomalous diffusion coefficient to distinguish between grit-blasted and sanded surfaces and presented a qualitative argument relating this value to fracture toughness. This diffusion argument explains that the increase in fracture strength is expected to increase with an increase in the diffusion coefficient of the surface. Despite the strong correlation between the fracture energy and the diffusion coefficient observed here, the constrained diffusional characteristics of the surface roughness force us to consider the relevant length scales from a fracture perspective. In the future work section experiments are proposed to solve this issue.

In the diffusion argument we have ignored the effect of the plastic deformation in the epoxy. It has been previously reported that sharp surface features can increase the local stress concentrations and induce plastic deformation in the adhesive⁵². This plastic deformation is capable of dissipating large amount of energy; therefore, future work in

this area should focus on how the surface roughness influences the plastic deformation in the adhesive. To increase the stress concentration leading to plastic deformation in the adhesive it is desirable to have a surface with many sharp peaks. This means that a surface governed by the anti-persistence correlation ($H < 0.5$) would be ideal for such a purpose. The surfaces formed in this study through mechanical abrasion all exhibit a persistence correlation ($H > 0.5$). Therefore, the design of surfaces with persistence would be expected to maximize the energy dissipation in the epoxy adhesive.

4.5 References

- (1) Abel, M.-L.; Allington, R. D.; Digby, R. P.; Porritt, N.; Shaw, S. J.; Watts, J. F. *International Journal of Adhesion and Adhesives* **2006**, *26*, 2–15.
- (2) Plueddemann, E. P. *Silane Coupling Agents*; 1982.
- (3) Pape, P. G.; Plueddemann, E. P. *Silanes and Other Coupling Agents*; Mittal, K. L., Ed.; VSP BV, 1992; pp. 105–116.
- (4) Digby, R. P.; Shaw, S. J. *International Journal of Adhesion and Adhesives* **1998**, *18*, 261–264.
- (5) Abel, M.; Watts, J.; Digby, R. *Journal of Adhesion* **2004**, *80*, 291–312.
- (6) Venables, J. D. *Journal of Materials Science* **1984**, *19*, 2431–2453.
- (7) Chaudhury, M. K.; Pocius, A. V. *Surfaces, Chemistry and Applications*; 1 st.; Elsevier: Amsterdam, 2002.
- (8) Liu, J. Ph.D. Thesis, Lehigh University, 2006.
- (9) Blohowiak, K. Y.; Cadwell-Stancin, L.; Anderson, R. A.; Mazzitelli, C. M.; Preedy, K.; Grob, J. W.; Glidden, M. *Proc. 2002 International SAMPE Symposium* **2002**.
- (10) Blohowiak, K. Y.; Grob, J.; Grace, W. B.; Cejka, N.; Berg, D. *Proc. 2007 International SAMPE Symposium* **2007**.

- (11) Russ, J. C. *Fractal Surfaces*; 1st ed.; Plenum Press: New York and London, 1994.
- (12) Liu, J.; Chaudhury, M. K.; Berry, D. H.; Seebergh, J. E.; Osborne, J. H.; Blohowiak, K. Y. *The Journal of Adhesion* **2006**, *82*, 487–516.
- (13) Amada, S.; Hirose, T. *Surface and Coatings Technology* **1998**, *102*, 132–137.
- (14) Amada, S.; Satoh, A. *Journal of Adhesion Science and Technology* **2000**, *14*, 27–41.
- (15) Amada, S.; Yamada, H. *Surface and Coatings Technology* **1996**, *78*, 50–55.
- (16) Bahbou, M. F.; Nylén, P.; Wigren, J. *Journal of Thermal Spray Technology* **2004**, *13*, 508–514.
- (17) Harris, A. F.; Beevers, A. *Adhesion and Adhesives* **1999**, *19*, 445–452.
- (18) Barnsley, M. F.; Devaney, R. L.; Mandelbrot, B. B.; Peitgen, H.-O.; Saupe, D.; Voss, R. F. *The Science of Fractal Images*; 1st ed.; Springer: New York, 1988.
- (19) Bonamy, D.; Bouchaud, E. *Physics Reports* **2011**, *498*, 1–44.
- (20) Feder, J. *Fractals*; New York, 1988.
- (21) Måløy, K.; Hansen, A.; Hinrichsen, E.; Roux, S. *Physical review letters* **1992**, *68*, 213–215.
- (22) Bouchaud, E. *Journal of Physics: Condensed Matter* **1997**, *9*, 4319–4344.
- (23) Daguiet, P.; Henaux, S.; Bouchaud, E.; Creuzet, F. *Physical review. E, Statistical physics, plasmas, fluids, and related interdisciplinary topics* **1996**, *53*, 5637–5642.
- (24) Bonamy, D.; Ponson, L.; Prades, S.; Bouchaud, E.; Guillot, C. *Physical Review Letters* **2006**, *97*, 135504.
- (25) Shewmon, P.; Sundararajan, G. *Annual Review of Materials Science* **1983**, *13*, 301–318.
- (26) Finnie, I. *Wear* **1960**, 87–103.
- (27) Schmittbuhl, J.; Delaplace, A.; Maloy, K. J.; Perfettini, H.; Vilotte, J. P. *Pure and Applied Geophysics* **2003**, *160*, 961–976.
- (28) Hurst, H. E.; Black, R. P.; Simaika, Y. M. *Long-Term Storage: An experimental study*; Constable: London, 1965.

- (29) Schmittbuhl, J.; Vilotte, J.; Roux, S. *Physical Review E* **1995**, *51*, 131–147.
- (30) Sayles, R.; Thomas, T. *Wear* **1977**, *42*, 263–276.
- (31) Whitehouse, D. J. *Handbook of Surface Metrology*; 1st ed.; London and Philadelphia, 1994.
- (32) Press, W. H.; Teukolsky, S. A.; Vetterling, W. T.; Flannery, B. P. *Numerical Recipes in Fortran*; Cambridge University Press, 1992.
- (33) Falconer, K. *Fractal Geometry*; John Wiley & Sons Ltd: Chichester, England, 1990.
- (34) Mandelbrot, B. B. *The Fractal Geometry of Nature*; W. H. Freeman: New York, 1982.
- (35) Sayles, R.; Thomas, T. *Nature* **1978**, *271*, 431.
- (36) Poon, C.; Sayles, R.; Jones, T. *Journal of Physics D: Applied Physics* **1992**, *25*, 1269–1275.
- (37) Longley, J. E.; Chaudhury, M. K. *Macromolecules* **2010**, *43*, 6800–6810.
- (38) Kuhbander, R. J.; Mazza, J. J. *38th International SAMPE Symposium* **1993**, 1225–1234.
- (39) Sung, N.; Kaul, A. *Polymer Engineering and Science* **1982**, *22*, 637–644.
- (40) Mannelqvist, A.; Ring Groth, M. *Applied Physics A Materials Science & Processing* **2001**, *73*, 347–355.
- (41) Vajpayee, S.; Khare, K.; Yang, S.; Hui, C.-Y.; Jagota, A. *Advanced Functional Materials* **2011**, *21*, 547–555.
- (42) Salminen, L. I.; Alava, M. J.; Niskanen, K. J. *The European Physical Journal B - Condensed Matter* **2003**, *32*, 369–374.
- (43) Yun, I. H.; Kim, W.-S.; Kim, K.; Jung, J.-M.; Lee, J.-J.; Jung, H.-T. *Journal of Applied Physics* **2011**, *109*, 074302.
- (44) Janarthanan, V.; Garrett, P.; Stein, R.; Srinivasarao, M. *Polymer* **1997**, *38*, 105–111.
- (45) Rider, A.; Arnott, D. *The Journal of Adhesion* **2001**, *75*, 203–228.

- (46) Lee, M. J.; Lim, J. M.; Lee, B. C. *The Journal of Adhesion* **2013**, 89, 205–224.
- (47) Cordisco, F. a.; Zavattieri, P. D.; Hector, L. G.; Bower, A. F. *Engineering Fracture Mechanics* **2012**, 96, 192–208.
- (48) Chung, J. Y.; Chaudhury, M. K. *Journal of the Royal Society Interface* **2005**, 2, 55–61.
- (49) Gao, H.; Rice, J. *ASME, Transactions, Journal of Applied Mechanics* **1989**, 56, 828–836.
- (50) Roux, S.; Vandembroucq, D.; Hild, F. *European Journal of Mechanics-A/ Solids* **2003**, 22, 743–749.
- (51) Chaudhury, M. K.; Goohpattader, P. S. *The European physical journal. E, Soft matter* **2012**, 35, 9808.
- (52) Packham, D. E. *International Journal of Adhesion and Adhesives* **2003**, 23, 437–448.

CHAPTER 5

Drop motion induced by repeated stretching and relaxation on a gradient surface with hysteresis²

Abstract

The motion of a droplet can be induced by periodically compressing and extending it between two similar gradient surfaces possessing significant wetting hysteresis. The shape fluctuation of the drop during repeated compression-extension cycles leads to its ratchet like motion towards the region of higher wettability. A simple model requiring the volume preservation of the drop during the compression-extension cycles is sufficient to account for the effect and predict drop velocity across the surface when drop size and cycle frequency are specified. In connection with this study, we also report a variation of the standard vapor phase adsorption method of preparing a chemically graded surface that allows for good control over the steepness and the length of the active zone. The method can be used to produce a linear or a radial gradient, which are employed here to drive droplet motion along these patterns. This type of discrete droplet motion can be used to move drops on surfaces to transport materials within miniaturized digital fluidic devices.

²This work has been published as: Jonathan E. Longley, Erin Dooley, Douglas Gilver, Bill Napier, Susan Daniel and Manoj K. Chaudhury, "Ratcheting Motion of Sessile Droplets Induced by Shape Deformation on Surface Energy Gradients", *Langmuir*, **2012**, 28, 13912-13918

5.1 Introduction

A chemical and/or a morphological gradient designed on a surface can be used to propel liquid drops in preferential directions^{1,2}. For this motion to occur, the gradient surfaces should be of negligible hysteresis. In the presence of the ubiquitous defects on a surface, a liquid droplet may not move unless the gradient force is strong enough to overcome the resulting hysteresis³⁻⁶. The effect of hysteresis can, however, be mitigated if additional energy is gained from, for example, the coalescence of multiple drops on a surface^{7,8}. There have also been some recent developments in drop fluidics in which an oscillatory electric field⁹⁻¹¹, vibration^{4,12-19} and electrowetting²⁰⁻²² have been used to overcome hysteresis. In a previous paper¹², we demonstrated that the periodic squeezing and extension of a pinned drop lends itself to an inchworm type motion on a gradient surface. Similar observations have also been made when a drop is squeezed and extended between two nonparallel surfaces in a scissoring mode^{23,24}. In both cases, the hysteresis rectifies the shape fluctuation of the drop and the resulting capillary force generates the motion. Since we reported the phenomenon a few years back¹², no systematic study has been performed to describe the velocity of the drop as a function of either the drop volume or the driving frequency. In this paper we extend our previous study, in which a drop of known volume is placed between two gradient surfaces, with one of the surfaces undergoing low frequency (1 to 10Hz) vibration. The sequential pinning and de-pinning of the front and rear edges of the drop causes it to translate uni-directionally. Velocity of drop motion increases with the drop volume as well as the frequency of oscillation, the

magnitude of which can be predicted with a simple volume conservation model as we show here.

5.2 Experimental

5.2.1 Preparation and characterization of surface energy gradients

Linear surface energy gradients were prepared on glass substrates by diffusion controlled silanization with dodecyltrichlorosilane, which is a variation of a method published previously⁷. The method is somewhat similar to those of recent publications^{25,26}, in which a gradient was prepared by image wise modulation of the diffusion path of an alkanethiol on gold. Glass slides (75 × 25 × 1 mm; Fisher Scientific) were first cleaned in a piranha solution (30% H₂O₂ (50% w/w in H₂O) and 70% H₂SO₄ by volume) for 30 minutes, which were then rinsed with copious amounts of deionized water (DI water; Barnstead) and blow dried with ultra high purity nitrogen (N₂, Praxair Inc.). Next, the glass slides were treated with oxygen plasma at 0.2 Torr for 45s (Harrick Plasma Cleaner, modelPDC-32G). Chemical gradients were established on all the glass slides within ~10 minutes after removing them from the plasma cleaner. This procedure was performed in a glove box purged with dry N₂ (<15% RH). After degassing a silane saturated filter paper under vacuum for 5 minutes, it was placed above a cleaned glass slide for 5 minutes at a controlled angle (Figure 5.1a), which created the desired gradient. The samples were stored inside a polystyrene petri dish under ambient condition for 24 hrs before their surfaces were characterized. Quasistatic advancing and receding contact angles were measured at different points along the gradient using a standard goniometer (Rame Hart) equipped with a CCD camera (Sony, Towada A, Model XC-75) that was

connected to a computer. The mean and the RMS (root mean square) roughnesses of the surfaces along the center line of the gradients were estimated using atomic force microscopy (AFM, Nanodimension V, Veeco) in tapping mode. The mean and RMS roughnesses were calculated using standard methods in the SPM software Gywddion.

Radial gradients were prepared on glass slides after they were cleaned using the above procedure. Here, a cone shaped piece of filter paper was used as the source of the silane (Figure 5.1b). The apex angle of the cone was approximately $\sim 80^\circ$.

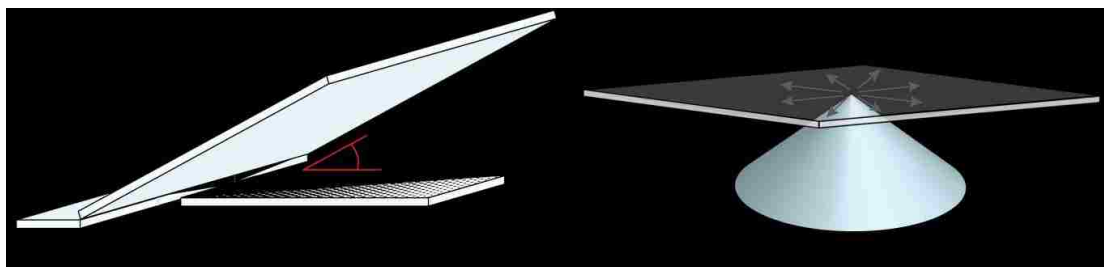


Figure 5.1: **a.** Schematic of the setup used to produce linear surface energy gradients. A filter paper soaked with dodecyltrichlorosilane is the source of silane. This source is placed at an angle above a plasma oxidized glass slide for 5 minutes. The surface energy gradient is formed on the surface through diffusion controlled silanization. The angle of inclination, θ , can be easily controlled to alter the length of the gradient. The source size is 3 times the width of the glass slide that reduces any lateral variation of the chemical gradient. **b.** Schematic drawing of the setup used to produce radial surface energy gradients. A cone shaped filter paper saturated with dodecyltrichlorosilane acts as the source. The plasma oxidized glass slide is placed above the cone for 5 minutes. A radial surface energy gradient is formed on the slide.

5.2.2 Droplet ratcheting motion on a linear gradient surface

Two glass plates with linear gradients prepared under identical conditions were placed parallel to each other at a distance of 1.5 mm. The top plate was firmly secured to a rigid stand whereas the lower plate was attached to a mechanical oscillator (Pasco Scientific,

Model SF-9324) that was connected to a signal generator (Agilent, Model33120A) and a power amplifier (Sherwood, Model RX-4105). The signal generator was used to produce a sinusoidal oscillation of the bottom plate at frequencies ranging from 1-10 Hz but with a constant amplitude of 0.6 mm. A deionized water droplet of controlled volume (10 or 20 μl) was placed near the hydrophobic end of the gradient near the middle portion of the slide. A CCD camera (Redlake, MotionPro, Model 2000) was used to capture the motion of the droplet once the mechanical oscillator was engaged (Figure 5.2). After the completion of each experiment, ultra pure nitrogen was blown over the surface before the next application. A video tracking software (MIDAS) was used to track the position as well as the advancing and receding contact lines of the droplet as it moved along the gradient.

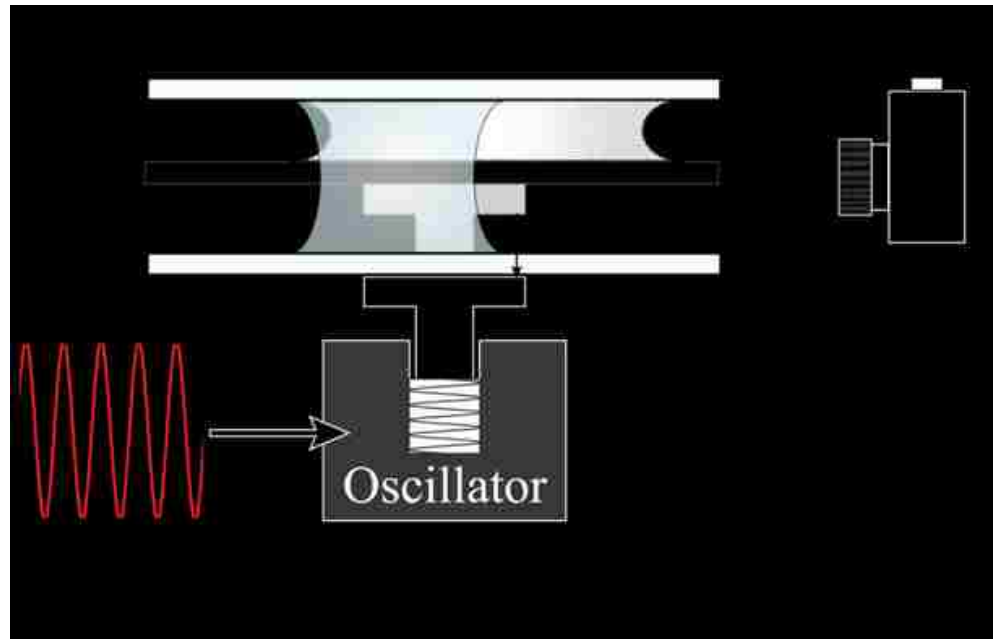


Figure 5.2: Schematic drawing of the setup used to induce shape fluctuation in a droplet. A signal generator is used to pass a sinusoidal output to the mechanical oscillator. The extended (solid lines) and compressed (dashed gray lines) forms of the droplet are shown.

5.3 Results and Discussion

5.3.1 Characterization of linear surface energy gradients

Figure 5.3 summarizes the advancing and the receding angle data as a function of distance on two linear gradient surfaces that were prepared at the inclination angles of 22° and 40° , respectively. The cosines of these contact angles can be fitted empirically with hyperbolic tangent functions, which are useful guides to the eye. The gradients appear to be rather linear over a certain distance depending upon the angle of inclination of the silane source from the horizontal plane. Several factors, such as the angle of inclination, time of adsorption, molecular weight of the silane, and the atmospheric humidity, can affect the length of the effective gradient. In certain cases, adsorption under ambient conditions led to significantly long gradients ~ 50 mm. However, these results were not as highly reproducible as those prepared in an environment purged with nitrogen. Results obtained from four different samples prepared on different days (Figure 5.3) illustrate the general reproducibility of these experiments under controlled environment. With the samples prepared at a 22° deposition angle, the receding contact angle increases from the edge over a distance of about 2 cm, before decreasing systematically beyond it. The latter decrease is due to the variation of the surface coverage of the silane, whereas the initial increase seems to be due to the variation of surface morphology (Figure 5.4) created by the over deposition of the silane. Atomic force microscopic investigation shows that there is indeed a nanometer scale gradient of surface roughness in the initial part of the gradient, which is due to the formation of clusters of the deposited silane. Although these clusters can be removed to some degree by sonicating the substrate in chloroform or hexanes, we have not pursued those studies

in detail here. Instead, we focused on the part of the surface that appears to be free of such clusters and where both the advancing and the receding contact angles vary smoothly with a hysteresis of about $\sim 5^\circ$. The quasistatic hysteresis is small and remains constant along the gradients within this zone, even though the density of surface coverage varies. This observation raises interesting issues about the relationship between the scale of heterogeneity and hysteresis that will be discussed elsewhere. Here we study the effect of the surface heterogeneity in the smooth regions of the gradient surfaces. In the linear part of the gradient, $d\cos\theta/dx$ is $\sim 0.10 \text{ mm}^{-1}$ for the surface prepared at 40° inclination, whereas its value is $\sim 0.065 \text{ mm}^{-1}$ for the surface prepared at 22° inclination. Clearly the gradient in the former case is steeper than the latter.

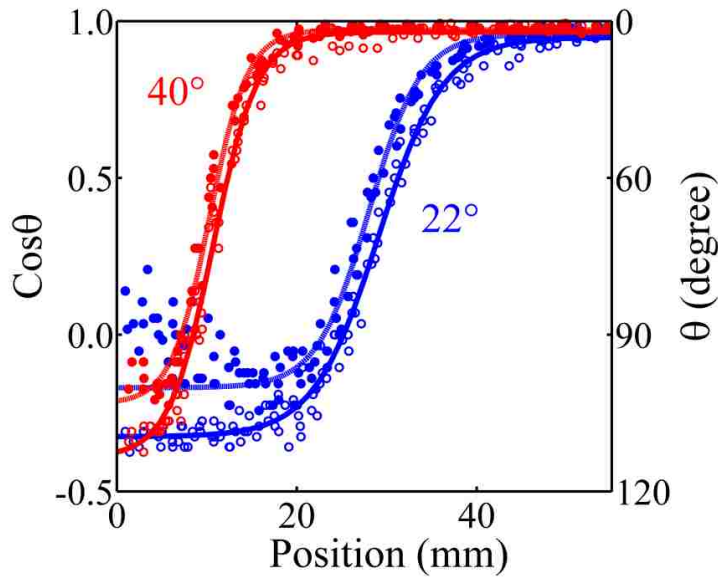


Figure 5.3: Advancing and receding contact angles on gradient surfaces prepared using the setup shown in Figure 5.1. The data shown is for surfaces prepared at two different angles of inclination: 22° and 40° . Advancing and receding angles for the 22° samples are represented by the open blue circles and closed blue circles respectively. Advancing and receding angles for the 40° samples are represented by the open red circles and closed red circles respectively. Solid lines represent an empirical fit of a hyperbolic tangent function to the contact angle data. The values of $d\cos\theta/dx$ on the linear portions of the gradients are estimated to be 0.065 mm^{-1} and 0.10 mm^{-1} for the gradients prepared at 22° and 40° inclinations, respectively.

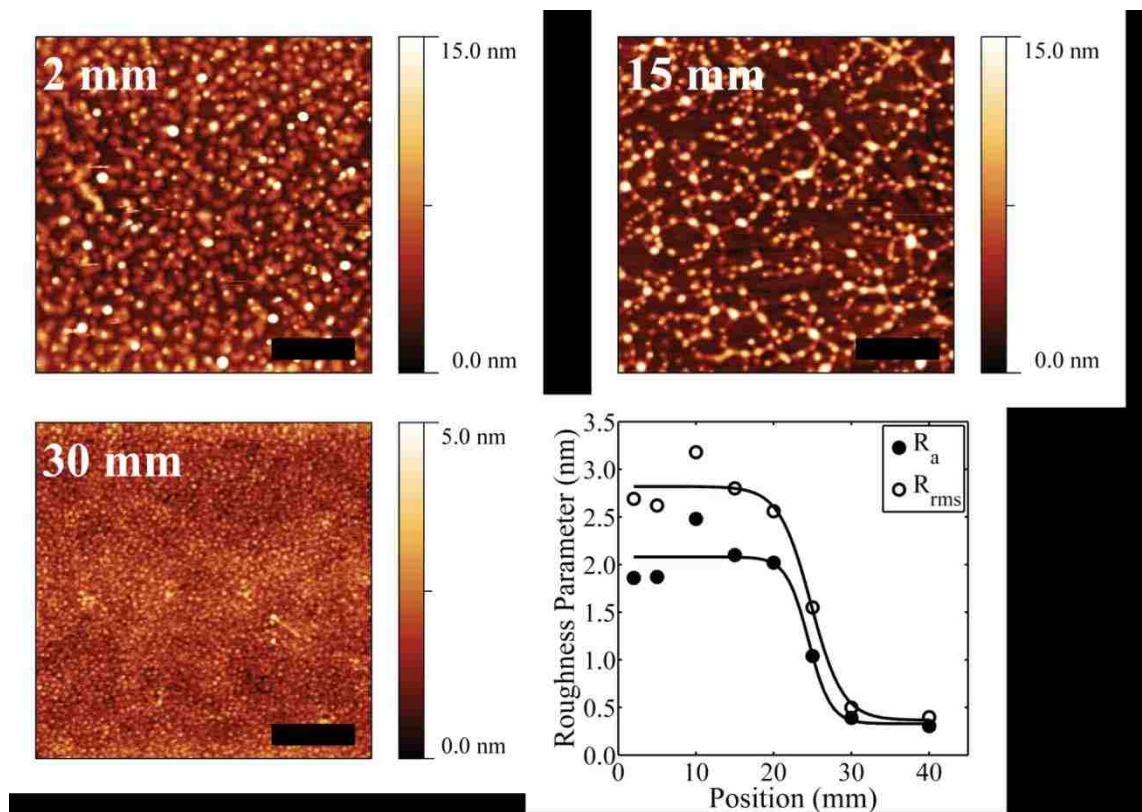


Figure 5.4: Tapping mode AFM images and the analysis of roughness performed along the center line of a gradient prepared at 22° . The AFM scan areas are $2 \mu\text{m}$ squares; the black scale bars represent 500 nm . The position along the gradient is noted in the upper left of each image. The nanoscale arithmetic (R_a , black circles) and RMS (R_{RMS} , open circles) roughness values of the gradient are calculated as a function of position along the gradient. The starting point of the gradient is at a position of 20 mm on the surface. Hyperbolic tan functions (solid black lines) are plotted through the roughness data in order to guide the eye.

5.3.2 Characterization of radial surface energy gradients

A typical technique to produce radial gradients is to diffuse silane from a droplet suspended above the target surface^{3,7}. The size and shapes of the gradient that can be produced with this drop method are somewhat limited. We demonstrate here that a radial gradient can be prepared with a cone shaped source of the silane (Figure 5.1b). Producing a gradient in this manner adds another degree of freedom in controlling the gradient size by controlling the apex angle of the cone. Figure 5.5 shows a typical radial

gradient prepared with a cone apex angle of $\sim 80^\circ$. The prominent characteristics of the gradient prepared with a filter paper cone are that the gradient comes to a sharp peak and is ~ 20 mm in length. While this paper is primarily concerned with the motion of drops on a linear gradient we also demonstrate drop motion on a radial gradient at the end of the discussion.

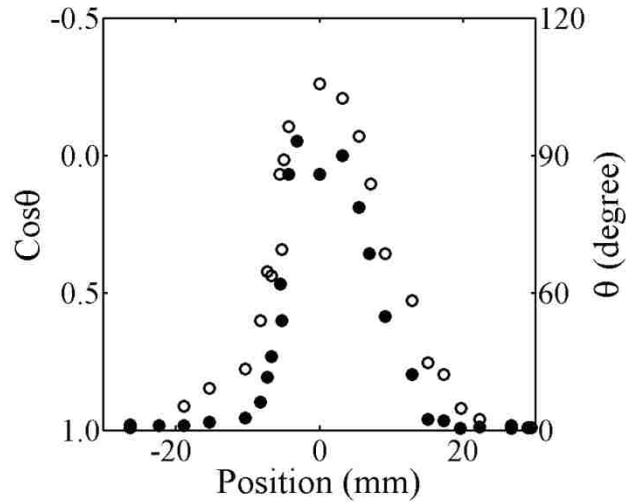


Figure 5.5: The profile of the contact angle on a radial gradient surface. The open and closed circles represent the quasi-static advancing and receding angles respectively. The gradient was prepared using a cone shaped filter paper with an apex angle of $\sim 80^\circ$.

5.3.3 The mechanism of droplet motion on linear gradients

The videographs of Figure 5.6 illustrate the ratcheting behaviors of two different size drops, each sandwiched between two similarly prepared gradient surfaces. To start with, the contact lines of the drops are pinned on the surfaces due to hysteresis. As a drop is compressed, its contact angle also increases. As soon as this transient angle becomes larger than the advancing angle, the contact line moves readily. Since the intrinsic advancing contact angle of the right side of the drop is smaller than its left side, the right side moves while the left side remains pinned. On the other hand, when the drop is

stretched, the contact angles on both sides of the drop decrease. In this configuration, the intrinsic receding angle is higher on the left side of the drop than on the right, so the left side moves while the right side remains pinned. This completes one full cycle and translation of the center of mass of the drop. Repeated cycles give rise to an inchworm-like motion of the drop along the gradient surface.

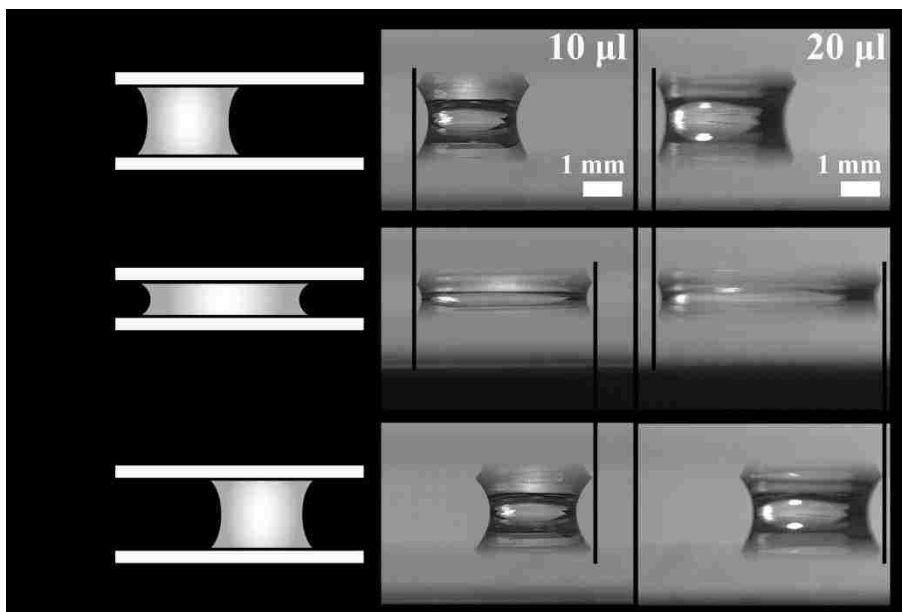


Figure 5.6: Ratcheting motion of 10 μl and 20 μl droplets sandwiched between two gradient surfaces. The upper surface is oscillated at a frequency of 1 Hz. The gradient of wettability here is a continuous decrease in hydrophobicity from the left side of the image to the right side. The snapshots show one complete oscillation of the bottom plate. The droplets go through extension-compression-extension cycle. The black lines show that during compression, the left side of the droplet is pinned while during extension the right side of the droplet is pinned. The schematic on the left of the figure highlights the change in plate spacing throughout the motion. All micrographs are taken at the same magnification.

As discussed in reference 12, the step size of the drop translation depends on the successive pinning and depinning of its advancing and receding edges during a compression-decompression cycle. As the drop is compressed the dynamic angle of the

front edge of the drop becomes larger than its intrinsic advancing angle, hence this edge moves while the receding edge remains pinned. Conversely, when the drop is stretched, the dynamic angle of the receding edge becomes smaller than its receding angle, thus this edge moves while the front edge remains pinned. The net result is an inch worm type motion of the drop during a complete compression-stretching cycle. Although, hysteresis plays the important role of pinning and depinning the contact line, its absolute magnitude is not crucial as long as the contact line does not slip, which is largely the case in our studies. However, as a second order correction, we could take into account the induction time of the drop, which is the time taken for it to reach to the advancing and receding angles, starting from their initial values. Further discussion of the subject is given in Appendix C. Here we present the first order model (i.e. ignoring the induction effect) that captures the basic physics of the drop motion reasonably well. We expect the velocity (V_{drop}) of the droplet to obey the following equation:

$$V_{drop} = \Delta x \omega \quad (5.1)$$

where, Δx and ω are the average displacement of the drop per cycle of oscillation and the frequency of oscillation, respectively. The data presented in Figure 5.7 show that the average droplet velocity for either the 10 μl or the 20 μl droplet indeed increases linearly with the frequency. From the slopes of these plots, we estimate the average step sizes for the drops to be 1.5 mm and 2.5 mm for the 10 μl and 20 μl droplets respectively. These step sizes correspond to the change of the diameter of the drop in each cycle resulting from the contact line slipping during compression or extension. The change in diameter can be estimated from the footprints of the drop.

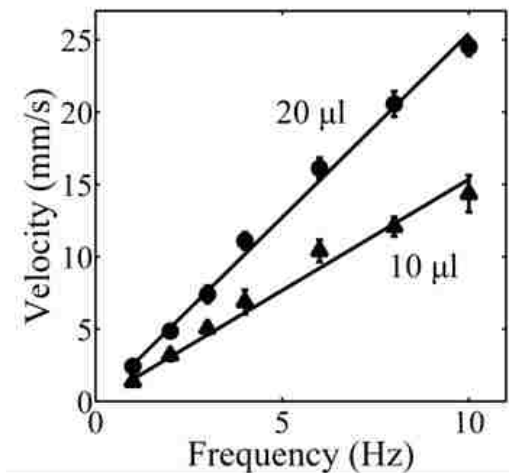


Figure 5.7: Velocity of droplets sandwiched between 2 gradients as a function of the frequency of vibration and the volume of the droplet. The velocities of the 10 μl and 20 μl droplets are represented by the triangles and circles respectively. The black lines are the results of a least squares regression of the data. The slopes of the lines are 1.5 and 2.5 mm/s for the 10 μl and 20 μl drops. For the velocities measured at low frequencies the error bars are less than the size of the marker.

To model the step size of a drop routinely squeezed between two gradient surfaces we begin by relating the drop footprint to the plate spacing, contact angle, and drop volume. We assume that the footprint of the drop as well as the meridian curvature of the air/liquid interface is circular. Figure 5.8 defines the necessary model parameters. Within this two dimensional drop slice, we also assume that the contact angle is equal on both sides of the drop (because of rapid equilibration of the Laplace pressure) and defined by the edge that moves during compression or extension of the drop.

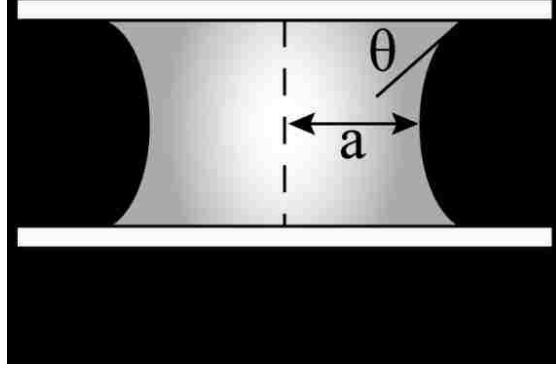


Figure 5.8: Schematic drawing of a drop sandwiched between two surfaces. The symbols are defined within the text.

At any given time or position on the gradient, the radius of curvature, R , of the air/liquid interface can be expressed as function of contact angle, θ , and plate spacing, h , by the following equation:

$$R = \frac{h}{2 \cos \theta} \quad (5.2)$$

Similarly we can write an equation for the drop base diameter, D_{base} , as:

$$D_{base} = 2 \left(a + \frac{h}{2 \cos \theta} (1 - \sin \theta) \right) \quad (5.3)$$

The plate spacing as a function of time is described by the following equation:

$$h = A \cos(2\pi ft) + h_0 \quad (5.4)$$

where A , f , t , h_0 are the amplitude and frequency of oscillation, the time, and the initial plate spacing, respectively. The volume of the drop is then calculated using the standard volume of revolution method, i.e.

$$\frac{V}{\pi} = k^2 h + R^2 h - \frac{h^3}{12} - kh \sqrt{R^2 - \frac{h^2}{4}} - 2kR^2 \tan^{-1} \left[\frac{h}{2\sqrt{R^2 - \frac{h^2}{4}}} \right] \quad (5.5)$$

where k is defined as $k = R + a$. Inserting equations 5.2 and 5.4 into equation 5.5 and then solving with respect to a , we obtain an expression for a in terms of t , A , h_0 , $\cos\theta$ and V . At this point, a value of $\cos\theta_d$ is required and depends on the position of the drop along the gradient and if the angle is advancing or receding during the cycle. $\cos\theta_d$ is obtained from the fits of the data in Figure 5.9. Now the expression for a can be substituted into equation 5.3, resulting in an expression for the drop base diameter in terms of all known variable sat any point in the cycle and any position along the gradient.

To describe the motion of a droplet along the gradient during repeated compression/extension cycles, we must determine the step size, or slip length, of each edge of the drop during each period. During the compression part of the cycle, the leading edge of the drop slips by an amount, Δ_{adv} , while the trailing edge is pinned. Then during the extension part of the cycle, the trailing edge slips by an amount, Δ_{rec} , while the leading edge is pinned. The amount each edge slips during each stroke of the cycle is given by:

$$\Delta_{adv}(x, t) = D_{base}(x, t) - D_{base}(x_0, h_{max}) \quad (5.6)$$

$$\Delta_{rec}(x, t) = D_{base}(x_0, h_{min}) - D_{base}(x, t) \quad (5.7)$$

Where $D_{base}(x, t)$ is the diameter at any time point through the cycle and position on the gradient, calculated as described above. h_{max} and h_{min} are the maximum and minimum plate displacement, respectively, and x_0 is the initial position of leading edge of the drop in Equation 5.6 and the initial position of the rear edge of the drop in Equation 5.7 at the beginning of each cycle.

Taking into consideration the dynamic angles, the above model describes the motion of a 10 μl drop rather well (Figure 5.10). The model, however, is less accurate in

predicting the motion of a 20 μl droplet for which a smaller step size is predicted than that observed experimentally. For this case, the drop is compressed so much that the differential Laplace force across the drop overcomes the hysteresis on its own. The superposition of this motion over that generated through the ratchet action causes the step size to be larger than that estimated on the assumption that the drop moves entirely by pinning-depinning transition. Another source of the discrepancy comes from the fact that the footprint of the 20 μl droplet is somewhat elliptical, whereas that of a 10 μl size droplet is rather circular (see Appendix C, Figure C2).

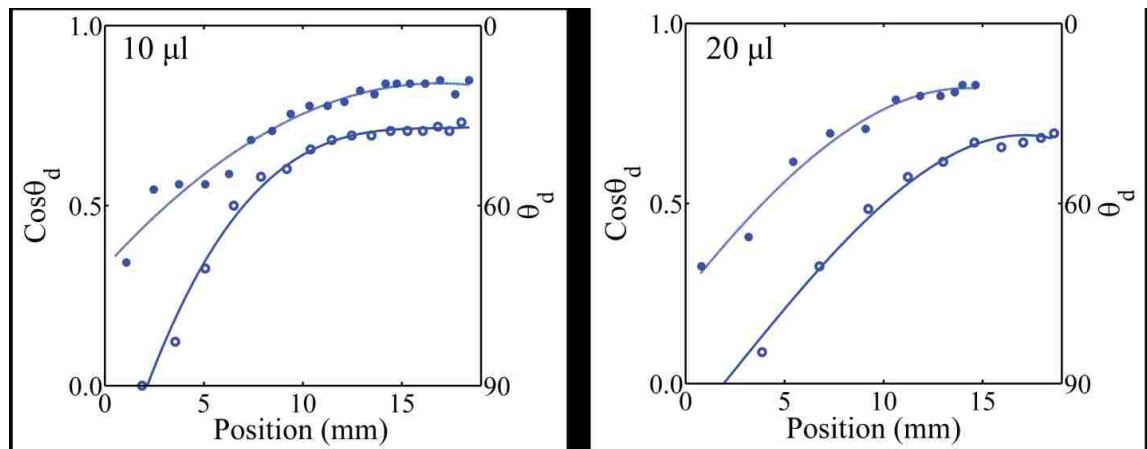


Figure 5.9: Dynamic advancing and receding contact angles for 10 μl and 20 μl droplets moving between two gradients prepared at an angle of inclination of 22°. The vibration frequency is 1 Hz. The open and the closed circles represent the dynamic advancing and receding angles respectively. Solid lines represent an empirical fit of a 3rd order polynomial function to the contact angle data, these functions are then used in the model as described in the text. The position zero on the x-axis is approximately the onset of the gradient.

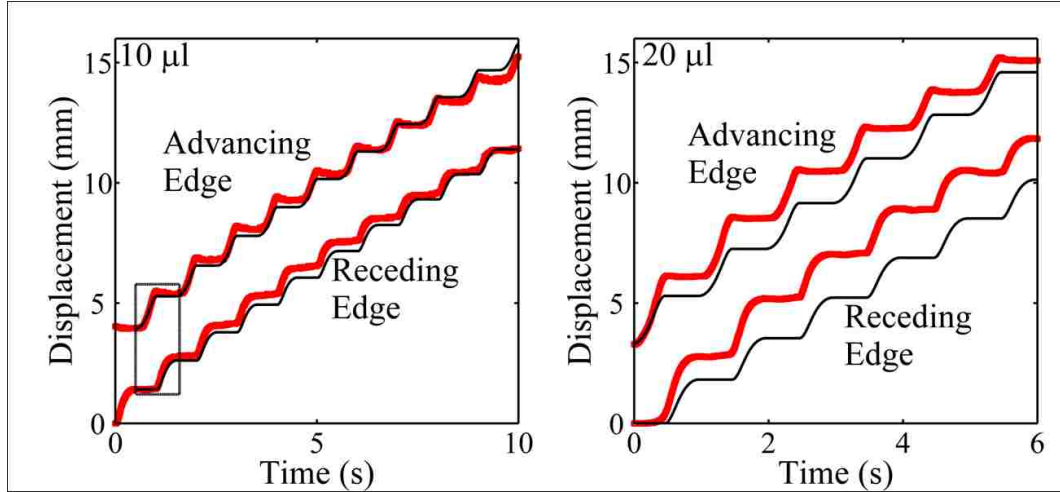


Figure 5.10: Motion of the advancing and retceding contact lines of a 10 μl and a 20 μl drop vibrated at 1 Hz (red squares). The black lines correspond to the fits generated from the model described in the text. The black rectangle in the 10 μl plot represents one cycle of drop compression and extension.

One notable feature of the ratcheting motion of the drop in these compression/extension experiments is that their movements are always unidirectional; i.e. no backward movement occurs at any stage. This contrasts the situation where a drop was vibrated parallel (laterally) to a surface with a strong periodic forcing^{4,12}. The results are however comparable to that observed with a drop subjected to very low frequency (0.1 Hz) lateral vibration pulses, where no backward motion of the drop was observed at any stage⁴.

At this point, it is tempting to compare the velocities obtained with these compression/extension cycles with that to be expected if the drop were to move without being influenced by hysteresis. By performing experiments with drops of different liquids and different viscosities, Daniel *et al.*¹² proposed that the velocity of a drop moving on a gradient should follow equation 5.8 in the absence of any hysteresis:

$$V_{drop} = \frac{0.01\gamma R}{\eta} \left(\frac{d(\cos\theta)}{dx} \right) \quad (5.8)$$

Here, V is the velocity of the drop; η is the viscosity of the liquid; γ is the surface tension; R is the radius of the drop and $d\cos\theta/dx$ is the gradient of the wettability. From Figure 5.3 the gradients $d\cos\theta/dx$ of the linear portion of the gradients are estimated to be 0.065 mm^{-1} and 0.10 mm^{-1} for the gradients prepared at 22° and 40° respectively. Although Equation 5.8 is for a sessile drop in contact with one surface, the same equation will also apply for a drop sandwiched between two surfaces. In this case, the driving force and the dissipation are both doubled.

Using a typical value of $R \sim 1.8 \text{ mm}$ for a $10 \text{ }\mu\text{l}$ drop, its velocity is estimated to be about 83 mm/s for the surface prepared at 22° . Similarly, for a $20 \text{ }\mu\text{l}$ size drop, this velocity is estimated to be about 115 mm/s . All the average velocities reported in Figure 5.7 are smaller than the above velocities. As the velocity increases with the frequency and amplitude of oscillation, we expect it to reach, and perhaps exceed, the above estimates. However, at high frequency of oscillation, viscous dissipation would be enhanced and the hysteresis, itself, could be modified. Furthermore, the contact line relaxation should lag behind the driving force. It would be interesting to carry out these high frequency experiments in future to determine if hysteresis can at some critical value be fully overcome and address the issue of whether or not an amplification of the drop motion would be observed in addition to the ratcheting motion described here.

5.3.4 Motion of drops on radial gradients

To highlight the motion of a drop on a radial gradient, an array of $20 \text{ }\mu\text{l}$ drops was sandwiched between a radial gradient surface and a uniform monolayer of the same silane. In this case we have only employed one gradient surface (on the bottom side) in

conjunction with a uniformly hydrophobic upper plate, rather than two gradients as was used in the linear gradient studies. This proof-of-concept demonstration was carried out this way in order to avoid any artifacts that could arise due to incomplete registration of the stacked radial gradients. The drops do, indeed, move outwards over the gradient as they are periodically stretched and compressed (Figure 5.11). The step size of these drops is ~ 1 mm. These radial gradient results also show the potential of this filter paper technique to create various surface energy patterns by simply changing the shape of the silane source.

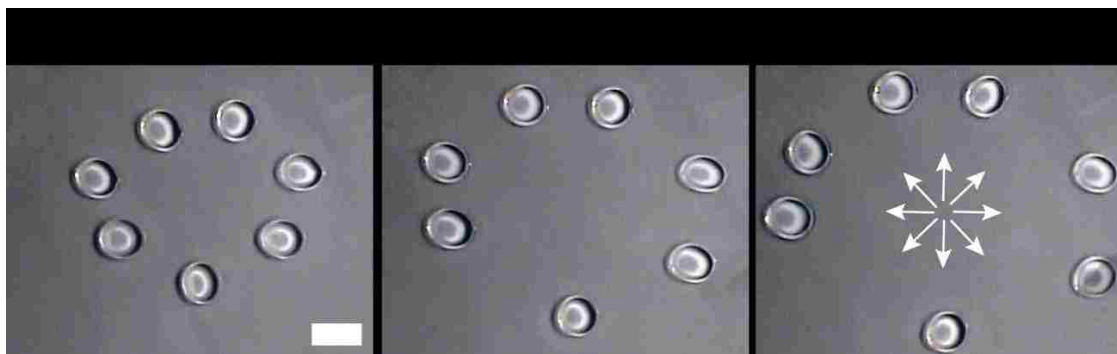


Figure 5.11: Several 20 μ l water drops sandwiched between a radial gradient and uniform hydrophobic surface. As the droplets are squeezed and compressed they move outward, toward the hydrophilic part of the gradient. The scale bar represents 5 mm. All images are of the drops in the compressed state.

5.4 Summary and Conclusions

A simple method to prepare a gradient surface is reported here. This method is an improvement over the standard vapor phase deposition previously reported, in that here the steepness of the gradient can be controlled better. An interesting aspect of this method is that a gradient of surface morphology can be produced at a nanometer length scale. It is indeed interesting to observe that the contact angle hysteresis is sensitive to such nanometer scale variation of the surface morphology. These nanometer scale

morphological gradients may be useful in certain applications, which we will explore in our future works.

The smooth, but chemically heterogeneous, part of the gradient is found to be useful in rectifying the externally provided harmonic vibration to create a ratcheting motion of a drop on the surface. The dependence of the velocity of a drop on the amplitude and the frequency of vibration can be explained using a simple volume conservation model. As postulated by Daniel et al⁴ the presence of hysteresis is vital to achieving fully rectified drop motion, in which no backwards movement of the drop is observed. This rectification through hysteresis is also the basis for the motion of a drop between two nonparallel surfaces in a scissoring mode as explained in references 23 and 24. It remains an open question as to whether an amplification of velocity in this configuration could be obtained beyond that predicted for a hysteresis-free gradient case, which will be addressed in our future works. Such controlled drop motion on surfaces is useful in a number of applications, in particular, digital fluidic applications for miniaturized batch processes on chip²⁷.

5.5 References

- (1) Genzer, J.; Bhat, R. R. *Langmuir* **2008**, *24*, 2294–2317.
- (2) Subramanian, R. S. *Soft Matter Gradient Surface*; Genzer, J., Ed.; 1st ed.; John Wiley & Sons, Inc, 2012.
- (3) Chaudhury, M. K.; Whitesides, G. M. *Science* **1992**, *256*, 1539–1541.
- (4) Daniel, S.; Chaudhury, M. K. *Langmuir* **2002**, *18*, 3404–3407.

- (5) Luo, M.; Gupta, R.; Frechette, J. *ACS applied materials & interfaces* **2012**, *4*, 890–896.
- (6) Decker, E. L.; Garoff, S. *Langmuir* **1996**, *12*, 2100–2110.
- (7) Daniel, S.; Chaudhury, M. K.; Chen, J. C. *Science* **2001**, *291*, 633–636.
- (8) Choi, S.-H.; Newby, B. M. Z. **2003**, *19*, 7427–7435.
- (9) Buguin, A.; Talini, L.; Silberzan, P. *Applied Physics A: Materials Science & Processing* **2002**, *75*, 207–212.
- (10) Sandre, O.; Gorre-Talini, L.; Ajdari, A.; Prost, J.; Silberzan, P. *Physical review. E* **1999**, *60*, 2964–2972.
- (11) Fouillet, Y.; Achard, J.-L. *Comptes Rendus Physique* **2004**, *5*, 577–588.
- (12) Daniel, S.; Sircar, S.; Gliem, J.; Chaudhury, M. K. *Langmuir* **2004**, *20*, 4085–4092.
- (13) Mettu, S.; Chaudhury, M. K. *Langmuir* **2008**, *24*, 10833–10837.
- (14) Mettu, S.; Chaudhury, M. K. *Langmuir* **2011**, *27*, 10327–10333.
- (15) Malvadkar, N. A.; Hancock, M. J.; Sekeroglu, K.; Dressick, W. J.; Demirel, M. C. *Nature Materials* **2010**, *9*, 1023–1024.
- (16) Hao, P.; Lv, C.; Zhang, X.; Yao, Z.; He, F. *Chemical Engineering Science* **2011**, *66*, 2118–2123.
- (17) Bennès, J.; Alzuaga, S.; Chabé, P.; Morain, G.; Chérioux, F.; Manceau, J.-F.; Bastien, F. *Ultrasonics* **2006**, *44 Supplement*, e497–502.
- (18) Sheng, X.; Zhang, J. *Applied Surface Science* **2011**, *257*, 6811–6816.
- (19) Shastry, A.; Case, M. J.; Böhringer, K. F. *Langmuir* **2006**, *22*, 6161–6167.
- (20) Li, F.; Mugele, F. *Applied Physics Letters* **2008**, *92*, 244108.
- (21) ‘t Mannetje, D. J. C. M.; Murade, C. U.; van den Ende, D.; Mugele, F. *Applied Physics Letters* **2011**, *98*, 014102.
- (22) Marinescu, M.; Urbakh, M.; Barnea, T.; Kucernak, A. R.; Kornyshev, A. A. *The Journal of Physical Chemistry C* **2010**, *114*, 22558–22565.

- (23) Bush, J. W. M.; Peaudecerf, F.; Prakash, M.; Quéré, D. *Advances in colloid and interface science* **2010**, *161*, 10–4.
- (24) Prakash, M.; Quéré, D.; Bush, J. W. M. *Science* **2008**, *320*, 931–4.
- (25) Kraus, T.; Stutz, R.; Balmer, T. E.; Schmid, H.; Malaquin, L.; Spencer, N. D.; Wolf, H. *Langmuir* **2005**, *21*, 7796–804.
- (26) Han, X.; Wang, L.; Wang, X. *Advanced Functional Materials* **2012**, *22*, 4533–4538.
- (27) Ahmadi, A.; Devlin, K. D.; Najjaran, H.; Holzman, J. F.; Hoorfar, M. *Lab on a chip* **2010**, *10*, 1429–35.

CHAPTER 6

How a blister heals

Abstract

A blister experiment was designed to study the healing of a crack between a thin PDMS film and a flexible glass cover plate. When a glass cover slip spontaneously heals against a PDMS film, the crack front is guided to trap the air and form a blister. The healing of the blister is then controlled by the diffusive mechanisms of the escaping air. From the kinetics of the blister healing, an effective permeability coefficient, k_D , for the trapped air was calculated. The permeability coefficient is found to be a strong function of the PDMS film thickness and varies as, $k_D \propto h_{PDMS}^{1.5}$. To explain the value of the exponent we propose that the air diffuses simultaneously through the PDMS film and PDMS/glass interface.

6.1 Introduction

A blister forms when a debonded region of a thin film is inflated by an increase in the internal pressure between the film and the substrate. The internal pressure of a blister can be increased by the flow of a fluid into the blister. This process occurs when a blister forms under irritated skin¹ or during the standardized blister test used to evaluate the adhesive properties of thin films²⁻⁵. Alternatively, the internal pressure can be increased via the diffusion of a species through the substrate into the blister, as is the case for the

formation of hydrogen blisters on metallic surfaces⁶. After nucleation at a defect or debonded region, the axisymmetric growth of a blister is well understood and determined through a balance between the internal pressure, adhesive forces, mode mixity, film elasticity, and the deformation of the film and substrate^{3-5,7,8}.

But how do blisters heal? Blisters formed by a hastily applied piece of tape or as a result of painting a wall on a hot and humid day can disappear over time. To the best knowledge of the authors, the mechanism through which the trapped fluid escapes has not been previously studied. To investigate the healing of a blister, we introduce a new type of blister experiment that follows the disappearance of a blister trapped between a thin glass cover slide and a PDMS film. With this experiment, we can study the mechanism of healing in a controlled environment. What distinguishes the healing process of the blister described here from previous works is that it is controlled via the escape of air from the blister as opposed to the traditional blister technique⁵, which requires an external load or pressure. This experiment has general applications for any system where the escape or removal of fluid is essential to form a uniform adhesive bond. The technique also provides an alternative method to study the more generalized topic of the healing of soft materials to each other or onto a hard surface. In addition to studying the healing process, we also analyze the fingering instability induced at the blister edge and approximate the work of adhesion.

6.2 Experimental

6.2.1 Materials

The glass slides (75 x 50 mm FisherBrand) and the cover slips (No. 1 Corning cover slips) were purchased from Fisher Scientific. The flexural rigidity of the cover slips was found to be 0.02 N.m, by following the method of Ghatak *et al.*⁹ The Slygard 184 (Dow Corning) that was used to make the thin PDMS films was purchased from Essex Browning. Feeler gauges of different thicknesses were obtained from a standard hardware store. To observe the rate of blister disappearance, a Nikon Optiphot microscope in reflectance mode was equipped with a CCD camera and a green light filter (516 nm with a bandwidth of 5 nm as analyzed using a VASE (J.A. Woollam Co.) in transmission mode). The output from the CCD camera was fed into a computer, where the programs WinTV and Matlab were used to record the data. The spin coated PDMS films were prepared using a Laurell WS-650MZ-23NPP/LITE.

6.2.2 Preparation of thin PDMS films

The glass slides were cleaned in piranha solution (70% v/v H₂SO₄, 30% v/v H₂O₂) for 30 mins and then rinsed with copious amounts of DI water. The slides were then cleaned further by exposing them to oxygen plasma at 2.0×10^{-4} atm for 45s. PDMS was mixed in a 10:1 base to curing agent ratio and degassed for one hour under house vacuum to remove any trapped air bubbles. Using the feeler gauges to control the spacing, a thin layer of PDMS was then sandwiched between a freshly cleaned glass slide and another slide which was pretreated with a self assembled monolayer (of doedecyltrichlorosilane) to act as a release coating. The self assembled monolayers are prepared by suspending a filter paper wet with a few drops of silane above a plasma cleaned glass slide for 2 hours

under reduced pressure. The glass slides are then clamped in position and the PDMS films cured at 80°C for 2 hrs. For films 40 μm and thinner, the PDMS films were spin coated onto cleaned glass slides. The thickness was controlled by changing the spin speed while maintaining a constant spin time of 10 minutes. The thickness of the films was found by making an incision on the film with a razor blade and then measuring the thickness with optical interferometry (ZeGage, Zometrics).

6.2.3 Formation of a Blister

The thin ($\sim 150 \mu\text{m}$) cover slips were cut in to 24x24 mm squares and then cleaned by rinsing thoroughly with MEK and acetone, followed by submersion in piranha solution for 30 minutes. Prior to running the experiment the glass slide and PDMS film are rinsed with DI water to remove any static charge and dried with N_2 . The glass cover slip is lightly placed onto the PDMS film. The healing process generally occurs immediately; as the coverslip heals to the PDMS film, the edge of a razor blade is quickly used to guide the crack front in order to create a blister. The blister radius initially decreases rapidly until the equilibrium between the internal blister pressure, work of adhesion and bending energy of the glass cover slip is reached. Once this equilibrium is reached the blister size then decreases at a slower rate as the trapped air slowly diffuses out. Blisters made using this method are circular and have an initial diameter of $\sim 8\text{-}10 \text{ mm}$. The experiments were carried out at room temperature and humidity, 23°C and 30% RH. The disappearance of the blister is then recorded using a microscope, CCD camera and a computer. Figure 6.1 shows a schematic of the setup.

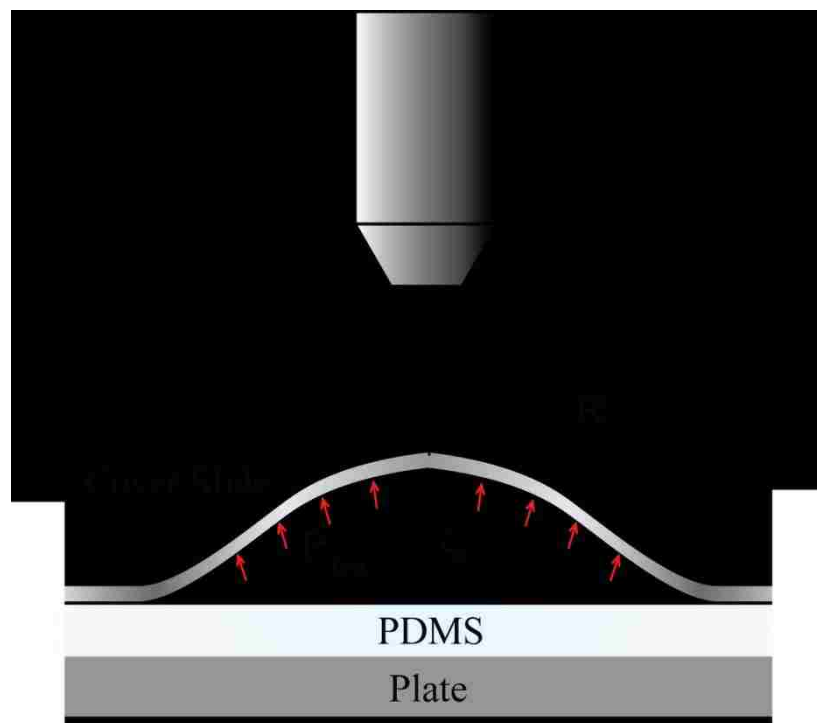


Figure 6.1: Schematic of experimental set up used to monitor the disappearance of a blister. R is the blister radius, P_{Int} the internal pressure of the blister and ζ the height of the blister. The deflection of the glass plate is greatly exaggerated in the schematic.

6.2.4 Determination of Blister Profile

Once the blister is formed between the glass cover slide and PDMS film, circular interference bands are observed, Figure 6.2. If we view the blister under a monochromatic light source and note the position and number of the interference bands, it is possible to construct a height profile for the blister. This technique has been used previously to obtain the blister profiles of amorphous silica on glass surfaces and blisters formed between thin layers of mica^{10,11}. The thickness of the glass coverslip is $\sim 150 \mu\text{m}$, and as this length is 3 orders of magnitude larger than the wavelength of visible light, it is safe to assume that it can be ignored in the formation of the interference bands. Therefore, we need only concern ourselves with the reflection and transmission of light at

the lower cover slip surface. Incorporating the phase shift due to reflection from the PDMS surface, we obtain the simple result that constructive interference will be observed at heights of $\frac{(2n-1)\lambda}{4}$ and destructive interference at $\frac{n\lambda}{2}$, where $n=1,2,3,\dots$ and λ is the wavelength of light. Thus, for the green light used here ($\lambda = 516\text{nm}$) the resolution of this technique is $\sim 129\text{ nm}$.

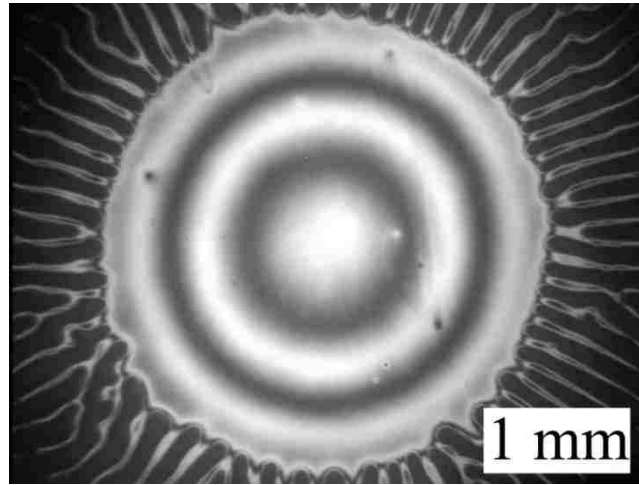


Figure 6.2: Blister healing on a $50\ \mu\text{m}$ thick film of PDMS. The height profile of the blister can be calculated from the interference patterns. Fingering instabilities are observed around the periphery of the blister

6.3 Results and Discussion

6.3.1 Analysis of fingering wavelength at blister edge and blister final life analysis

The wavelength of the fingering instability is independent of the radius of the blister and increases linearly with film thickness (Figure 6.3). Fingering instability of a confined soft elastic layer has been rigorously studied by several authors and found to vary as $\lambda=4 h_{\text{PDMS}}$ for a crack front^{9,12} and $\lambda=3 h_{\text{PDMS}}$ in isotropic stress fields^{13,14}, where h_{PDMS} is the PDMS film thickness. The finger wavelength for the blisters is plotted against data collected by Ghatak et al⁹ (Figure 6.3). Above a PDMS film thickness of 40

μm the blister data closely matches the data from Ghatak et al⁹ following the relation $\lambda=4h_{\text{PDMS}}$. At thicknesses below $40 \mu\text{m}$ the blister finger wavelength deviates such that, $\lambda>4 h_{\text{PDMS}}$. A detailed explanation of this effect is reserved for future work. The interference bands observed at the tip of the fingers strongly suggest that the deformation of the PDMS film is very steep in the regions where it contacts the glass slide. In order to visualize this directly, a $50 \mu\text{m}$ PDMS film was partially cured at 65°C for 30 minutes. A blister was then made on the film using a glass cover slip treated with a monolayer of dodecyltrichlorosilane. The sample was then placed back in the oven for 4 hours to complete the cure. Once the film was cured the glass coverslip was removed and the fingering impressions remained on the film. Optical profilometry was then used to visualize the fingers, Figure 6.4. As expected from the interference bands, the PDMS deforms suddenly close to the region of contact with the glass slide.

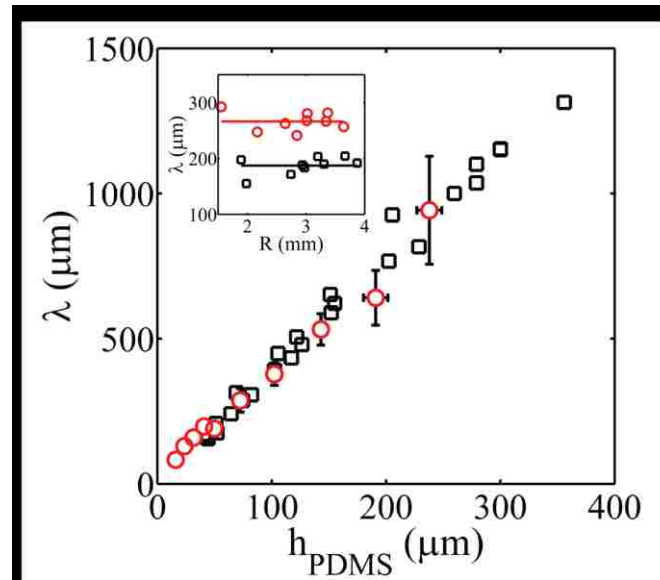


Figure 6.3: Wavelength of the fingering instability as a function of PDMS film thickness. The length used to calculate the finger wavelength is measured along the ends of the fingers. Red circles represent the finger wavelengths calculated for the blister experiments. For the thicknesses measured below $100\mu\text{m}$ error bars are less than the size of the marker. Black squares represent the finger wavelength data collected by Ghatak *et al.*⁹ for two different geometries. Insert: Fingering wavelength as a function of blister radius for PDMS films of thicknesses $75\mu\text{m}$ (red circles) and $50\mu\text{m}$ (black squares). Fingering wavelength remains constant as the blister shrinks.

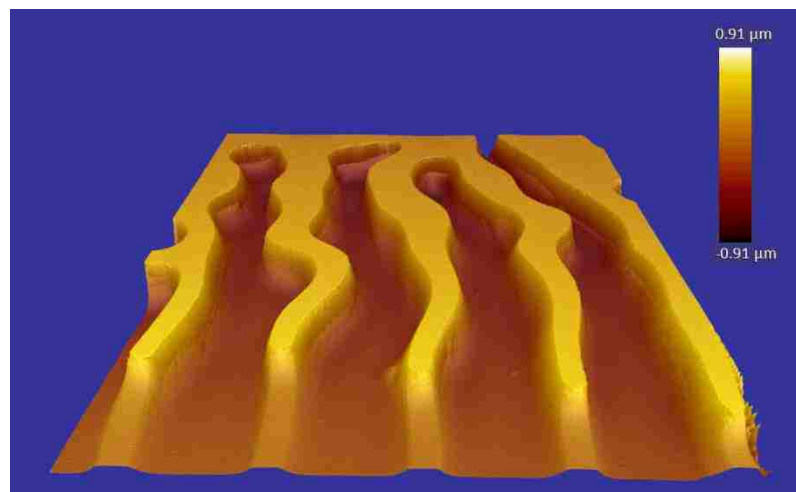


Figure 6.4: Optical profilometry scan of the fingering instability formed around the periphery of a blister formed on a $50\mu\text{m}$ thick PDMS film. The scan size is $830\times 830\mu\text{m}$

In the final stages of the blister life, the blister forms a branched network of fingers on the surface, Figure 6.5. Further examination of the finger wavelength in Figure 6.5 reveals that the wavelength is constant with measurement radius. Thus, the branching of the fingers occurs as the system attempts to maintain the same finger wavelength at different radii from the blister center.

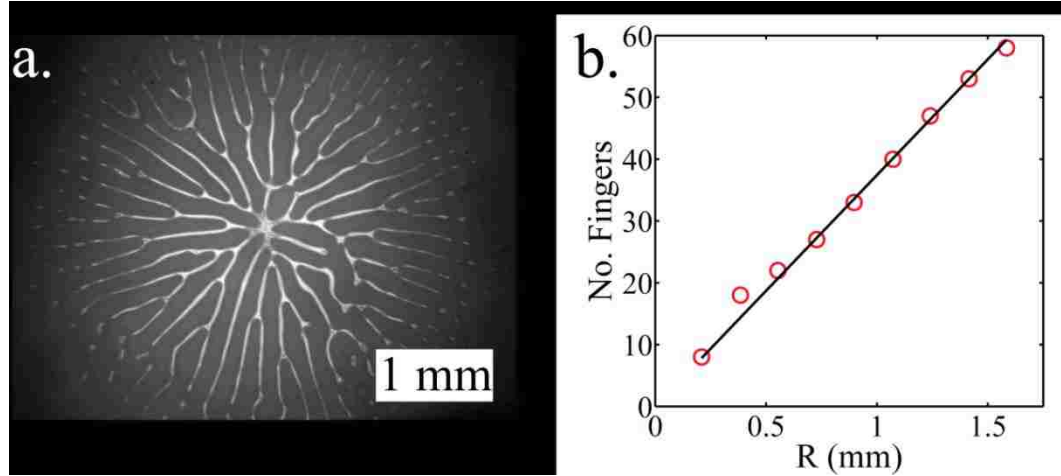


Figure 6.5: **a.** Final branched network of fingers/channels formed just prior to blister disappearance on a 50 μm thick PDMS film. **b.** No. fingers counted at different measurement radius R . The linear relationship between No. fingers and R proves that the wavelength is independent of measurement radius. The wavelength can then be found from the equation, $No. Fingers = \frac{2\pi}{\lambda} R$. The gradient calculated from the linear least squares regression fit is 37 mm^{-1} which corresponds to a fingering wavelength of $\sim 170 \mu\text{m}$.

6.3.2 Analysis of blister profile and estimation of the internal pressure of the blister

The energy of a plate undergoing a small bending deformation (vertical deformation \ll plate thickness) is given by¹⁵,

$$D\nabla^4\zeta = P \tag{6.1}$$

where D , ζ , P are the plate flexural rigidity, vertical plate displacement and pressure applied to the plate respectively. We assume at each instance in time that the boundaries of the blister are in equilibrium (quasi-static). Equation 6.1 is solved in cylindrical coordinates using the boundary conditions $\zeta = 0$ at $r=R$ and $\frac{d\zeta}{dr} = 0$ at $r=R$. The blister profile is given by,

$$\zeta = \frac{P}{64D}(R^2 - r^2)^2 \quad (6.2)$$

where z , P and R are the vertical displacement, internal pressure (gauge), and radius of the blister, respectively. D is the flexural rigidity of the glass cover slide. Figure 6.6 shows the model fit (blue lines) for height profiles obtained at different times. These profiles are taken from a blister on a 50 μm thick film. The quality of this fit is representative of the experimental data. Close inspection of the fingers show that the interference fringes begin at the end of the finger. Due to the sharp deformation of the PDMS at the end of the finger it is not possible to directly measure the number of fringes in the finger that correspond to the plate deflection. Therefore, in the analysis of a blister on a 50 μm thick PDMS film, an approximate number of 5 interference fringes along the length of the finger is used. In order to obtain a good fit of the model to the blister profiles, the number of interference fringes estimated in the finger was altered depending on the PDMS film thickness. The number of fringes estimated in the fingers is 1, 2, 3, 3 and 4 for 10, 15, 25, 30 and 40 μm thick PDMS films, respectively. For PDMS films 50 μm thick and above, 5 fringes are used. The model treats R and P as adjustable parameters in obtaining the fit. The value of R calculated from the fit is, on average, within 3% of the actual measured radius.

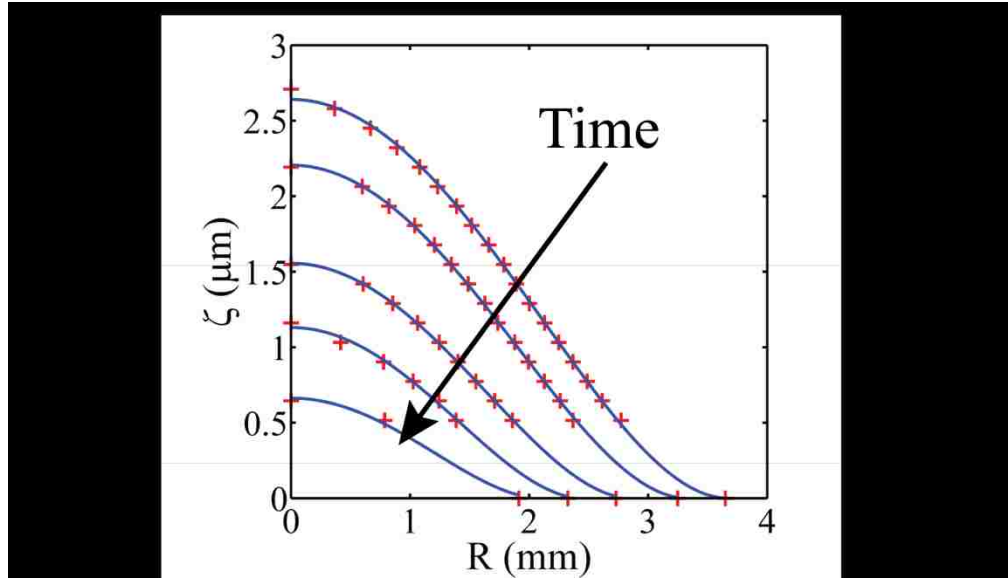


Figure 6.6: Height profiles of a blister on a 50 μm thick PDMS film plotted at different instances in time. The height profile, red crosses, is determined from the interference fringes observed when viewing the blister under monochromatic light ($\lambda=516\text{ nm}$). A simple model (blue lines) which only considers the deformation of the glass cover slide is used to fit the data (equation 6.2).

6.3.3 The energy release rate of a blister healing on a PDMS substrate

The healing process is driven by the work of adhesion between the glass plate and the PDMS. Here we calculate the energy release rate of the system using a simple model and compare it to the expected work of adhesion. As a first approximation, the calculation of the energy release rate of the system used the standard result of Williams for a circular blister³, $G = \frac{P^2 R^4}{128D}$. Here G, P and R are the energy release rate, the pressure difference across the glass cover slide and the blister radius, respectively. This model only considers the bending deformation in the glass plate, i.e. any deformation in the PDMS is ignored. The values for P and R are obtained from the fitting of equation 2 to the blister profile (Figure 6.6). Williams's expression for the energy release rate can be rewritten as

$G = 32 \frac{DH_{max}^2}{R^4}$, which has the same general form as Ombreioff's classical result for the

peeling of mica¹⁶. For very thin films ($h_{\text{PDMS}}=10\mu\text{m}$) this model predicts the energy release rate to be, $G \sim 42 \text{ mJ/m}^2$. This value is very close to the work of adhesion for a crack healing between a glass plate and PDMS film¹⁷, $W \sim 44 \text{ mJ/m}^2$. However, as we increase the film thickness, we find using Williams's equation that $G < W$. This discrepancy is most likely due to the deformation in the PDMS at the crack tip which we have not accounted for in the simple model. Further improvement of the model would involve a detailed analysis of the PDMS deformation at the crack tip and along the fingers. As our current work is focused on the mechanism of healing, the detailed adhesion analysis is reserved for the future.

6.3.4 Modeling the escape of air from inside the blister to the surroundings

Due to the complexity of the processes involved in the disappearance of the blister we start our analysis using a modified version of Darcy's law,

$$\frac{dn}{dt} = -k_D P \quad (6.3)$$

where $\frac{dn}{dt}$ is the molar flow rate, k_D the permeability coefficient, and P is the pressure difference across the glass cover slide. Using equation 6.2, the volume of the blister can

be expressed as $V = \frac{\pi P R^6}{192D}$. Substituting this relation for V , the ideal gas law and

Williams's equation ($W_A = \frac{P^2 R^4}{128D}$) into equation 6.3 and rewriting in terms of R yields,

$$[AR^5 + BR^3] \frac{dR}{dt} = -k_D \quad (6.4)$$

where A and B are constants defined as $A = \frac{P_2\pi}{48\bar{R}TD}$ and $B = \frac{\pi}{\bar{R}T}\sqrt{\frac{W_A}{72D}}$. \bar{R} and T represent the molar gas constant and temperature. Equation 6.4 is integrated to give,

$$\frac{A}{6}R^6 + \frac{B}{4}R^4 = -k_D t + C \quad (6.5)$$

where C is the constant of integration. Therefore, a plot of the left hand side of equation 6.5 (defined as f(R)) vs. t should yield a straight line with a gradient of $-k_D$ (Figure 6.7a). The calculated permeability coefficient shows a strong trend with increasing film thickness (Figure 6.7b). This increase in the permeability coefficient with the film thickness obeys a power law of the form $k_D = A(h_{PDMS})^B$, where $A = 1.3 \times 10^{-7}$ (pmol $m^2/(N.S)(\mu m)^{-B}$ and $B = 1.5$. It is important to note that in this analysis we assume Williams's equation to hold over all film thicknesses. At first, this assumption appears contrary to the results presented in the previous section. The lower value of G calculated for thicker films suggests that the pressure inside the blister is lower for a given radius (as $G = \frac{P^2 R^4}{128D}$). If we take the value of G estimated for the most extreme case ($h_{PDMS}=250 \mu m$) and substitute it into equation 6.5 we observe a 5% reduction in the value of k_D . This result strongly implies that the system is relatively insensitive to the absolute pressure inside the blister, which is important for the current model as we are primarily concerned with the rate of change of the internal pressure. In addition, the internal pressure is likely to be higher than that estimated from Williams's equation as additional force will be required to deform the PDMS film. Therefore, using Williams's equation in this analysis is a good approximation.

One possible method for the air to escape is via diffusion through the PDMS film. The air has two possible directions for diffusion in the PDMS; it can diffuse into the film

directly below the blister and/or diffuse through the annulus formed at the edge of the blister. We assume that the diffusion through the annulus is the rate controlling step. The area of this annulus, $A = 2\pi R h_{PDMS}$, is linearly proportional to the film thickness. If this is the only mechanism at work we would expect k_D to be a linear function of film thickness. However, Figure 6.7b shows that $k_D \propto h_{PDMS}^{1.5}$. As this exponent is greater than one, an additional mechanism of escape must be responsible. Another possible mechanism is the escape of air through the PDMS/cover glass interface. In order for the air to escape in this manner, it must form microchannels along the interface. To support this theory we now examine the final branched networks formed as the blisters disappear.

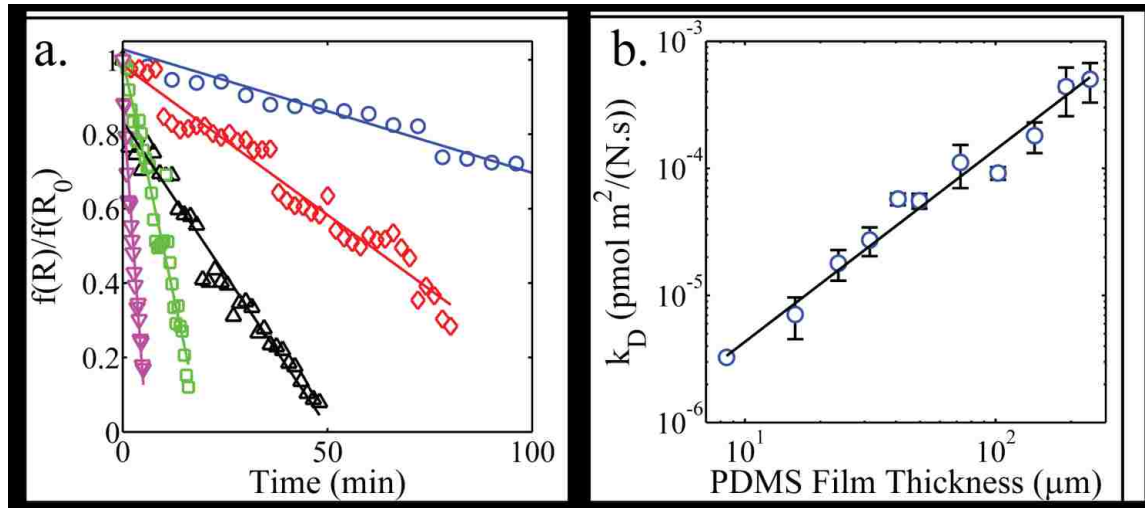


Figure 6.7: **a.** Plot of $f(R)/f(R_0)$ vs. time for a blister healing on PDMS films of different thickness. The function $f_1(R)$ is defined as the left hand side of equation 6.5. $f(R_0)$ is the value of the function at $t=0$. The blue circles, red diamonds, black triangles, green squares and magenta inverted triangles represent 15, 30, 40, 140, 240 μm thick PDMS films. The gradient of each least square fit is equal to the permeability coefficient, k_D , for that particular thickness (Equation 6.5). **b.** Permeability coefficient, k_D , as a function of film thickness. The permeability coefficient increases with the film thickness obeying a power law trend of the form $k_D = A(h_{PDMS})^B$, where $A = 1.3 \times 10^{-7}$ ($\text{pmol m}^2/(\text{N.S})$)(μm) $^{-B}$ and $B = 1.5$.

6.3.5 Evidence of Channel formation

At the end of the life of a blister, a branched network of channels forms as shown in Figure 6.5. In order for the branching pattern to form it is necessary that the ends of the fingers become pinned as the center of the blister shrinks. This pinning effect becomes apparent (Figure 6.8) if we study the change in the outer radius of the blister (measured at the ends of the fingers) over time vs. the inner radius (measured at the base of the fingers). The outer radius of the blister (blue circles, Figure 6.8) displays a stick-slip motion; the fingers are sequentially pinned, stretched, and broken due to the shrinkage of the blister. The data presented in Figure 6.8 is from the blister healing on a 50 μm thick film.

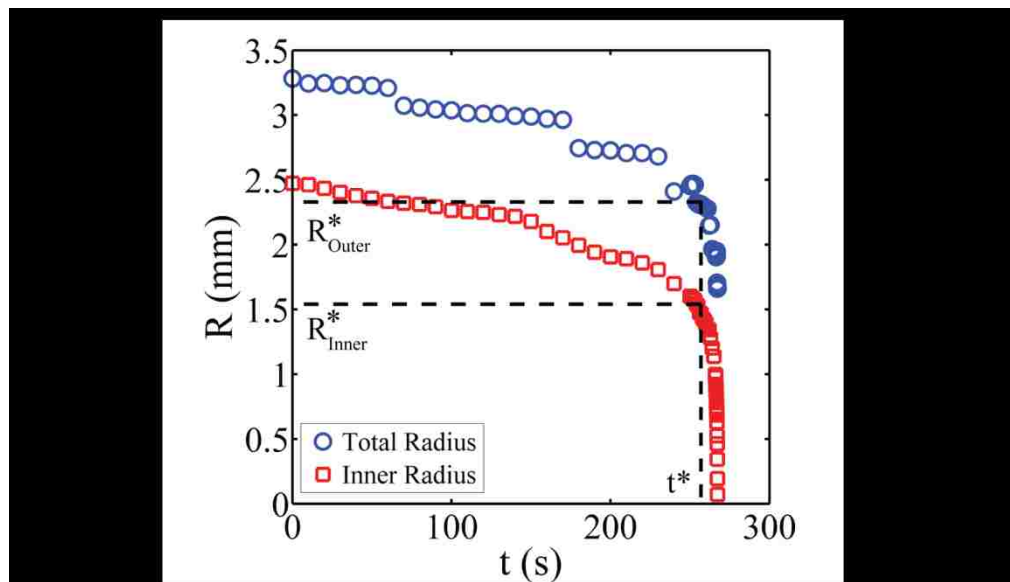


Figure 6.8: Outer radius of the blister (blue circles, measured at the ends of the fingers) and inner radius (red squares, measured at the base of the fingers) as a function of time for the healing of a blister on a 50 μm thick PDMS film. In the final stages of blister life the outer radius remains constant while the inner radius rapidly decreases. This final stage is characterized by a critical outer radius R_{Outer}^* , inner radius R_{Inner}^* and time (t^*).

The channel width varies as a function of radius in the branching pattern formed just prior to blister disappearance. The width of the channels decreases with increasing measurement radius (Figure 6.9). This response is expected if the air escapes through channels formed at the glass/PDMS interface. Therefore, this observation provides evidence that the air is escaping through channels forming at the cover glass/PDMS interface.

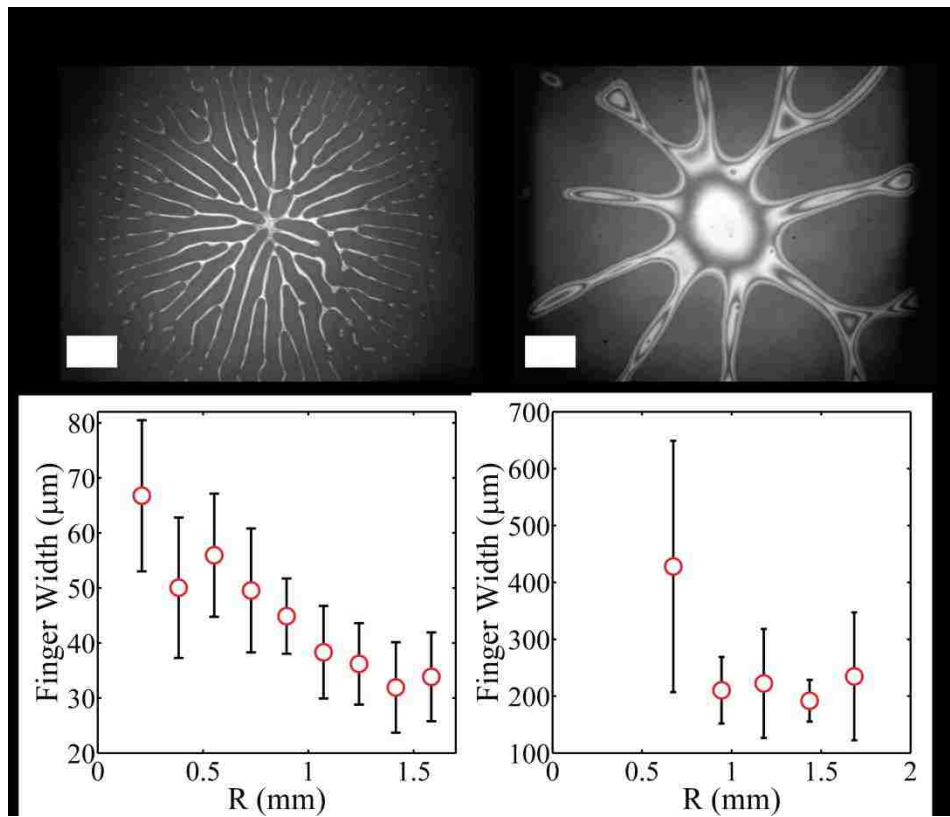


Figure 6.9: Micrograph snapshots taken just before blister disappearance for experiments on 50, and 240 μm thick films. White scale bars represent 0.5 mm. The corresponding finger width as a function of measurement radius is shown beneath each micrograph. For 50 and 100 μm thick PDMS films the finger width decreases as we move away from the blister center.

To permit the formation of microchannels, the pressure inside the blister should be larger than a critical cavitation pressure; the escaping air must be able to lift the coverslip

off the PDMS film. Ghatak *et al.* estimated a critical cavitation pressure of 0.6 bar for a similar system¹⁸. We calculate the average pressure inside a blister to increase from 1.1-1.3 bar as the blister shrinks. While this is comfortably above the critical value, it is not clear how this pressure is transmitted beyond the end of the fingering instability. It is the pressure in the region beyond the end of the fingers which must be above the critical value so that it is energetically favorable for the system to cavitate, and this complex issue is reserved for future work. In addition, Ghatak *et al.*¹⁸ postulated that for a thin PDMS film adhering to glass, the surfaces are not in perfect contact and have an average separation of ~2 nm. It is possible that the air is escaping through this region or that this initial separation allows the air to create channels along the interface.

6.4 Summary and Conclusions

The healing dynamics of a blister have been studied using a simple system of a flexible glass cover slip healing against a PDMS film. Wavelength of the fingering instability around the periphery of the blister varies with film thickness as $\lambda = 4h_{PDMS}$. This result agrees with previous studies on the fingering instability formed between glass and PDMS^{9,12}. Williams's equation³ is used to calculate the energy release rate for the blister. For thin PDMS films ($h_{PDMS} < 10$ nm), the energy release rate, 42 mJ/m², is close to the previously reported value for the work of adhesion between glass and PDMS¹⁷, 44 mJ/m². As the thickness of the PDMS film is increased, the energy release rate calculated using Williams's method under predicts the work of adhesion, 44 mJ/m². To resolve this issue, a future work will develop a model to take into account the deformation of the PDMS film around the contact line.

A modified version of Darcy's law was used to determine a permeability coefficient for the air escaping from the blister. The permeability coefficient was found to be a function of the PDMS film thickness, $k_D \propto h_{PDMS}^{1.5}$. As the value of the exponent is greater than 1, this strongly suggests that the air must be escaping through a combination of mechanisms. We propose that in addition to the diffusion of air through the PDMS film, it also diffuses through the PDMS/glass interface. Evidence for this interfacial mechanism is provided by the channel networks formed in the final stages of the blister life. Interfacial diffusion is an important mechanism occurring in natural processes such as the rotting of ice¹⁹ or the growth of bio-films²⁰. The experimental system developed in this work provides a model system to study interfacial diffusion. Future work should be focused on a more detailed analysis of the problem so that the diffusion (D) and solubility (S) coefficients of air in PDMS can be extracted. This addition would provide a simple, low cost technique to determine the values of D and S in thin polymer films.

6.5. References

- (1) Townes, D. A.; Talbot, T. S.; Wedmore, I. S.; Billingsly, R. *Journal of Emergency Medicine* **2004**, *27*, 161–165.
- (2) Dannenberg, H. *Journal of Applied Polymer Science* **1961**, *5*, 125–134.
- (3) Williams, M. L. *Journal of Applied Polymer Science* **1969**, *13*, 29–40.
- (4) Gent, A. N.; Lewandowski, L. H. *Journal of Applied Polymer Science* **1987**, *33*, 1567–1577.
- (5) Briscoe, B.; Panesar, S. *Proceedings of the Royal Society A* **1991**, *433*, 23–43.
- (6) Condon, J. B.; Schober, T. *Journal of Nuclear Materials* **2007**, *207*, 1–24.

- (7) Hutchinson, J. W.; Suo, Z. *Advances in Applied Mechanics* **1992**, 29, 63–191.
- (8) Hutchinson, J. W.; Thouless, M. D.; Linger, E. G. *Acta Metall. Mater.* **1992**, 40, 295–308.
- (9) Ghatak, A.; Chaudhury, M. K. *Langmuir* **2003**, 2621–2631.
- (10) Hull, D. *Acta Materialia* **1997**, 45, 233–244.
- (11) Thouless, M. D. *J. Am. Ceram. Soc.* **1993**, 76, 2936–2938.
- (12) Ghatak, A.; Chaudhury, M. K.; Shenoy, V.; Sharma, A. *Physical review letters* **2000**, 85, 4329–32.
- (13) Mönch, W.; Herminghaus, S. *EPL* **2001**, 53, 525–531.
- (14) Shenoy, V.; Sharma, A. *Physical Review Letters* **2001**, 86, 119–122.
- (15) Landau, L. D.; Lifshitz, E. M. *Theory of Elasticity*; 3rd ed.; Elsevier, 1986; pp. 38–42.
- (16) Obreimoff, J. *Proceedings of the Royal Society of London. Series A* **1930**, 127, 290–297.
- (17) Ghatak, A.; Mahadevan, L.; Chaudhury, M. K. *Langmuir* **2005**, 19, 1277–1281.
- (18) Ghatak, A.; Mahadevan, L.; Chung, J. Y.; Chaudhury, M. K.; Shenoy, V. *The Royal Society* **2004**, 460, 2725–2735.
- (19) Nye, J. F. *Journal of Crystal Growth* **1991**, 113, 465–476.
- (20) Wilking, J. N.; Zaburdaev, V.; De Volder, M.; Losick, R.; Brenner, M. P.; Wertz, D. A. *Proceedings of the National Academy of Sciences of the United States of America* **2013**, 110, 848–852.

CHAPTER 7

Summary and Future Work

7.1 Summary

This work investigated several problems in the area of surface modification. The first investigation focused on the problem of characterizing the elastic modulus of a thin sol-gel film and its relationship to the fracture properties of an epoxy/sol-gel/aluminum joint. To study these properties a mixture of fracture mechanics and metrology techniques were used. The modulus of the sol-gel film was rigorously evaluated using a buckling instability technique and to study interfacial fracture, we utilized the ADCB technique. Second, a detailed study was performed on the inchworm type motion of a drop that results when it is sandwiched between two surface energy gradients. To perform this study, a new technique to manufacture surface gradients was developed. The motion of the drop was studied as a function of driving frequency and was well described with a simple theory. Finally, the healing of a blister formed between a glass cover slip and a thin PDMS film was studied. To investigate this phenomenon we designed an experiment which tracked the radius and height profile of the blister as a function of time. A rudimentary analysis of the diffusion of air from inside the blister to the surroundings provided evidence for an interfacial diffusion process.

The motivation for the first investigation originated from the difficulties involved in evaluation of the elastic modulus of an adhesion promoting sol-gel film. Evaluating the modulus of nanometer thick sol-gel films is a problem for conventional techniques such as nano-indentation. To circumvent this issue, the elastic modulus of a sol-gel was determined using the technique of buckling instability. This method was used to determine the elastic modulus as a function of different curing conditions. Elastic modulus was found to be a strong function of curing temperature up to 85 °C. Increasing the cure temperature above this value did not yield any substantial change in the elastic modulus. An empirical correlation between the modulus of the sol-gel coating and its adhesive performance was found; when the elastic modulus of the sol-gel coating was increased above a critical value of ~50 MPa, the adhesive performance of an epoxy/sol-gel/aluminum joint decreased. This trend was identical for joints tested in wet and dry conditions, suggesting that interpenetration of the epoxy into the sol-gel film is more important to the formation of a durable adhesive joint than a high level of cross linking in the film. The change in the buckling morphology due to humid exposure qualitatively showed that increasing the cure temperature of the sol-gel film increases its barrier properties.

The effect of hydrophobic additives on the material barrier and adhesive properties of the sol-gel film was investigated. The buckling instability technique proved to be an effective method to study the elastic modulus as a function of the chemical composition of the sol-gel film. It was found that decreasing the length of the alkyl chain on the silane component of the sol-gel film led to an increase in the elastic modulus of the film. Salt spray studies and buckling experiments found that increasing the level of MTEOS in the

sol-gel coating increased the barrier properties of the coating, especially at high cure temperatures. Presumably the combined effect of higher crosslink density and the hydrophobic functional groups are responsible for the improvement of barrier properties. Both the critical and threshold fracture energies were found to decrease as the level of MTEOS was increased in the sol-gel film and this was attributed to an increase in the modulus of the film and the reduction of epoxide functional groups in the coating. It is theorized that techniques which improve the sol-gel coating barrier properties do not directly translate to increasing the durability of a sol-gel reinforced joint.

A detailed study examining the interplay of various sol-gel processing parameters on the strength of an epoxy/sol-gel/aluminum joint was performed. The parameters studied were sol-gel concentration, curing temperature and surface morphology. Increasing the cure temperature of the thin sol-gel films on FPL etched and grit-blasted surfaces was found to improve both the threshold (G_{th}) and critical fracture energies (G_c). For sanded surfaces, increasing the cure temperature improved G_{th} , while reducing G_c . Polished surfaces show a significant decrease in the adhesive performance of a thin sol-gel film when it is cured at high temperatures. Increasing the cure temperature of thick sol-gel films (~250 nm) lead to a significant decrease in both G_c and G_{th} for polished, FPL etched and sanded surfaces. This finding strongly suggests that there is a critical thickness above which a highly cross linked sol-gel film fails to perform as an effective adhesion promoter. This effect was not present for room temperature cured films due to the high level of interpenetration of the epoxy into the partially cured sol-gel layer. This set of experiments revealed that the sanded and grit-blasted surfaces yield significantly different fracture energies.

To distinguish between the macro-rough grit-blasted and sanded surfaces, the fractal dimension was evaluated. It was found that the fractal dimension is the same for grit-blasted and sanded surfaces. This finding correlated well with current literature on bulk fracture, which has proposed a universal value of the fractal dimension for fracture surfaces. An anomalous diffusion coefficient of the surface was found to be a more effective method to distinguish the two surface pretreatments. These results permitted the development of a qualitative theory relating the surface morphology to the fracture toughness of a joint. The underlying principle of the theory is that processes are controlled by low frequency events. In fracture surfaces, such low frequency events are physically manifested as large changes in surface height. Therefore, the roughening method that produces a surface with a higher probability of large changes in surface height will exhibit a higher fracture energy.

A new technique to prepare surface energy gradients was developed to study the motion of a water drop between two surfaces possessing a chemical gradient. This technique uses a filter paper saturated with dodecyltricholosi-lane placed at an angle over the target surfaces for 5 minutes. By changing the angle of deposition, the length and steepness of the gradient could be controlled. In addition, a radial gradient could be prepared by folding the filter paper source into a cone. This technique offers a simple and flexible way to prepare gradient surfaces of multiple shapes and sizes. The initial work of Daniel et al¹, motivated the detailed study of the inchworm motion of a drop as it is sandwiched between two gradient surfaces. The velocity of the drop as a function of driving frequency was described using a simple relationship between the average step size and the frequency. A more detailed model was developed to predict the motion of

the advancing and receding contact lines of the drop. The model was found to be in good agreement with the experimental data for a 10 μl drop. The model was not able to replicate the motion of a 20 μl drop due to elliptical deformation of the drop upon compression. The step wise motion of a drop is important in a number of applications, in particular, digital fluidic applications for miniaturized batch processes on a chip.

Finally, the healing of a blister controlled by a hydrodynamic process was investigated. A simple experiment was conceived to monitor the healing of a blister formed between a piece of cover glass and a thin PDMS film. The formation of interference patterns between the glass and PDMS permitted the height profile of the blister to be measured as a function of time. The profile of the blister was fit using the simple beam equation solved for fixed boundary conditions. Motivated by the quality of this fit, the number of moles in the blister was expressed as function of the blister radius by combining the ideal gas law and Williams's equation. Using this relationship with a modified version of Darcy's law, the Darcy permeability coefficient was evaluated as a function of thickness. The permeability coefficient was found to vary with film thickness as, $k_D \propto h_{PDMS}^{1.5}$. If the air is escaping via diffusion through the PDMS annulus, then we would expect an exponent of one. As the exponent is greater than one the air must be escaping through an additional mechanism. Through the observation of the final life of a blister, we conjecture that this mechanism is interfacial diffusion. This experiment proved that hydrodynamic effects can be very important in the healing of simple systems and, therefore, has implications in the analysis of complex biological systems which form and heal through complex diffusion processes.

7.2 Future Work

7.2.1 Elastic modulus of ultra thin sol-gel films

It has been shown theoretically and experimentally that the surface of an amorphous polymer film has a lower modulus than the bulk²⁻⁴. Using the method of buckling instability, the elastic modulus of thin polystyrene (PS) and polymethylmethacrylate (PMMA) films was shown to decrease with film thickness below a critical length scale of 40 nm⁴. A simple two layer buckling model was able to explain this decrease by assuming a thin low modulus layer on the surface of the polymer. Is this also the case for ultra thin films formed through the sol-gel technique? If so, then the low modulus surface layer may permit a greater level of interpenetration of the epoxy into the sol-gel film. This could explain why the fracture does not occur at the epoxy/sol-gel interface, even for fully cured films (see Chapter 4). Preliminary buckling experiments on ultra thin (~11 nm) zirconia films cured at 120°C for 30 minutes have estimated the elastic modulus to be ~10 GPa, Figure 7.1. This value is somewhat lower than that reported in the literature (~30 GPa) for similar systems⁵. The discrepancy could be due to a low modulus layer on the surface of the zirconia film. In addition, when the film is exposed to moisture, the buckles relax significantly, suggesting that water is able to penetrate and swell the film. A systematic study using the buckling instability to estimate the modulus of the sol-gel film as a function of thickness would test this hypothesis. Neutron and x-ray reflection studies on thin (h<10 nm) films of GTMS have shown the crosslink density of the film varies throughout the thickness⁶. This proposed study would evaluate the effect of this density variation on the observed modulus and provide insight on the internal structure of the film.

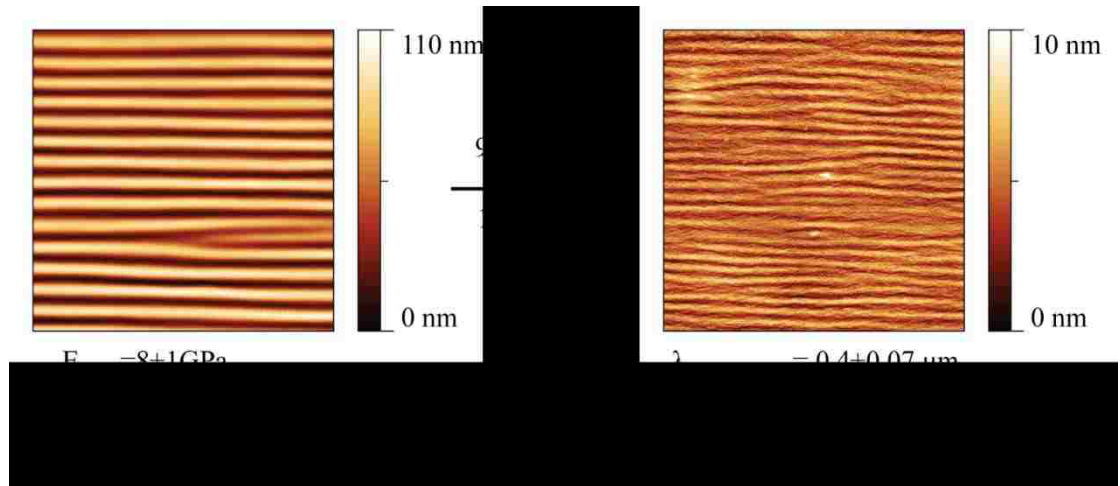


Figure 7.1: Elastic modulus and the effect of humidity on a thin (~10 nm) thick zirconia films prepared via the sol-gel process. The zirconia film was cured at 120°C for 30 minutes. E , λ , A and D represent the elastic modulus, buckling wavelength, buckle amplitude and flexural rigidity of the film. The elastic modulus of the film after humid exposure is not reported as the change in film thickness due to swelling is not known.

7.2.2 Systematic study on the role of micro/nano scale roughness and surface porosity on the fracture strength of an epoxy/aluminum joint

The fracture between an epoxy adhesive on a macro-rough or porous surface is an extremely complex three dimensional fracture problem. To increase our understanding of the adhesive mechanisms involved, it would be useful to study the fracture process using a simplified system. For example, if the roughness of the aluminum could be controlled on a micro or nano-meter level, then the effects of the spacing of defects/discontinuities, on the fracture strength could be easily studied. Previous work in this area has focused on 2D surface morphologies such as, grooves, sinusoidal, sawtooth and square waves⁷⁻¹¹. For 3D arrays of discontinuities, studies have mainly focused on purely elastic systems^{12,13}. These studies should be extended to metal/structural adhesive systems so that the simultaneous effects of crack direction and crack pinning maybe studied. This

study will enable the identification of the relative roughness length scales from the perspective of the fracture process zone, as discussed at the end of Chapter 4. Another model study would be to investigate the effect of the density of nanoscale pores on the adhesive system. The effect of surface porosity has been studied on the macroscale for an elastomeric adhesive¹⁴, but a detailed study on the effect of a nano-scale pores on the plastic deformation in a structural adhesive remains to be done.

A versatile surface patterning technique which could be used to address the above issues has been developed by Prof. Cheng at Lehigh University. A film comprised of silicon particles is first prepared on a glass surface using the method of Kumnorkaew et al¹⁵. The film of silicon spheres is then indented into the surface of an aluminum coupon, producing a surface morphology that is the negative imprint of the silicon sphere master. By controlling the radius of the particles, the final morphology on the aluminum surface can be tightly controlled. This surface would be an ideal way with which run the fracture experiments suggested in the previous paragraph. In addition performing phosphoric acid anodizing on these imprinted surfaces at the correct voltage causes the pores to form preferentially in the valleys of the impressions. Thus, by controlling the size of the silicon particles, the pore spacing can be controlled, producing an ideal surface to test the effect of porosity on fracture. As the surface profile is now known, observation of the change in the size of the plastic zone after fracture would provide information on the effect of surface morphology and porosity (on the plastic deformation) in the adhesive.

7.2.3 Measurement of the diffusion of water in a thin sol-gel film

In a humid environment, failure of an epoxy/sol-gel/aluminum joint can be through either the dissolution of the sol-gel film or due to damage to the aluminum oxide layer¹⁶⁻¹⁹. In both cases water must penetrate into the sol-gel layer. Knowledge of the rate of diffusion of water into a sol-gel layer as a function of film cure temperature and chemical composition would be extremely useful in the prediction of joint strength in humid environments. To determine the rate of diffusion of water into a sol-gel film two techniques could be used. If the rate of swelling of the film with water is low then variable angle spectroscopic ellipsometry could be performed using a fluid cell to measure the change in height over time. Information regarding the diffusion coefficient could then be extracted from the rate of change in height. It may also be possible to estimate the interaction coefficient for the water and sol-gel from the total swelling ratio. The second method is to use buckling instability to monitor the diffusion into the film^{20,21}. This method is accomplished by first capping the film with a barrier coating and then making defects in the barrier layer. When the system is exposed to solvent vapor, the vapor will diffuse into the film through the defects; as the solvent swells the film this will cause a buckling instability to form in the barrier layer, Figure 7.2. The diffusion coefficient for the system can be estimated by tracking the front of this instability²¹.

Preliminary work on a 400 nm thick sol-gel film cured at room temperature was performed. The sol-gel film was spin coated on a silicon wafer. In order to create a barrier layer, a ~10 nm thick layer of AuPd was sputter deposited on the surface. The sample was then placed in a humid environment for 15 hours. Examination of the sample after humid exposure showed a series of buckling patterns on the surface around natural

defects and also around a scratch on the surface, Figure 7.3. Close inspection of the buckling pattern at the scratch shows a transition from isotropic buckling to 1D buckling because the compressive stress cannot be transferred across the scratch. The length of this transition region would give a direct measure of the stress decay zone from which material properties could be found.

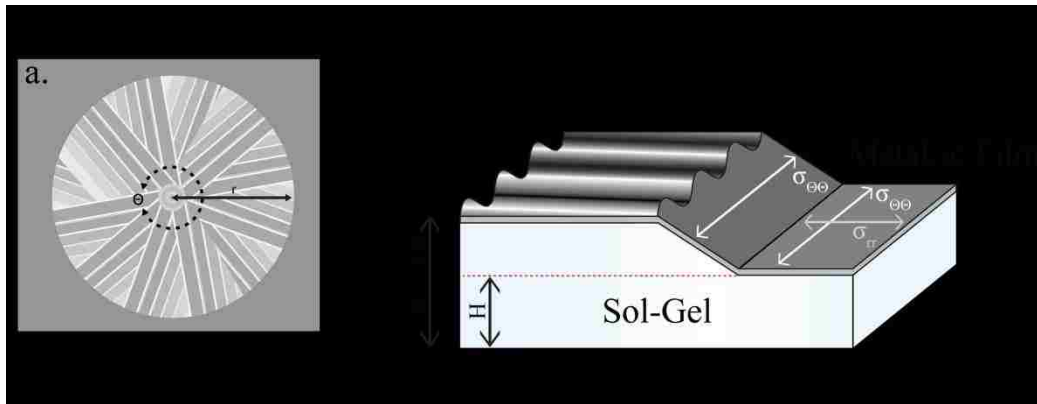


Figure 7.2: Schematic of buckling patterns induced by the swelling of a metal capped sol-gel film in a humid environment.

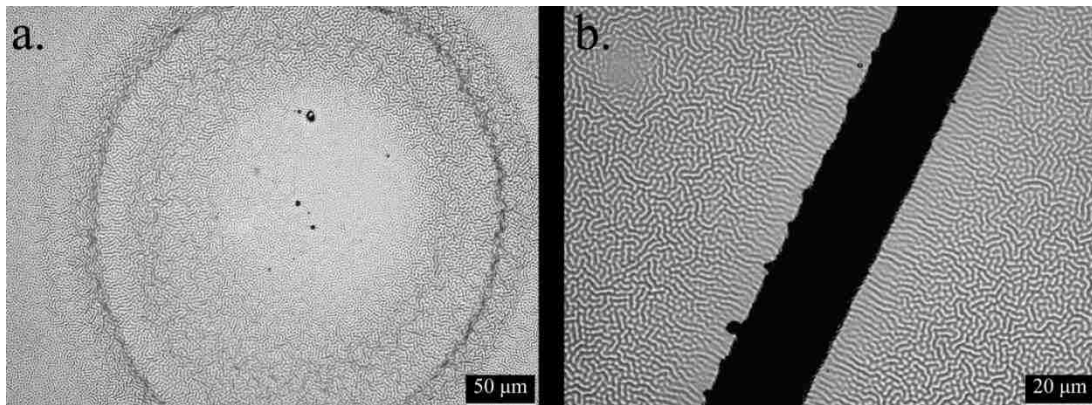


Figure 7.3: Buckling patterns formed by exposing a 400 nm thick sol-gel film capped with a 10 nm thick AuPd layer to ~98% RH for 15 hrs. a. Buckling Pattern formed around a natural defect in the AuPd coating. b. Buckling pattern formed around a scratch in the film.

7.2.4 Effect of metal alkoxides as additives in the sol-gel formulation.

In Chapter 4 we found that the highest fracture energy (G_c and G_{th}) for an epoxy/sol-gel/grit-blasted aluminum joint occurs when the curing temperature is 120°C. As we elevate the cure temperature, the cross link density of the sol-gel film increases, raising the elastic modulus²². The mechanism responsible for increasing the cross link density in this system is the condensation reaction occurring between the silanol groups on the hydrolyzed GTMS. As it is impractical to cure large aircraft parts at elevated temperatures, it is desirable to seek a room temperature curing catalyst. The effect of different metal alkoxides on the hydrolysis, condensation, epoxy ring opening, solution and gel structure have been extensively studied by Hoebbel et al²³⁻²⁷. The effect of metal alkoxides on the condensation degree of GTMS follows this reactivity hierarchy, $Si(OEt)_4 \ll Sn(OBu^t)_4 < Zr(OBu^n)_4 < Al(OBu^s)_3 < Al(OEtOBu)_3 < Ta(OEt)_5 < Ti(OEt)_4$ ²³. Discounting TEOS, the degree of epoxy ring opening follows the reverse trend. From this hierarchy, titanium based alkoxides increase the level of condensation vs. zirconium based alkoxides. Therefore, the addition of titanium-n-propoxide (TPOT) to the sol-gel solution should increase the rate of room temperature cure. Preliminary experiments were conducted to investigate the effect of replacing TPOZ with TPOT in the sol-gel formulation on a one to one molar basis. Due to the increased reactivity of the TPOT a stronger complexing agent, acetyl acetone, was used to stabilize the TPOT before adding it to the GTMS/water solution. The GAA was added directly to the GTMS/water mixture. All TPOT modified sol-gel solutions were found to underperform the standard sol-gel solution, Figure 7.4. The difference between the fracture energies at different cure temperatures for the TPOT films is less pronounced than for the TPOZ

films. However, as these are the preliminary results, other metal alkoxides and/or different concentrations of TPOT with different complexing agents should be investigated as room temperature curing catalysts. It should be noted that due to the importance of forming an IPN between the epoxy adhesive and sol-gel film the cross-link density of the sol-gel film should not be too high. The ideal situation would be to produce a fully cross-linked network which still permits the interpenetration of the epoxy; this issue is brought up in the next section.

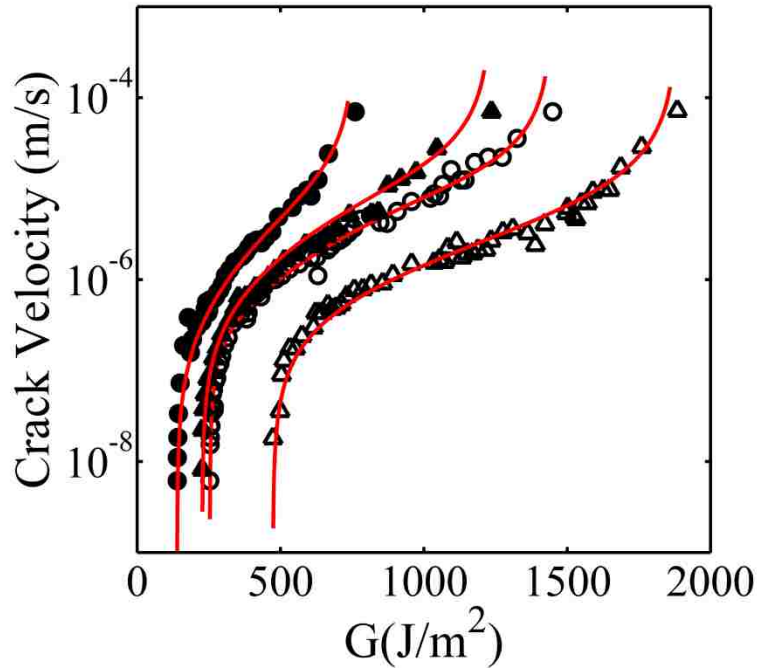


Figure 7.4: Crack velocity vs. energy release rate for epoxy/sol-gel/grit-blasted Al joints for TPOT modified sol-gel coatings. The filled circles and triangles represent the results for the TPOT modified coating cured at room temperature (50% RH, 75 mins) and 120 °C (30 mins) respectively. The open circles and triangles represent the results for the standard sol-gel coating cured at room temperature (75 mins) and 120 °C (30 mins) respectively.

7.2.5 The use of amine functionalized silanes to form hybrid organic-inorganic sol-gel films for adhesion promotion

While evidence exists to suggest that epoxy ring opening occurs during the reaction of GTMS with TPOZ²³, the resultant hydroxyl groups do not appear to react further to form crosslinks under low temperature sol processing conditions²⁸. Therefore, the backbone of the sol-gel network is principally inorganic in nature. One can then speculate that by increasing the number of organic crosslinks, the film toughness and barrier properties may increase. In addition, the porosity of the film to epoxy may also be increased, promoting the formation of an IPN. An effective technique to adjust the ratio of organic to inorganic crosslinks in the film is to introduce a silane with amine functionality²⁹. These amine silanes react with the epoxy group on the GTMS molecule to form organic crosslinks. Preliminary experiments using Aminoethylaminopropyltrimethoxysilane (AEAPTMS) in the sol-gel solution in a stoichiometric ratio to GTMS were performed. AEAPTMS is added to the sol-gel solution 5 minutes before coating the solution. The reasoning for this is that the amino groups can catalyze the condensation reactions and cause rapid gelation in the sol before coating, which leads to non-uniform coatings³⁰.

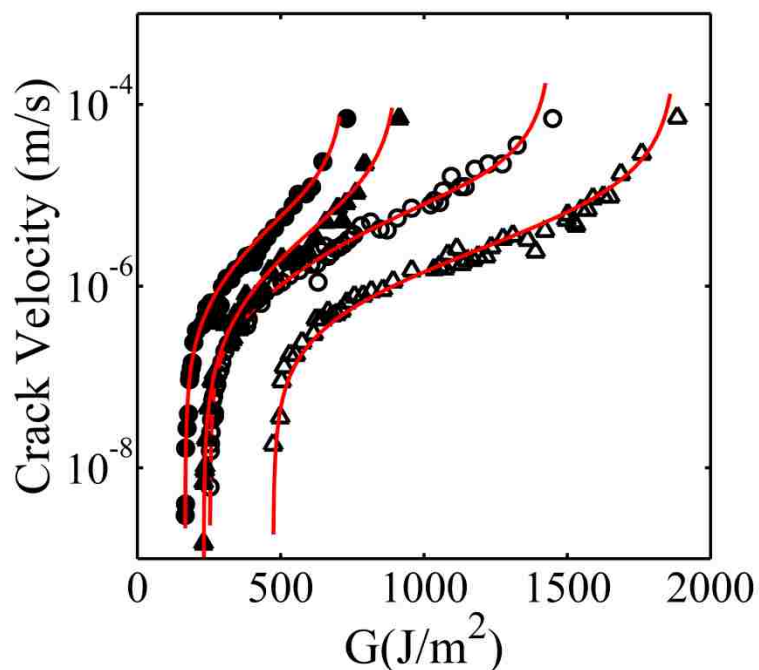


Figure 7.5: Crack velocity vs. energy release rate for epoxy/sol-gel/grit-blasted Al joints for AEAPTMS modified sol-gel coatings. The filled circles and triangles represent the results for the prehydrolyzed AEAPTMS modified coating cured at room temperature (50% RH, 75 mins) and 120 °C (30 mins) respectively. The open circles and triangles represent the results for the standard sol-gel coating cured at room temperature (75 mins) and 120 °C (30 mins) respectively.

The amine additive reduces the adhesive performance of the coating. One possible reason for this could be that the amino group can absorb strongly on the aluminum surface blocking potential sites for covalent linkage between the aluminum oxide and the TPOZ. As many amino silanes are available and a range of concentrations has not been tested here, it is possible that an effective coating could be produced as amino-silanes have seen use in both adhesion promoters and barrier coatings²⁹. An additional consideration is the catalytic potential of the amine group to increase the rate of condensation of silanol groups³⁰. This catalytic activity has only been studied in the

solution³⁰. Using the method of buckling instability this future work would also determine if the catalytic activity is still present when the sol-gel is in the form of a condensing thin film.

7.2.6 The effect of nanoscale surface roughness on contact angle hysteresis

On the linear energy gradients formed in Chapter 5 we observed a large change in the contact angle hysteresis in the region just before the onset of the gradient. AFM examinations of this region found a varying nano-scale morphology on the surface. The model developed by Joanny and De Gennes³¹ to explain contact angle hysteresis suggested that hysteresis occurs only when the strength of a surface defect reaches a critical value. More recently, using an AFM tip containing small defects researchers have found this critical value to be on the order of ~1 nm for a morphological heterogeneity³². The formation of the nano-scale morphology in our experiments offers an opportunity to further investigate the effect of nano-scale roughness on hysteresis. Surfaces of different nano-scale morphology could be generated via a simple modification to the filter paper technique presented in Chapter 5. If the filter paper is wet with silane and then held above a glass surface at different heights in a controlled environment it should be possible to form different nano-scale morphologies on the surface. Contact angle experiments and AFM scans on the surfaces would then allow for a detailed study to be conducted. In addition a more accurate way of characterizing the morphology, instead of RMS, could be developed from the roughness work presented in Chapter 4.

7.2.7 A simple experiment to determine the solubility coefficient of a gas in a thin polymer film

Chapter 6 presented a detailed study of the healing of a blister formed between a glass cover slip and PDMS film. The rate of healing was controlled by the escape of the air trapped inside the blister. Using this simple experiment it may also be possible to determine the solubility of a gas in a thin polymer film. When the air filled blister is trapped between the glass cover slip and PDMS film, it shrinks over time as the air escapes. If the initial radius of the blister is below a critical size, then the blister will disappear almost instantly. One possible explanation of this effect is that the pressurized air in the blister can be fully absorbed in the PDMS region directly below the blister, i.e. no radial diffusion is required. A preliminary model of this effect follows. The total number of moles contained within the blister maybe written as,

$$n_{blister} = \frac{V}{\bar{R}T} (P_0 + P) \quad (7.1)$$

where $n_{blister}$, V , \bar{R} , T , P_0 and P are the number of moles in the blister, volume of the blister molar gas constant, temperature, atmospheric pressure and pressure difference across the glass cover slip respectively. From Chapter 6 the volume and pressure difference can be expressed in terms of the blister radius as,

$$V = \frac{\pi PR^6}{192D} \quad \& \quad P = \frac{\sqrt{128DW_a}}{R^2} \quad (7.2)$$

where D is the flexural rigidity of the glass cover slip, R the blister radius and W_a the work of adhesion. Substituting 7.2 into 7.1 an expression for the total number of moles as a function of blister radius is obtained,

$$n_{blister} = \frac{\pi}{RT} \left(P_0 R^4 \sqrt{\frac{W_a}{288D}} + \frac{2}{3} W_a R^2 \right) \quad (7.3)$$

The additional number of moles that can be absorbed by the PDMS film due to the increase in the air pressure caused by the blister is,

$$\Delta n_{PDMS} = S\pi R^2 h_{PDMS} (P + P_0) - S\pi R^2 h_{PDMS} P_0 \quad (7.4)$$

where S is the solubility and h_{PDMS} is the thickness of the PDMS film. At a critical radius, R_{crit} , where the blister disappears rapidly the above theory assumes the condition that $n_{blister} = \Delta n_{PDMS}$. Equating eqs. 7.3 and 7.4 we arrive at,

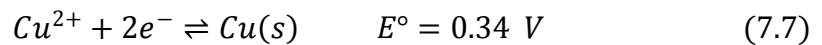
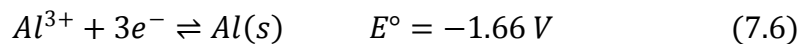
$$AR_{crit}^4 + BR_{crit}^2 = Sh_{PDMS} \quad (7.5)$$

where $A = \frac{P_0}{192RTD}$ and $B = \sqrt{\frac{W_a}{288D}}$. By evaluating the critical radius for different PDMS film thicknesses a plot of the left hand side of equation 7.5 vs. h_{PDMS} should yield a straight line with a gradient equal to the solubility of the polymer. By controlling the environment, other gases would be easily studied. The main difficulty in the implementation of this technique is the formation of a blister with a well defined radius. This could be done using a series of metal punches on the glass cover slip to force the size of the blister. If such a technique was effective it would provide an extremely cheap and easy way to measure the solubility of gases in thin polymer films. Care must be taken that the interfacial diffusion process, described in Chapter 6, does not lead to large errors in the estimation of the solubility.

7.2.8 Electroless deposition of copper through a hydrogel

Preliminary investigations on the electroless deposition of copper on aluminum surfaces have been conducted. The deposition is performed from a hydrogel swollen in a 0.4M CuSO₄ solution. Conducting the deposition through a gel instead of a liquid causes the copper to deposit in well-defined regions. In addition, the copper deposits are confined to the interface formed between the gel and the aluminum. This section will briefly introduce the background of electroless deposition and then review current work and propose future directions for study.

When a copper sulphate solution is placed in contact with an aluminum surface, the copper ions will be reduced and deposit on the surface. The reaction can be explained in terms of the electrochemical series by using the standard electrode potentials of copper and aluminum to calculate the overall potential for the reaction cell. The electrode potentials of the reduction of copper and aluminum along with the potential for the overall reaction cell are given in equations 7.6-7.8³³,



where E° is the standard electrode potential for a 1 molar solution vs. a standard hydrogen electrode at 25 °C and 1 atm. The Gibbs free energy of the reaction can be expressed as $\Delta G_{cell}^{\circ} = -nF\Delta E_{cell}^{\circ}$, where n is the number of moles of electrons per mole of product and F the Faraday constant. The Gibbs free energy for the reaction given by equation 7.8 is negative, thus, the deposition of copper will occur spontaneously. It should be noted that while equations 7.6 and 7.7 are the dominant electrochemical

reactions involved in the deposition, both copper and aluminum can form a variety of species during oxidation and reduction. During the electroless deposition of copper onto aluminum, a random distribution of cathodic and anodic sites will form on the surface³⁴. Here the anodic reaction is the oxidation of aluminum and the cathodic reaction the reduction of the copper (II) ions. The reaction will proceed until a $\sim 1 \mu\text{m}$ thick copper film is formed on the surface of the aluminum³⁴. The copper coating then acts as a barrier layer and prevents further dissolution of the aluminum, which terminates the reaction. To continue copper deposition beyond this point, it is necessary to introduce a reducing agent, such as formaldehyde, to the system. For all experiments reported here, no reducing agent is used.

The experimental set up is shown in Figure 7.6. A physically crosslinked poly(N-(hydroxymethyl)-acrylamide) gel is formed in the shape of either a cylindrical block or a lens. The gels are then swollen in a 0.4M copper sulphate solution for a minimum of 4 days. In a typical experiment, a gel is removed from the copper sulphate solution, blown with N_2 to remove the excess water, and then clamped to an aluminum surface. The glass plate used to clamp the gel is pretreated with a monolayer of dodecyltrichlorosilane. The aluminum is cleaned and grit-blasted according to the procedures outlined in Chapter 3. The deposition experiments are performed in a humid environment ($\sim 98\%$ RH) or in mineral oil. The elastic modulus of the gel and the work of adhesion of the gel to a glass sphere are found to be $\sim 150 \text{ kPa}$ and 100 mJ/m^2 , respectively using a traditional JKR technique^{35,36}.

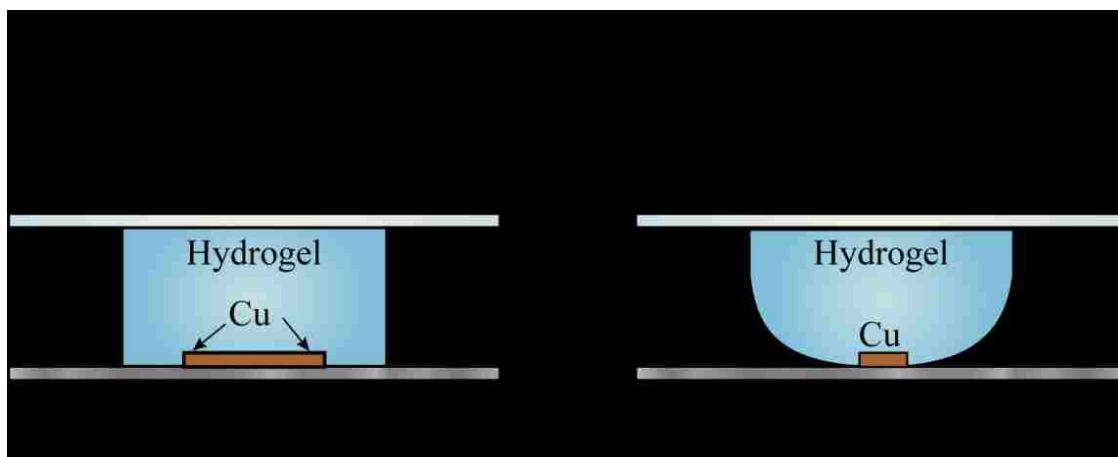


Figure 7.6: Schematic of the experimental setup for electroless deposition of copper. The typical height of the swollen hydrogel cylinder is ~4.5 mm. The hydrogel cylinder is compressed to a height of 3 mm for the deposition experiment. The average height of the swollen hydrogel lens is ~12 mm. The lenses are compressed by 1-2 mm when they are clamped to the aluminum surface.

When the deposition is conducted in a humid environment from a cylindrical gel, the copper deposition initially occurs uniformly over the region of contact between the gel and the aluminum. After this preliminary stage, the copper deposit forms primarily in a central circular region, Figure 7.7a. The deposition is minimal in an annular region at the edge of the gel. At long deposition times the outer edge of the copper deposit turns black, suggesting the formation of copper oxide. During the deposition process conducted in a humid environment, the gel shrinks due to the evaporation of water. To avoid the occurrence of shrinkage, the experiment was performed by immersing the gel and aluminum in a mineral oil environment.

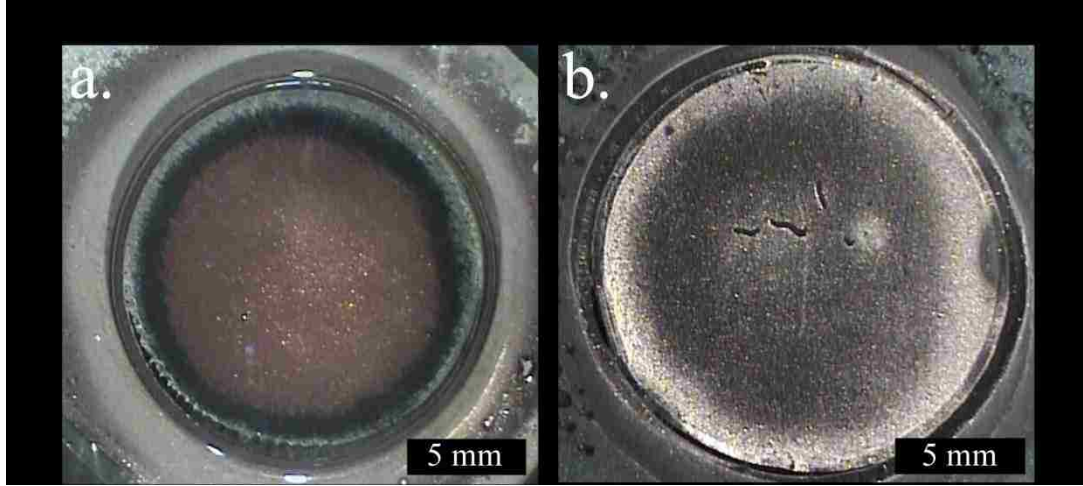


Figure 7.7: a. Electroless deposition of copper from a hydrogel clamped to a grit-blasted aluminum surface. The deposition time was 20 hours and the experiment was conducted in a humid environment at ~98%RH. b. Electroless deposition of copper from a hydrogel clamped to a grit-blasted aluminum surface. The deposition time was 20 hours and the experiment was conducted in an oil environment to prevent shrinkage of the gel.

When the deposition is performed in an oil environment the copper deposits uniformly on the aluminum surface, Figure 7.7b. The well defined annular region of low copper deposition formed during the deposition in a humid environment is no longer observed. It is possible that this annular region forms due to a change in the stress distribution in the gel when the deposition is performed in a humid environment. As evaporation of water from the gel will occur preferentially at the edges, we expect the compressive stress in these regions to be somewhat relaxed. To test this theory we investigated the deposition from a hydrogel lens.

When a soft gel lens is compressed against a rigid glass surface the stress distribution inside the lens can be defined from the following equation³⁷,

$$\sigma(r, 0) = \sqrt{\frac{2WE}{\pi a(1 - \nu^2)}} \frac{1}{\sqrt{1 - r^2/a^2}} - \frac{2aE}{\pi R(1 - \nu^2)} \sqrt{1 - r^2/a^2} \quad (7.9)$$

where σ is the normal stress at the interface, W the work of adhesion, E the gel modulus, ν the gel Poisson ratio, R the radius of curvature of the lens, a the radius of contact and r the position within the contact zone. Equation 7.9 makes the following assumptions: the rigid surface is smooth and flat, the interface is frictionless, both materials are in the linear elastic regime, the modulus of the gel is much smaller than that of the glass and the ratio of the contact radius to the radius of curvature of the lens is small, $a/R < 0.4$ ³⁷. The stress profile calculated using the system parameters of $E=150$ kPa, $W=100$ mJ/m², $R=27$ mm and $a=7.5$ mm is shown in Figure 7.8. The magnitude of the compressive stress decreases towards the edge of contact before becoming tensile in a small outer region. The development of the tensile stress is due to the work of adhesion between the gel and aluminum surface. As our aluminum surface is rough, this tensile region will be smaller than that predicted by equation 7.9 due to the deformation of the gel at local asperities on the surface³⁸.

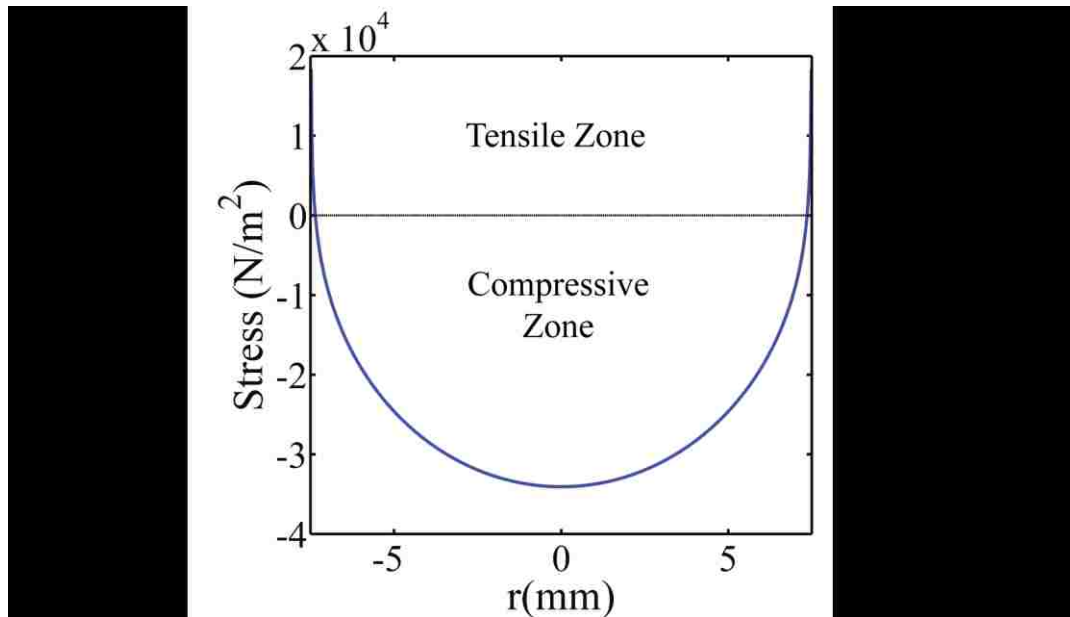


Figure 7.8: Stress distribution formed at the interface when a hydrogel is brought into contact with a rigid surface.

Figure 7.9a highlights the results from the deposition experiments performed using a hydrogel lens in an oil environment. The deposition patterns formed can be broken down into 5 different regions. Region 1 represents the central copper deposit; region 2, the black band of copper oxide; region 3, the annulus with a low level of copper deposition; region 4, a thin copper deposit forming around the initial edge of contact; and region 5, the additional contact area formed by the viscoelastic creep of the gel. Regions 1-3 are very similar to the patterns formed in the case of a cylindrical gel in a humid environment, Figure 7.7a. Regions 4 and 5 are unique to the lens. It is possible that region 4 is generated by the copper deposition from a thin band of water which is 'squeezed' out from the gel upon contact. The increase in contact area represented by region 5 is shown to increase with time, Figure 7.10. Inspection of the deposition pattern after the gel lens is removed (Figure 7.9b), reveals that region 5 has a white to light grey color. The corrosion product formed on aluminum in aqueous environments is generally $\text{Al}(\text{OH})_3$, which is insoluble in water and precipitates as a white gel³⁹. Therefore, the formation of this white deposit suggests that the aluminum was oxidized in region 5. A detailed surface analysis to ascertain the chemical composition of the 5 different regions would provide insight on the flow of charge between these different regions on the surface.

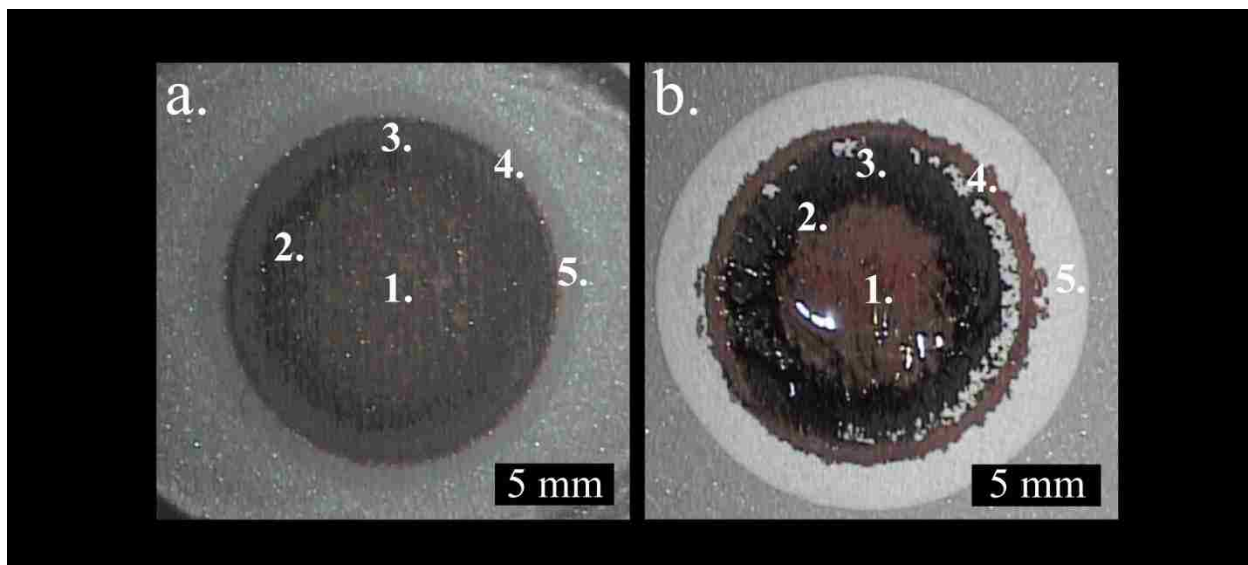


Figure 7.9: a. Electroless deposition of copper from a hydrogel lens clamped to a grit-blasted aluminum surface. The image was taken at deposition time of 20 hours for direct comparison with the results shown in Figure 7.7. The experiment was conducted in an oil environment. The regions labeled 1-5 are explained in the text. b. Image taken after the gel lens was removed from the aluminum after a deposition experiment lasting 140 hours. The regions labeled 1-5 are explained in the text.

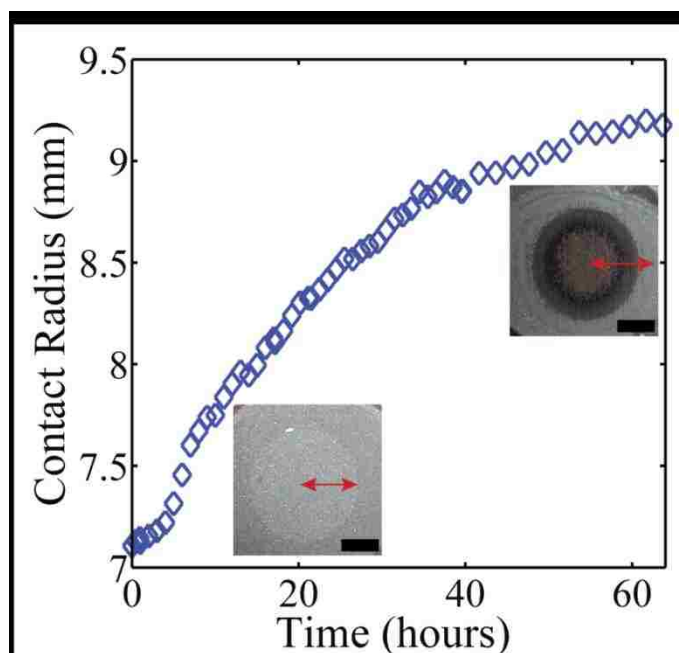


Figure 7.10: Increase in the contact radius of a gel clamped to a grit-blasted aluminum surface. The inserts of the deposition experiment correspond to the initial and final points on the curve. Black scale bars represent 5 mm

It is clear from these deposition patterns that the cathodic regions form in the center of contact and at the very edge of contact. The anodic regions appear to form in the annular regions at the edge of contact and in the region defined by the creep of the gel. A first hypothesis is that the level of compression within the gel is responsible for the formation of these deposition patterns. It is tempting to see if the size of the anodic annulus region corresponds with the size of the tensile zone. Using equation 7.9, we predict the size of the tensile zone to be 0.14mm. From Figure 7.9, we see that the size of this anodic region is 1.3 mm. Therefore, the formation of the anodic region cannot be explained by a change in the orientation of the stress field. In addition, the standard JKR equations^{35,37} do not accurately predict the area of contact, suggesting that the deformation in the gel is too large or that the shape of the gel cannot be approximated as a section of a sphere. At this point, it is not clear how the level of compression will change the activity of the copper ions, thus altering the deposition. In addition, some other factors must also be considered. As the surface is rough, it is not clear if the gel forms intimate contact with the aluminum surface in the contact zone. In order for the gel to maintain intimate contact with the rough surface at zero load, the work of adhesion must be sufficient to supply the necessary deformation energy for the gel to deform into contact. Therefore, we could be observing an effect of decreasing contact. This, in itself, would be a significant result as it would provide a unique way with which to characterize a material surface and/or extract the material properties of a gel. The change in stress distribution will also induce a flow of water inside the gel due to poro-elastic effects, which may alter the copper deposition. Finally, the hydrogel/oil interface is likely to be negatively charged, and whether this has any effect on the distribution of copper ions is unclear.

Future work in this area should initially focus on using ideal aluminum surfaces such as those formed by metal vapor deposition. If the deposition still occurs preferentially in the center, then the above surface roughness argument can be eliminated. This experiment was conducted using polished aluminum, but the results could not be accurately interpreted due to the removal of the inter-metallic particles during the polishing procedure. If, indeed, we are observing a stress induced deposition, this finding would have implications in the understanding of chemiosmotic processes in biological systems.

Finally, after the deposition experiment, the hydrogels become adhered to the aluminum surface. Presumably this is due to the trapping of the gel matrix within the copper deposit. By adding a reducing agent to the gel, it may be possible to get significant auto-adhesion of a gel to a metallic surface via electroless deposition. This method would present a novel means of adhering gels to metallic surfaces and could be used to coat metallic implants for use within the body.

7.7 References

- (1) Daniel, S.; Sircar, S.; Gliem, J.; Chaudhury, M. K. *Langmuir : the ACS journal of surfaces and colloids* **2004**, *20*, 4085–92.
- (2) Yoshimoto, K.; Jain, T. S.; Nealey, P. F.; de Pablo, J. J. *The Journal of chemical physics* **2005**, *122*, 144712.
- (3) Mansfield, K. F.; Theodorou, D. N. *Macromolecules* **1991**, *24*, 6283–6294.
- (4) Stafford, C. M.; Vogt, B. D.; Harrison, C.; Julthongpiput, D.; Huang, R. *Macromolecules* **2006**, *39*, 5095–5099.

- (5) Maddalena, A.; Raccanelli, A. *Journal of Non-Crystalline Solids* **1992**, *151*, 115–118.
- (6) Yim, H.; Kent, M. S.; Hall, J. S.; Benkoski, J. J.; Kramer, E. J. *The Journal of Physical Chemistry B* **2002**, *106*, 2474–2481.
- (7) Rider, A.; Arnott, D. *The Journal of Adhesion* **2001**, *75*, 203–228.
- (8) Janarthanan, V.; Garrett, P.; Stein, R.; Srinivasarao, M. *Polymer* **1997**, *38*, 105–111.
- (9) Kim, W.-S.; Yun, I.-H.; Lee, J.-J.; Jung, H.-T. *International Journal of Adhesion and Adhesives* **2010**, *30*, 408–417.
- (10) Vajpayee, S.; Khare, K.; Yang, S.; Hui, C.-Y.; Jagota, A. *Advanced Functional Materials* **2011**, *21*, 547–555.
- (11) Singh, A. K.; Bai, Y.; Nadermann, N.; Jagota, A.; Hui, C.-Y. *Langmuir* **2012**, *28*, 4213–22.
- (12) Chung, J. Y.; Chaudhury, M. K. *Journal of the Royal Society Interface* **2005**, *2*, 55–61.
- (13) Ghatak, A.; Mahadevan, L.; Chung, J. Y.; Chaudhury, M. K.; Shenoy, V. *The Royal Society* **2004**, *460*, 2725–2735.
- (14) Gent, A.; Lin, C. *The Journal of Adhesion* **1990**, *32*, 113–125.
- (15) Kumnorkaew, P.; Ee, Y.-K.; Tansu, N.; Gilchrist, J. F. *Langmuir* **2008**, *24*, 12150–7.
- (16) Abel, M.-L.; Allington, R. D.; Digby, R. P.; Porritt, N.; Shaw, S. J.; Watts, J. F. *International Journal of Adhesion and Adhesives* **2006**, *26*, 2–15.
- (17) Pavlovic, E.; Kramer, E. *The Journal of Adhesion* **2011**, *87*, 272–289.
- (18) Liu, J.; Chaudhury, M. K.; Berry, D. H.; Seebergh, J. E.; Osborne, J. H.; Blohowiak, K. Y. *The Journal of Adhesion* **2006**, *82*, 487–516.
- (19) Kinloch, a. J.; Korenberg, C. F.; Tan, K. T.; Watts, J. F. *Journal of Materials Science* **2007**, *42*, 6353–6370.
- (20) Vandeparre, H.; Damman, P. *Physical Review Letters* **2008**, *101*, 1–4.

- (21) Chung, J. Y.; Nolte, A. J.; Stafford, C. M. *Advanced Materials* **2009**, *21*, 1358–1362.
- (22) Longley, J. E.; Chaudhury, M. K. *Macromolecules* **2010**, *43*, 6800–6810.
- (23) Hoebbel, D.; Nacken, M.; Schmidt, H. *Journal of Sol-Gel Science and Technology* **2001**, *21*, 177–187.
- (24) Hoebbel, D.; Nacken, M.; Schmidt, H. *Journal of Sol-Gel Science and Technology* **2000**, *19*, 305–309.
- (25) Hoebbel, D.; Nacken, M.; Schmidt, H. *Journal of Sol-Gel Science and Technology* **1998**, *12*, 169–179.
- (26) Hoebbel, D.; Nacken, M.; Schmidt, H. *Journal of Sol-Gel Science and Technology* **1998**, *12*, 37–43.
- (27) Hoebbel, D.; Reinert, T.; Schmidt, H. *Journal of Sol-Gel Science and Technology* **1997**, *10*, 115–126.
- (28) Innocenzi, P.; Brusatin, G.; Guglielmi, M.; Bertani, R. *Chemistry of Materials* **1999**, 1672–1679.
- (29) Innocenzi, P.; Kidchob, T.; Yoko, T. *Journal of Sol-Gel Science and Technology* **2005**, *35*, 225–235.
- (30) Brusatin, G.; Innocenzi, P.; Guglielmi, M.; Mati, C. D. *Journal of Sol-Gel Science and Technology* **2003**, *26*, 303–306.
- (31) Joanny, J. F.; de Gennes, P. G. *The Journal of Chemical Physics* **1984**, *81*, 552–562.
- (32) Delmas, M.; Monthieux, M.; Ondarçuhu, T. *Physical Review Letters* **2011**, *106*, 136102.
- (33) Milazzo, G., Caroli, S., Sharma, V. K. *Tables of Standard Electrode Potentials*; Wiley: Chichester, 1978.
- (34) *Electroless Plating Fundamentals and Applications*; Mallory, G. O.; Hajdu, J. B., Eds.; William Andrew Publishing, 1991.
- (35) Johnson, K. L.; Kendall, K.; Roberts, A. D. *Proceedings of the Royal Society of London. Series A: Mathematical and Physical Sciences* **1971**, *324*, 301–313.
- (36) Chaudhury, M. K.; Whitesides, G. M. *Langmuir* **1991**, *7*, 1013–1025.

- (37) Maugis, D. *Contact, Adhesion and Rupture of Elastic Solids*; 1st ed.; Springer: Verlag Berlin Heidelberg, 2000.
- (38) Persson, B. N. J.; Tosatti, E. *The Journal of Chemical Physics* **2001**, *115*, 5597.
- (39) Vargel, C. *Corrosion of Aluminium*; Elsevier: Oxford - New York, 2004.

Appendix A

Preparation of sol-gel solution

The standard sol-gel solution used throughout this dissertation is based on the Boegel EPII formulation developed by The Boeing Company. The following materials are used to prepare the sol-gel solution: glycidoxypropyltrimethoxysilane (GTMS, Gelest), Zirconium-n-Propoxide (TPOZ, 70% w/w in propanol, Alfa Aesar), glacial acetic acid (GAA, Sigma Aldrich) and Antarox BL-240 (Rhodia Inc.) and de-ionized water (18 M Ω cm). The mixing procedure to prepare 100 ml of Boegel EPII is outlined below, the volume of the components is given in Tables A1 and A2.

1. Stir 100 ml of DI water in a 500 ml flask.
2. Add the GAA to a small glass vial.
3. Add the TPOZ to the GAA and shake mixture for 5 minutes. Mixture should become warm.
4. Add the GTMS to the DI water and mix for 5 minutes.
5. Slowly add the TPOZ+GAA mixture to the GTMS+DI water mixture and stir for 55 minutes at room temperature. Mixture should be clear to slightly cloudy.
6. Add 50 μ l Antarox BL-240 to the solution and mix for an additional 5 minutes.

For the MTEOS modified coatings the MTEOS is added in stage 4. Table A1 gives the composition of the x1, x3 and x7 formulations used in Chapters 3 and 4. Table A2 gives the composition of the MTEOS modified sol-gel solutions used in Chapter 3.

Formula Designation	Volume of GTMS/100 ml DI water (ml)	Volume of TPOZ/100 ml DI water (ml)	Volume of GAA/100 ml DI water (ml)	Volume of Anatrox/100 ml DI water (μ l)
x1	m	n	0.45	50
x3	3m	3n	1.35	150
x5	5m	5n	2.25	250
x7	7m	7n	3.15	350
x9	9m	9n	4.05	450

Table A1: Composition of standard sol-gel solutions. All values are per 100 ml de-ionized water. m and n represent the volumes used in the Boegel EPII formulation. The values for m and n are reported elsewhere^{1,2}.

MTEOS:GTMS molar ratio	Mole fraction of GTMS relative to MTEOS	Volume of MTEOS/100 ml DI water (ml)	Volume of GTMS/100 ml DI water (ml)
100:0	0	1.8	0
75:25	0.25	1.5	0.45
50:50	0.5	1	0.9
25:75	0.75	0.5	1.35
0:100	1	0	2

Table A2: Composition of MTEOS modified sol-gel solutions. The volumes of TPOZ, GAA and Antarox remain the same as given in Table A2 for the standard x1 formulation.

References

1. Blohowiak, K. Y.; Osborne, J. H.; Krienke, K. A. US Patent 5814137 **1998**.
2. Liu, J.; Chaudhury, M. K.; Berry, D. H.; Seebergh, J. E.; Osborne, J. H.; Blohowiak, K. Y. *Journal of Adhesion Science and Technology* **2006**, 20, 277–305.

Appendix B

Standard Salt spray tests on MTEOS modified sol-gel films

The standard sol-gel films modified with MTEOS were subjected to the following tests at Boeing:

1. Stand alone neutral salt spray for up to 168 hours as specified in BSS7249 on 2024-T3 bare aluminum.
2. Filiform corrosion using a non-chrome primer and topcoat as specified in BSS7258, Type I (includes non-chrome primer and topcoat) on 2024-T3 clad aluminum.
3. Dry/Wet crosshatch adhesion as specified in BSS7225, Type I and III, Class 5 (includes non-chrome primer and topcoat) on 2024-T3 bare and clad aluminum.

All tests were performed at Boeing using standard protocol and procedures as outlined in the Boeing standards. Two different concentrations of sol-gel were tested, one based on the standard x1 formulation and the other based on the x7 formulation, see Appendix A for details. To test the effect of MTEOS on the coating performance the molar ratio of MTEOS to GTMS was varied in the sol-gel. The results of tests 1-3 were then recorded as a function of MTEOS:GTMS molar ratio. Details of formulations are given in Appendix A.

For the filiform and adhesion tests, only the 100:0 MTEOS:GTMS coatings failed the criteria specified in BMS10-72 “Exterior Decorative Paint System”. Therefore, the results will not be covered in detail here. The results from the salt spray tests, showed a clear trend in the corrosion resistance as a function of coating formulation. Figure B1 shows the salt spray results for the sol-gel film cured at room temperature as a function of

the molar ratio of MTEOS to GTMS. The results for an elevated cure temperature of 120 °C for 30 minutes are given in Figure B2.

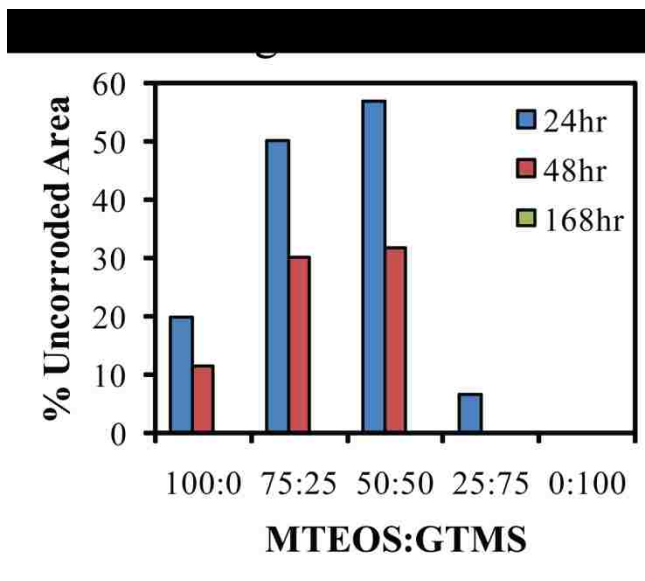


Figure B1: Salt spray test results as a function of the molar ratio of MTEOS to GTMS in the sol-gel film. All films were cured at 25°C for 30 minutes.

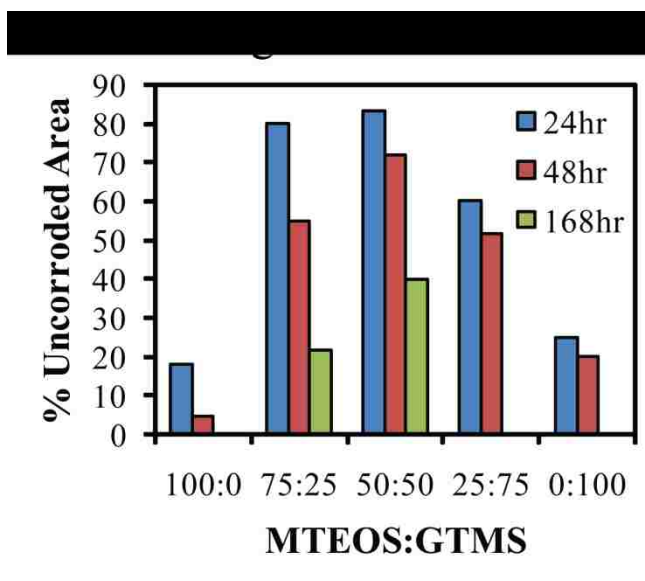


Figure B2: Salt spray test results as a function of the molar ratio of MTEOS to GTMS in the sol-gel film. All films were cured at 120°C for 30 minutes.

From Figures B1 and B2 we observe that that corrosion protection of the film increases with increasing cure temperature. The 75:50 MTEOS:GTMS coating exhibits the best performance both at room and elevated cure temperatures. The low performance of the 100:0 MTEOS:GTMS films may be due to film thickness effects; this formation produces the thinnest coatings, see Chapter 3. To conclude, the addition of MTEOS to the standard GTMS sol-gel formulation was found to improve the barrier properties as assessed using the standard salt spray test. This corresponds with the results presented in Chapter 3 which use the change in the buckling morphology to qualitatively predict the barrier properties.

Appendix C

Analysis of the induction time and the effect of hysteresis on the drop step size

In order to analyze the induction time, let us consider one complete cycle of oscillation for a 10 μl drop (Figure C1). There are three regions (A, B and C) where the drop is stationary. Region A corresponds to the induction time ($t_A \sim 0.16\text{s}$) for the angle of the advancing edge to increase to the critical advancing angle (i.e. when the edge moves) during the compression phase of the drop. Region B is the induction time ($t_B \sim 0.05$) for the contact angle at the receding edge to decrease to the critical receding angle while the drop is stretched. This difference in the induction times between regions A and B can be understood using a simple geometrical argument. Let us consider that a drop is sandwiched between two hypothetical surfaces with the following properties, $\theta_a = 70^\circ$ and $\theta_r = 60^\circ$. Using our model described in the text, we apply the constraint that the drop base diameter is constant. This constraint allows the estimation of the induction time required for the contact angle to transit between the advancing and receding angles (schematic of Figure C1). For a 10 μl drop vibrated at 1 Hz, we calculate t_A and t_B to be 0.14 s and 0.04 s respectively. As the plate spacing at the start of regions A and B are h_{max} and h_{min} , respectively, we conclude that the difference in the induction time at points A and B is due to the degree to which the drop is confined. The induction time identified at region C is due to the fact that the net displacement of the drop is controlled by the advancing step. This causes a period of ~ 0.12 s when the drop is stationary. In total, the drop is stationary for $\sim 1/3$ of the cycle of oscillation.

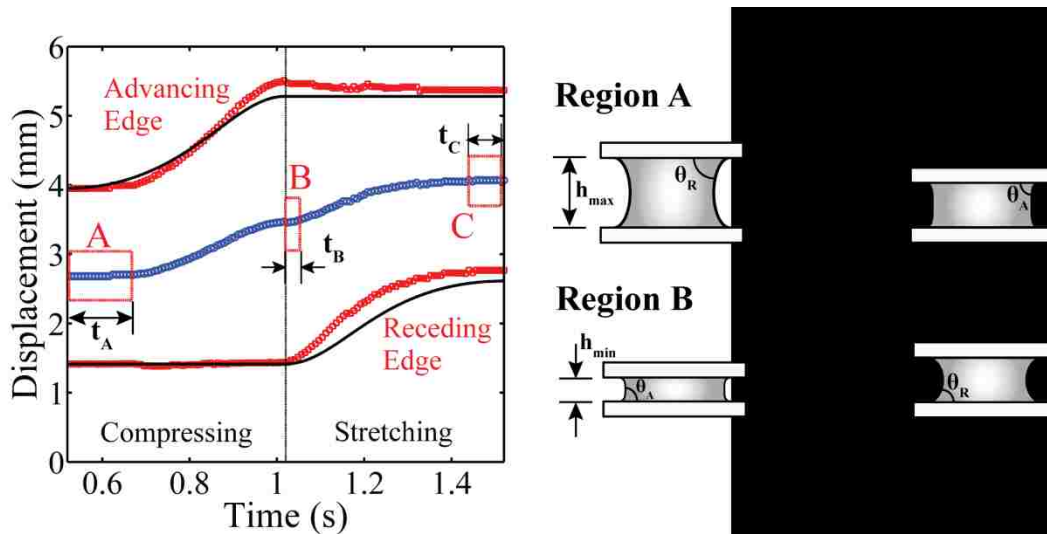


Figure C1: Magnified region of Figure 5.10 in the text. This region shows one complete cycle of oscillation of a $10\ \mu\text{l}$ drop vibrated at 1 Hz. The motion of the center of mass of the drop is represented by the blue line. The fits of the simple model are shown as solid black lines. The regions labeled as A, B and C correspond to the points when the drop is stationary. t_A , t_B and t_C are the induction times in the regions A, B and C, respectively. The left and the right sides of the plot are the compression and stretching stages respectively. The schematic on the right illustrates idealized drop behavior in regions A and B, which are used for the calculation described in the text.

We now examine the effect of hysteresis on the step size, Δx , of a drop. Figure C2 shows the simulation results for the base diameter for a $10\ \mu\text{l}$ drop in the fully compressed and fully stretched states as a function of contact angle. The step size corresponds to the difference between the diameters of the drops that lie on these two curves at a given angle. As the contact angle decreases, so does the step size. Let us consider a drop at point A initially in the stretched state on a part of the surface where the advancing and receding angles are 80° and 60° , respectively. As the fully stretched drop with a contact angle of 60° (point A) is compressed, the contact angle must exceed 80° before the contact line moves. The contact line comes to rest when the drop is in the fully compressed state with a contact angle of 80° (point B). The step size of this process

is then the length BC, ~ 1.13 mm. If the surface had zero hysteresis such that the contact angles of the fully stretched and fully compressed drop are 80° , the step size would be the length BD, ~ 1.36 mm. Therefore, in this simple model, a 20° hysteresis results in a $\sim 17\%$ decrease in step size. Despite this factor the simple model reported in the paper fits the data well without considering the effect of hysteresis on the step size. In order to account for this discrepancy we now relax the assumption that the drop footprint is circular. When the $10\ \mu\text{l}$ drop is compressed it is observed that the drop footprint becomes slightly elliptical with the semi-major axis orientating along the direction of the gradient. In order to compensate for the aforementioned decrease in step size due to hysteresis, the elliptical deformation would need to increase the step size by ~ 0.23 mm. From this requirement we approximate the elliptical dimension of the footprint to be ~ 2.15 mm and 1.9 mm for the semi-major and semi-minor axes respectively. As a frame of reference, the radius of a compressed drop with a circular footprint and contact angle of 80° is ~ 2 mm. Thus, it is reasonable to consider that a small elliptical deformation of the drop can compensate the reduction in step size due to hysteresis. It appears that it is due to the cancellation of these two factors that the simple model in the paper fits the data for the $10\ \mu\text{l}$ drop well. For the case of the $20\ \mu\text{l}$ drop it is possible that the elliptical deformation of the drop not only mitigates the effect of hysteresis but also enhances the drop velocity.

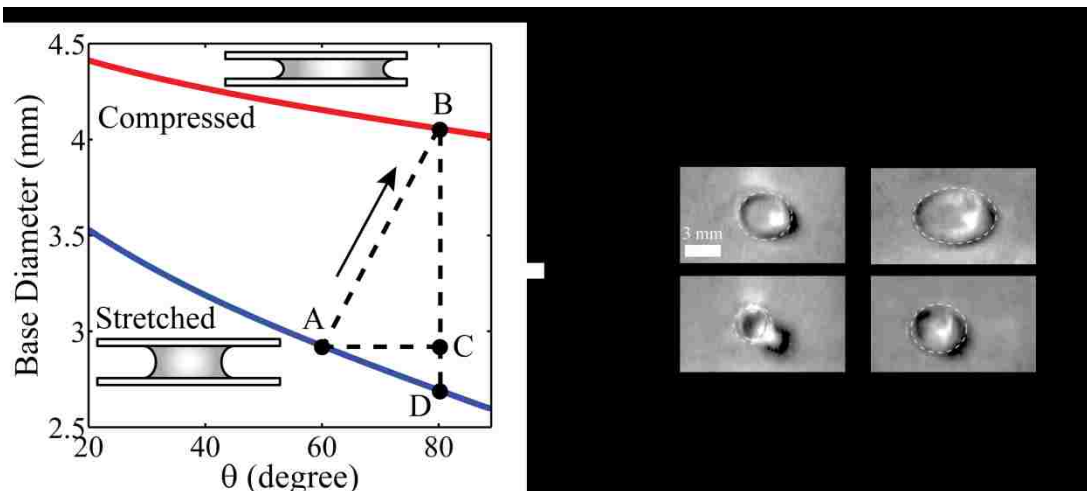


Figure C2: Left: The base diameters of a 10 μl drop in the fully stretched and fully compressed states as a function of the equilibrium contact angle. The red and blue lines represent the base diameter of the droplet in the fully compressed and fully stretched states, respectively. The markers A, B, C and D are used to highlight the effect of hysteresis on the drop step size, as explained in the text. Right: Droplet foot prints for 10 μl and 20 μl droplets moving along gradients prepared at 22° . The dashed circles are drawn around the peripheries of the drops in order to guide the eye. During the compression stage, the 20 μl drop footprint becomes elliptical whereas the 10 μl drop footprint is somewhat circular in comparison. During the extension cycles, the footprints of both the drops become circular.

Vita

Date of Birth 7th of December, 1981

Place of Birth Huddersfield, Yorkshire, England

Parents Sarah Anne Gwillam and David Neil Longley

Education

Lehigh University, Bethlehem, PA, USA, May 2013

Doctor of Philosophy in Chemical Engineering

Dissertation: Surface Modifications in Adhesion and Wetting

Nottingham University, Nottingham, England, May 2006

Masters of Engineering in Chemical Engineering

First Class Honours Degree

Publications

1. Jonathan E. Longley, L. Mahadevan and Manoj K. Chaudhury, "*How a Blister Heals*", under preparation
2. Jonathan E. Longley and Manoj K. Chaudhury, "*Electroless Deposition of Copper Through a Gel*", under preparation
3. Jonathan E. Longley and Manoj K. Chaudhury, "*An Anomalous Diffusion Coefficient to Characterize Surfaces Prepared using Mechanical Abrasion Techniques and its Relation to the Fracture Toughness of Bi-Material Interfaces*", under preparation
4. Jonathan E. Longley, Erin Dooley, Douglas Gilver, Bill Napier, Susan Daniel and Manoj K. Chaudhury, "*Ratcheting Motion of Sessile Droplets Induced by Shape Deformation on Surface Energy Gradients*", *Langmuir*, **2012**, 28, 13912-13918

5. Jonathan E. Longley and Manoj K. Chaudhury, "*Determination of the Modulus of Thin Sol-Gel films Using Buckling Instability*", *Macromolecules*, **2010**, 43, 6800-6810

Conference talks and Presentations

1. Office of Naval Research review meeting, Portland, OR, Feb **2011**, "*Edge effect from molecular-level surface features: the settlement response of cyprids to heterogeneous silanized surfaces*", Nick Aldred, Jonathan E. Longley, Manoj K. Chaudhury and Tony Claire
2. Adhesion Society Conference, Daytona, FL, Feb **2010**, "*Determination of the Modulus of Thin Sol-Gel films Using Buckling Instability*", Jonathan E. Longley and Manoj K. Chaudhury
3. Office of Naval Research review meeting, St. Petersburg, FL, Dec **2009**, "*Settlement behaviour of cyprids on surfaces with gradients in surface energy*", Nick Aldred, Tony S. Claire, Jonathan E. Longley and Manoj K. Chaudhury
4. Society of Plastics Engineers Polymer Nanocomposite conference, Bethlehem ,PA, Mar **2009**, "*Determination of the Elastic Moduli of Sol-Gel films using the method of Buckling Instability*", Jonathan E. Longley and Manoj K. Chaudhury
5. P.C. Rossin College of Engineering Undergraduate Research Symposium, Bethlehem, PA, May **2005**, "*The Weissenberg Phenomenon and its Relation to the Mixing of Oil Additives*", Jonathan E. Longley, Louis Yandoli and Antony McHugh

Invited Talks

- NIST polymer Surface/Interface Consortium, Eastman Chemicals, Kingsport, TN, March **2010**. "*Determination of the Modulus of thin Sol-Gel films using Buckling Instability*", Jonathan E. Longley and Manoj K. Chaudhury

Awards

- Society of Plastics Engineers Award for Excellence in Polymer Science and Engineering, Oct **2010**
- Adhesion Society 2nd place Alan Gent Distinguished Student Paper Award, Feb **2010**
- Adhesion Society Peebles Award for Graduate Student Research in Adhesion Science, Feb **2010**
- Society of Plastics Engineers, Mar **2009**, 1st prize Polymer Nanocomposites graduate student poster competition
- University of Nottingham Frank Witt award for outstanding student in Engineering, Jun **2006**

Leadership and Teaching experience

- Supervision of students throughout an Opportunity for student innovation course. Responsibilities were the organization and guidance for 3 undergraduates working on a research project. The work lead to a research paper published in Langmuir.
- Teaching assistant for unit operations laboratory and aqueous chemistry. Responsibilities for unit operation laboratory included experimental supervision and improvement of experiments and operation manuals. For aqueous chemistry preparation of lectures, exams (midterms and final) running review sessions and grading

Activities

- Endurance races, ultramarathons, obstacle course racing and triathlons. Completed Pennsylvania 1/2 IronMan. Placed 2nd in the team division in Worlds Toughest Mudder (WTM) 2012. WTM is an international qualification only non-stop 24hr endurance race featuring various obstacles.